Prediction and mitigation of cavity instabilities resulting from fluid-structure interactions

Mark Noun

RÉPUBLIQUE FRANÇAISE
Liberté Égalité Fraternité

Université de Toulouse

Doctorat de l'Université de Toulouse

préparé à Toulouse INP

Prédiction et mitigation des instabilités de cavités issues de l'interaction fluide-structure

---

Thèse présentée et soutenue, le 10 janvier 2024 par

Mark NOUN

École doctorale
MEGEP - Mécanique, Energétique, Génie civil, Procédés

Spécialité
Dynamique des fluides

Unité de recherche
CERFACS

Thèse dirigée par
Laurent GICQUEL et Gabriel STAFFELBACH

Composition du jury
M. Stéphane AUBERT, Président, Ecole centrale de Lyon
Mme Marlene SANJOSE, Rapporteure, École de technologie supérieure
M. Guillaume BALARAC, Rapporteur, Institut National Polytechnique de Grenoble
M. Antoine DAZIN, Examinateur, Ecole Nationale Supérieure d'Arts et Métiers
M. Laurent GICQUEL, Directeur de thèse, CERFACS
M. Gabriel STAFFELBACH, Co-directeur de thèse, CERFACS
M. Pavanakumar MOHANAMURALY, Co-encadrant de thèse, CERFACS

Membres invités
M. Matthieu Queguineur, Centre Nartional d'Etudes Spatiale (CNES)
M. Martin Seive, ArianeGroup

Résumé

Les phénomènes complexes et instationnaires au sein des cavités rotor/stator des turbopompes spatiales sont renommées en raison de leur capacité à engendrer des problèmes de vibrations ayant un impact dangereux sur le fonctionnement des moteurs. Cette problématique a en effet considérablement compliqué le développement et l'exploitation des moteurs de fusées. Ces dynamiques, couramment désignées sous le terme de "bandes de pression", résultent d'un mouvement oscillatoire du fluide, induisant un couplage avec la structure environnante, posant ainsi un risque significatif sur le fonctionnement de la turbopompe. L'objectif principal de cette thèse est de comprendre et de prédire numériquement l'origine de ces "bandes de pression" dans un contexte multiphysique. Dans cette optique, cette étude initie une investigation numérique et théorique des problèmes de vibrations forcées au sein d'une cavité académique, ainsi que des problèmes d'interaction fluide-structure, en mettant l'accent sur les instabilités hydrodynamiques et aéroélastiques. Ces écoulements se caractérisent intrinsèquement par leur tridimensionalité, principalement en raison de la présence de couches limites sur le rotor, le stator et le carénage de la cavité. En conséquence, et bien que les nombres de Reynolds de ces écoulements soient élevés, l'instabilité se manifeste sous forme de structures cohérentes, à la fois axisymétriques et/ou sous formes de spirales, qui peuvent être influencées par des forces dynamiques générées soit par la fusée elle-même soit par la turbopompe. Des expériences ont démontré que les écoulements dans les cavités axiales des turbopompes présentent un autre type d'instabilité provoquant un phénomène de flottement du rotor. Ces deux problèmes sont abordés dans cette étude en utilisant une simulation des grandes échelles (SGE), une approche dynamique des fluides numériques instationnaire. Cet outil a en effet révélé que la dynamique sous-jacente de l'écoulement peut être retrouvée, contrairement aux approches stationnaires telles que les simulations de type Navier-Stokes moyennées de Reynolds (RANS), qui ont échoué dans le passé à prédire de tels phénomènes. Grâce à la prédiction basée sur la SGE de l'écoulement, il est démontré que l'instabilité de l'écoulement à l'intérieur d'une turbopompe à hydrogène à échelle réduite est liée à des tourbillons qui présentent le potentiel de se coupler avec le rotor, ainsi qu'avec l'acoustique de la cavité. Ce couplage tripartite entre le fluide, le rotor et la cavité est spécifiquement traité en développant un code de mécanique des structures basé sur la méthode des éléments finis, permettant des analyses modales ainsi que des calculs élastodynamiques. Grâce à l'ensemble de ces outils numériques, des problèmes de vibrations forcées peuvent être abordés et sont d'abord étudiés en utilisant une configuration simple comprenant une géométrie cylindrique. Ce premier volet de l'étude est ensuite étendu aux écoulements de cavité en rotation, où la vibration du rotor provoque un décalage des modes hydrodynamiques et, dans certains cas, une suppression totale de ces modes. En réaction à ces réponses de l'écoulement seul, et pour aborder le context multiphysique, le solveur de mécanique des structures est couplé au code LES grâce à une chaîne de couplage numérique. Cette approche permet de résoudre des problèmes instationnaires et couplés fluide-structure. La stratégie de couplage adoptée est d'abord validée avec succès à l'aide de deux cas test: une poutre vibrante immergée dans un fluide immobile et un

cas de vibration induite par les tourbillons (VIV), où une allée de tourbillons de Kármán se détache d'un carré rigide et provoque des vibrations d'amplitude élevée d'une plaque élastique. Le solveur couplé est ensuite utilisé pour simuler l'interaction fluide-structure entre le rotor et l'écoulement interne de la turbopompe. Les résultats confirment le couplage vibroacoustique entre le fluide, le disque du rotor et la cavité, tel qu'observé lors des expériences. Cette simulation multiphysique a également permis de calculer la quantité nécessaire d'amortissement pour stabiliser un tel système, démontrant ainsi l'efficacité du couplage développé. Enfin, un cadre d'analyse de stabilité linéaire globale (GLSA) est détaillé et mis en œuvre pour fournir un aperçu des modes propres dominants et de leurs taux de croissance correspondants à l'intérieur de ces systèmes.

Abstract

Complex unsteady phenomena within rotor/stator cavities of space turbopumps have gained notoriety because of their propensity to induce vibration issues that are clearly detrimental to the operation of the engine. This problem has indeed rendered the development and operation of rocket engines a formidable undertaking. These dynamics, referred to as "pressure bands", are a consequence of a self-sustained oscillatory motion of the working fluid, thereby engendering a coupling with the solid structure posing a paramount risk to the operation of the turbopump and the structural integrity of its components. Understanding and predicting the source of "pressure bands" in a multi-physics context is the primary objective of this thesis. For instance, this work provides a numerical and theoretical investigation of forced vibration problems in enclosed rotating flows as well as fluid-structure interaction problems with a focus on hydrodynamic and aeroelastic instabilities. Note that these flows are inherently three dimensional due to the presence of boundary layers on the impeller, stator and cylindrical shroud. Consequently, at high Reynolds numbers, the flow instability is manifested through coherent axisymmetric and/or spiral structures that can be affected by dynamic loads either generated by the rocket or the turbopump itself. Experiments have shown that axial cavity flows also exhibit a different type of instability that lead to a flutter-like phenomena of the rotor. Both problems are addressed in this work using Large Eddy Simulation, an unsteady CFD approach, in conjunction to multiple predictive numerical strategies like Power Spectral Density (PSD) and Dynamic Mode Decomposition (DMD). All tools show that the underlying dynamics of the flow can be retrieved contrarily to steady approaches like Reynolds Averaged Navier-Stokes Simulations (RANS) that failed in the past to predict such phenomena. Thanks to LES flow only prediction, the flow instability inside a reduced scale hydrogen turbopump is retrieved and has the potential of coupling with the rotor as well as the acoustics of the cavity. To address this problem, a structural mechanics code based on the finite element method is developed to perform modal analyses as well as elastodynamic calculations. Thanks to all these numerical tools, forced vibration problems are first investigated using a bluff body configuration where a "lock-in" phenomenon is identified whenever a vortex shedding frequency converges to the forced vibration frequency. This first content of this study is later extended to enclosed rotating cavity flows where the vibration of the rotor causes a shift in the hydrodynamic modes and in some cases, a total suppression of these modes. Following these flow only responses and to go further, the structural mechanics solver is further developed and coupled to the LES code thanks to a numerical coupling chain that allows to solve fully unsteady and fully coupled fluid-structure interaction problems. The adopted coupling strategy is first successfully validated through two test cases: a vibrating beam immersed in a still fluid demonstrating that the fluid viscosity dampens the structure motion and brings it back to its initial position, and a Vortex Induced Vibration (VIV) case where a Kármán vortex street sheds from a rigid square and causes large amplitude vibrations of an elastic plate. The coupled solver is then used to simulate the fluid-structure interaction between the rotor disk and working fluid of the turbopump. Results confirm the vibroacoustic

coupling between the fluid, rotor disk and cavity obtained by experiments. This multi-physics simulation also allowed the calculation of the necessary amount of damping to stabilize such system demonstrating the capability of the developed coupling. To finish, a Global Linear Stability Analysis (GLSA) framework is detailed and performed to give more insight about the leading eigenmodes and their corresponding growth rate inside such systems.

Acknowledgements

I would like to begin by expressing my heartfelt gratitude to the French Space Agency (CNES) and ArianeGroup, not only for funding this PhD, but also for their trust and valuable partnership over the past few years that have truly enriched my academic journey. I am especially grateful for working alongside the exceptional engineers at both organizations, including Anaïs Brandeley (ArianeGroup), Fabien Juillet (ArianeGroup), Ariane Deneuve (ArianeGroup), Theophanie Cunat (ArianeGroup), Martin Seive (ArianeGroup), Sebastien LeMartelot (CNES) and Matthieu Queguineur (CNES). Matthieu, I vividly remember our initial encounter at CERFACS when you were a student. Your patience and dedication during those early discussions were fundamental to the successful start of this project.

I must also express my deep appreciation for my PhD advisors, Laurent Gicquel and Gabriel Staffelbach. Their unwavering support and availability, even amid their demanding schedules, have been a constant source of guidance. Beyond their expertise in our technical and research discussions, their calm, patient, and methodical approach to problem-solving has been an inspiration.

I would also like to extend my gratitude to all the senior researchers at CERFACS whome I interacted with, including Nicolas Odier, Olivier Vermorel, Florent Duchaine and Marc Montagnac. Their advice and insightful ideas have significantly shaped this work and I'm grateful for the collaborative atmosphere at CERFACS. A significant part of this work would not have been possible without the help of Pavan Mohanamuraly, with whom I had fruitful discussions around linear algebra and code coupling which sometimes took delightful detours into history and Indian gastronomy.

I'd like to extend my heartfelt thanks to the administrative department of CERFACS, particularly Michèle Campassens and Chantal Nasri for their support from the very first day. You always made time to answer all my administrative questions, whether they were work-related or personal.

I also want to acknowledge the camaraderie and friendships formed with fellow students at CERFACS during countless hours spent around launches and coffee breaks. Your presence has made workdays less stressful and more enjoyable.

Finally, I would like to express my deepest gratitude to my family. Despite the long distance that separates us, their unwavering encouragement and belief in me have been a constant source of strength and motivation. Their support has been the foundation upon which I've built my academic and professional journey.

To my parents,
to my sister,

Contents

Chapter 1

Foreword

Contents

In recent years, the space market has witnessed a staggering increase in demand of low orbit satellites and a clear explosion during the last decade. In parallel, the continuous increase of the number of space actors with different visions and objectives has undoubtedly pushed forward the scientific and technological race as well as the economic and political one. In this context, the European market clearly plays a key role with two major players: the French Space Agency (CNES) and ArianeGroup. This work is the result of a joint collaboration between these two actors which aim at addressing the muliphysical aspect of fluid/structure instabilities in space turbopumps. Indeed, mastering and if possible overcoming such problems is a major milestone towards building durable and reusable rocket engines. This foreword chapter introduces the topic of this Ph.D. with a brief history of rocketry and the major breakthroughs of the space sector that lead to today's turbopump technology. To finish, a detailed overview of the work performed in this context and for the past years is proposed through the description of each chapter of the present dissertation.

1.1 Space industry

Historical perspective

One of the most significant breakthroughs in space in the last century was the launch of the first artificial satellite, Sputnik 1, by the Soviet Union on October 4th, 1957. This event not only marked the inception of the "Space Age" but also ignited a technological and ideological competition between the Soviet Union and the United States, commonly referred to as the "Space Race." The launch of Sputnik 1 unequivocally demonstrated that a man-made object could be propelled into orbit around the Earth which had a profound impact on the world. It sent shockwaves throughout the world at large, leading to a heightened emphasis on science, technology and education. Additionally, it served as the catalyst for the creation of NASA, the United States' space agency, in 1958. Similarly in Europe, The French space agency, CNES (Centre National d'Etudes Spatiales), was created few years later in 1961 as part of France's efforts to develop its own independent space capabilities. Since its inception, CNES has played a major role in shaping the French space program and has contributed significantly to space science and exploration. One of CNES's most notable achievements is its role in the development of the Ariane rocket, which has become one of the most reliable and successful launch vehicles in the world. This successful achievement stems from a joint collaboration with Arianegroup, a European aerospace company that specializes in the production and operation of space launchers, particularly the Ariane family of rockets. These rockets have been a cornerstone of Europe's space launch capabilities and have played a crucial role in placing satellites, spacecraft, and payloads into various orbits including geostationary, polar, and Sun-synchronous orbits. The first member of the family, Ariane 1, made its maiden flight in 1979. It was a four-stage rocket and was primarily used for launching communication satellites into geostationary orbit. It had a

payload capacity of around 1.7 to 2.2 metric tons to geostationary transfer orbit (GTO). Sequential improvements led to Ariane 2 and 3, with enhanced capabilities through added strap-on boosters, followed by the highly versatile Ariane 4, operational in various configurations during the 1980s and 1990s for missions spanning communication, earth observation and scientific purposes. The introduction of Ariane 5 in 1996 marked a significant leap renowned for its heavy-lift capacity and accommodating multiple payloads including commercial satellites, scientific instruments and ISS supplies. Evolving further, Ariane 6, available in Ariane 62 and Ariane 64 variants, emerged as a modern, cost-effective successor, aiming to sustain Europe's competitive edge in the dynamic global launch market. The Ariane rockets have been used to launch numerous satellites and other spacecraft, including the European Space Agency's (ESA) Herschel Space Observatory and Planck Satellite, as well as many commercial payloads. CNES has also been active in the field of satellite technology. The agency has developed a number of Earth observation satellites, including the Spot series and the Pleiades series, which provide high-resolution imagery and are used for a wide range of applications, such as mapping, natural resource management and disaster monitoring. Additionally, CNES has also been involved in the development of a number of scientific satellites, such as the CNES-ESA Corot satellite, which was used to search for exoplanets and the CNES Microscope satellite which was dedicated to test the equivalence principle with unprecedented accuracy. In addition to its contributions to space technology, CNES has also played an important role in human spaceflight. The French astronaut Jean-Loup Chrétien was the first non-American or Soviet astronaut to conduct a spacewalk and the first Western European astronaut to visit space. Another monumental breakthrough in space during the past century was the landing of the first human on the Moon, achieved by NASA's Apollo 11 mission on July 20th, 1969. This achievement was widely regarded as a triumph of human accomplishment and technology. The Apollo program not only served as a crowning achievement but also laid the foundation for future space exploration, including the Space Shuttle program and the International Space Station, as well as fostering a new era of international cooperation in space.

These remarkable achievements are the result of more than two millennia of invention, experimentation, and discovery. Indeed, according to Pan (1987) the origins of rocket technology can be traced back to China, where the invention and utilization of gunpowder for military purposes occurred as early as the 10^{th} century. In 1897 the Russian mathematics professor Tsiolkovsky (1903) proposed the idea of space exploration by rocket and who later became known as the founding father of modern rocketry. In his work, he was the first to advocate the use of liquid propellant rocket engines. He also published his famous rocket equation which allows one to determine the maximum velocity of a rocket given a weight and fuel supply. The equation reveals that the relationship between speed and fuel is exponential. Despite the revolutionary nature of this equation, Tsiolkovsky (1903) did not convert his mathematical equations into an actual model. Nevertheless, his equation later helped the American physicist Goddard (1920) in building the first liquid fueled rocket in 1926 that flew for only two and a half seconds, climbed 12.5 meters and landed 56 meters away. Thereafter, Goddard published a pamphlet entitled "A Method of Reaching Extreme Altitudes" which is a mathematical analysis of what is today called

the meteorological sounding rocket. At the same period, Oberth (1924) published a book about rocket travel into outer space. This and other books inspired the development of the V-2 rocket which was the first long range guided ballistic missile and the first rocket ever to leave the boundary of the atmosphere and enter outer space. The German V-2 (*Vergeltungswaffe 2*, "Vengeance Weapon 2") was developed and built during the second world war in Germany by a team lead by Wernher Von Braun. This rocket witnessed its first successful launch in 1942. The V-2 rocket used a 75% C_2H_6O/O_2 (ethanol/water) mixture for fuel and liquid oxygen (LOX) as oxidizer as shown in Figure. 1.1. It was also the first rocket ever to make use of a turbopump, the main topic of this thesis that will be explained in the next section.

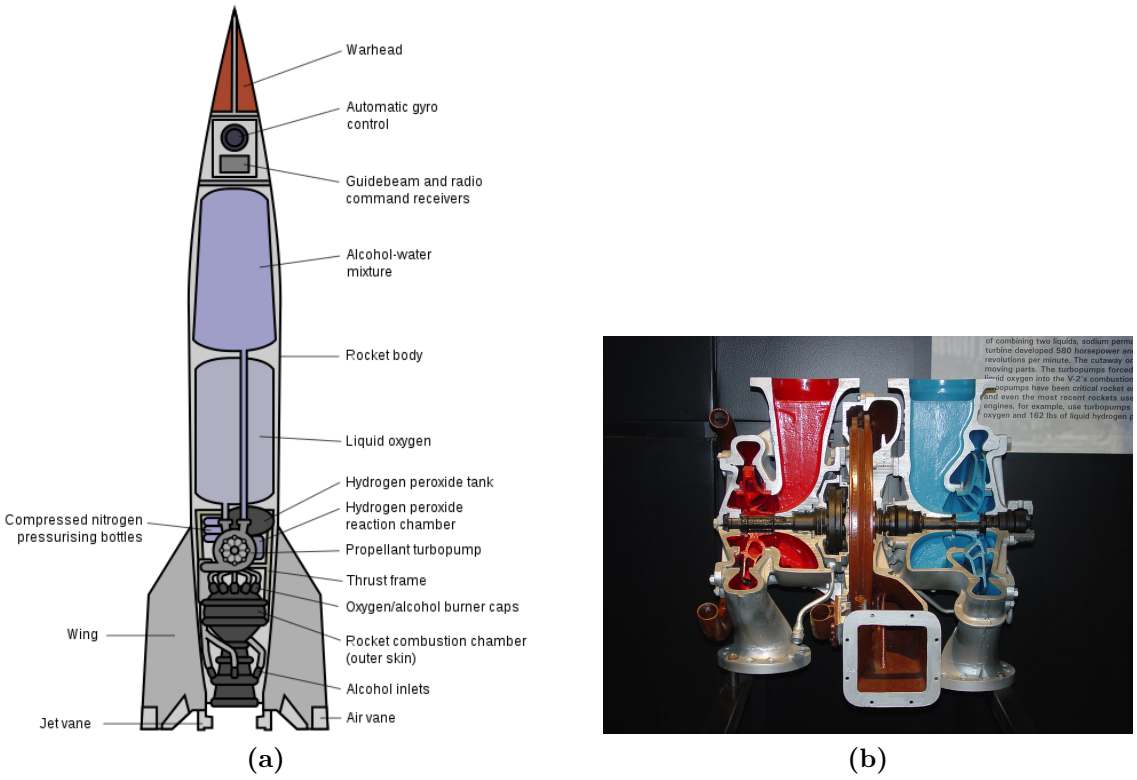

Figure 1.1: (*a*) Schematic diagram of the V-2 rocket, (*b*) V-2 rocket turbopump

Space propulsion systems and launcher technologies

Propulsion is the result of the force that propels an object through the air or into space. There are two predominant forms of propulsion solutions: solid and liquid based propellants. Solid rocket propulsion systems use solid propellants, while liquid rocket propulsion systems use liquid propellants (see Fig. 1.2). Each form of propulsion possesses its unique advantages and disadvantages, and the choice depends on the specific application and mission requirements.

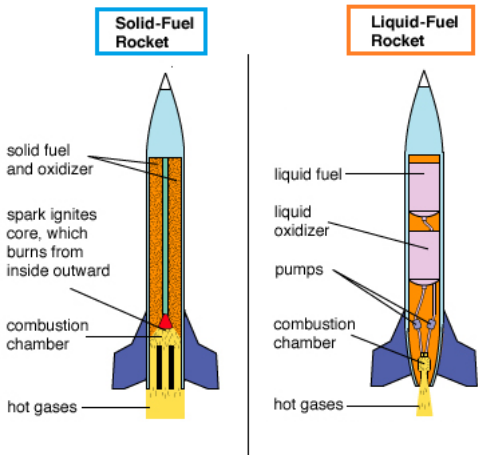

Figure 1.2: Cross section views of liquid and solid propellant rockets

Solid propellants are compounds containing the fuel and an oxidizer that are embedded within a solid casing. The propellant mixture is ignited at the base of the rocket and burns through the entire length of the casing, thereby generating thrust. Solid rocket propulsion systems are relatively simple to design and reliable in operation. They do not necessitate pumps, injectors, or other mechanical devices. They can be stored for prolonged periods without deterioration, making them particularly well-suited for military applications like missiles. Solid rocket propulsion is also frequently utilized as strap-on boosters, to increase thrust during the initial phase of flight, when a launch vehicle is still near the ground and atmospheric drag is significant.

Liquid propellants are chemical substances that are stored in tanks in their liquid form and pumped into the combustion chamber of the engine, where they are mixed and ignited to produce thrust. They are more intricate than solid rocket propulsion systems, but they also possess greater flexibility and efficiency. They provide more precise control over thrust and specific impulse. They can be shut off and restarted, allowing for multi-stage space launches. Finally, they have a higher specific impulse (a measure of the efficiency of the engine). They are usually preferred for high thrust and high-performance applications: *i.e.*, the main engines of heavy lift launch vehicles and upper stage propulsion engines. Note that there exist several types of liquid propellant rocket engine cycles, all have great implications for the turbomachines:

- **Pressure-fed cycle**, Fig. 1.3(a): It is a relatively simple type of liquid rocket engine cycle that is used primarily for small spacecraft and missiles. The fuel and oxidizer

are stored in tanks at high pressure and the pressure of the stored propellants is used to feed them into the engine combustion chamber. The pressure-fed cycle has the advantage of being relatively simple, reliable and lightweight, but it has lower thrust than other types of liquid rocket engine cycles. This system is similar to the one used by Goddard (1920).

- **Pump-fed cycle**, Fig. 1.3(b): It is a more complex type of liquid rocket engine cycle that is used for larger spacecraft and launch vehicles. The fuel and oxidizer are stored in tanks and pumped into the engine combustion chamber using external fuel dedicated pumps. This allows for greater flexibility in engine design and allows for a higher mass flow rate of propellants into the engine, which can result in higher thrust. The pump-fed cycle is more complex than the pressure-fed cycle, but it can provide much higher thrust and specific impulse.

- **Expander cycle**, Fig. 1.3(c): also known as the open cycle, it uses a gas generator to heat the propellants and drive a turbine that powers the pumps which are used to feed the propellants into the engine. The combustion products are then expelled directly into the nozzle to provide thrust. This cycle is simpler than the closed cycle, more reliable and easy to maintain. It's mostly used for low thrust and high specific impulse applications such as upper stage engines.

- **Gas generator cycle**, Fig. 1.3(d): The gas generator cycle, is similar to the expander cycle but with an additional combustion chamber that burns a small portion of the propellants to drive the turbine, while the rest of the propellants are expelled directly into the nozzle to provide thrust. This type of cycle is also considered as a reliable design, but less efficient than the closed cycle. It is mostly used for low thrust and high specific impulse applications such as upper stage engine or spacecraft propulsion.

Unlike the pressure-fed cycle, all other cycles possess a fuel and oxidizer pump to feed the propellants to the combustion chamber.

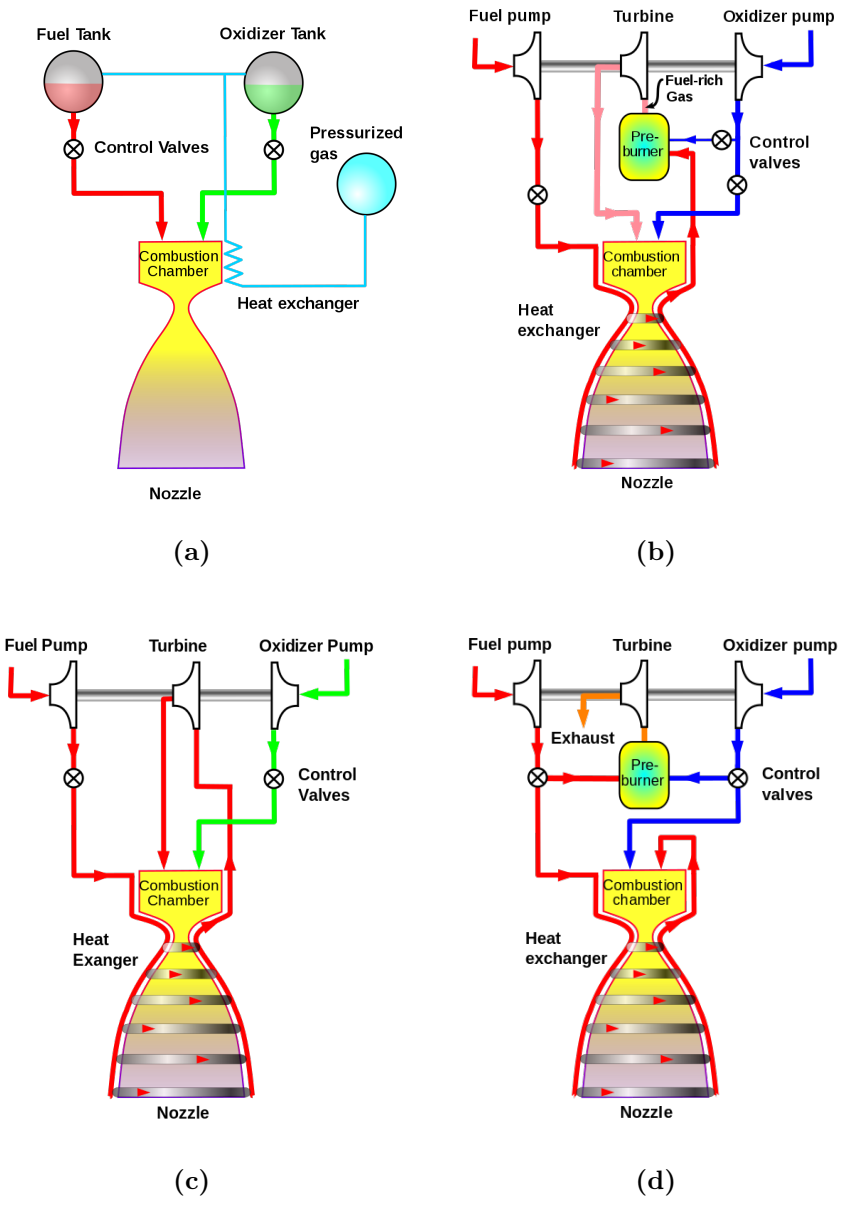

Figure 1.3: Schematic of a (a) pressure-fed cycle (b) staged/pumped combustion cycle (c) expander cycle (d) gas generator cycle.

Coming back to the historical perspective, the V-2 rocket operated using a gas generator cycle and a dedicated turbopump. The turbopump marked an inflection point in the design of modern rocketry. Indeed, this revolutionary device enabled rockets to reach unprecedented performance compared to any previous rocket. Thanks to this device, the V-2 rocket was able to sustain a maximum velocity of $1600\,m/s$ and a flight range of $320\,km$. The propellants were fed directly from the missile's tanks and injected at high pressure into the combustion chamber to ensure high thrust levels. The fuel and

oxidizer pumps were in this case steam turbines driven by exhaust gases from a steam generator, which catalyzed hydrogen peroxide into superheated steam and oxygen. The turbine wheels in turn powered the pump impellers for the two main propellants. The Vulcain 2 engine powering the Ariane 5 rocket for example possesses two different turbopumps: The TPH for the liquid hydrogen LH_2 and the TPO for the liquid oxygen LO_2 both shown on Fig. 1.4. Both systems are equipped with two stage turbines fed by exhaust gases coming from a single gas generator chamber. Different designs have since then been used for the assembly of rocket turbopumps. In the past, gears were commonly used in some engines but have since been replaced by pumps that are driven directly by turbines. It is possible to have one turbine driving both the fuel and oxidizer pump on a single shaft, and the decision of which design to use depends on a balance between cost, complexity and efficiency. For the pumps, both axial and radial designs are present in different configurations, radial pumps being the most prevalent and often equipped with an inducer to prevent cavitation.

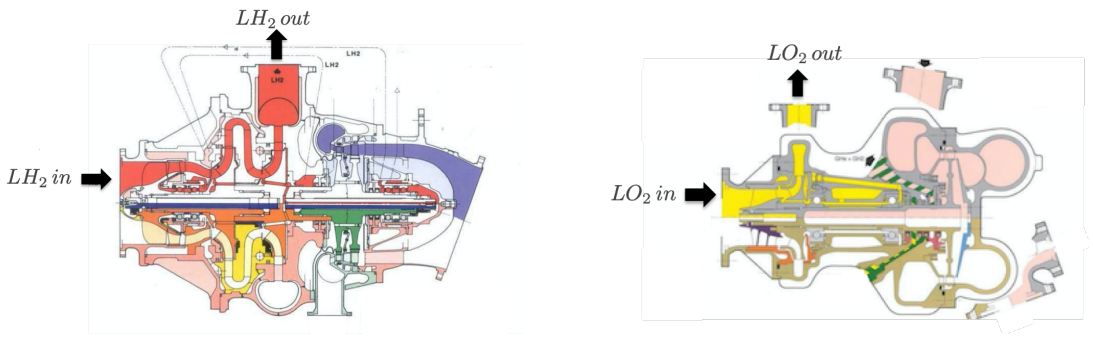

Figure 1.4: Schematic of (a) a liquid hydrogen turbopump and (b) a liquid oxygen turbopump

Such turbopumps are part of the Vulcain engine that has powered the Ariane 5 launcher, one of the most reliable heavy-lift launch vehicle in space history that is capable of launching large payloads, such as telecommunications satellites, into geostationary transfer orbit (GTO) and low Earth orbit (LEO). Ariane 5 has a payload capacity of up to 10 tons to GTO and up to 21 tons to LEO. The next generation of launcher, Ariane 6, will provide increased flexibility, reliability, and competitiveness for all types of missions, from small to heavy payloads and from low to highly elliptical and geostationary orbits. Ariane 6 will come in two versions: Ariane 62 with two P120 solid rocket boosters and Ariane 64 with four P120 solid rocket boosters (See Fig. 1.5). The main core stage will be powered by the Vinci re-ignitable cryogenic engine ensuring Ariane 6 to have a payload capability of up to 11 tons. Re-ignitable engines have also been developed by SpaceX with the Merlin engine series. The objective was here to develop the first reusable first stage launcher since it is the most expensive component. Reusability is considered to be the "holy grail" in rocket technology. Currently, exploited and reusable rockets are developed by SpaceX: *i.e.*, the Falcon 9 as well as Falcon Heavy rockets. In Europe, a joint collaboration between the European Space Agency (ESA) and the French space

agency (CNES) is aimed to build a single-stage reusable vehicle. With this goal in mind, the objective of the demonstrator is to test and demonstrate the feasibility of reusable rocket technology for use in future missions. Typically, the Themis demonstrator is a suborbital rocket that is designed to take off and land vertically, similar to the SpaceX's Falcon 9 rocket. Its first stage is designed to be reusable, meaning it can be used multiple times to reduce the cost of launches. This demonstrator has indeed be used for several test flights as well as research flights, but it is not used for commercial purposes.

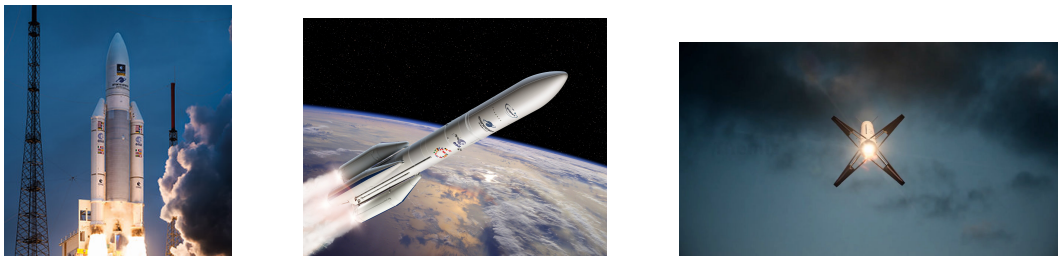

(a) **(b)** **(c)**

Figure 1.5: (*a*) Ariane 5 launcher (*b*) Ariane 64 (*c*) Themis demonstrator

1.2 PhD context

A major task in the development of rocket turbopumps is to ensure that the moving components, such as the blades or discs, as well as the static components do not have to sustain extreme vibration and associated structural problems. This means that during the design phase, the structural integrity of the different components should be maintained at the target operating point. This involves frequency calculations and stress analyses. A standard practice is to avoid disc and blade frequencies that are integral multiples of the harmonics of the rotation speed. The result is a so called Campbell diagram where the frequencies for different running conditions are plotted versus the rotor speed. According to Smith (1965), vibrations in turbomachinery can be split into two types: local vibrations and machine vibrations. The former refers to the vibrations that occur in a specific part or a component of a machine. It is usually caused by a problem or malfunction within the part or component, such as an unbalanced rotor or a malfunctioning bearing. The latter involves widespread motion throughout the entire machine which induces periodic reactions at the bearings, hence causing the static components to vibrate. It is caused by a variety of factors, like the interactions of multiple components, the alignment of the machine and the dynamic forces acting on the machine. Note that Baumgartner *et al.* (1995) have also classified the origin of these vibrations into two classes: forced or self-excited (see Fig. 1.6).

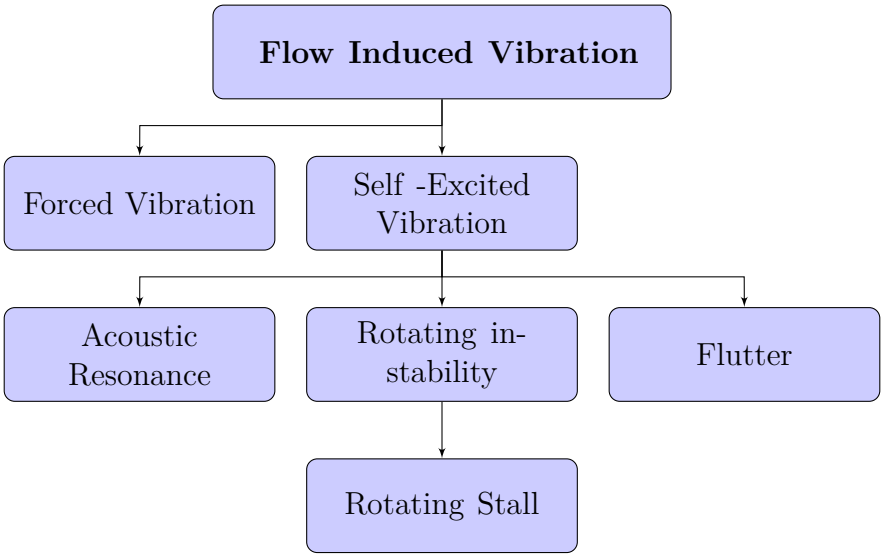

Figure 1.6: Classification of flow-induced vibration

Forced vibration refers to vibrations that are externally applied to a system, such as a rotor experiencing a cyclic pressure fluctuation due to the rotation of the blades in a steady non-uniform field. On the contrary, self-excited vibrations, also called autonomous or self-sustained vibrations are a type of vibration generated by the inherent dynamic characteristics of a system, such as flutter or an aeroelastic instability which occurs at or near the natural frequency of the rotor blade. Acoustic resonance is also a result of self-excited vibrations. High pressure levels can only be generated if the acoustic resonant

frequencies match the geometrical length of bleed cavities in turbomachinery devices. The frequency is determined primarily by the geometry. For example, the acoustic frequency of a Helmholtz-Resonator is affected by the resonator volume, the speed of sound and neck/hole diameter (Woodhouse (1991)). In terms of fluid dynamics, the excitation is caused by a vortex shedding frequency from the inlet hole. Parker & Stoneman (1985) found that vortex shedding from rotor/stator blades or support struts is a potential source of acoustic resonance and excitation in turbomachines. However, vortex shedding does not always excite an acoustic field; pressure fluctuations can be generated near blades with a different propagation speed. Rotating instabilities are a type of self induced vibration widely regarded as rotating stall. It happens when a section of the rotating blade row loses its ability to extract energy from the air flow, causing the air to separate from the blade surface and creating a region of low pressure. This leads to a stall condition where the blades are no longer able to produce the required lift and begin to stall, creating pulsations in the airflow and potentially damaging the machine. The onset of rotating stall can be caused by a number of factors, including changes to the inlet flow conditions, reductions in rotational speed, or an increase in the incidence angle of the blades. The reader can refer to Kameier (1994) and Kameier & Neise (1997) for more information on this topic.

Experimental campaigns have highlighted the presence of unsteady phenomena in rotor/stator cavities of turbopumps. Such features are referred to as *"Pressure band phenomenon"* which is a self-sustained oscillatory motion of the fluid characterized by constituent frequencies. This phenomenon has been first studied by Bridel-Bertomeu (2016*a*) at CERFACS. In his thesis, he focused on enclosed rotating flows in academic as well as industrial cases where he was able to identify the *"Pressure band phenomenon"* that manifests through dominant frequencies. This was possible by virtue of an unsteady CFD approach: *i.e.*, Large Eddy Simulation (LES). He later confirmed the inherent three dimensional nature of these modes through two predictive numerical strategies: Dynamic Mode Decomposition (DMD) and Local Linear Stability Analysis (LSA). Finally he was able to compute the sensitivity of these modes to geometric and temperature changes.

This initial project was then carried on through a second Ph.D. by Queguineur (2020) at CERFACS who put up different control strategies to suppress the *"Pressure band phenomenon"*: *i.e.*, either by shifting the frequencies found away from the natural frequency of the critical components of the turbopump or in some cases suppress them if possible. To do so, first a Large Eddy Simulation (LES) was carried out on an academic rotor/stator cavity as well as an industrial first stage turbine of a turbopump in order to extract the modes found in the *"Pressure band phenomenon"*. Then, a global linear stability analysis was used to identify the stability of these modes. The control strategy developed by Queguineur (2019) called Dynamic Mode Tracking and Control (DMT) was in this case shown to be an efficient method to compute a steady state flow by filtering the unstable temporal frequencies, essential to conduct stability analysis. One key advantage of the DMT over SFD (Selective frequency Damping) (Åkervik *et al.* (2006)) is that it enables the identification of modes present in periodic flows as well as their spatial and temporal evolution even in the nonlinear regime.

The main objective of this Ph.D. work is to extend the investigation of rotor/stator

cavities initiated by the previous two Ph.D's to take into account multiphysics aspects involving the fluid and the structure. Both LES and LSA are used in the following to address forced vibration and fluid-structure interaction (FSI) problems of enclosed rotating flows and axial cavity flows respectively. To this aim, a structural mechanics code is developed to perform modal analyses as well as elastodynamic calculations. This solver is then used as a basis to produce a fully coupled fluid-structure LES solver able to address FSI problems. Finally, a linear stability analysis is conducted to analyze fluid modes in all the addressed problems.

1.3 Overview of the thesis content and objectives

This Ph.D. work is divided into four main parts and focuses on the multiphysics phenomena of vibrations in axial flow and rotating flow cavities. The first part lays the groundwork of this thesis by demonstrating that LES is able to capture flow instabilities in a reduced-scale liquid hydrogen turbopump. An acoustic analysis of the cavity as well as a modal analysis of the rotor show that there is a risk of vibroacoustic coupling in this specific case. The second part is dedicated to forced vibration flow problems: *i.e.*, how the *"Pressure Band phenomenon"* reacts to external vibrations. The third part encapsulates a development work oriented to solve numerically fluid-structure interaction problems. Two test cases are considered to validate the approach which is then followed by a fully coupled FSI simulation of the turbopump. The last part of this document contains all the Global Linear Stability Analyzes (GLSA) used to retrieve hydrodynamic modes. All parts are composed of chapters, the details of which are as follows:

Chap 1, Foreword

The space market has witnessed a massive increase in competition throughout the past years. This trend will likely continue during the next few years to fulfill the demand for commercial satellites and to accelerate projects related to reusable launchers. A brief history of space achievements has been discussed at the beginning of this first chapter in addition to a presentation of the different types of launcher technologies that have been developed or are still under development. The key component of these launchers is also discussed in details: the turbomachinery device called turbopump. To this day, the turbopump remains a critical component with a tough scientific challenge for researchers and engineers to design and manufacture. In this context, the major problem that faces the development of these machines is referred to as *"Pressure Bands"*, also discussed in this chapter. It results in self-sustained oscillatory motions of the fluid that can couple to the surrounding structural parts of the cavity jeopardizing the structural integrity of the whole engine.

PART 1 Large eddy simulation of a reduced scale liquid hydrogen turbopump

Chap 2, Flow dynamics of the first stage rotodynamic pump using large eddy simulation

This chapter focuses on the hydrodynamic modes that arise inside the first-stage rotodynamic pump of a turbopump. First, the Large Eddy Simulation (LES) framework is established to identify the formation and distribution of these modes within such a cavity. The analysis is supported by Power Spectral Density (PSD) and Dynamic Mode Decomposition (DMD) techniques to reconstruct the spatial organization of the modes and their corresponding frequencies. To complement the flow analysis, an acoustic modal analysis is conducted on the cavity, likewise, a structural modal analysis is conducted on the rotor. To do so, a new in-house tool, developed to perform modal analysis on both fixed and rotating structures, is used to identify the natural frequencies of these components. Such structural frequencies are indeed an important indicator for designers to avoid resonance. Both structural and acoustic frequencies are found to match experimentally reported results from ping-tests as well as acoustic excitations, indicating the likelihood of a fluid-structure coupling with the first acoustic mode of the cavity.

PART 2 Forced vibration

Chap 3, Flow dynamics of forced vibration problems through large eddy simulation

This chapter addresses the first category of machine vibration, known as imposed vibration. First, two test cases are examined for illustration and preliminary validation of the code capacities: the flow past a vibrating cylinder and an academic rotor/stator cavity subject to periodic rotor oscillations. The first case identifies a lock-in phenomenon, where the vortex shedding frequency past a circular cylinder converges towards the forced frequency. This phenomenon occurs only within a specific range defined by the amplitude and frequency of vibration at a given Reynolds number. The second part of the chapter deals with the numerical investigation of the flow in an academic rotor/stator cavity subject to periodic rotor oscillations. The objective is to accurately capture the dynamics of such high Reynolds number rotating flows when subject to external forcing at a frequency equal to the two dominant modes found in the non-forced case. The results indicate that the periodic forcing in the flow indeed affects the stability of the modes retrieved, with new unstable modes emerging in the system while other modes present in the non-forced case completely disappears.

PART 3, Fluid-structure interaction using large eddy simulation

Chap 4, Development of a structural mechanics solver

This chapter addresses the development of a structural mechanics solver which is

a key element for simulating fluid-structure interaction problems. The solver is developed in FreeFEM++, an open source partial differential solver based on the finite element method. The steady and transient equations are both developed and evaluated using two numerical schemes: the Newmark beta method and the Generalized alpha method. The solver is then verified through a series of test cases from the literature. In the first test case, the static deflection of a rectangular beam subject to a constant loading is studied. The second test case consists in evaluating the dynamic response of a beam when subject to a time dependent loading. linear and quadratic elements are considered in each case to asses their capabilities in dealing with such problems. To enhance computational efficiency, direct solving methods are implemented when the size of the problem is relatively small and indirect methods with preconditioning are used for large problems whenever the memory requirement of the direct problem becomes a bottleneck.

Chap 5, Development of a numerical fluid-structure interaction chain

This chapter is the main focus of this thesis and involves a significant amount of numerical developments. Despite the fact that LES is not frequently used in FSI (Fluid-Structure Interaction) problems, the capacity of a flow solver to interact with a structure code is essential for understanding such a multiphysics phenomenon involving complex flow dynamics and structure motion. This is particularly critical in turbomachinery applications. To address this challenge, a structure mechanics solver is developed using FreeFEM++ to solve the transient elasticity equation. The solver is then coupled to the LES code through a Multiple Program Multiple Data (MPMD) communication model. MPMD is a type of parallel computing model in which multiple independent programs are executed simultaneously on multiple processors or computing nodes, each working on its own set of data. The communication between the two codes is achieved through the Coupling With Interpolation Parallel Interface (CWIPI), an open-source library developed by ONERA that handles data transfer and interpolation between codes through a non-conforming mesh interface. For our context, a CWIPI interface is also developed for FreeFEM++. To efficiently deform the mesh at the fluid-structure interface, a mesh management method called Laplacian smoothing is developed in the LES code to handle the mesh deformation of any structure. The coupled solver is then validated through two test cases: an immersed beam in a still fluid and a Vortex Induced Vibration (VIV) case. The first case demonstrates that, regardless of the fluid and solid parameters chosen, a vibrating beam in a still fluid returns to its equilibrium position after a certain time due to the fluid viscosity acting as a damper for the motion of the structure. The second case successfully captures the eigenmode and amplitude of vibration of a thin elastic plate proving that fluid-structure modes can be retrieved by the proposed LES-based solution.

Chap 6, Investigation of the coupled fluid-structure phenomena in a reduced scale LH2 turbopump

This chapter investigates the fluid-structure interaction phenomena inside the first-stage rotodynamic pump. The coupled FSI solver is used to simulate the fluid-structure interaction between the working fluid the rotor disk to identify potential multiphysics phenomena that are responsible for the detrimental vibration levels of the turbopump. Results show that the coupled FSI mode retrieved is responsible for destabilizing the axial balancing system of the turbopump. This mode causes the fluid and structure to oscillate at an identical frequency that is close to the natural frequency of the rotor as well as the natural acoustic frequency of the cavity leading to a vibroacoustic phenomenon between the two. In response to this issue, the required damping level necessary to stabilize the axial balancing system is meticulously calculated. This parameter is crucial for manufacturers to design a stable configuration. Finally, the undamped configuration is simulated and results show that the axial balancing system does indeed become unstable under certain operating conditions. Overall, these findings exhibit strong alignment with experimental data affirming the potential of the coupled solver to effectively simulate an industrial configuration.

PART 3, Mode identification of hydrodynamic instabilities

Chap 7, Global linear stability analysis

This chapter discusses both hydrodynamic and aeroelastic instabilities. A literature review covering both topics is presented first. Then, linear stability analysis is conducted on simple flow problems and enclosed rotating flow cavities. The method is also applied to forced vibration problems, demonstrating its capacity to reveal the underlying dynamics of the flow from a purely hydrodynamic perspective. Subsequently, the hydrodynamic based method is applied to fluid-structure interaction problems revealing certain limitations in these cases. The hydrodynamic analysis requires solving the linearized Navier-Stokes and continuity equations, which lack information about the structure dynamics. Nevertheless, the method can extract fluid modes of the fluid-structure coupling and display their spatial organization.

Chapter 2

Flow dynamics of the first stage rotodynamic pump using large eddy simulation

Contents

Self-induced vibrations are detrimental to the operation of space turbopumps. The origin of this phenomenon depends on multiple factors such as the static, the dynamic forces and moments acting on the system, the gas flow and the mechanical components. The purpose of the current investigation is to elucidate this phenomenon through numerical simulations. To do so, Large Eddy Simulation (LES) is used to retrieve the flow dynamics of the first stage of a reduced scale liquid hydrogen turbopump, for which unsteady phenomena are reported. Results show that the flow dynamics retrieved by LES can be attributed to pressure fluctuations in the fluid as confirmed by Power Spectral Density (PSD) and Dynamic Mode Decomposition (DMD). The instability takes the form of vortices forming near the upper valve clearance of the cavity and propagating downstream the housing. Acoustic and Modal analyses are then performed to complement this pure flow analysis. To do so, the Helmholtz and natural structural frequencies of the various components of this ideal turbopump are detailed. Good agreement is found with acoustic and ping tests obtained from experiments. The results suggest that the first acoustic frequency of the cavity is very close to the first natural structural frequency (or zero nodal diameter node) of the disc, indicating a possible three way coupling between the fluid, rotor disk and cavity acoustic and the appearance of a vibroacoustic phenomenon.

2.1 Introduction

Controlling the vibration and stability of turbopumps is an important factor that is required and considered in the design and operational phases. Vibrations in a turbopump can be caused by static as well as dynamic forces and moments, such as impeller rotation, flow oscillation. Mechanical components are also in this context to be addressed. These vibrations can cause wear and tear of the system and reduce its efficiency. Self-induced instabilities are particularly critical due to their detrimental effect on the structural integrity of the turbopump. One such instability is the flutter-like phenomenon of the rotor shaft designed with an Axial Balancing System (ABS). Such an axial balancing system is a mechanism used to balance the forces acting on the two faces of the rotor as shown on Fig. 2.1. In a self-balancing system, a piston is located at the back of the impeller and an inlet orifice of variable axial gap is present at the outer radius. When axial thrust on the rotating parts becomes important, the impeller moves in the axial direction (to the right of the figure) so that the clearance of the inlet orifice is adjusted resolving the imbalance through a pressure differential in the balance piston chamber. This Axial Balancing System (ABS) can however become unstable under certain conditions. For instance Shimura *et al.* (2012, 2013) have conducted many studies on such systems where they evaluate their dynamic stability by varying the chamber volume of the piston chamber, the clearance height of each orifice and the working fluid. They concluded that large axial vibrations can be suppressed by reducing the chamber volume and that fluid compressibility can destabilize the system. The problem is exacerbated when the acoustic frequencies of the cavity have the same order of magnitude as the natural

frequencies of the rotor which lead to resonance. Pereboom *et al.* (2016) have conducted experimental investigations on coupled acoustic-structural modes and the effect of fluid density and speed of sound. Within the same framework, a reduced scale liquid hydrogen

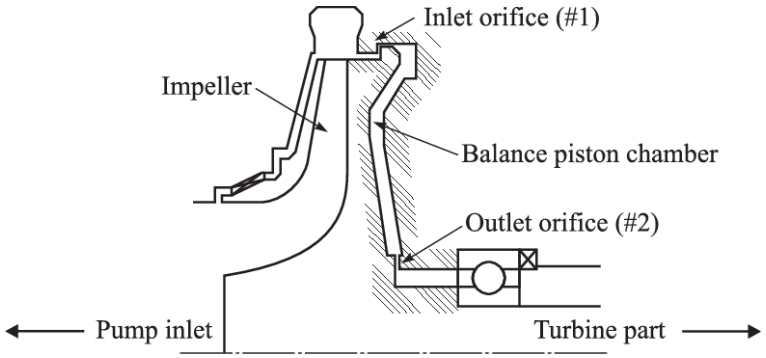

Figure 2.1: Schematic of a self-balancing system

turbopump has been developed by ArianeGroup and CNES to investigate the stability of an ABS (Edeline *et al.* (2002, 2004)). In that case, the ABS and turbopump can be tuned to mimic certain operating conditions including stable or unstable configurations. More details on this device can be found in Martin *et al.* (2022). As a complement, they also developed a coupled model between the shaft dynamics (modal analysis), the fluid inside the ABS and a linear model for the valves. A different test bench has also been developed within the same scope of study to investigate certain unstable configurations (see Fig. 2.2). The objective here is to investigate possible coupling between acoustic modes of the cavity and natural frequencies of the rotor. The associated experimental campaign is also of great interest from a numerical point of view since its geometrical simplicity allows for CFD computations. Brunier-Coulin *et al.* (2022) and Deneuve *et al.* (2020) conducted exhaustive experimental and numerical studies to investigate unsteady ABS configurations that exhibit a fluid-structure coupling. They found that for a set of flow rates and axial gap clearances, the ABS is unstable. They also pointed out a potential fluid-structure coupling between the first natural frequency of the disc and the first acoustic frequency of the cavity forming a type of Helmholtz oscillator and a hydraulic oscillator created by the upper valve. In order to address this particular configuration, a modal analysis is first conducted on the cavity as well as the rotor and results are compared to the experimental results of Brunier-Coulin *et al.* (2022). Then, LES is performed to investigate the potential appearance or need for a fluid-structure coupling.

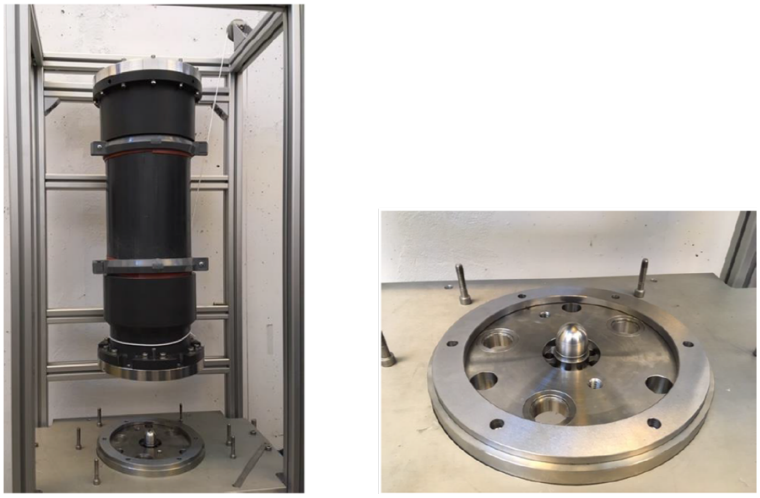

(a) **(b)**

Figure 2.2: (*a*) Test bench model (source: Deneuve *et al.* (2020)) (*b*) rotor disc

2.2 Cavity characteristics

The cavity of interest is designed to replicate the test bench geometry used for experimental studies. Only the ABS is considered here and represented on Fig. 2.3. The test bench design consists of a radial cavity of radius ϕ_{in} with a disk of height $\phi_{in} < \phi_{disk}$ and thickness h mounted on its shaft. The upper valve clearance, noted a_0, is secured by a steel ring that separates the housing from the upstream cavity. This clearance can be modified by using rings of variable thicknesses. However only one value is taken into account in this work. The CAD model used for all simulations is obtained by performing a 1° azimuthal extrusion of the complete axisymmetric model resulting in a similar configuration used by Deneuve *et al.* (2020) for their RANS and URANS calculations. The rotor is also fixed in this case to address the instabilities that arise from an axial flow. If the disk is rotating various instabilities may indeed appear. Their structure are discussed by Kang & Raman (2004) and D'Angelo & Mote (1993). In this configuration, the flow enters the first cavity and exits the second cavity at atmospheric pressure. The flow is laminar in the first cavity as well as through the upper valve as highlighted by experimental campaigns for the different inlet flow rates used and upper valve clearance heights. Instabilities may appear in the second cavity downstream the housing depending on the aforementioned parameters. The flow dynamics will be analyzed using the geometric parameters summed up in Tab. 2.1. Note that the geometric parameters of the cavity as well as the macroscopic quantities are normalized by their corresponding maximum values for confidentiality purposes.

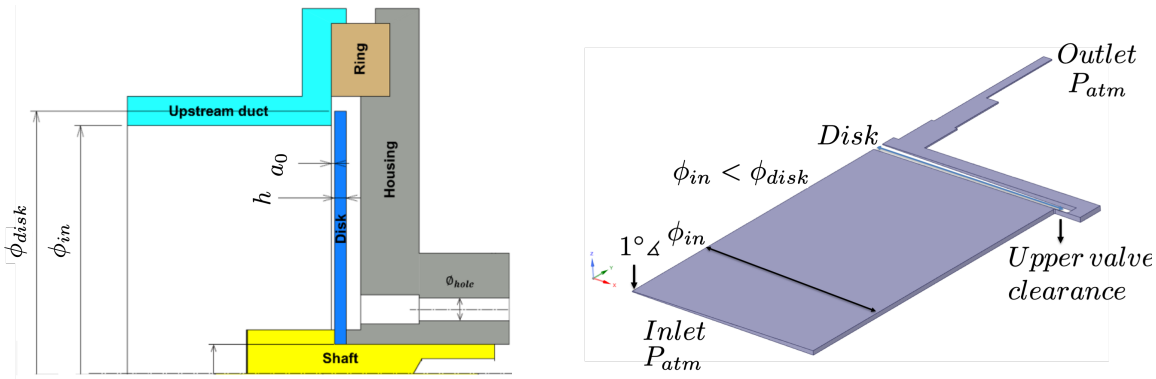

(a) **(b)**

Figure 2.3: (*a*) Test bench geometry (source:) (*b*) CAD model used for the simulation

Geometric parameters	
ϕ_{disk}	Disk Diameter
ϕ_{in}	Cavity Diameter
h	Disk thickness
a_0	Upper valve clearance

Table 2.1: Characteristic parameters of the cavity shown on Fig. 2.3.

2.2.1 Acoustic analysis

The propagation of acoustic waves in a medium is described by a second order partial differential equation called the acoustic wave equation (Helmholtz equation). It is typically written in the form:

$$\frac{\partial^2 p_{ac}}{\partial {x_i}^2} - \frac{1}{c^2}\frac{\partial {p_{ac}}^2}{\partial t^2} = 0, \tag{2.2.1}$$

where p_a is the acoustic pressure, x_i is a space direction described using Einstein's notation and c is the speed of sound. When dealing with linear acoustic, it is suitable to introduce $\hat{p}(x_i, \omega_{ac})$ the frequency domain counterpart of p_{ac}. The two quantities are related through the Fourier transform:

$$p_{ac}(x_i, t) = \int_{-\infty}^{+\infty} e^{i\omega_{ac}t}\hat{p}(x_i, \omega_{ac})d\omega. \tag{2.2.2}$$

Applying the Fourier transform and injecting it back in the Helmholtz equation yields a linear real eigenvalue problem and the angular frequencies of oscillation of a system.

To predict the natural acoustic frequencies of the cavity: *i.e.*, solve the resulting eigenvalue problem, a $3D$ Helmholtz solver called AVSP (Nicoud *et al.* (2007)) is used in the following. Note that this code solves the discretized wave equation on unstructured meshes in the spectral domain. The acoustic domain considered is illustrated on Fig. 2.4. For boundary conditions, infinite impedance is applied on walls ($\vec{V}_{ac} \cdot \vec{n}$ where $\vec{n}$ is the unit normal vector to the wall pointing outward). Zero velocity fluctuation ($u_{ac} = 0$) is imposed at the inlet and zero pressure fluctuation ($p_{ac} = 0$) is set at the outlet.

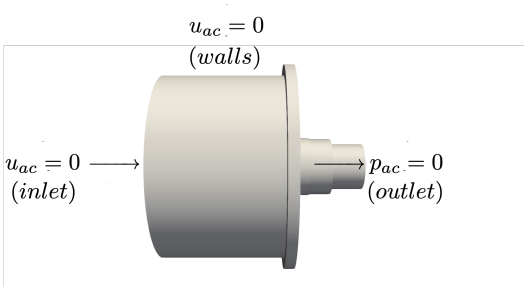

Figure 2.4: CAD model used for the acoustic calculations. The inlet condition is a velocity node and the outlet condition is a pressure node.

The first three acoustic frequencies are then calculated by solving the appropriate eigenvalue problem for a mean pressure of 101325 Pa. Their frequencies and corresponding mode shapes and phase angles are shown on Tab. 2.2 and Fig. 2.5 respectively. Note that the tabulated frequencies are normalized by the first acoustic mode of the cavity f_{ac_1} obtained by the experiments of Deneuve *et al.* (2020) using a microphone and speaker integrated in the balancing cavity. The first resulting acoustic mode is an axisymmetric one that pulsates in the axial direction and has a frequency of $1 f_{ac_1}$ matching the experimental value. All the characteristic frequencies related to this study are normalized by the first acoustic frequency of the cavity serving as a base reference and are denoted by the superscript $(*)$. The second and third modes are azimuthal modes that pulsate at higher frequencies. Note however that the study is restricted to the first mode as to address instabilities that arise from an axial flow.

	Normalized acoustic frequencies $f^*_{ac} = f/f_{ac_1}$
Mode 1 (axial)	1
Mode 2 (azimuthal)	1.82
Mode 3 (azimuthal)	2.03

Table 2.2: First three natural acoustic frequencies of the cavity.

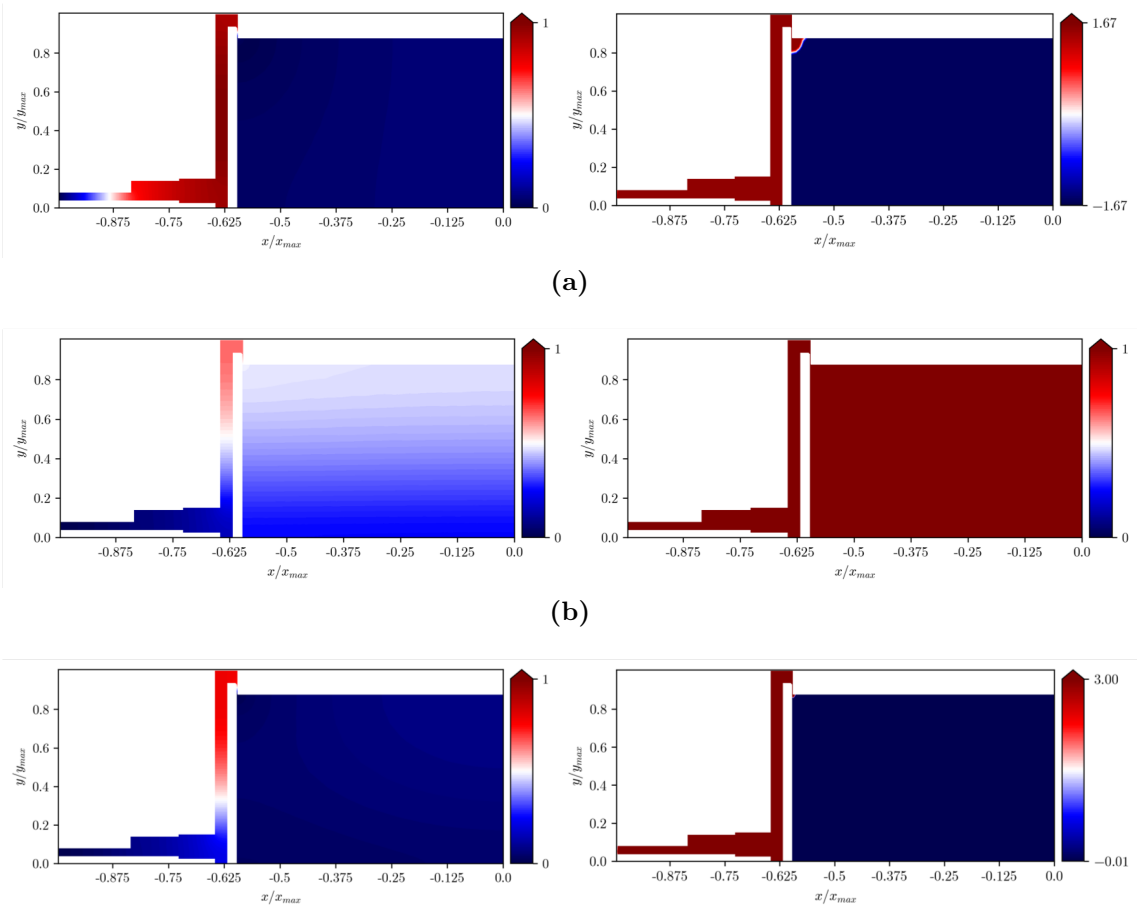

Figure 2.5: acoustic pressure mode shapes (left) and phase angles (right) of the first three natural acoustic frequencies: (*a*) Mode 1 (*b*) Mode 2 and (*c*) Mode 3

2.2.2 Structural modal analysis

Modal analysis is a technique also used to determine the dynamic characteristics of a structure: *i.e.*, its natural frequencies and modes of vibration. The goal is to identify the specific modes of vibration of the structure and to understand how the structure responds to different types of excitation. The mathematical model describing the dynamic response of a structure is written as,

$$\rho_s \frac{\partial^2 \xi}{\partial t^2} = \nabla \cdot \mathbf{P} + \rho_s \mathbf{f}. \tag{2.2.3}$$

This equation is known as the elastodynamic equation where ξ represents the displacement, $\mathbf{P}$ is the second Piola-Kirchoff stress tensor and $\mathbf{f}$ are the resultant external forces. This equation is derived in details in Chap. 5. For simplicity, the elastodynamic equation can be recast in a matrix form to model a multiple degrees of freedom (MDOF) linear mechanical system with viscous damping,

$$\mathbf{M}\ddot{U}_s + \mathbf{D}\dot{U}_s + \mathbf{K}U_s = \mathbf{F}_{ext}, \tag{2.2.4}$$

where $\ddot{U}_s$, $\dot{U}_s$ and U_s are vectors of the generalized acceleration, velocity and displacement while $\mathbf{F}_{ext}$ is the vector of the generalized (external forces) acting on the system. $\mathbf{M}$, $\mathbf{D}$ and $\mathbf{K}$ represent the matrices of inertia, viscous damping and stiffness coefficients respectively. In most conservatives systems, the inertia and stiffness matrices are symmetric, meaning $\mathbf{M} = \mathbf{M^T}$, $\mathbf{K} = \mathbf{K^T}$. In systems with multiple degrees of freedom, a natural state implies a certain configuration or shape taken by the system during motion. Note that a MDOF system possess not one but a finite number of states known as natural modes of vibration. Depending on the initial conditions or external forcing excitation, the system can vibrate following any of these modes or a combination of them. However, each mode corresponds to a unique frequency known as natural frequency. There are as many natural frequencies as natural modes. In the modeling of a n coupled 2^{nd} order ordinary differential equation, the motion in the direction of one degree of freedom depends on the coupling with other degrees of freedom. In the analysis below, the principal or natural coordinates are chosen to represent the system of n ordinary differential equations because in this particular generalized coordinate the equations become independent of each other (uncoupled). The natural coordinates are linear combinations of the (actual) physical coordinates. Hence, the motion in physical coordinates can be construed or interpreted as the superposition or combination of the motions in each natural coordinate. For the structure model to be studied one first considers an undamped case without external forces, so Eq. (2.2.4) reduces to,

$$\mathbf{M}\ddot{U}_s + \mathbf{K}U_s = 0. \tag{2.2.5}$$

This is a second order homogeneous differential equation that can be solved by assuming the solutions to be of the form,

$$u_s = \hat{u}_s e^{i\omega_s t}. \tag{2.2.6}$$

Solving Eq. (2.2.5) yields the free vibrational responses of the system each being associated to the set of natural frequencies ω_s. This equation is in the following solved using FreeFEM++ (Hecht (2012)), an open source tool focused on solving partial differential equations using the finite element method.

To do so, one transforms the PDE into its variational or weak form. It results in the mass matrix $\mathbf{M}$ which corresponds to the unsteady term and the stiffness matrix $\mathbf{K}$ which corresponds to the stress tensor term. After taking into account the Fourier decomposition of Eq. (2.2.6), the weak form of Eq. (2.2.5) for the displacement $\mathbf{u}_s(x_i) \in \mathbf{\Psi}_s$ is,

$$-\int_{\Omega_s} (\sigma(\mathbf{u}_s) : \epsilon_{ij}(\mathbf{\Psi}_s))d\Omega = \omega_s^2 \int_{\Omega_s} \rho_s((\mathbf{u}_s)\cdot(\mathbf{\Psi}_s))d\Omega, \tag{2.2.7}$$

$$-\int_{\Omega_s} (\lambda_s \boldsymbol{\nabla}\cdot\mathbf{u}_s\boldsymbol{\nabla}\cdot\mathbf{\Psi}_s + 2\mu_s\epsilon_{ij}(\mathbf{u}_s) : (\mathbf{\Psi}_s))d\Omega = \omega_s^2 \int_{\Omega_s} \rho_s((\mathbf{u}_s)\cdot(\mathbf{\Psi}_s))d\Omega \quad \forall \mathbf{\Psi}_s \in V. \tag{2.2.8}$$

$\mathbf{\Psi}_s$ is a linear closed subspace of $H^1(\Omega_s^2)$, ρ_s is the density of the structure and λ_s and μ_s are the Lamé coefficients. Solving this eigenvalue problem yields the natural frequencies associated to a structure fixed in a certain reference frame.

For problems involving a rotating structure such as a disc in rotation, additional terms are required. Indeed, while the structure is rotating it is subject to the Coriolis and centrifugal effects that are non-negligible forces where the former acts as a damping mechanism on the system while the latter acts as a stiffener. In a system of polar coordinates (r, θ, x) these forces are expressed as,

$$\boldsymbol{F}_{ext} = \underbrace{-2\rho_s\omega_s\partial t(u_r\mathbf{e}_\theta - u_\theta e_r)}_{\text{Coriolis}} + \underbrace{\rho_s\omega_s^2(r\mathbf{e_r} + u_r\mathbf{e_r} + u_\theta\mathbf{e}_\theta)}_{\text{Centrifugal}}. \tag{2.2.9}$$

The variational form of this damped system after Fourier decomposition hence becomes,

$$\begin{aligned}\int_{\Omega_s} (\omega_s^2\rho_s(\mathbf{u}_s) - \lambda_s\boldsymbol{\nabla}\cdot\mathbf{u}_s\boldsymbol{\nabla}\cdot\boldsymbol{\Psi}_s - 2\mu_s\epsilon_{ij}(\mathbf{u}_s) : (\boldsymbol{\Psi}_s) + 2\rho_s\omega_s\partial t(u_r\mathbf{e}_\theta - u_\theta e_r) \\ -\rho_s\omega_s^2(r\mathbf{e_r} + u_r\mathbf{e_r} + u_\theta\mathbf{e}_\theta)).(\boldsymbol{\Psi}_s)d\Omega\end{aligned} \tag{2.2.10}$$

where $\omega_s = \lambda_s + \omega_r$ is split into a growth rate and pulsation term. Such a quadratic system can be solved using the shift-invert transformation in conjunction with the subspace iteration method to track the fastest growing eigenmodes. To do so, the generalized eigenvalue problem $Au = \omega Bu$ is solved by first defining the matrix $OP = A - sB$ where s is the shift value (the eigenvalues computed are close to this value), A is the mass-normalized stiffness matrix and B is the mass-normalized damping matrix. The validation of the modal analysis solver is detailed in App. A.

In the present study, the mechanical eigenmodes of the rotor are of particular interest to investigate potential coupling with the acoustic modes of the cavity. In other words, check if the elastic wave pulsation of the disc is near the acoustic wave pulsation of the cavity. To do so, the rotor of Fig. 2.2 is modeled and meshed in FreeFEM++. It is a non-bladed hollow disc characterized by an internal radius r_i, an external radius r_o and a thickness h. Regarding boundary conditions, zero displacement and velocity are imposed at the inner radius ($U_s = 0$, $\dot{U}_s = 0$). The resolution of the corresponding problem provides the mode shapes of the disc for a fixed and rotating case (see Fig. 2.6). Their matching frequencies are presented in Tab. 2.3. The two modes correspond to the first eigenmode found exhibiting an axial vibration around its initial position and for which the nodal diameter is set equal to zero (axisymmetric deformation). The difference in natural frequencies is attributed to the added damping and stiffness effects of the rotating disc. Indeed, the Coriolis effect is an added term to the damping matrix while the centrifugal effect is an added term to the stiffness matrix. Hence, the resulting natural frequency is expected to be slightly modified due to the new nature of the system.

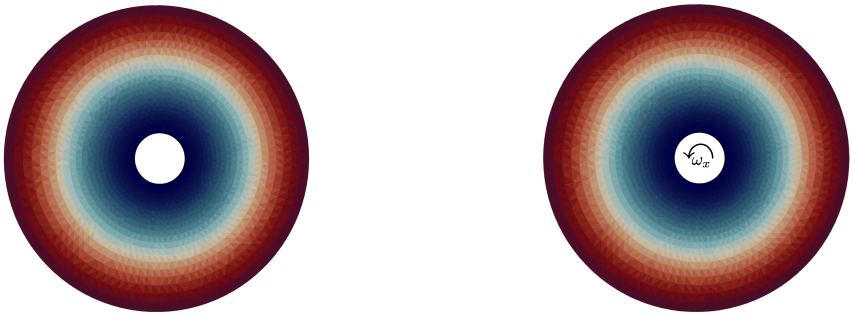

(a) **(b)**

Figure 2.6: (a) 1^{st} mode shape of the fixed disc (b) 1^{st} mode shape of the rotating disc

	Modal analysis	**Ping test**
$\omega^*_{d_{0ND}}$ (fixed)	0.97 $(0.97 f_{ac_1})$	0.99 $(0.99 f_{ac_1})$
$\omega^*_{d_{0ND}}$ (spinning)	$-0.0002 + 0.95i$ $(0.95 f_{ac_1})$	–

Table 2.3: Natural frequencies of the disc calculated via modal analysis and ping test experiments.

It is finally noted that the natural frequency of the disc in the fixed case matches the frequency obtained via ping test experiments from Brunier-Coulin *et al.* (2022) corroborating the probability of a fluid-structure coupling with the first acoustic mode of the cavity at $f^*_{d_{0ND}} \approx f^*_{ac_1}$

2.3 Large Eddy Simulation

The inherent unsteady nature of flows in turbomachines requires advanced modeling capabilities to successfully capture both large-scale flow structures and small-scale unsteady features. These small-scale structures are defined on a scale known as the Kolmogorov scale (Kolmogorov (1991)) while the large-scales are usually of the order of the domain size in which the flow proceeds. Large Eddy Simulation (LES) is often a suitable candidate for such cases (Sagaut (2006)), as it is a compromise between Direct Numerical Simulation (DNS) and Reynolds-Averaged Navier-Stokes (RANS) methods. While DNS can resolve all turbulence scales (either in time or space) thereby resulting in highly accurate flow predictions, it requires very fine mesh cells to capture small eddies and has a very high computational cost. On the other hand, although RANS does not require fine meshes, it does not resolve any scales of the turbulent spectrum but models it. As a result, only averaged quantities of the governing equations are obtained. These describe the statistically stationary mean flow and thus is limited to a steady vision of these flows.

LES equations

The system of equations describing LES is obtained by applying a spatial filer dependent on the mesh grid size to enable the separation of the large and small turbulent scales. This operation is mathematically described using a convolution product between a non filtered quantity Φ and a spatial filter G_Δ of a characteristic size Δ. The filtered quantity $\bar{\Phi}$ is then obtained from,

$$\bar{\Phi}_{(x,t)} = \int_\Omega G_\Delta(x,x')(x,x')\Phi(x',t)dx'. \tag{2.3.1}$$

Applying this filter results in the distinction of the unresolved or sub-grid scales Φ' which can be obtained by subtracting the filtered scale $\bar{\Phi}$ from the exact multi scale field Φ,

$$\Phi' = \Phi - \bar{\Phi}. \tag{2.3.2}$$

This decomposition is similar to the Reynolds decomposition for statistical methods and leads to the same problems when the flow is compressible. Thus, by analogy with the Favre average, the Favre filtered variable $\tilde{\Phi}$ (Favre (1983)) is usually introduced,

$$\tilde{\Phi} = \frac{\overline{\rho\Phi}}{\bar{\rho}}. \tag{2.3.3}$$

The filtered LES system of equations describing a compressible multispecies flow can then be written (using Einstein's notation where i, j and l represent the 3 space directions) as follows,

Filtered mass flow conservation:

$$\frac{\partial\bar{\rho}}{\partial t} + \frac{\partial}{\partial x_j}(\bar{\rho}\tilde{u}_j) = 0. \tag{2.3.4}$$

Filtered Momentum conservation:

$$\underbrace{\frac{\partial\bar{\rho}\tilde{u}_i}{\partial t}}_{\text{I}} + \underbrace{\frac{\partial}{\partial x_j}(\bar{\rho}\tilde{u}_i\tilde{u}_j)}_{\text{II}} = -\underbrace{\frac{\partial\bar{P}\delta_{ij}}{\partial x_j}}_{\text{III}} + \underbrace{\frac{\partial\bar{\tau}_{ij}}{\partial x_j} + \frac{\partial\bar{\tau}^t_{ij}}{\partial x_j}}_{\text{IV}}, \tag{2.3.5}$$

The terms highlighted in Roman numerals in Eq. (2.3.5) denote: the unsteady filtered term (I), the resolved convective term (II), the filtered pressure gradient (III) and the resolved viscous as well as turbulent stress tensor gradient (IV). The resolved viscous stress tensor $\bar{\tau}_{ij}$ is given by,

$$\bar{\tau}_{ij} = 2\mu(\tilde{S}_{ij} - \frac{1}{3}\delta_{ij}\tilde{S}_{ll}), \tag{2.3.6}$$

where $\tilde{S}_{ij}$ is the rate of the strain tensor defined as,

$$\tilde{S}_{ij} = \frac{1}{2}(\frac{\partial \tilde{u}_j}{\partial x_i} + \frac{\partial \tilde{u}_i}{\partial x_j}). \tag{2.3.7}$$

Similarly the unresolved stress tensor, $\bar{\tau_{ij}}^t$ is given by models that are detailed later.

Filtered species conservation:

$$\underbrace{\frac{\partial \bar{\rho}\widetilde{Y_k}}{\partial t}}_{\text{I}} + \underbrace{\frac{\partial}{\partial x_j}(\bar{\rho}\widetilde{Y_k}\tilde{u}_j)}_{\text{II}} = -\underbrace{\frac{\partial}{\partial x_j}[\overline{J_{k,j}} + \overline{J_{k,j}}^t]}_{\text{III}}. \tag{2.3.8}$$

This transport equation is needed for all chemical species k. Each term represents: an unsteady filtered term (I), a resolved convective term (II) and a filtered resolved and turbulent diffusion term (III).

Filtered Energy conservation:

$$\frac{\partial \bar{\rho}\widetilde{E}}{\partial t} + \frac{\partial}{\partial x_j}(\bar{\rho}\widetilde{E}\tilde{u}_j) = -\frac{\partial}{\partial x_j}[\overline{u_j(P\delta_{ij} - \tau_{ij})} + \bar{q}_j + \bar{q}_j^t], \tag{2.3.9}$$

where E is to the total energy and q_j is the heat flux.

To close this system of equations, an equation of state linking pressure, temperature and density is required. Assuming an ideal gas, this equation of state translates into,

$$\bar{P} = \bar{\rho} r \bar{T} \quad with \quad r = \frac{R}{W}, \tag{2.3.10}$$

where $R = 8.3143 J/mol/K$ is the universal gas constant and W is the mean molecular weight of the mixture: *i.e.*, summed over all the species so that,

$$\frac{1}{W} = \sum_{k=1}^{N} \frac{Y_k}{W_k}. \tag{2.3.11}$$

One key component that remains to be detailed is turbulence modeling. As said above, filtering induces a closure problem which is in our context modeled using gradient based approaches and the use of a so-called turbulent viscosity. Such sub-grid scale models are a type of turbulence models used to represent the effects of the small-scale unresolved turbulence that cannot be resolved by the numerical grid. These terms are $\bar{\tau}_{ij}^t$, $\bar{q}_j^t$ and $\overline{J_{k,j}}^t$ in Eqs.(2.3.4-2.3.9).
The subgrid-scale Reynolds stress tensor can be expressed as,

$$\bar{\tau_{ij}}^t = 2\bar{\rho}\nu_t(\widetilde{S}_{ij} - \frac{1}{3}\delta_{ij}\widetilde{S}_{ll}) \quad with \quad \widetilde{S}_{ij} = \frac{1}{2}(\frac{\partial \tilde{u}_i}{\partial x_j} + \frac{\partial \tilde{u}_j}{\partial x_i}), \tag{2.3.12}$$

where ν_t is the turbulent viscosity. To close this term, there exists many eddy viscosity models implemented in AVBP (CERFACS (2008)) that can be used.

One of the most commonly used eddy viscosity models for LES is the Smagorinsky model,

$$\nu_t = (C_S\Delta)^2\sqrt{2\widetilde{S}_{ij}\widetilde{S}_{ij}}, \tag{2.3.13}$$

where Δ is the filter length (square root of the node volume). This model assumes that the eddy viscosity is proportional to the square of the local strain rate and is scaled by a constant C_s, known as the Smagorinsky constant. The Smagorinsky model constant C_s is an *a priori* input usually set to 0.18. This model is capable of providing the right amount of dissipation of turbulent kinetic energy in homogeneous isotropic turbulent flows. However it presents some drawbacks because it introduces too much diffusion into the flow (Hoffman & Johnson (2006)) and the eddy viscosity does not vanish for a laminar flow.

To overcome these problems, Lilly (1967) introduced the dynamic Smagorinsky model that uses local flow information to calculate a local eddy viscosity that varies spatially and temporally. The key idea is to relate the magnitude of the subgrid-scale stresses to the resolved-scale quantities (through double filtering) in order to determine an appropriate value for the eddy viscosity. To do so, the closure coefficient C_{SD} is adjusted based on local flow conditions and is no more a user defined variable. By dynamically estimating the eddy viscosity based on local flow information, the dynamic Smagorinsky model provides a more accurate representation of the unresolved turbulence and improves the fidelity of the simulation compared to the original Smagorinsky model with a constant coefficient.

For wall bounded flows, Nicoud & Ducros (1999) proposed the WALE model to capture the effect of the wall boundaries on the turbulence, particularly in regions close to the walls where the turbulence is strongly influenced by the presence of the solid surface. In the following, the turbulent viscosity is expressed as,

$$\nu_t = (C_w\Delta)^2\frac{(s^d_{ij}s^d_{ji})^{3/2}}{(\widetilde{S}_{ij}\widetilde{S}_{ij})^{5/2} + (s^d_{ij}s^d_{ji})^{5/4}}, \tag{2.3.14}$$

where Δ is the filter length and $C_w = 0.325$ is the closure coefficient. Neveretheless, locality is lost with this model and only global quantities are to be trusted similar to the Smagorinsky model.

There exists a model that combines the best features of the dynamic Smagorinsky model as well as the WALE model which is the sigma model written as,

$$\nu_t = (C_\sigma\Delta)^2\,\frac{\sigma_3(\sigma_1-\sigma_2)(\sigma_2-\sigma_3)}{\sigma_1^2}. \tag{2.3.15}$$

This model is suitable for performing $3D$ computations however the Wall-adapting local eddy-viscosity model (WALE) model is preferred in this work.

2.4 Numerical model

For the LES, a mesh is generated on the CAD model of Fig. 2.3 by use of CENTAUR[1]. It is a fully unstructured tetrahedral mesh as shown on Fig. 2.7. Three elements in the azimuthal direction are used along the shaft and shroud to accurately capture the physics between the two periodic in-plane faces. In the upper cavity, the mesh size increases linearly starting from the inlet to the rotor. Since the underlying physics of the flow is dictated by the upper valve clearance, a particular attention is given to this region by enforcing five nodes in the gap. Note that a second mesh has also been generated with eight nodes in this region for validation purposes. All mesh characteristics are given in Tab. 2.4.

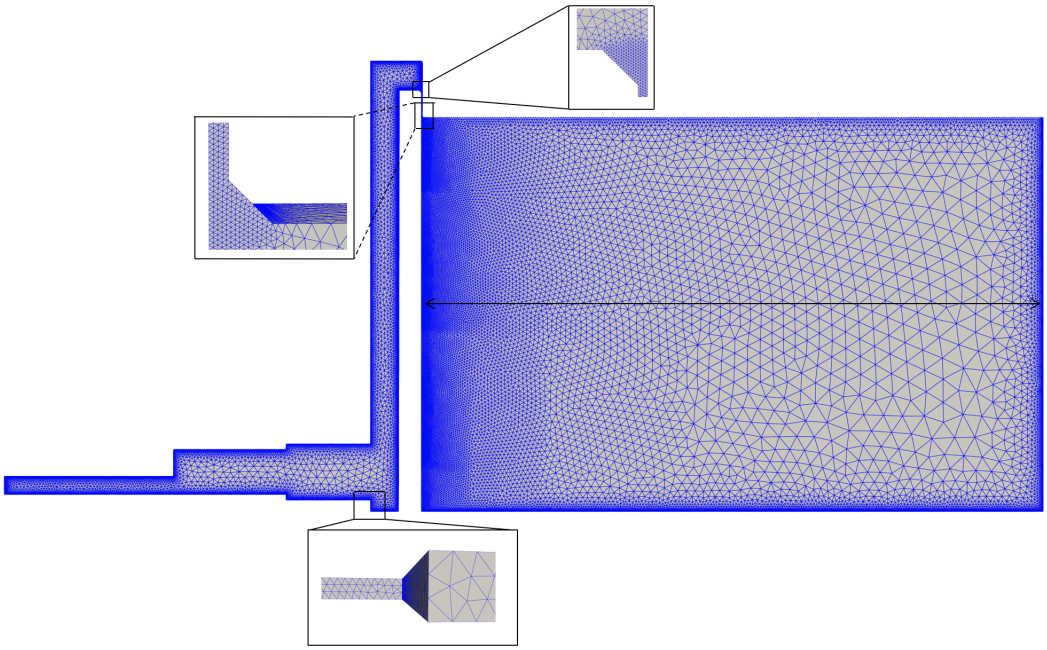

Figure 2.7: Fluid domain and its associated mesh

In order to evaluate the quality of the mesh at the walls, the non-dimensional wall distance $z^+ = z_1 u_\tau / \nu$ is computed. In this case, u_τ is the friction velocity at the nearest wall and ν is the local kinematic viscosity of the fluid while z_1 is the physical distance to wall of the first mesh point off the wall. For both cases, $z^+_{max} \approx 15$ or 10 is found in the clearance walls where the fluid experiences the highest wall shear stress. While this value is relatively large to ensure a wall resolved approach, it is important to underline that the flow in the gap does not reach a turbulent regime and always remains laminar. This is further discussed in the next section where the dynamics of the flow in the cavity is analyzed.

The LES is performed with the AVBP code (Gourdain *et al.* (2009)) developed by CERFACS. This massively parallel code is widely used in both academia and industry

[1] https://www.centaursoft.com/

	Mesh 1	**Mesh 2**
h_{min} [m]	1.46×10^{-5}	4.62×10^{-6}
h_{max} [m]	4.8×10^{-3}	4.46×10^{-3}
N_{nodes}	2.14×10^{5}	3.24×10^{5}
N_{cells}	9×10^{5}	1.5×10^{6}
z^{+}_{max}	15	10

Table 2.4: Mesh characteristic parameters of the cavity shown on Fig. 2.7.

	Numerical parameters
Solver type	Navier-Stokes
Convection scheme	Law-Wendroff
Sub-grid scale model	WALE
Laminar viscosity	Sutherland's law ($\mu_{ref} = 1.716 \times 10^{-5} Kg/m/s, T_{ref} = 2324K$)
Artificial viscosity	Colin sensor ($\epsilon_2 = 0.01, \epsilon_4 = 0.005$)

Table 2.5: Characteristic parameters of the cavity shown on Fig. 2.3.

(Seguí *et al.* (2018)). In this simulation, the second order Lax-Wendroff scheme is used. The time step is not fixed, but is dictated by the acoustic Courant Friedrichs Lewy number (CFL). In the present simulation, the CFL number is set to 0.7. The laminar viscosity of the flow is determined by Sutherland's law with the constants μ_{ref} and T_{ref} defined in Tab. 3.3, and the sub-grid turbulence model used is the WALE model (presented in section 2.3). It is more adequate than the classical Smagorinsky or dynamic Smagorinsky-Lilly (Lilly (1966)) models when dealing with wall bounded flows and low Reynolds number problems. To avoid small-scale numerical oscillations, a second-order artificial viscosity is introduced to smooth unresolved gradients and a fourth-order viscosity to dissipate potential wiggles. The artificial viscosity is applied based on the Colin sensor (Colin & Rudgyard (2000*b*); Colin (2000)) with a low level second-order coefficient, $\epsilon_2 = 0.01$ along with a fourth-order coefficient value of $\epsilon_4 = 0.005$. All the numerical parameters used for the simulation are reported in Tab. 2.5.

Regarding the numerical boundary treatments, a no-slip boundary condition is applied on all surfaces defining the shroud, hub and housing. This translates mathematically to $u_x = u_r = u_\theta$ on these surfaces where $\mathbf{u} = (u_x, u_r, u_\theta)$ are the three velocity components in the cylindrical coordinate system (x, r, θ). A periodic condition is enforced in the azimuthal direction between the two faces of the cavity. This greatly reduces the

computational domain size and reduces the number of grid points needed to accurately model the flow. Finally, all walls are treated as fully adiabatic walls.

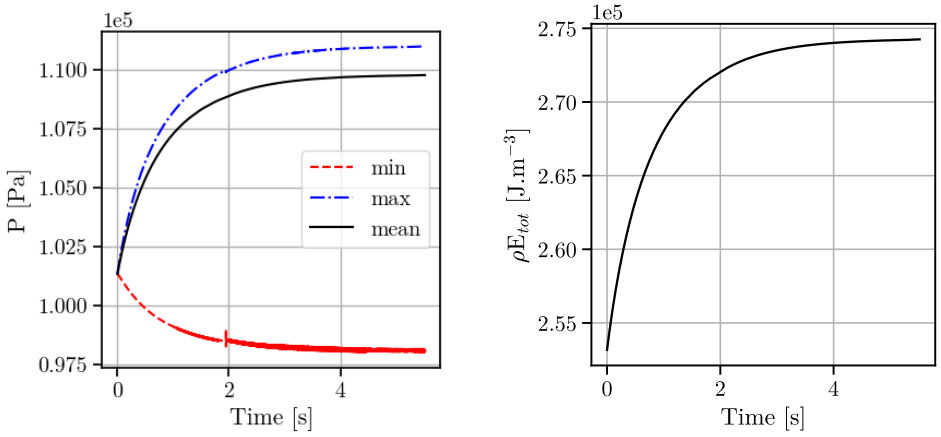

Figure 2.8: (*a*) Time evolution of the pressure and (*b*) average volumetric kinetic energy used to determine numerical convergence.

In terms of process, the simulation is first started with a no flow cavity using Mesh 1. The flow then establishes progressively through the imposition of the inflow conditions. Numerical convergence is attained when the volume average kinetic energy inside the domain reaches its maximum value and when the slope of the volume-average mean static temperature becomes almost constant. This specific evolution is shown on Fig. 2.8 for various macroscopic quantities as a function of time. Note that, the kinetic energy appears to fluctuate when approaching the flow limit cycle as indicated by Fig. 2.9 hinting that an unsteady behavior of the fluid inside the cavity effectively arises.

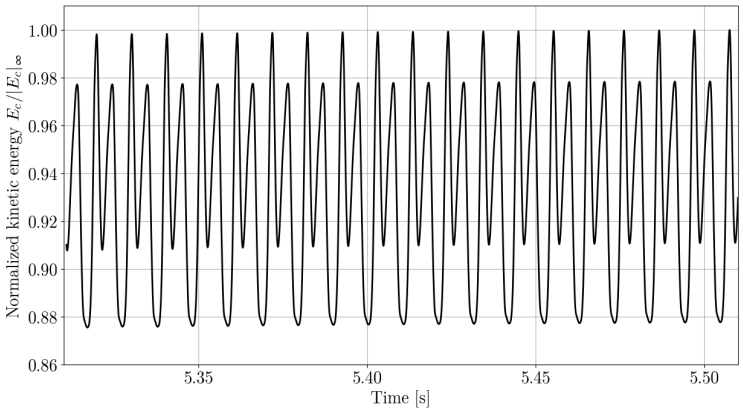

Figure 2.9: Time evolution of the dimensionless volume-averaged kinetic energy.

2.5 LES results and discussion

The LES results are presented in more details and discussed in the present section. The mean flow is first evaluated, followed by a thorough discussion of the instantaneous flow activity. To do so, use of Power Spectral Density (PSD) and Dynamic Mode Decomposition (DMD) is done.

2.5.1 Mean flow

At convergence, a pressure differential is created between the upstream and downstream cavities as demonstrated on Fig. 2.10(a). Indeed, since the two cavities are only separated by a small cross sectional area, a pressure build-up occurs in the upstream cavity to push the fluid through the upper valve clearance. In addition, this leads to an increase of the fluid velocity magnitude in this region. This observation is consistent with the fluid continuity equation. The continuity equation implies here that for a decrease in the cross-sectional area, the exit velocity (inlet of the upper valve) of the flow increases to conserve mass. Conversely, when the flow enters the housing, the cross sectional area increases and the flow velocity magnitude decreases. Figure. 2.10(b) shows the mean velocity magnitude at steady state. A small recirculating region is observed near the upper valve, along with slightly weaker velocity magnitude structures propagating within the housing. In the next section, a particular attention is given to this flow dynamics by analyzing instantaneous fields and dedicated post-processing tools.

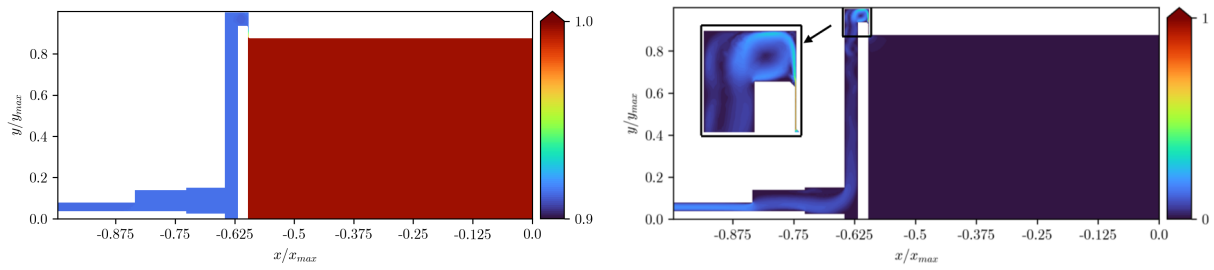

(a) **(b)**

Figure 2.10: (a) Mean pressure and (b) mean velocity magnitude at steady state

2.5.2 Flow activity

Instantaneous $2D$ cuts of the axial and radial velocities u_x and u_r are presented on Fig 2.11. The axial velocity is null in the upper valve clearance where the flow direction is purely radial and attains its maximum velocity. The rotor is fixed in this case rendering the azimuthal velocity negligible compared to the other two components. The flow hence runs through the parallel plates formed by the rotor and cavity walls. In this region the flow Reynolds number can be estimated to be,

$$Re = \frac{\rho D U}{\mu} = \frac{\rho a_0 \bar{u}_r}{\mu} = 898, \tag{2.5.1}$$

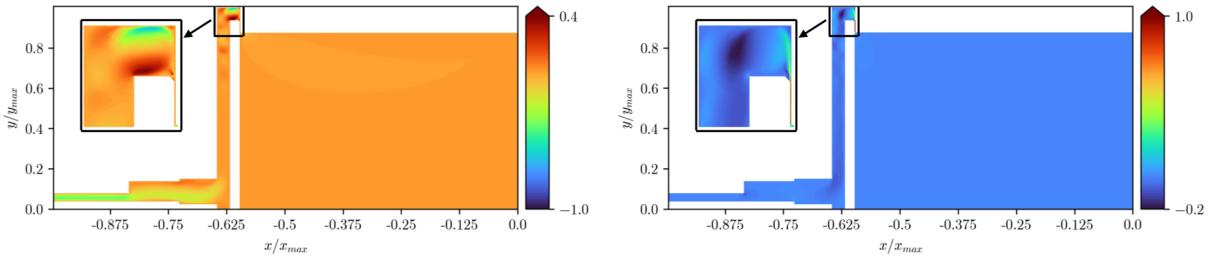

(a) **(b)**

Figure 2.11: (a) Instantaneous axial velocity and (b) instantaneous radial velocity

confirming that the flow is laminar in this region. However, as the flow enters the second cavity, the abrupt change in cross section area occurs resulting in a variation of the shear stress of the fluid. The flow which carries high momentum along the upper cavity wall then hits the shroud at a 90° angle at the exit of the valve. This creates a strong recirculation zone shown on Fig. 2.12 consistent with the observed mean field. However and as a result of non-linearity, vortical structures shed and propagate downstream the housing.

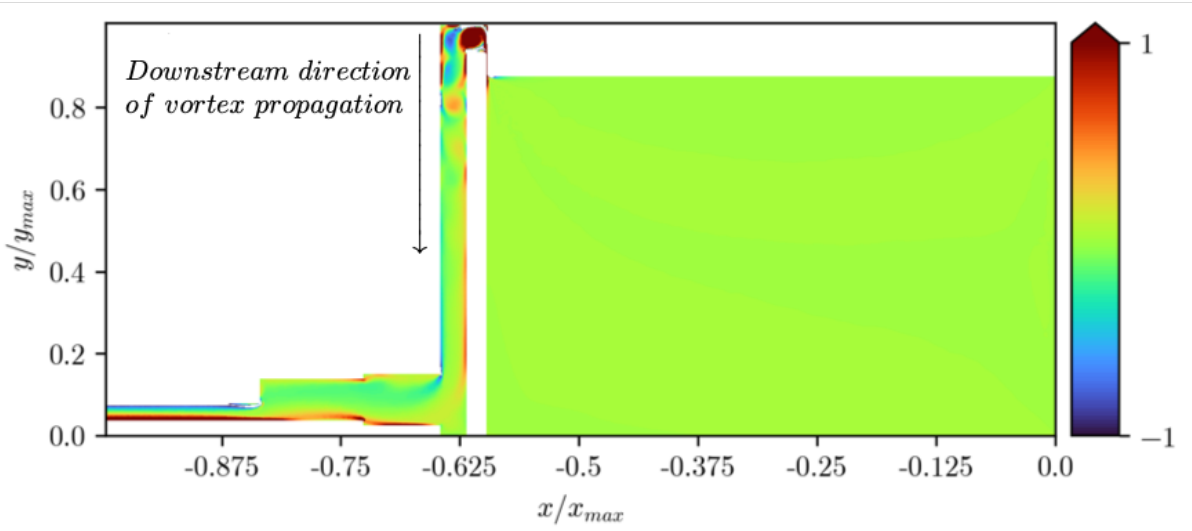

Figure 2.12: Instantaneous vorticity field

Figure. 2.13 combines different instantaneous snapshots of the velocity field focusing specifically on the housing. A recirculating flow clearly dominates positioned in the spacing located between the rotor and shroud. The corresponding unsteady activity appears such that: first, vortices are shed from the bigger bubble issued by the rotor gap

flow. Later downstream vortices appear to combine creating a periodic vortex shedding with a recombination phenomenon. This phenomenon is seen to occur once every $5 \times 10^{-3}\, s$ or for a frequency of $f^* = 0.328$.

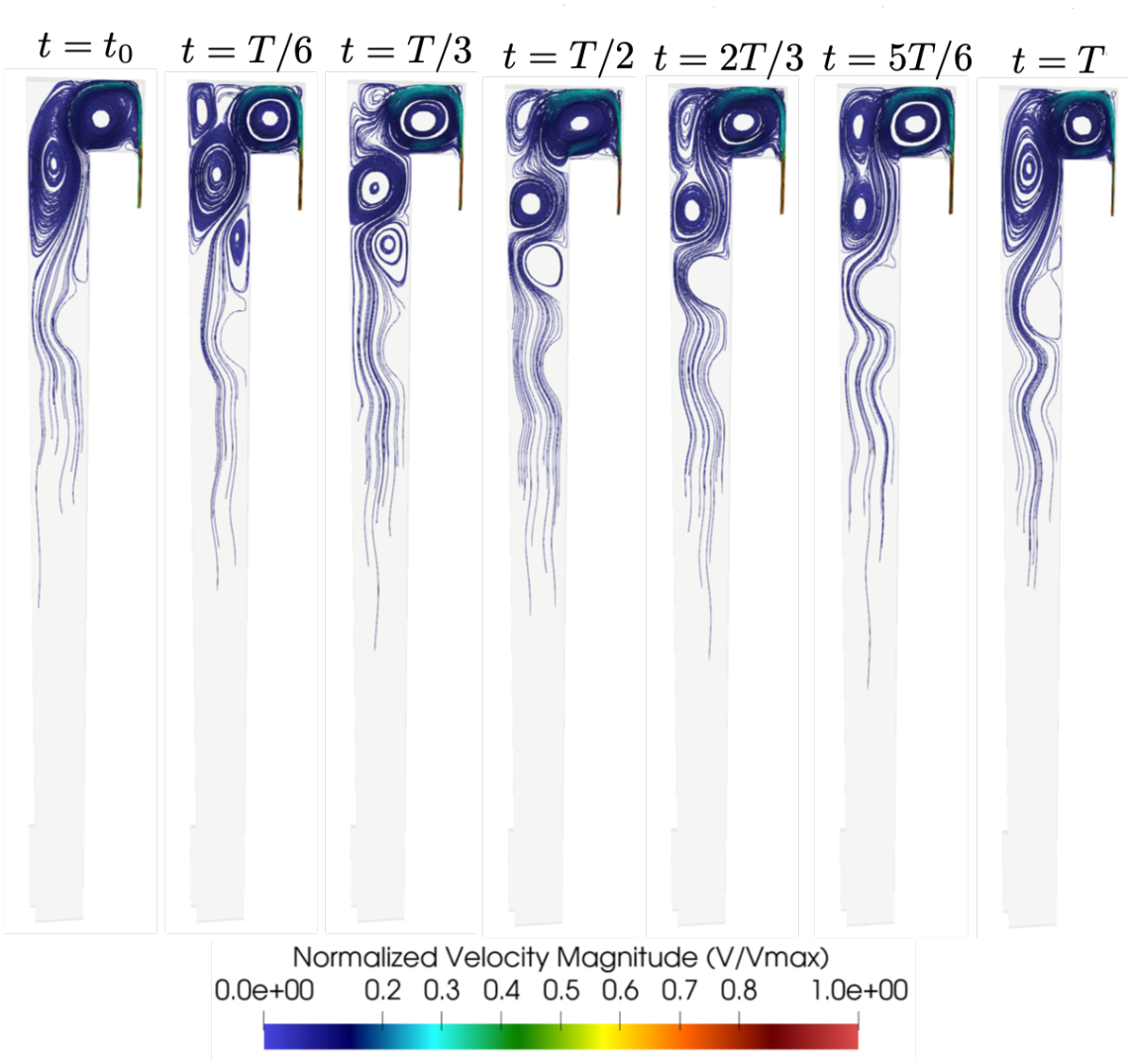

Figure 2.13: Snapshots of the velocity stream plot constituting one period of vortex shedding.

To identify the driving modes of the above described unsteady activity, numerical probes are placed in the upper valve clearance and housing to gather temporal data. Figure. 2.14 highlights the probes distribution inside the cavity. Multiple positions are placed near the upper valve as well as in the housing similarly to the instrumented test bench. For a clear identification the notations $UV - P$ and $H - P$ are introduced. They refers to the Upper Valve Probes (UV-P) and Housing Probes (H-P) respectively. Temporal data is then extracted during the flow limit-cycle. The pressure discrete signal is first used for the PSD and results are illustrated on Fig. 2.15(a) and Fig. 2.15(b) for the upper valve and housing respectively. Significant variation in energy across the spectra

are present as indicated by the multiple peaks. Two dominant peaks, respectively noted f_1^* and f_2^*, are observed in the spectrum, irrespective of the region indicating that the flow oscillates as a whole at $f_1^* = 0.157$ and $f_2^* = 0.314$. All other peaking frequencies are harmonics of these two hence their decreasing energy content. One also notes that the energy content of the frequencies increases as a function of distance from the upper valve then decreases in the housing. This is demonstrated by the difference in signal strength of $UV - P1$ and $UV - P6$ and $H - P1$ and $H - P4$ indicating that the source of the instability appears near the gap between the rotor and cavity and then dissipates in the housing. Note also that while both frequencies are predominant in both regions, a slight difference in amplitude can be observed. Near the upper valve, the highest peaking frequency corresponds to $f_1^* = 0.314$ while $f_2^* = 0.314$ corresponds to the secondary instability. Conversely, in the housing, the opposite phenomenon is observed with f_2^* being the primary instability and f_1^* the secondary instability indicating a potential transfer of energy: *i.e.*, mode interaction. Note that additional mesh refinements did not alter the behavior of these instabilities nor their constituent frequencies, subsequently only the post processing results of mesh 1 are described.

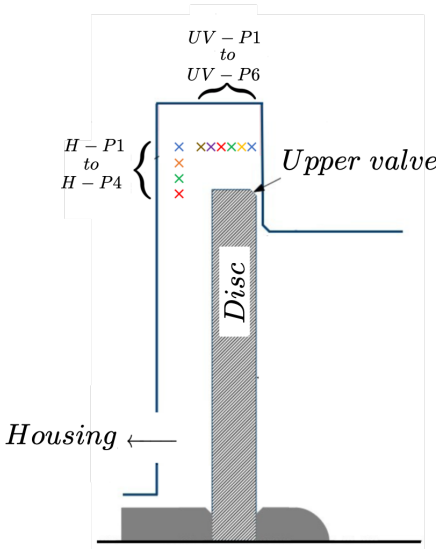

Figure 2.14: Repartition of the numerical probes inside the cavity. $UV - P$ and $H - P$ refer to the probes located near the upper valve and housing respectively. (Figure not to scale)

Based on the observed instantaneous fields and the spectral analysis, two different flow activities can be evidenced; the recirculaion zone oscillation and the corresponding vortex shedding downstream. Complemented by the fact that, as vortices start to shed, a larger vortex appear and form beneath the recirculation zone in a periodic fashion exhibiting a vortex pairing phenomenon.

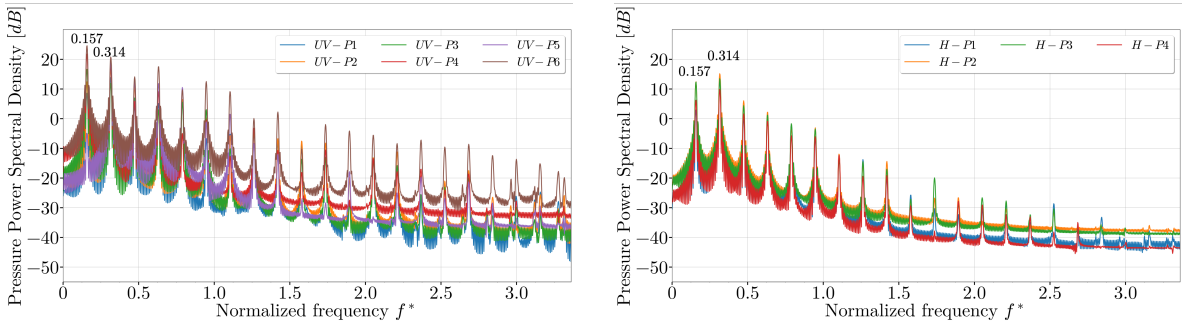

(a) **(b)**

Figure 2.15: Pressure power spectral densities computed at (a) upper valve and (b) housing.

Unlike PSD, modal decomposition techniques based on data-driven methods can extract coherent patterns as well as their frequencies thereby providing better insight to the underlying dynamics of the system. The most commonly used methods in the field of fluid dynamics are: Proper Orthogonal Decomposition (POD), Spectral Proper Orthogonal Decomposition (SPOD) and Dynamic Mode Decomposition (DMD). POD is based on the singular value decomposition (SVD) of the data matrix; it extracts spatially orthogonal and time independent energy ranked modes (Schmidt & Towne (2019); Brouzet *et al.* (2020)). This may lead to a merging of the modes of distinct frequencies in the same POD mode (Sieber *et al.* (2016)). DMD decomposes a time-series into a set of modes each of which is a combination of spatial patterns and temporal dynamics. In other words, each mode is associated with a certain frequency and growth rate, its stability being dictated by the sign of the latter (Brouzet *et al.* (2020)). Note that modes are in that case not ranked based on their energy content. SPOD is a variation of the POD method used to identify and analyze the dominant frequency dependent modes in a system while preserving the energy ranking feature of POD. The frequency dependent modes correspond to the optimally averaged DMD modes for a statistically stationary flow (Towne *et al.* (2018)). This last element represents one key advantage over DMD because of its inherent spatio-temporal consideration as well as its ability to rank modes based on energies. This is however at the expense of the notion of stability criterion. Consequently , it is chosen from here on to use the DMD (Schmid (2010)) approach so that results can be compared to a Global Linear Stability Analysis as detailed in the last chapter of the thesis.

DMD is thus applied by collecting a sequence of 100 equi-spaced snapshots from the unsteady predictions. To do so, the flow data is sampled at twice the maximum frequency of the signal to satisfy the Nyquist criterion and an overall duration of $0.25\,s$. Figure. 2.16 shows the spectrum found by DMD which confirms the PSD findings with two dominant peaking frequencies at $f_1^* = 0.164$ and $f_2^* = 0.328$. However, the second mode f_2^* constitutes the main instability inside the cavity. Figure 2.17 illustrates the perturbed velocity magnitude corresponding to the two frequencies. These two modes are seen to co-exist in the upper-valve region and entrance of the housing, the first mode

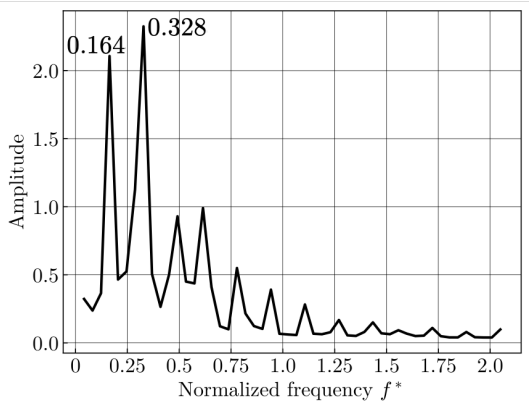

Figure 2.16: DMD signal spectrum.

being the most dominant in the former. This is attributed to the fact that the mode is stronger when the instability arises: *i.e.*, near the upper valve. The second mode f_2^* is spatially active in two regions. The first one locates between the upper valve and rotor while the second appears downstream beneath the rotor indicating that this mode can be attributed to the vortex shedding of the flow from the cavity. The spatial organization of these modes are in agreement with the PSD findings indicating that two hydrodynamic instabilities f_1^* and f_2^* interact with each other between the upper valve clearance and the housing. The dynamic of the flow is however dictated by the mode f_2^* as seen by the instantaneous snapshots and confirmed by the DMD signal amplitude.

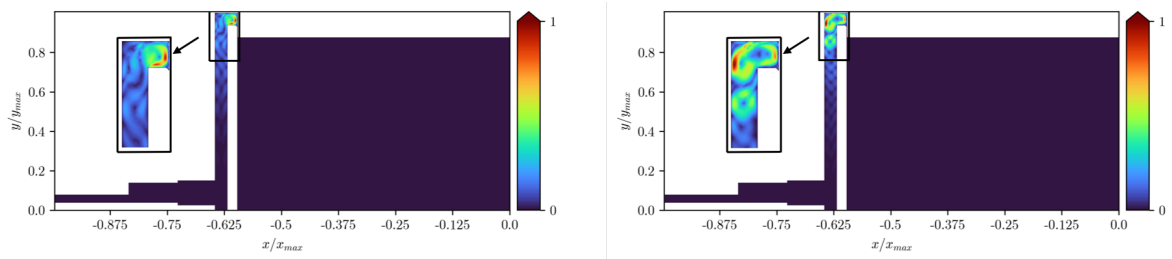

(a) **(b)**

Figure 2.17: Perturbed velocity magnitude mode shapes of the two most dominant modes in the cavity (a) f_1^* and (b) f_2^*.

2.6 Conclusion

The preliminary investigations of the single stage rotodynamic pump by LES evidences the presence of hydrodynamic, acoustic as well as structural modes with the potential convergence of all such processes in terms of frequency. Post-processing the LES results using techniques like PSD and DMD, show that for a fixed rotor, a flow instability arises near the upper valve which then propagates downstream creating vortex shedding. Two modes are effectively identified as responsible for the observed unsteady prediction. Their frequencies differ from the reported acoustic frequency of the cavity or natural frequency of the rotor. This indicates that such a flow only analysis may be insufficient to model the true response of an axial balancing system. This could have been anticipated since no prior knowledge guarantees that systems instabilities are purely hydrodynamic or acoustically driven, and the previous prediction confirms that is *a priori* not the case. To address this, the remainder of the thesis focus is on developing numerical tools to solve such multiphysics problem, specifically fluid-structure interaction. The next chapter examines first how hydrodynamic modes react to external vibrations, the first class of machine vibration. This is a preliminary step towards investigating fully coupled fluid-structure problems.

Chapter 3

Forced vibration problem in axial and rotating flows

Contents

Imposed vibration is the first class of machine vibration that can lead to structural fatigue and eventually failure. This periodic oscillatory motion can also affect the flow dynamics and alters its behavior by modifying the existing features of the system. To evaluate such a phenomenon while validating the approach, two test cases are considered: the flow past an oscillating cylinder and an academic/rotor stator cavity subject to rotor oscillations. In the former case, a "lock-in" behavior is observed: i.e., the frequency of the vortex shedding from the cylinder wake equals the imposed frequency of vibration. This particularity occurs for a certain range of frequencies and amplitudes of vibration at a given Reynolds number. In the following, multiple values of amplitude and frequency are considered for the same Reynolds number and results from simulations are found in agreement with experiments. In the second case, the external forcing is equal to the frequency of the two most unstable modes found in a non forced case. The objective is to mimic the rotor response at these frequencies. However, due to non-linearities and the high Reynolds number flow, flow modes are anticipated to respond differently. Indeed, the mode of the rotor boundary layer manifests with a very low energy content, as for the other modes in the system, new unstable modes have emerged in the cavity. Thanks to the previously established predictive numerical tools, LES in conjunction with DMD and PSD are proven to recover such dynamics when external forcing is applied.

3.1 Introduction

The flow past a circular cylinder is perhaps one of the most classical fluid mechanics problem and has been the prototype of many numerical as well as experimental studies as outlined in the reviews of Morkovin (1964), Norberg (1987) and Beaudan & Moin (1994). In fact, it is a main component to understand flow dynamics while being of interest to a large number of applications in many engineering fields. The flow configuration is in this case governed by a single non-dimensional parameter: the Reynolds number, $Re_D = \frac{U_\infty d}{\nu}$, where U_∞ is the free-stream velocity, d is the cylinder diameter and ν the kinematic viscosity of the fluid. Vastly different behaviors appear as the Reynolds number increases. For $Re_D < Re_c$, where Re_c is the critical Reynolds number roughly equal to 47, the flow is asymptotically steady with a pair of symmetric counter-rotating vortices forming behind the cylinder for $Re_D > 5$. At $Re = Re_c$, the flow undergoes the first instability through a Hopf bifurcation and becomes unstable leading to a vortex street as identified by Bernard (1908) and Kármán (1911). This laminar vortex shedding also referred to as Kármán vortex street, is seen for flows up to $Re_D \approx 190$. A second instability indeed arises near $Re_D = 188.5$, characterized by spanwise structures. Barkley & Henderson (1996) identified this instability by performing a $3D$ floquet analysis. Past this Reynolds number, the regime is referred to as the Williamson regime (Williamson (1996)) or mode A instability and occurs for $190 < Re_D < 260$. Beyond this interval, three dimensional spanwise structures become more predominant, which is known as mode B instability. As a result, the flow becomes more chaotic when the Reynolds

number continues to increase as pointed by Prasad & Williamson (1996) and Beaudan & Moin (1994). At around $Re_D \approx 1200$, a shear layer transition occurs followed by a boundary layer transition at $Re_D \approx 10^5$ accompanied by a dramatic decrease of the drag coefficient of the cylinder. The classification of these regimes was primarily based on experiments rendering the transition between them a difficult task to accurately define. Nevertheless, two non-dimensional parameters known as the Strouhal number and the base pressure coefficient curve allowed a classification of those regimes. When a periodic vortex shedding is established, the vortex shedding frequency f_s can be represented by the non-dimensional Strouhal (1878) number $St = \frac{f_s}{U_\infty}$. The relationship between St and Re has been a subject of intense scrutiny for a long time. Indeed, both Norberg (1987) and Fey *et al.* (1998) have reported a $St - Re$ relationship starting from Re_c where $St = 12$ to $Re = 2 \times 10^5$, the onset for boundary layer transition. All of the aforementioned studies have been conducted for a fixed cylinder. There are however cases where the cylinder is not fixed. In such cases, it can interact with the vortex shedding process. The present study is focused on two parts: first, the forced vibration of a $2D$ cylinder is analyzed for a Reynolds number of 100 by varying the amplitude and frequency of vibration. It appears that there is a complex relationship between the amplitude of the cylinder vibration and the flow Reynolds number for which a "lock-in" phenomenon is observed; *i.e.*, the frequency of the vortex shedding converges towards the imposed frequency of vibration. This preliminary study is done to validate all the necessary numerical tools required to solve such problems. Then, the analysis is extended to $3D$ enclosed rotating flows at high Reynolds number representing turbomachinery applications. In this context, the effect of the rotor vibration on the inherent flow instabilities inside an academic rotor/stator cavity is assessed. Such flow instabilities manifest through three dimensional structures at multiple locations inside the cavity and are sensitive to geometry as well as boundary conditions. Subsequently, any external perturbation can alter the dynamics of the flow. The aim of this study is to mimic real life problems where imposed vibrations can alter the flow behavior inside a turbomachinery device and eventually shift its operating point.

3.2 $2D$ Cylinder test case description

The problem and computational domain retained for the upcoming analyzes is represented on Fig. 3.1. As indicated, d is the diameter of the cylinder and for all simulations to come, the height of the computational domain H is $20d$. The upstream distance, L_u, between the inlet flow boundary and the center of the cylinder is chosen to be $10d$ to minimize inflow induced interaction. Likewise, the downstream distance, L_d, between the center of the cylinder and the outlet boundary is $20d$ for a total axial length, L, of $30d$. Note that the size of the domain can be critical and to avoid any errors caused by the effect of the boundary conditions, it needs to be addressed with care. Indeed, when Re_D is small, the flow is mainly governed by viscous effects whose region of influence varies with Re_D^{-1}. In such a regime Persillon & Braza (1998) showed that the aspect ratio of the domain should not be smaller than $\frac{H}{d} = 22$ for $Re_D = 100$ and the effects of the outlet boundary condition become negligible if $\frac{L}{d} \geq 34$. Although the actual size of the domain

is slightly smaller than the one advocated by Persillon & Braza (1998), the primary objective is to limit the number of cells in the domain and since Placzek *et al.* (2009) used a smaller configuration that provided accurate results, the above dimensions are retained.

Regarding boundary conditions, slip wall conditions are applied on the two lateral opposing walls. Only the streamwise velocity $u = U_\infty$ is imposed at the inlet, and pressure is imposed at the outlet. For the cases with a moving cylinder, a zone delimited by two fictive horizontal lines is defined as shown on Fig. 3.1 to facilitate the moving mesh procedure. The size of this block is $6d$ and is chosen to maintain the quality of the mesh around the cylinder as well as upstream and downstream the flow. When it comes to the mesh, it is fully unstructured and composed of triangular elements with 33 285 cells and 16 220 nodes. The mesh stretching is also introduced along the streamwise and axial directions around the cylinder, so that the mesh is finer near the cylinder wall and becomes coarser away from it. A probe $P1(2d;d)$ is added in the vicinity of the cylinder (relative to the origin of the coordinates which coincides with the cylinder center) to extract all the information needed for post-processing. Note that this point is slightly outside of the wake to minimize the influence of the upper vortex street and minimize the influence of the opposite vortex street in the measurement. When the cylinder is moving, a new formalism is introduced to account for the moving mesh: the Arbitrary Lagrangian-Eulerian method (ALE) developed by Hirt *et al.* (1974) and implemented in the code by Moureau *et al.* (2005). The ALE is a technique that combines the best features of both the Lagrangian and Eulerian approaches. In this framework, the nodes move in the continuum in a normal Lagrangian arbitrary way to provide a continuous banding capability. This computational framework allows greater deformation of the continuum compared to a Lagrangian approach with a superior resolution than the one allowed by a purely Eulerian method. This method has been extensively validated on piston engine simulations (Misdariis (2015)) and in rotating channels (Fransen *et al.* (2013)). Particular attention is however needed to maintain conservation around the moving block. Typically, the continuity of the velocities imposes the following equality at a walls,

$$v = \dot{y_c} \quad \text{on } \Gamma, \tag{3.2.1}$$

where v is the fluid velocity while $\dot{y_c}$ is the cylinder wall velocity and Γ denotes the moving interface. More details around the numerical implementation of the moving mesh is discussed thereafter.

All simulations discussed hereafter are performed with AVBP (Gourdain *et al.* (2009)) using a finite-element scheme TTGC (Colin & Rudgyard (2000*b*)) based on a two steps Taylor-Galerkin formulation. This scheme has very low diffusion and dispersion properties making it appropriate for LES by providing a third order accuracy in time and space. The flow field is governed by the Navier–Stokes equations described in Chap. 2. However, the cylinder motion which is taken into account by the fluid model written in the ALE formulation introduced previously, slightly modifies the convective term in the Navier-Stokes equations by introducing an additional term related to the mesh velocity. Hence the Navier-Stokes equation becomes,

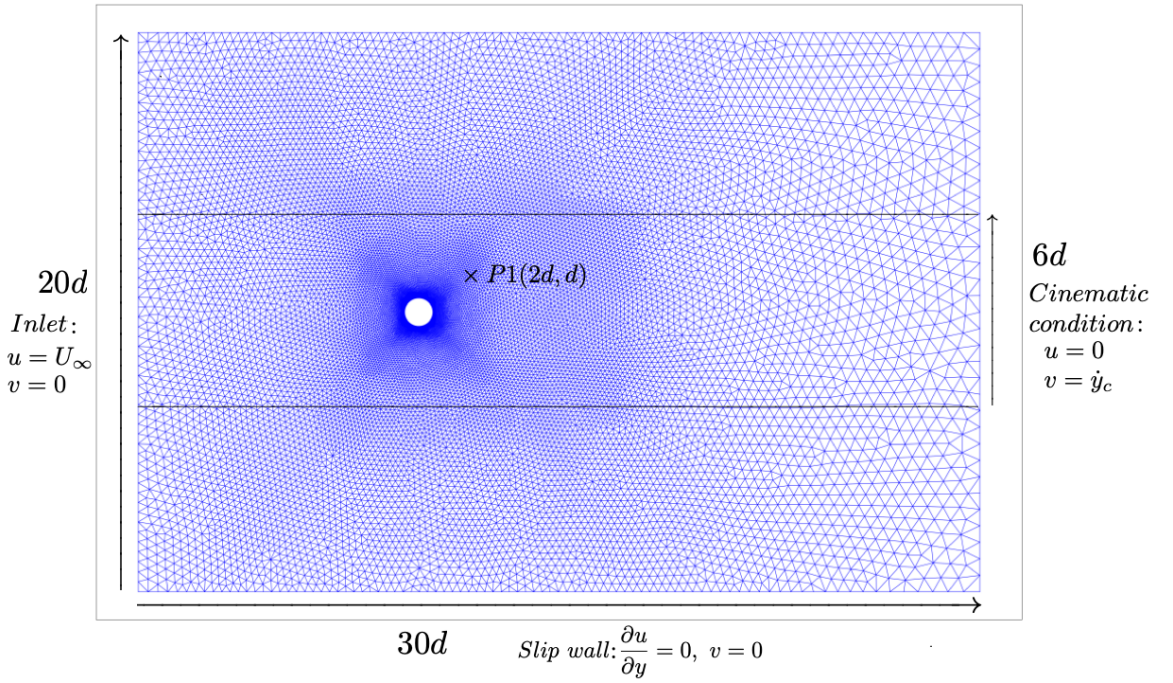

Figure 3.1: Mesh configuration of the computational domain highlighting the different boundary conditions

$$\frac{\partial \mathbf{u}}{\partial t} = ((\mathbf{u} - w).\nabla)\mathbf{u} = -\nabla p + \frac{1}{Re}\nabla^2 \mathbf{u}, \tag{3.2.2}$$

$$\boldsymbol{\nabla} \cdot \mathbf{u} = 0, \tag{3.2.3}$$

where $\mathbf{u} = (u, v)$ is the velocity vector containing the streamwise and transverse components u and v, p is the pressure, ρ and ν are the fluid density and kinematic viscosity. In the cases considered, the Reynolds number is inferior to 190 meaning that the flow is assumed to be laminar and two-dimensional according to the description of Williamson (1996). The mesh velocity represented by w is here equal to $\dot{y}_c$, the motion of the cylinder imposed as a forced vibration whenever needed. Even though the nodes of the domain have the same velocity as the cylinder velocity $\dot{y}_c$, their corresponding displacement varies according to their location. For such simulations, it is chosen that the cells inside the moving block do not deform so their displacement is a pure translation. All remaining nodes in the domain are then made so that they move according to a linear deformation law, their displacement being maximal near the moving block and stationary at the wall of the channel. For the cases involving forced oscillations, the motion is known *a priori* and can be directly imposed in the code for the moving mesh. In this case the motion of the cylinder is simply characterized by the following sinusoidal velocity equation,

$$y_c(t) = y_{c_{max}} sin(2\pi f_0 t), \tag{3.2.4}$$

where y_{max} is the maximum amplitude of displacement and f_0 is the forced oscillation frequency. The cylinder hence oscillates independently from the flow.

3.3 Fixed cylinder problem

The flow dynamics past a fixed cylinder is investigated in this section for two Reynolds numbers $Re_D = 40$ and $Re_D = 100$. The goal of such cases is to validate the simulations by checking several characteristic parameters. Simulations are carried out until the total kinetic energy of the system has converged as shown on Fig. 3.2. Note that simulations have been carried out well beyond the convergence time to collect sufficient data for post-processing purposes.

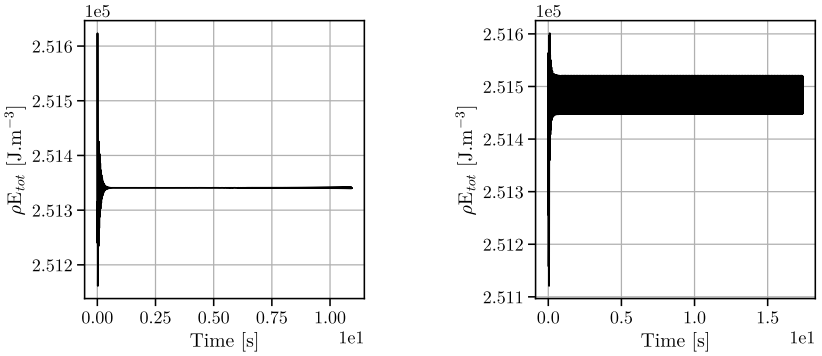

(a) **(b)**

Figure 3.2: Evolution of the total volumetric kinetic energy in function of time for (a) $Re_D = 40$ and (b) $Re_D = 100$.

During the transient state, the wake behind the cylinder establishes and at first starts to oscillate with a small amplitude without any vortex shedding for both cases. In the second case however, when the flow reaches its limit cycle, the amplitude of oscillations start increasing until vortices start to shed downstream. For the first case, the Reynolds number is below the critical Reynolds number (≈ 47) for which no bifurcation should occur. The wake is characterized by two strong re-circulation zones attached to the rear cylinder wall. In this region, the vorticity is large and the pressure levels are low. When the Reynolds number rises past the first critical value, the flow undergoes a Hopf bifurcation leading to vortex shedding. At $Re_D = 100$, the wake becomes fully unsteady while two staggered rows of vortices shed alternately from either side of the cylinder as shown by Fig. 3.3. At the flow limit cycle, the wake is characterized by a shedding frequency and Strouhal number as explained in the first section.

For the second simulations, the fundamental shedding frequency f_s can be obtained by performing a Fast Fourier Transform of the stream-wise velocity temporal recording of the established flow at probe $P1$. The corresponding Strouhal number yields a value of $St = 0.1656$ for the second case which agrees with the numerical calculations of Placzek *et al.* (2009) and the experiments of Williamson (1988). Results also agree with the direct numerical simulations (DNS) in 2D and 3D of Persillon & Braza (1998) confirming that the flow did not develop a three dimensional structure at this Reynolds number. Indeed, it is the second critical Reynolds number Re_{c_2} that dictates this condition meaning that for $Re_D < Rec_2$ 3D effects are not present. For further diagnostics, drag, C_D, and lift, C_L,

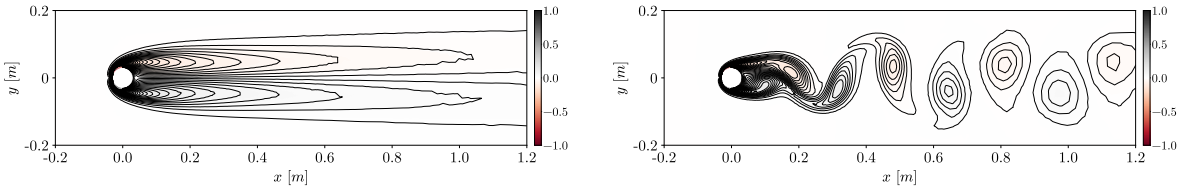

(a) **(b)**

Figure 3.3: vorticity contours plots in the wake for (a) $Re_D = 40$ and (b) $Re_D = 100$.

coefficients have also been recorded numerically and are reported on Fig. 3.9. For case $Re_D = 40$, the lift coefficient, C_L, remains null because of the perfect symmetry of the flow field . For case $Re_D = 100$, the vortex shedding leads naturally to the fluctuation of the aerodynamic coefficients. The expressions of the aerodynamic coefficients are reminded below:

$$C_D = \frac{F_D}{1/2\rho U_\infty^2 d} \qquad C_L = \frac{F_L}{1/2\rho U_\infty^2 d}$$

where F_D and F_L are the drag and lift forces expressed by unit of length and U_∞ is the free stream velocity. The aerodynamic coefficients can be evaluated by calculating the mean value of the drag and the average maximum lift over multiple periods. The mean drag and maximum averaged lift obtained for this case are $\bar{C_D} = 1.36$ and $\bar{C}_{Lmax} = 0.32$. These values are in good agreement with Placzek *et al.* (2009) and Tuann & Olson (1978), and they are slightly different from the values obtained by Henderson (1997). Indeed, Placzek *et al.* (2009) highlighted the effect of the aspect ratio on such aerodynamic coefficients and with an aspect ratio similar to the one adopted in the present study ($H/D/ \approx 0.3$) which resulted in a slight overestimation of these coefficients as seen here. Overall, the relative error is however acceptable since it is below 5%.

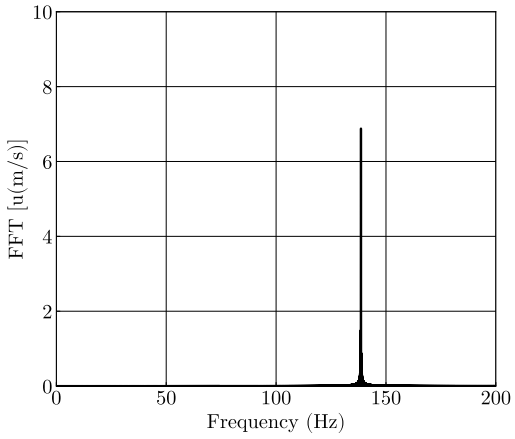

Figure 3.4: Magnitude of the Fast Fourier transform (FFT) of the lift coefficient at point $P1$ at $Re_D = 100$

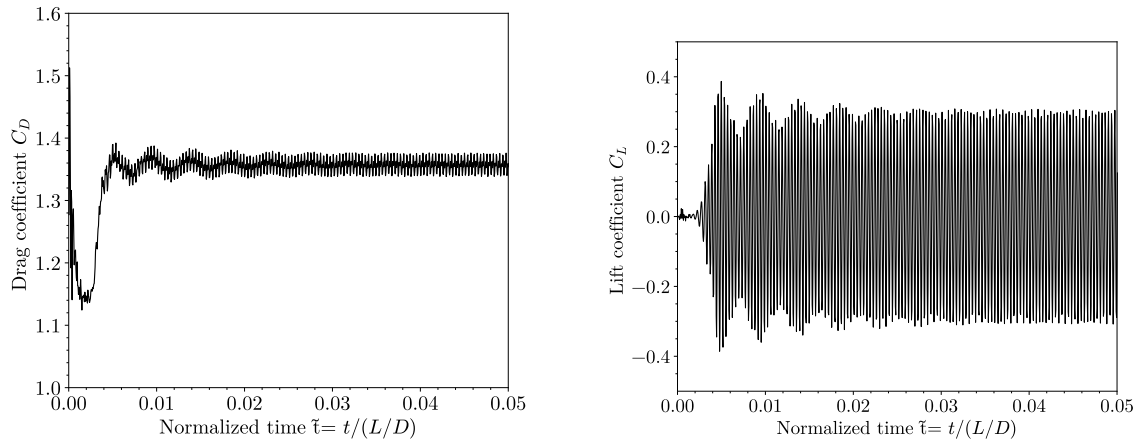

(a) **(b)**

Figure 3.5: Evolution of the aerodynamic fluctuating coefficients (the time is normalized by the domain aspect ratio L/D) at $Re_D = 100$.

3.4 Forced Vibration cylinder test cases

In this section, results from simulations of cylinder subject to forced vibration are presented. The forcing frequency is conveniently represented using the ratio $F = f_0/f_s$, where f_0 is the forcing frequency and f_s is the natural frequency of the flow instability. This allows a direct comparison between the flow natural frequency of oscillation for a forced case and the fixed cylinder problem. The objective is in the following to determine the effect of forcing on the vortex shedding of a flow at $Re_D = 100$. Computations are started using a previously established solution for the fixed case. For comparison Koopman (1967) experiments are used. In his experimental work, a cylinder is forced to vibrate at a frequency different from the flow Strouhal frequency and as a result, he established a region where for some values of $y_{c_{max}}$ and f_0, the flow oscillation converges towards the imposed frequency f_0. While performing the same experiment but at different Reynolds numbers ($Re_D = 100$, $Re_D = 200$ and $Re_D = 300$) whereby extending his analysis to the Williamson regime, modes A and B, he observed similar behaviors. This phenomenon , where the flow oscillation frequency converges to the forced one, is usually named "lock-in" vortex shedding: when the frequency of the vortex street becomes the same as the one imposed by the vibration. In the present study, the amplitude of vibration is fixed and set to $A = 0.25$ where $A = y_{c_{max}}/d$ is the normalized amplitude. This value corresponds to the upper range of value for which "lock-in" appears as observed by Koopman (1967). This specific choice indeed helps highlighting the different response regimes of the cylinder while maximizing the vibration effect on the flow wake. Even though the "lock-in" region is defined by both the amplitude and the frequency of vibration, it is easier to fix one quantity and vary the other to cross in or out of the region of interest. In the present case, the lock-in region is evidenced on Fig. 3.6 in the (A, F) plane. It is characterized by two almost symmetric limits, blue lines defined using the data points of

Koopman (1967). Test cases simulated hereafter are added to Fig. 3.6 by triangles: *i.e.*, for a fixed amplitude of $A = 0.25$ and varying the forcing frequency f_0.

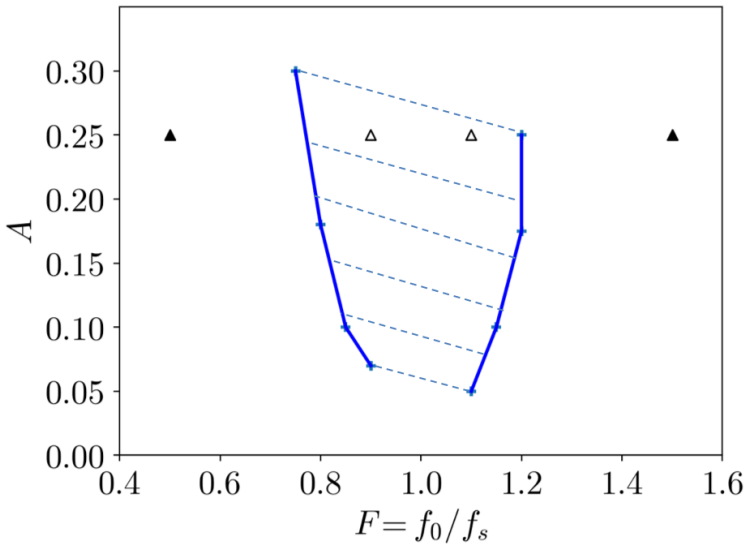

Figure 3.6: Lock-in zone for forced oscillations. The solid lines in blue represent the limits of the lock-in region at $Re_D = 100$ according to the data points (+) of Koopman (1967). The simulations performed here are represented with triangles: (△) correspond to locked configurations and (▲) correspond to unlocked ones.

3.4.1 Results and discussion

Locked configurations

The cases presented here are the locked-in configurations highlighted by an open triangle △ on Fig. 3.6: *i.e.*, $F = 0.9$ and $F = 1.1$. Figures 3.7 and 3.8 show first the vorticity contours in the wake at successive instants over one period of vibration (the values have been normalized with respect the maximum vorticity value in each case for comparison). Although the vortex structures are still aligned and parallel to the cylinder, their topology and spatial organization differ from the fixed case of 3.3(b). Indeed, a vibration of the cylinder at a frequency lower than the flow Strouhal frequency causes the street to expand, meaning that the longitudinal extent covered by the oscillating wake and the size of the vortices increase. The vortices composing the wake near the cylinder wall are also elongated in the y direction, *i.e.*, in the direction of vibration. On the opposite, imposing higher frequency of vibration causes the compression of the street yielding a decrease in the longitudinal extent of all these vortices. The vortices are also seen to shrink in the axial direction. As a result of these aerodynamics changes, all aerodynamic coefficients are affected in such cases. Both these coefficients depict a pure sinusoidal response as indicated by Fig. 3.9. For $F = 0.9$, the drag coefficient experiences a strong increase reaching a mean value $\bar{C}_D = 1.52$ compared to $\bar{C}_D = 1.36$

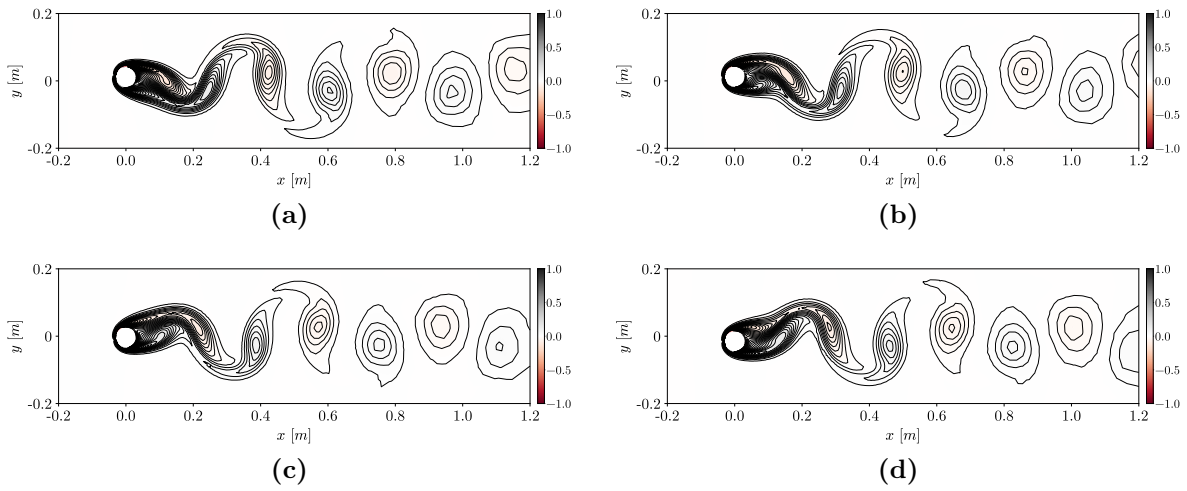

Figure 3.7: vorticity contours plots over one amplitude of vibration for $F = 0.9$. (a) $t = T/4$, (b) $t = T/2$, (c) $t = 3T/4$, (d) $t = T$ where T stands for the case period of forced oscillation.

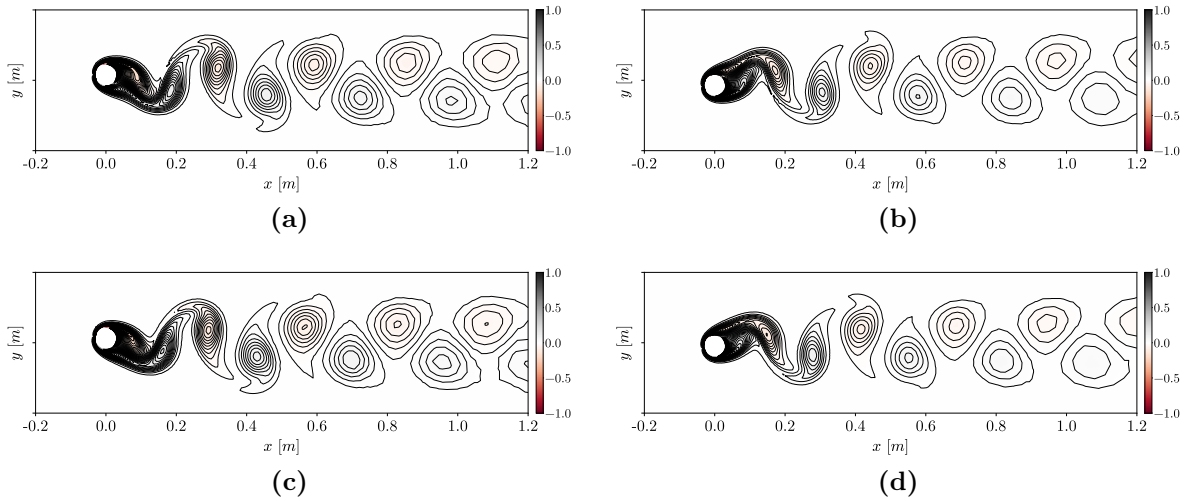

Figure 3.8: Vorticity contours plots over one amplitude of vibration for $F = 1.1$ for $F = 0.9$. (a) $t = T/4$, (b) $t = T/2$, (c) $t = 3T/4$, (d) $t = T$ where T stands for the case period of forced oscillation.

for the fixed case. Likewise, the peak value of the lift coefficient reaches $\bar{C}_L = 0.32$ when it was $\bar{C}_L = 0.2$ in the fixed case. For $F = 1.1$, the drag increases yielding $\bar{C}_D = 1.8$ and the peak lift coefficient increases to $\bar{C}_L = 0.7$. All results are seen to be in good agreement with the numerical predictions of Placzek *et al.* (2009). Finally, the Fast Fourier transforms of the signal retrieved from probe $P1$ and shown on Fig. 3.10 clearly demonstrate that lock-in has indeed happened in both configurations. Since the new vortex shedding frequency f_s^* equals the imposed frequency of vibration f_0. As a result, during this regime, the aerodynamic forces are controlled by the frequency of vibration,

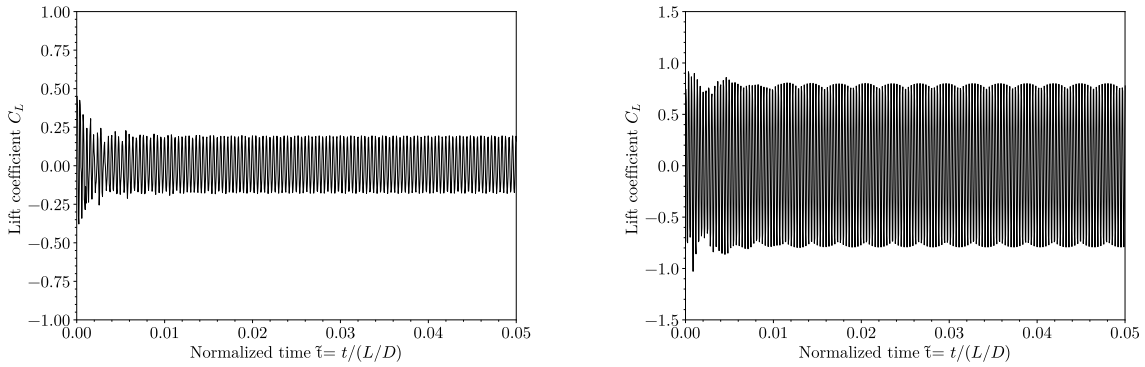

Figure 3.9: Evolution of the fluctuating lift coefficients for $F = 0.9$ ((a)) and $F = 1.1$ ((b)).

f_0.

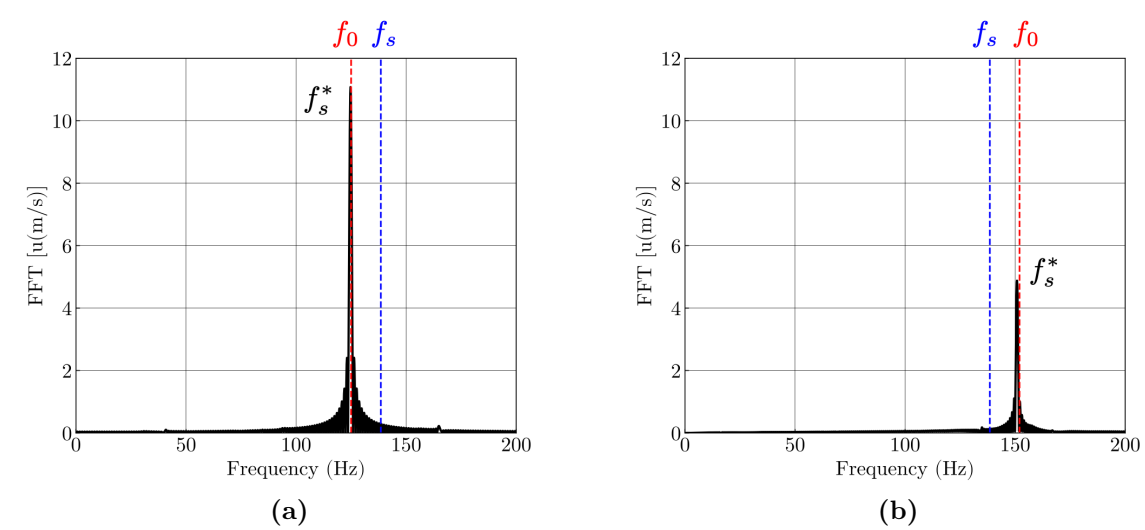

Figure 3.10: Magnitude of the Fast Fourier transform (FFT) of the lift coefficient at point $P1$ for (a) $F = 0.9$ and (b) $F = 1.1$

Unlocked configurations

The focus is now brought to the unlocked configurations of Fig. 3.6 evidenced by filled triangles, and for which $F = 0.5$ and $F = 1.5$. The respective vorticity contour are illustrated on Fig. 3.11. For $F = 0.5$, the structure of the wake seems to be coherent with the one formed in the fixed case. This similarity however does not guarantee a fully similar flow dynamics. This similarity also does not apply to the second

unlocked configuration, $F = 1.1$, which displays a completely different vortex shedding phenomenon and wake structure. Indeed, vortices are no longer purely symmetric with respect to the cylinder and their periodic release is no longer truly present.

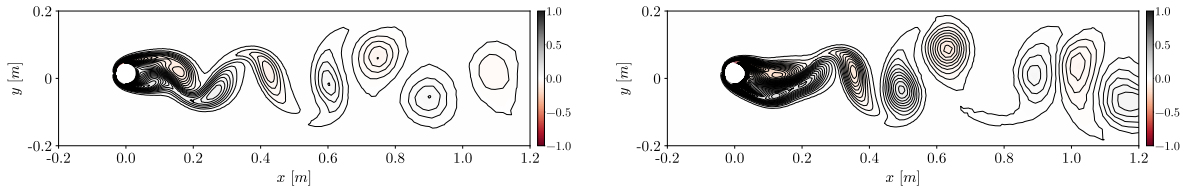

(a) **(b)**

Figure 3.11: Instantaneous vorticity contours plots for (a) $F = 0.5$ and (b) $F = 1.5$

A careful examination of the time series of the fluctuating lift coefficients is provided for both cases by Fig. 3.12. As suspected by Fig. 3.11, both time series do not exhibit pure sinusoidal shape. Although they appear periodic over several cycles of oscillation as observed by Placzek *et al.* (2009), a beating or standing wave behavior arises. Such a cycle-to-cycle period clearly evidenced by Fig. 3.12 has also been pointed out by Anagnostopoulos (2000) who emphasized that this behavior is typical of cases $F > 1$ or $F < 1$ outside the lock-in region leading to quasi periodic vortex shedding patterns. This resulting behavior is often reported in the case of surge when aerodynamic coefficients are compared to the fixed case. In our case, the lift coefficient attains a maximum value of $C_L = 0.36$ for $F = 0.5$ and $C_L = 2.2$ for $F = 1.5$. Similarly for the drag (not shown), the mean values obtained are $\bar{C}_D = 1.35$ for $F = 0.5$ and $\bar{C}_D = 1.54$.

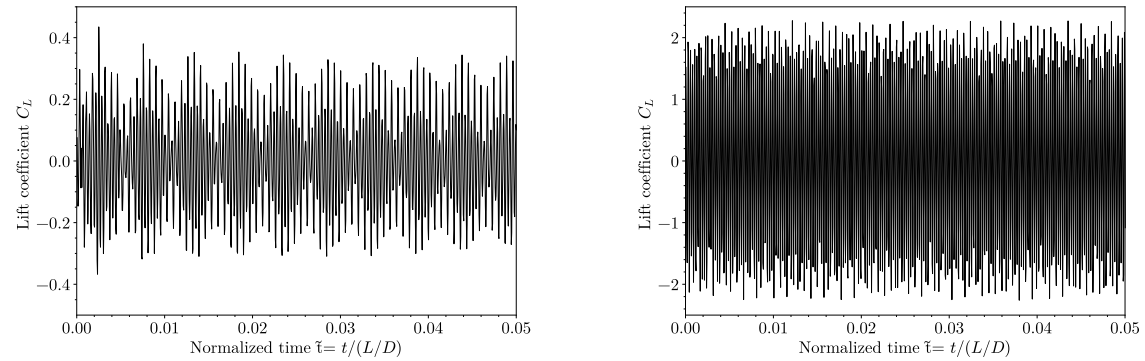

(a) **(b)**

Figure 3.12: Evolution of the fluctuating lift coefficients for (a) $F = 0.5$ and (b) $F = 1.5$

.

The corresponding Fourier transforms shown on Fig. 3.13 confirm the presence of a beating behavior for both cases. Indeed, the FFT's display two peaking frequencies equal to the imposed vibration frequency f_0 and one corresponding to the flow frequency of

oscillation of the fixed case, f_s. The presence of these two peaks has also been identified by Nobari & Naderan (2006) and Mittal & Kumar (2001) for transverse vibrations. In our predictions, the flow frequency for $F = 1.5$ looks slightly shifted with a relative error of $\approx 5.7\%$. This case however still demonstrates an unlocked configuration. While both spectra clearly depict two dominant peaks, small amplitude peaks are also present which do not appear to affect the flow structure nor the aerodynamic coefficients. Note that Placzek *et al.* (2009) did not observe such low magnitude modes of oscillation. He also found that forcing frequency at f_0 results into a main peak for $F = 1.5$ and a secondary one for $F = 0.5$, while both vortex shedding frequencies f_s remain dominant in these cases.

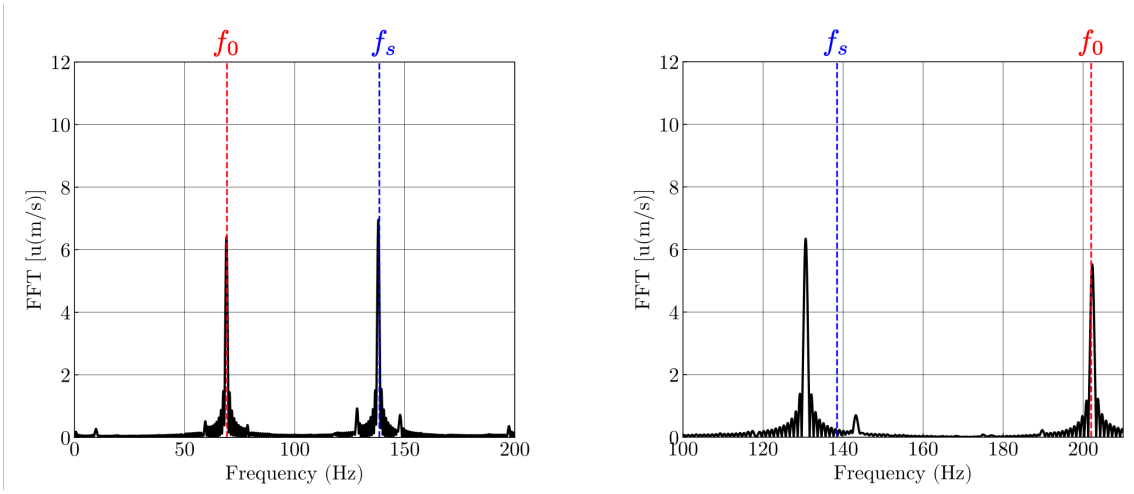

Figure 3.13: Magnitude of the Fast Fourier transform (FFT) of the lift coefficient at point $P1$ for (a) $F = 0.5$ and (b) $F = 1.5$

Overall, the results confirm that forced vibrations do indeed affect the flow structure and its underlying dynamics. Lock-in must however satisfy certain criteria which apply to the frequency and the amplitude of vibration for a given Reynolds number. Although, the flows simulated are all laminar in this preliminary study for which one leading hydrodynamic mode is attributed to a vortex shedding (to be confirmed with a linear stability analysis in the last chapter), the tool is confirmed to be capable of addressing such problems. However, complex rotating flows in enclosed cavities might react differently to forcing. The next part of this chapter is hence dedicated to the effect of imposed vibrations in rotor/stator cavities and with higher Reynolds numbers.

3.5 Enclosed cavity rotating flows

Flow instabilities are known to arise in rotating flows at high Reynolds numbers. Identifying and controlling the stability of these flows and their source remain a numerical and experimental challenge as pointed out by Queguineur (2020) and Bridel-Bertomeu

(2016*a*). Although the problem is exacerbated by the complexity of real world industrial applications, numerous experimental and numerical studies have been dedicated to enclosed rotor/stator cavities which serve as a preliminary model for turbomachinery devices (Serre *et al.* (2004); Tuliszka-Sznitko *et al.* (2009); Bridel-bertomeu & Gicquel (2017); Queguineur (2019)).

It is now known that the dynamics of these flows is heavily influenced by the cavity's geometric parameters and shape. Indeed, rotating flows on simple discs or even complex cavity flows can be classified under the BEK (Ekman (1905); Karman (1921); Bödewadt (1940)) flow family. This type of flows characterizes different possible configurations of a rotating boundary layer over a disc, and the reader can refer to the thesis of Bridel-Bertomeu (2016*a*) for a thorough description of these types of flows. The Ekman (1905) and Bödewadt (1940) type of flows are of special interest in this case since they describe enclosed cavity rotating flows. The Bödewadt (1940) layer arises when the disc is stationary and the fluid is rotating hence representing the boundary layer near the stator. The Ekman (1905) layer on the other hand arises on the surface of the rotor where both the rotor and the fluid hold the same rotational velocity. Lance *et al.* (1962) demonstrated numerically that laminar flows inside these cavities can be classified into two distinct categories depending on the length h between the stator and the rotor. If the gap is large enough, the stator and rotor boundary layers are separated. Otherwise the two boundary layers merge and the flow behaves like a 'torsional Couette flow". Daily & Nece (1960) extended this classification to turbulent flows by defining four regimes governed by two dimensionless parameters: the global Reynolds number and the aspect ratio of the cavity,

$$Re = Re_{rmax} = \frac{R_1^2 \Omega_d}{\nu}, \qquad G = h/R_1,$$

where R_1 is the outer disc radius, Ω_d is the rotational frequency of the rotor and G is the aspect ratio of the cavity. Figure 3.14 shows the different regimes plotted in the (Re, G) plane for cavities with $G << 1$. It evidences four distinct regimes:

- Regime I: Laminar flow with merged boundary layers,
- Regime II: Laminar flow with separated boundary layers,
- Regime III: Turbulent flow with merged boundary layers,
- Regime IV: Turbulent flow with separated boundary layers.

Note that the two laminar regimes are separated by a curve following the expression $Re\, G^{11/5} \approx 2.9$, while the two turbulent regimes are separated by the relationship $Re\, G^{16/3} \approx 7.8 \times 10^{-3}$. The transition to turbulence for flows with separated boundary layers (Regime II and IV) occurs at $Re \approx 1.58 \times 10^5$ and the two regimes with merged boundary layers (Regime I and III) are separated with a curve following $Re\, G^{10/9} \approx 366$.

Owen & Rogers (1989) highlighted flow structures that can be found in enclosed cavities and confirmed that they are a source of complex phenomena affecting the dynamics of the fluid in rotation. This dynamics is furthermore heavily dependent on the geometrical parameters and shape of the cavity itself. In fact, two geometric parameters can

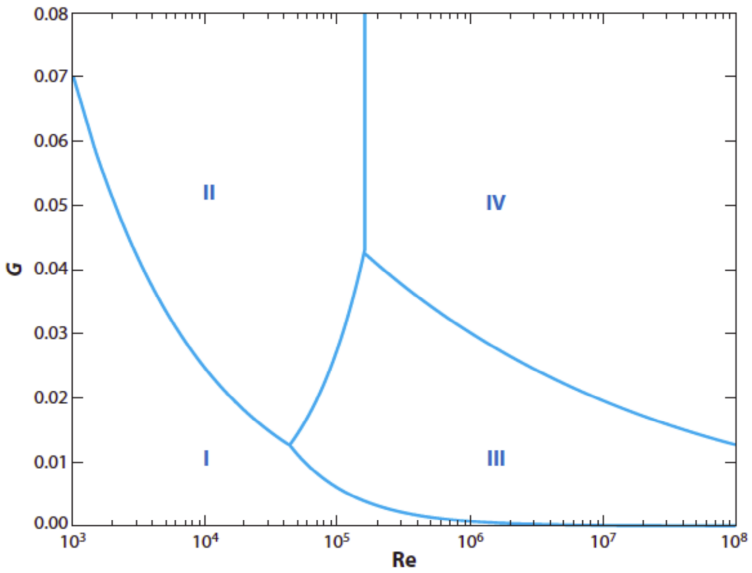

Figure 3.14: Map of the different flow categories of enclosed rotor/stator cavities in the (Re, G) plane.

alter the behavior of the flow: the finite disc radius r_{max} and end wall effect due to the presence of a shroud and/or hub. The finite disc radius is a crucial aspect that affects the parallel flow approximation introduced for infinite disc studies. This approximation allowed the auto-similar solutions to be proposed by Batchelor (1951) finding an axially symmetric solution to the Navier-Stokes equations for a steady incompressible and viscous fluid between two radially infinite discs. From the same perspective, a finite disc length can induce disturbances arising from its circumference and traveling inward. This feature can greatly alter the frequencies and mode shapes of the flow in the cavity as demonstrated by the experiment of Pier (2013) who confirmed that if the local Reynolds number $Re_r = r_{max}/h$ becomes greater than the critical Reynolds number Re_c, (in other words a local bifurcation of the flow), a global mode will be imposed by the boundary condition at $r = r_{max}$. Similarly, for an annular cylindrical cavity, if the local Reynolds number at the hub is greater than the critical Reynolds number, then the flow instability near the stator is transmitted to the rotor boundary layer. Queguineur (2019) confirmed such claims through control strategies using a method called Dynamic Mode Tracking and control (DMTC). He found that the suppression of the unstable mode near the stator prevented the emergence of a different unstable mode near the rotor.

In the context of the present Ph.D. work, a simple enclosed rotor/stator cavity taking the form of a cylindrical shape is analyzed. In particular, one wants to study what happens when the rotor is subject to forced vibration. This question is here addressed based on the above approach since validated on a simpler problem. Without forcing the flow developed in the cavity of interest corresponds to the Batchelor (1951) type of flow with two separated boundary layers (regime IV) and the frequencies of vibration to be imposed for analysis are equal to the two most dominant hydrodynamic modes found in the non forced case. These express respectively in the mid-cavity and near

stator. Although this configuration has been subject to many experimental (Itoh *et al.* (1992); Schouveiler (2001)) and numerical (Queguineur (2020); Bridel-Bertomeu (2016*a*)) studies, the objective therein is to asses the effect of the imposed vibration on the obtained hydrodynamic modes for a complex rotating flow at high Reynolds number. Recall that what we refer to here are modes corresponding to flow activities taking the form of circular waves around the hub and spiral vortices around the rotor and stator. The flow dynamics of the non forced case is first briefly presented then a detailed investigation of forced vibration cases is given.

3.5.1 Description of the geometric configuration

The geometric model considered is illustrated in Fig. 3.15. It represents an enclosed cylindrical rotor/stator cavity of height h composed of two smooth discs: the rotor and the stator. The rotor rotates at a constant angular velocity $\Omega_d = 2\pi F_0$, F_0 being the frequency of rotation of the rotor around the z-axis. The stator, on the other hand, remains stationary and is delimited by a cylindrical shroud of radius $r = R_1$. The cavity also includes an annulus of radius R_0 that rotates at the same speed as the rotor. The curvature parameter R_m is usually used to define such annular cavities. In the present case, $R_m = 1.8$ and equals to value used by Séverac *et al.* (2007) experimentally and by Tuliszka-Sznitko *et al.* (2009) numerically. The mean flow inside the cavity is controlled by the aspect ratio G defined as $G = h/\Delta R$ where $\Delta R = R_1 - R_0$ and the global Reynolds number $Re_G = \Omega R_1^2/\nu$ where ν is the kinematic viscosity of the fluid. G is often used in the literature and its value is here fixed so it is a first order approximation of a real turbomachine model (Tuliszka-Sznitko & Zielinski (2007); Serre *et al.* (2001)). All the geometric and physical parameters are summarized in Tab. 3.1.

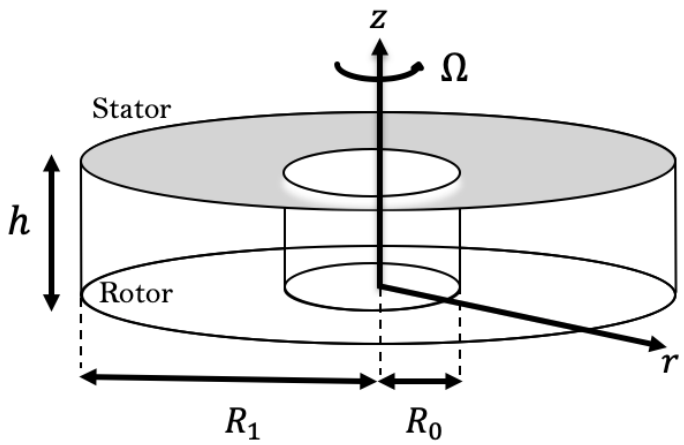

Figure 3.15: Schematic drawing representing the annular rotor/stator cavity. (Figure not to scale)

	Geometric parameters	
Internal Radius R_0	71	mm
External Radius R_1	250	mm
Cavity height h	35	mm
Aspect ratio G	0.2	-
Curvature parameter R_m	1.8	-
Global Reynolds number Re_G	10^5	-
Angular velocity F_0	50	Hz

Table 3.1: Characteristic parameters of the Tuliszka cavity.

3.5.2 Numerical Setup

Mesh and boundary conditions

To create the mesh of the configuration shown on Fig. 3.15, a $2D$ annular disk made of fully unstructured triangular elements is built and then extruded in the axial direction. Mesh clustering is carefully taken into consideration to minimize errors at walls where interactions are important. Note that the final $3D$ mesh is consequently made of only prismatic elements that are equally distant in the z direction. All the resulting mesh characteristic parameters are summed up in Tab. 3.2 below and where z_1 corresponds to the thickness of an element and is taken to be of the same order as the boundary layer thickness. Note that N_{layers} represents the number of mesh layers used for extrusion while $z+$ is the dimensionless wall normal coordinate.

	Mesh characteristics	
z_1	5.14×10^{-4}	m
N_{layers}	70	-
N_{nodes}	5.51×10^6	-
N_{cells}	10.9×10^6	-
z^+_{max}	5.45	-

Table 3.2: Mesh Characteristic parameters of the cavity shown on Fig. 3.15.

Regarding the imposed oscillating movement of the rotor, the Arbitray Lagrangian Eulerian (ALE) description given by Hirt *et al.* (1974) and implemented by Moureau *et al.* (2005) is used. The ALE is implemented in this case by first defining three zones in the numerical domain shown on Fig. 3.16. The zones are defined in such a way as to facilitate the use of the moving mesh procedure when the rotor oscillates as well as to preserve the quality of the mesh at walls by maintaining a first grid node wall normal coordinate $z+ < 5$ as advised for wall resolved LES. Likewise the objective is to limit mesh distortion as much as possible. Grid dependency tests have already been performed for the same cavity by Bridel-Bertomeu *et al.* (2016*a*) using the same strategy and LES solver. The

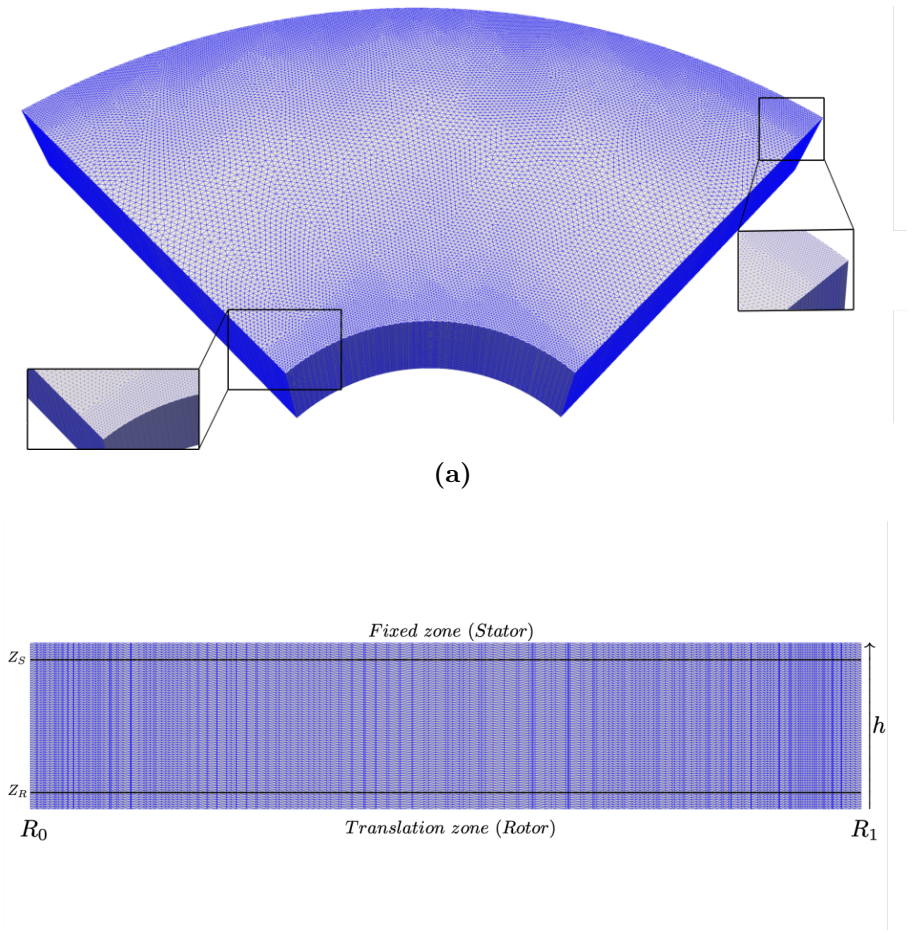

Figure 3.16: (a) $3D$ sector cut of the mesh, (b) axial cut of the mesh with the different blocks used.

configuration of the zones and cells have been built according to these observations. The zone containing the rotor has therefore 5 times the cell thickness and moves in translation along the z direction according to the following imposed velocity signal,

$$z(t) = z_{max} sin(2\pi f_0 t), \tag{3.5.1}$$

where $z(t)$ is the instantaneous position of the rotor in space, z_{max} is the maximum amplitude of vibration and f_0 is the imposed frequency of vibration in Hertz (Hz). Note that the rotor moves as a block without distortion. In the compression zone, all mesh elements also move in translation and deform linearly according to the position of the rotor. Finally, the zone around the stator is fixed meaning that the nodes do not move inside this region. This zone is defined by taking the first five mesh elements relative to the stator in the z direction to maintain the quality of the mesh at the wall. The nodes displacement in each zone is mathematically described as:

- Translation zone:

$$z_{nodes} = z_{nodes} + z_{max} sin(2\pi f_0 t), \tag{3.5.2}$$

where z_{nodes} is a vector containing the z coordinate values for all the nodes in the domain.

- Compression zone:

$$z_{nodes} = z_{nodes} + z_{max} sin(2\pi f_0 t) \times (\frac{z_{nodes} - Z_C}{Z_R - Z_C}), \tag{3.5.3}$$

with Z_R and Z_C representing the boundary limits of the rotor and stator mesh zones respectively.

- Fixed zone:

$$z_{nodes} = z_{nodes} \tag{3.5.4}$$

The boundary limit or coordinates of the rotor are finally also displaced in time to conserve the height of the translation zone following,

$$Z_R = Z_R + z_{max} sin(2\pi f_0 t). \tag{3.5.5}$$

Large eddy simulation modeling

The code chosen to perform the LES is AVBP (Gourdain *et al.* (2009)). The convective Two-Step Taylor Galerkin (TTGC) (Colin & Rudgyard (2000*a*)) scheme based on the finite element method is used. The low diffusion and dispersion properties makes it appropriate for LES by providing a third order accuracy in time and space. The time step of the simulation is dictated by the Courant Friedrichs Lewy number (CFL) and it is set to 0.7. As introduced in Chap. 2, the sub-grid turbulence model used is here the WALE model since adequate for wall resolved simulations. Artificial viscosity is applied based on the Colin sensor (Colin & Rudgyard (2000*b*); Colin (2000)) to damp non-physical oscillations with a low level second order coefficient $\epsilon_2 = 0.01$ and forth order coefficient $\epsilon_4 = 0.001$. All the numerical parameters used for the simulation are reported in Tab. 3.3.

	Numerical parameters
Solver type	Navier-Stokes
Convection scheme	Law-Wendroff
Sub-grid scale model	TTGC
Laminar viscosity	constant ($\mu_{ref} = 2.23442 \times 10^{-4} Kg/m/s, T_{ref} = 300K$)
Artificial viscosity	Colin sensor ($\epsilon_2 = 0.01, \epsilon_4 = 0.001$)
Time step (fixed case) Δt	$7.6 \times 10^{-7} s$

Table 3.3: Numerical parameters used for the LES.

Regarding the treatment of the boundary conditions, all walls are treated as adiabatic. Radial and axial no slip conditions are applied on the rotating disc and shaft. This translates in the system of cylindrical coordinates (r, θ, z) to $u_r = u_z = 0$ and $u_\theta = r\Omega_d$. A slip-wall condition is enforced on the stationary disc and shroud.

3.5.3 Results and discussions

Non-forced case

This type of study has already been realized and validated by Séverac *et al.* (2007), Bridel-Bertomeu (2016*b*) and Queguineur (2020). However since it lays as the reference case for the forced vibration cases it is briefly covered hereafter. Note that only the main results focusing on the instantaneous flow dynamics are discussed, the reader can refer to the aforementioned references for additional details.

In this section the fluid is initially at rest and the rotor is at its initial position. At time $t = 0$ the rotor is brought to its rotation speed $\Omega = 2\pi F_0\, rad/s$ and the fluid accelerates due to viscous entrainment. The flow organization at its limit cycle is shown on Fig. 3.17 where $2D$ cuts near the rotor, mid-cavity and stator highlight the axial velocity fluctuation. The fluctuating axial velocity u'_z is obtained by subtracting the mean axial velocity ($\bar{u}_z$) from the instantaneous axial velocity: *i.e.*, $u'_z = u_z - \bar{u}_z$. It is an important parameter because when instability arises in the flow, the base flow which is stable departs from a purely parallel flow and the perturbations around it can be measured using the magnitude of u'_z (Lopez *et al.* (2009); Serre *et al.* (2001)). Vortex structures clearly dominate the cavity with distinct patterns near the rotor, the mid-cavity and the stator. Indeed, the rotating disc boundary layer exhibits spiral-like structures with increasing radial magnitude outward starting from the hub to the shroud. In the mid-cavity, the spiral vortices are also active near the hub. The stator boundary layer depicts a different form of patterns highlighted by the presence of spiral vortices as well as annular ring structures near the hub. The spiral vortices appear to stem from the outmost ring with a shorter span compared to the two other vortices. Overall the patterns recovered demonstrate a coherent azimuthal organization throughout the cavity.

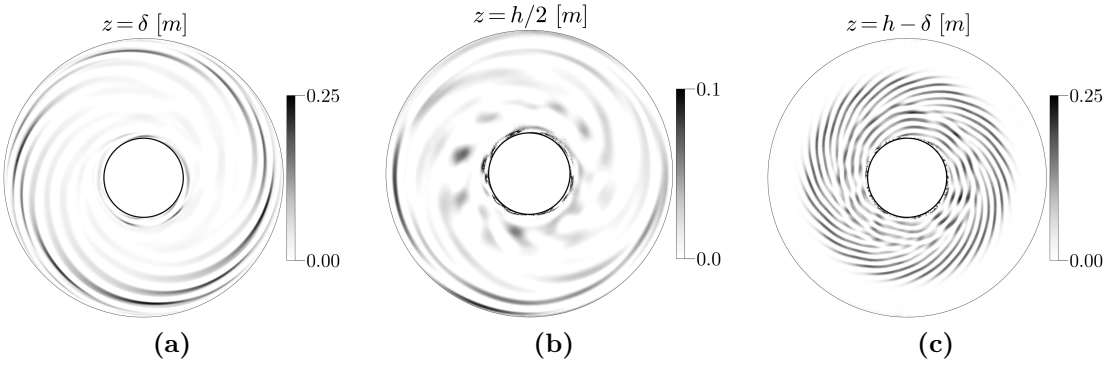

Figure 3.17: Axial velocity fluctuation $u'_z > 0$ normalized by its maximum amplitude at different locations inside the cavity.

To identify the driving modes responsible for these instabilities, a DMD (Schmid (2010)) is performed using instantaneous $2D$ solutions in (r, θ) planes from LES. The DMD solutions retrieved are shown on Fig. 3.19 and represent the three most dominant modes found in the system that correspond to: $F = 0.35F_0$; $F = 3.24F_0$ and $F = 3.61F_0$.

DMD confirms the LES findings thus indicating that these vortex structures are indeed associated with an instability synchronized at a unique frequency. The three modes have distinct wavenumbers resulting from a single bifurcation in the flow. The mode $F = 3.24F_0$ is characterized by the formation of annular rings around the hub, so its wavenumber is zero. The lowest and highest modes exhibit a different form of instability through the existence of 12 and 29 spiral arms respectively. The wavenumber of these modes are hence respectively noted $m = 12$ and $m = 29$. Note that based on these LES results, modes $m = 0$ and $m = 29$ appear to coexist near the stator boundary layer where both instabilities have been identified.

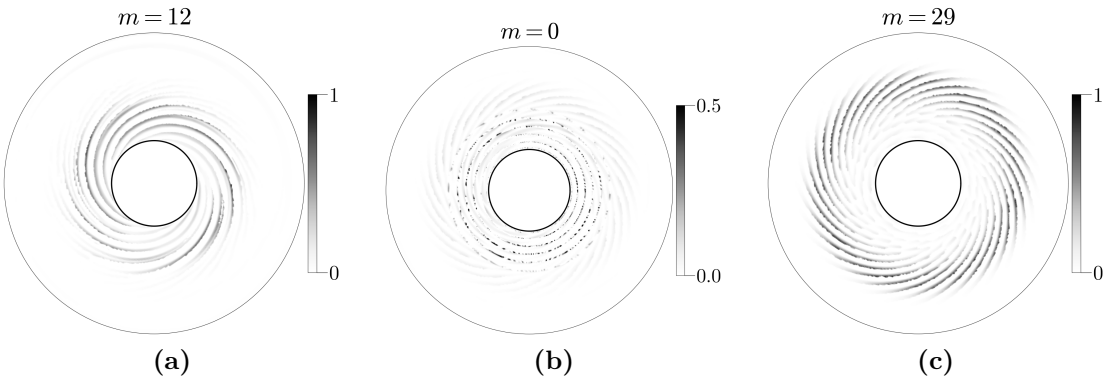

Figure 3.18: DMD axial velocity fluctuation modes in the (r, θ) plane near the stator boundary layer: (a) $F = 0.35F_0$ (b) $F = 3.24F_0$ (c) $F = 3.61F_0$. (only the positive part is shown)

These dominant modes have been identified by Bridel-Bertomeu (2016*a*) and Queguineur (2020). These studies also demonstrated through PSD that each of these modes originated from a certain location inside the cavity. For instance, mode $m = 0$ originates from the mid-cavity whereas modes $m = 12$ and $m = 29$ originate from the rotor and stator boundary layers respectively. They furthermore indicate that these modes are not only three dimensional in space but their magnitude also changes according to the axial position inside the cavity. The present DMD performed in the (r, z) plane corroborates these claims.

All three modes display clear three dimensional shapes and organizations inside the cavity with each dominating a certain region. The mode $F = 0.35F_0$ is present near the stator at $R_0 < r < 0.13$ with a stronger amplitude near the rotor at $0.22 < r < R_1$. The annular mode dominates the entire cavity with annular rings forming near the stator at $R_0 < r < 0.15$ and vortex structures close to the hub as well as near the rotor boundary layer. The highest frequency mode $F = 3.61F_0$ is strongly present near the stator with spiral vortex structures forming at mid radius.

The present simulation although reconducted from previous works on this academic rotor/stator cavity sheds light on the various forms of rotational instabilities that can occur in turbomachinery applications. However, external vibrations may also occur and impact observed features potentially disrupting the operating point of the turbomachinery

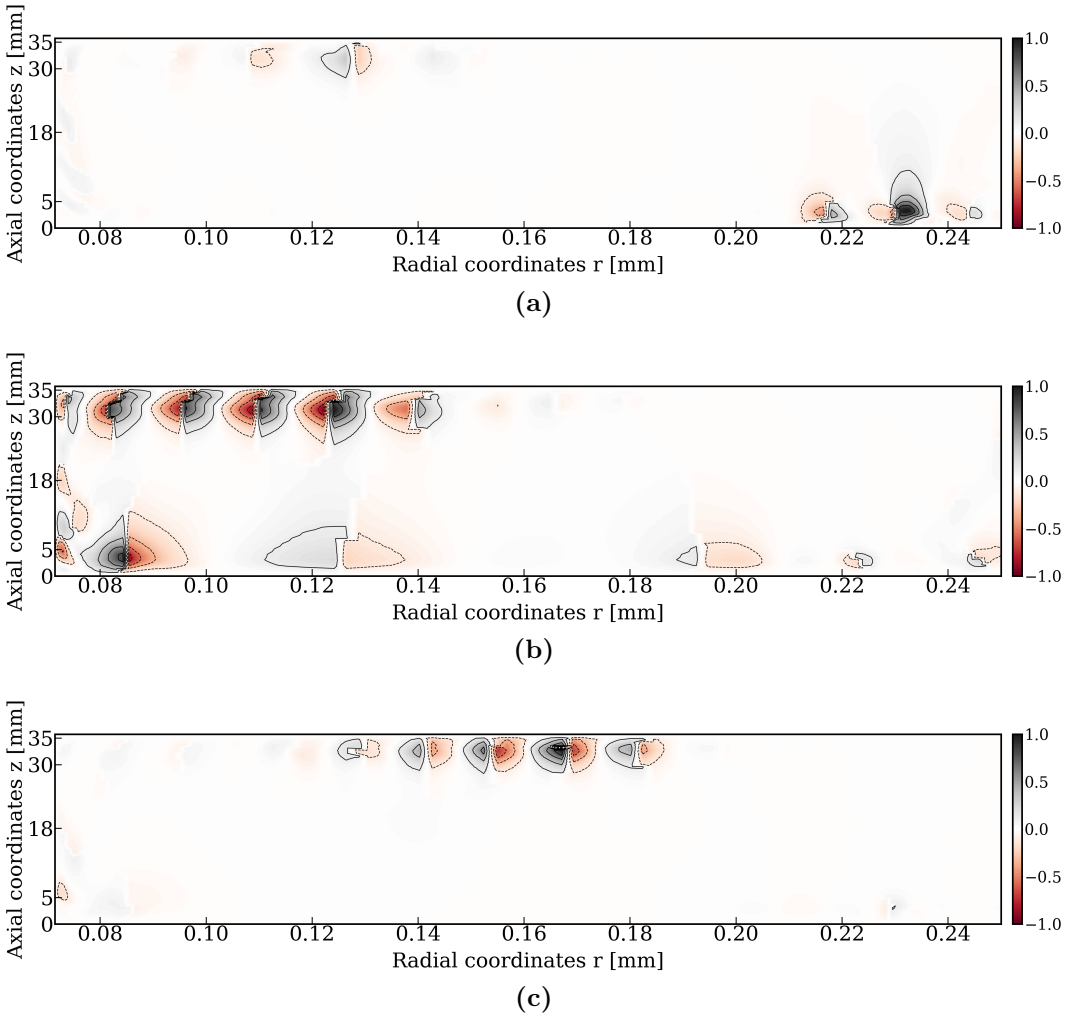

Figure 3.19: Axial velocity fluctuation DMD modes in the (r, z) normalized by their respective maximum amplitude : (a) $F = 0.35F_0$ (b) $F = 3.24F_0$ (c) $F = 3.61F_0$.

device. In the following, one examines this phenomenon by inducing a periodic oscillation of the rotor. To do so, one considers two cases each with a unique forcing frequency that corresponds either to the annular or stator modes identified in the non-forced case.

Forced cases

Two different Large Eddy simulations are carried out for the annular academic cavity introduced earlier. For both cases, one imposes an axial motion as if the rotor exerted an axial vibration (see Eq. (3.5.1)). All discussed simulations hence start from the previously established solution. In the first case, the imposed frequency f_0 equals the annular mode frequency, $f_0 = 3.24F_0$, while for the second case, the imposed frequency equals the stator mode frequency $f_0 = 3.61F_0$. The amplitude of vibration imposed is fixed in the study and corresponds to $A = 0.05h$. Such a motion can for instance, be

representative of a forced vibration issued from mistuned bladed disks which can lead to an axial vibration $0.035h - 0.057h$ depending on the operating conditions of the turbomachine and structural properties of the rotor as reported by Zhao *et al.* (2019). The effect of amplitude change is not studied in the following. However preliminary tests indicate that for small values of A the flow dynamics is not altered while for large values of A, the flow structure is completely modified indicating the existence of a relationship between the frequency and amplitude of vibration similar to the "lock-in" region identified in the first part of this chapter. The objective is thus here to understand the behavior of the flow when subject to an external forcing at frequencies corresponding to its predetermined hydrodynamic modes prior to the use of more advanced approaches. For the coming predictions recall that all numerical parameters introduced in the previous section are maintained for all current simulations with the exception of the moving mesh procedure. With such settings, 438 time steps are approximately needed for each cycle of vibration of Case 1 while only 397 are needed for Case 2 to reach the flow limit cycle. Numerical convergence is obtained similarly to the first reference simulation: *i.e.*, when the average volumetric kinetic energy inside the cavity reaches a plateau. The new limit cycles are illustrated on Fig. 3.20 and for which each case is seen to be characterized by an oscillation attributed to the imposed frequency of vibration.

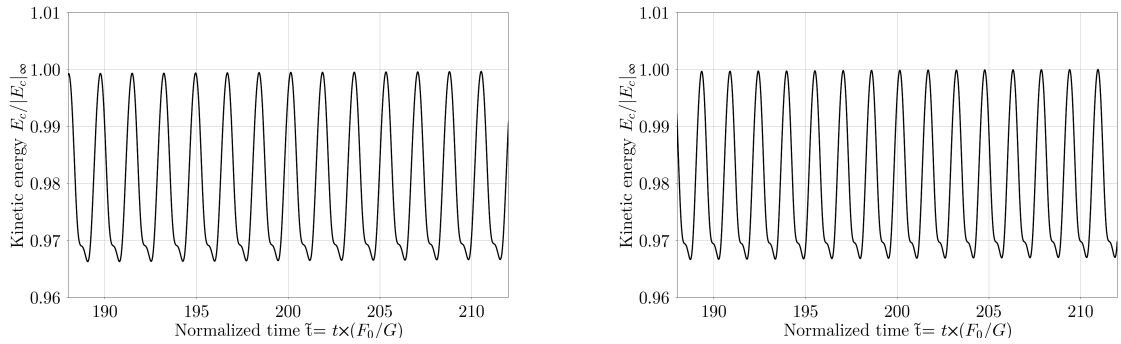

Figure 3.20: Evolution of the normalized volume-averaged kinetic energy at the flow limit cycle for (a) **Case** 1 and (b) **Case** 2.

Figures 3.21 and 3.22 show $2D$ cuts of the axial velocity fluctuation u'_z relative to the rotor and removing the mean local flow velocity. The boundary layer height δ is now measured based on the mean flow relative to the rotor average position after one period of oscillation: *i.e.*, at the fixed case position. Near the stator boundary layer, both cases feature the same instability patterns as demonstrated by the outward propagation of spiral vortices starting at $r \approx 0.13$ towards the shroud up to $r \approx 0.2$. Near the hub for $R_0 < r < 0.13$, a set of dislocated circular patterns are identified. The former instability is clearly three dimensional and is referred to as a type I instability, whereas the latter can be interpreted as a type II instability Pikhtov & Smirnov (1993) . These two instabilities arise due to two distinct bifurcations that yield this system of spiral rolls coexisting

with the circular one Schouveiler (1998). The statoric boundary layer features 28 and 30 arms spiral structures for Case 1 and Case 2 respectively. These exist at high radii whereas near the hub, spirals turn into quasi-concentric annular ones. For the rotating boundary layer, the magnitude of u'_z is small near the hub due to important viscous forces at the wall which damp the axial velocity fluctuation. However, at high radii and near the shroud, inertial forces dominate the viscous forces at the wall and the magnitude of the instability is higher. The spiral patterns are also identified in this case as co-winding rotating vortices that propagate outward toward the shroud. The mid-height of the cavity exhibits low amplitude variations of the axial velocity fluctuations with a slightly higher activity near the hub where the flow appears to be spatially organized similarly to the rotor boundary layer.

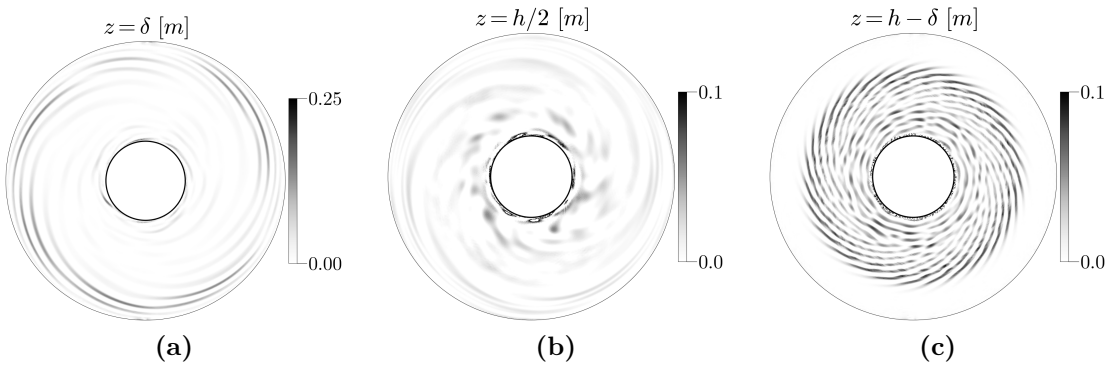

Figure 3.21: Axial velocity fluctuation $u'_z > 0$ normalized by its maximum amplitude at different locations inside the cavity for **Case** 1.

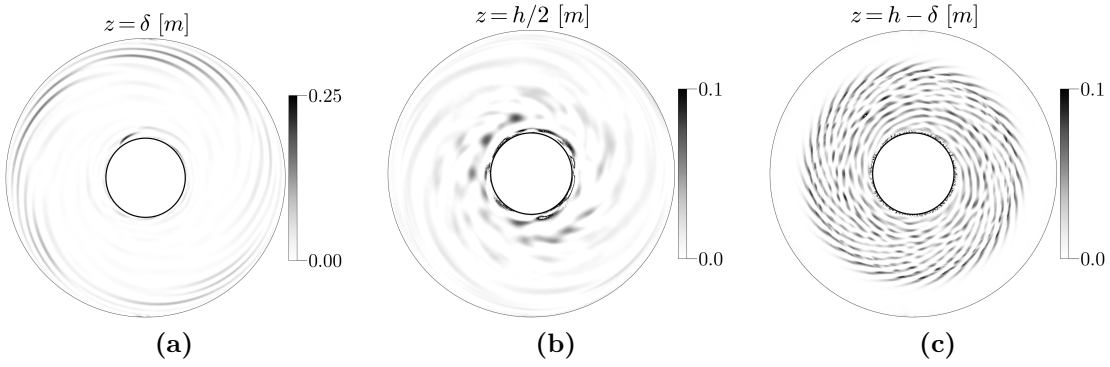

Figure 3.22: Axial velocity fluctuation $u'_z > 0$ normalized by its maximum amplitude at different locations inside the cavity for **Case** 2.

To further investigate the underlying structures and their stability, DMD is applied again to these cases. To do so, a signal of duration of $1s$ containing all the necessary flow data is taken at steady state after approximately 196 cycles of vibration for Case 1 and 216 cycles for Case 2. Such a signal contains therefore a sequence of 120 equi-spaced

snapshots which is sufficient for the solution to converge. Figure 3.23 presents the most energetic modes constituting Case 1. Two modes appear to be dominant inside the cavity. At the stator boundary layer, the first one has a temporal frequency of $F = 3.64F_0$ and a wavenumber of $m = 28$. It is made of counter-winding vortices starting at $r \approx 0.13\ m$, where approximately 3 cylindrical vortices exist around the hub, and propagate outward. This mode appears to coexist with the second one that has a temporal frequency of $F = 4.64F_0$ and the same cylindrical vortices as found in the first mode. In the core of the cavity the two modes appear to shift to a different radial location mainly around the hub and shroud. Overall their amplitude is low compared to the modes found near the statoric boundary layer. Mode $F = 3.64F_0$ appears to mark the middle of the cavity with 6 spiral vortices compared to 5 for mode $F = 4.64F_0$. At the rotor boundary layer the flow seems to exhibit modal patterns at the same radial interval as for the core of the cavity. Nevertheless, for the two modes, the axial velocity fluctuation appears stronger near the shroud as demonstrated by the seen 12 spiral arms for mode $F = 3.64F_0$ and 10 spiral arms for the mode $F = 4.64F_0$. As previously shown on Fig. 3.21, the LES predictions appear to match the patterns found by DMD for the mode $F = 3.64F_0$. This mode was also retrieved in the non-forced case, however the annular mode found previously has its frequency shifted by $1.4F_0$.

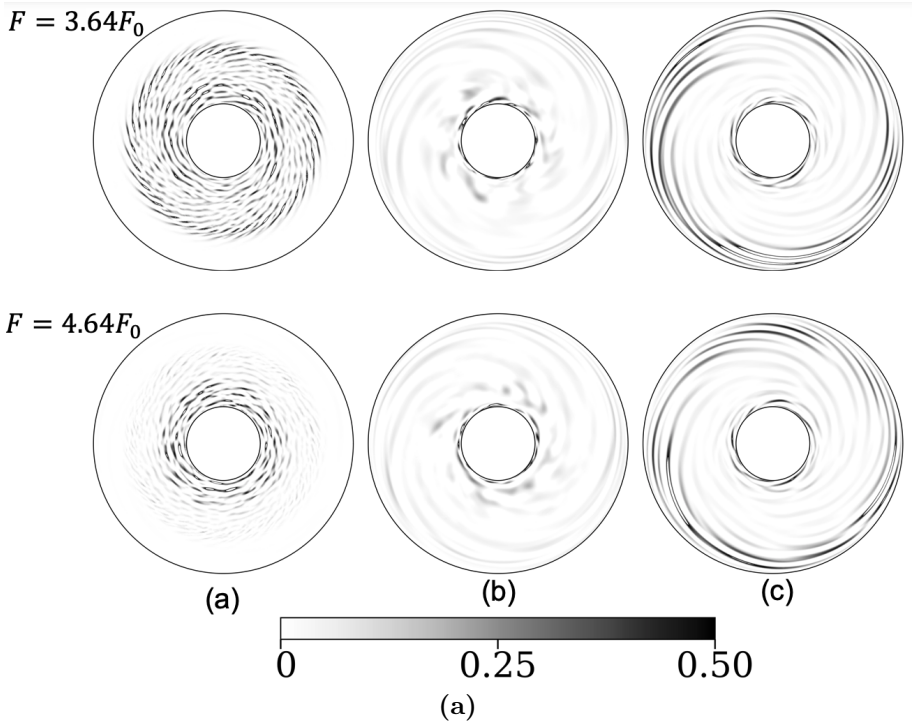

Figure 3.23: DMD axial velocity fluctuation modes at (a) $z = h - \delta$ (b) $z = h/2$ (c) $z = \delta$ constituting **Case** 1.

Figure 3.24 shows the amplitude of the axial velocity DMD modes $\hat{u}_z$ constituting Case 2. The most energetic modes retrieved correspond in that case to $F = 3.26F_0$ and $F = 5F_0$. The former has also been identified in the non-forced case; whereby the latter

has emerged and appears to dominate the cavity as shown in the LES predictions of Fig. 3.21. Both modes exhibit the same radial distribution at the rotor boundary layer and the core of the cavity. Near the stator, mode $F = 5F_0$ is characterized by 30 spiral vortices with less dominant cylindrical ones near the hub. The second mode coincides with the opposite structural organization, a quasi-concentric dislocated circular waves near the hub and spiral arms of negligible magnitude. These preliminary results indicate that the hydrodynamic modes responsible for the flow instability did react due to the forcing of the flow at a matching frequency.

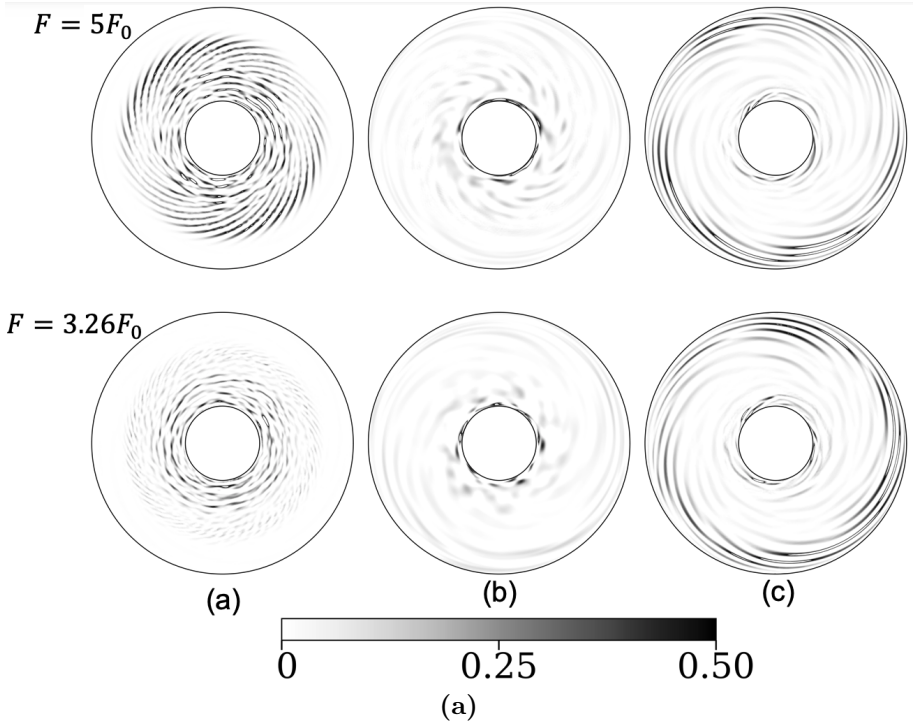

Figure 3.24: DMD axial velocity fluctuation modes at (a) $z = h - \delta$ (b) $z = h/2$ (c) $z = \delta$ constituting **Case** 2

The spectral content of the flow and the frequencies responsible for the underlying instabilities can be directly monitored through point-wise power spectral densities carried out on multiple numerical probes spread radially and in azimuth at the rotor and stator boundary layer, as well as throughout the core of the cavity. The objective is to confirm that the driving modes present in the flow are coherent with the DMD results. Due to the inherent three dimensional structures of the present patterns (azimuthal and axial distribution); only the spectral content of the modes present near the stator boundary layer is presented. The core cavity and the rotating boundary layer indeed express the same spectral content in terms of frequency but with a slightly different amplitude. A total of 5 circles consisting of 60 probes each are spread in the axial direction between the two discs at $z = \delta$ and $z = h - \delta$ as well as the mid section of the cavity at $z = h/2$. Figures 3.25 and 3.26 show the location of the numerical probes in the cavity and used to extract all the relevant data and the power spectral densities (PSD) of the axial velocity

fluctuation u'_z. Note that the nomenclature C_iP_j is used to refer to the current probes where $i \in [1, 5]$ denotes the number of the circle and $j \in [0, 15]$ the number of the probe point.

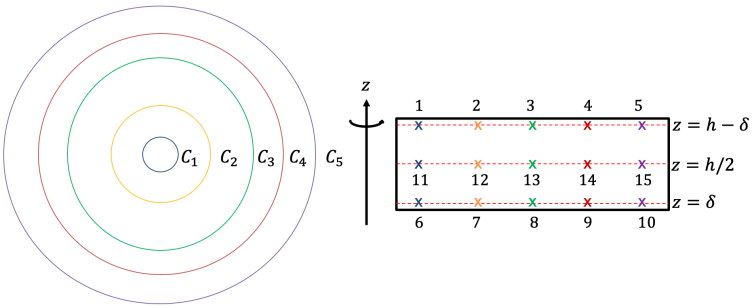

Figure 3.25: Location of the numerical probes in the cavity associated with Case 1 and Case 2 (figure not to scale). Numbering of the circles match the color of the probes and the corresponding PSD signal.

Multiple peaking frequencies can be identified on both spectra. However, not all these frequencies are associated with a unique hydrodynamic mode. Using the PSD confirms the presence of the modes retrieved by DMD. Three main frequencies can be identified in Case 1, *i.e.*, $3.24F_0$, $3.61F_0$ and $4.7F_0$, and in Case 2, *i.e.*, $3.24F_0$, $3.61F_0$ and $5F_0$. All other frequencies are either harmonics or linear combinations of these modes that contribute to a much lesser extent to the system. As a consequence, their respective mode shapes are considered irrelevant. Note that Queguineur (2020) also pointed out the presence of such additional frequencies that were disregarded in the non-forced study. The magnitude of the peaks appear to be consistent with the radial distribution of the three dimensional patterns inside the cavity. For Case 1, mode $3.61F_0$ appears to be the same mode as identified by DMD at $3.64F_0$ and the main driver of the statoric instability shown by LES predictions on Fig. 3.21. Indeed, this mode is present at $0.13 < r < 0.2$ where the highest peak of axial velocity PSD are identified by C_3P_0. The emerging mode at $4.7F_0$ that is mostly concentrated around the hub, has also its highest axial velocity PSD magnitude present in that region as shown by the point C_1P_0. Finally the frequency of vibration imposed $f_0 = 3.24F_0$ is clearly retrieved. It perturbs the flow the most in the region between C_1P_0 and C_3P_0. The constituent frequencies of Case 2 also match the ones retrieved by DMD with three major peaking frequencies *i.e.*, $3.24F_0$, $3.61F_0$ and $5F_0$. Mode $3.24F_0$ corresponds in this case to the hydrodynamic mode characterized by circular spirals near the hub therefore yielding the highest peak at point C_1P_0 with a magnitude of 40 dB. The forcing frequency $f_0 = 3.61F_0$ is also present alongside a built up of a frequency at $4F_0$. This frequency does not appear to have any contribution to the DMD spectrum hence it might be linked to noise inside the system. The dominant frequency found in the stationary disc by LES is identified by the PSD at a peak at $5F_0$ with a magnitude of 60 dB between C_2P_0 and C_3P_0. In general, both PSD spectra exhibit a similar magnitude range, ranging from $60dB$ to $95dB$, with the latter showing a slightly higher order of magnitude. Finally, the rotor mode at $0.35F_0$ identified in the non-forced study is barely discernible in both spectra

which explains why DMD does not recover this mode. That said, it implies that forcing has effectively suppressed the rotor mode. Similarly, Queguineur (2020) discovered that

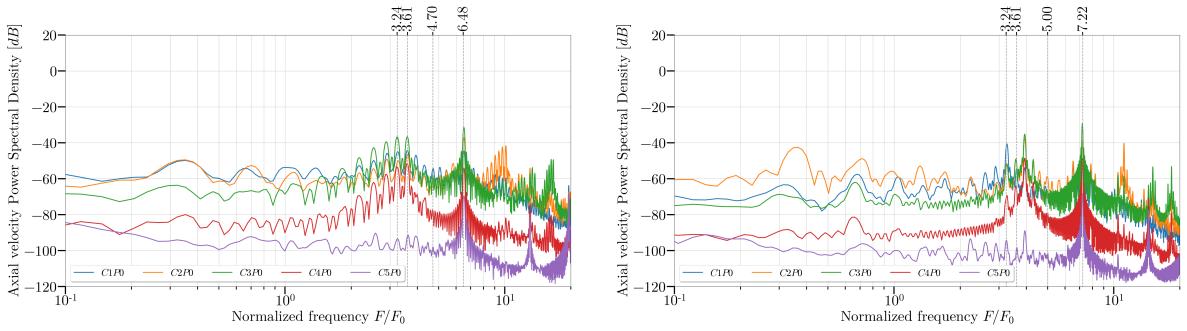

Figure 3.26: Power spectral densities of the axial velocity fluctuation u'_z in the statoric boundary layer ($z = h - \delta$) registered by probes C_1P_0 to C_5P_0 for (a) **Case** 1 and (b) **Case** 2.

this specific mode can be mitigated through control strategies. His developed dynamic mode tracking and control (DMTC) strategy revealed that the rotor mode is dependent on the presence of the stator mode. Consequently, by suppressing the latter mode, the former mode can be effectively suppressed as well. However, this was not the case for the mid-cavity mode, as suppressing it allowed the other two cavity modes to persist. Nonetheless, to regulate the additional peaking frequencies observed in the spectra, a base flow modification was required. This modification involved conducting a wavemaker analysis to identify the region that is the source of the instability. By applying injection and suction processes from the wavemaker region to a different area inside the cavity, the base flow was modified accordingly. The results demonstrated successful suppression of the cavity modes, although new modes emerged in the system. These cavity modes are susceptible to external perturbations as well as flow disturbances. The former scenario is more likely to occur in real-life applications, while the latter is employed to prevent resonance of the structural components by shifting the hydrodynamics mode away from the natural frequency modes.

3.6 Conclusions

The first class of machine vibration has been studied numerically in this chapter through two series of test cases. In the first series, the flow past an oscillating bluff body is investigated at $Re = 100$ using Large Eddy Simulation. The objective is here to validate the tools and proposed strategy prior to a more complex turbopump like problem. In this test, the vortex shedding frequency and the imposed frequency of vibration are linked according to the so called "lock-in" region where the natural Strouhal frequency of the flow vortex shedding converges to the imposed one. Attention is brought in this case to both locked and unlocked configurations that are backed by a Fourier transform analysis in each regime. The second part of this chapter deals with rotating flow instabilities. These are intrinsic phenomena of enclosed cavities that depend on the Reynolds number, the geometric configuration of the cavity and its boundary conditions. Such instabilities can furthermore significantly impact the structural integrity of a turbomachine and must be understood for real-life applications. The objective of produced simulations is to investigate the effect of an imposed vibration on such a flow. To do so, and to mimic the effect of external vibrations, the local vibration of a rotor for an academic rotor/stator cavity is assessed by imposing two frequencies that correspond to the most unstable fluid modes inside the cavity for the non-forced case. Large Eddy simulations of the flow responses of these two forced cases show that new instabilities emerge in the system whereas others disappear. This confirms the possibility of using dedicated control strategies as proposed by Queguineur *et al.* (2019) where the same shifting behavior of the various frequencies involved has been observed for the same cavity. The Dynamic Mode Decomposition then successfully sees the perturbation of the flow providing views of the shape of these new instabilities. Complemented by pointwise spectral density analyses performed at different locations inside the cavity, these reveal a broad spectrum of frequencies including hydrodynamic and mechanical modes, making it challenging to identify the flow instabilities. To address this issue and further validate the findings of DMD, a global linear stability analysis is proposed later on to study both forced cases. Such results are to be discussed in the final chapter of the thesis.

Chapter 4

Development of a structural mechanics solver

Contents

This chapter presents the structural mechanics solver developed during this Ph.D work and which is a key element towards fluid-structure interaction simulations. A state of the art review is first provided to lay the foundation of the theories and methods usually used in such a field followed by a thorough description of the concerned equations. Both steady and unsteady (time dependent) problems are considered, the latter being evaluated using two numerical schemes: the Newmark-Beta and the Generalized-alpha algorithms. Two reference problems are then used to verify the obtained solver using linear and quadratic elements. Furthermore, preconditioning methods are also addressed to speed up calculations for various problem sizes .

4.1 Structural mechanics

There exists several possible approaches to build a system of equations describing a material domain. One of them is to decompose the volume of interest into a sum of elementary particles. With a set of assumptions, it is then possible to conceive a description of the physical behavior of these particles. The main work then consists in using this elementary description to construct valid behavioral laws at the macroscopic scale. The kinetic theory of gases is a typical example of such an approach. A continuum approach can also be used to describe large scale dynamics. In that case, instead of describing every single particle, only the average properties at the macroscopic scale are observed. Mathematically, a material domain can be considered as continuous if, at any fixed time t, the physical properties considered are continuous and differentiable with respect to the space variables. In other words, during the modeling process of the material, the discontinuous aspect of matter at the molecular scale is not taken into account. In the current description, the material volume is denoted by $\Omega_s(t) \in \mathbb{R}^3$ and assumed to be entirely occupied by some material. The non-deformed or initial sate is thus denoted by $\Omega_s(t_0)$. For every particle $\tilde{x} \in \Omega_s(t_0)$, the location of any particle at $t \neq t_0$ will be denoted by $x(\tilde{x}, t) \in \Omega_s(t)$. The hypothesis of the continuum makes it possible to ensure that the path between the position of a material particle in $\Omega_s(t_0)$ and its instantaneous position $\Omega_s(t)$ is biunivocal and continuous. Hence the mapping function ζ which associates the coordinates $\tilde{x}$ of a certain particle in $\Omega_s(t_0)$ with a particle x in $\Omega_s(t)$ is invertible,

$$\zeta(\tilde{x}, t) = x, \tag{4.1.1}$$

$$\zeta^{-1}(x, t) = \tilde{x}. \tag{4.1.2}$$

The displacement field can then be defined as the difference between the positions in the instantaneous configuration and the reference configuration,

$$\tilde{\boldsymbol{\xi}}(\tilde{x}, t) = x(\tilde{x}, t) - \tilde{x}. \tag{4.1.3}$$

Differentiating the previous equation with respect to time, one obtains the material velocity,

$$\frac{\partial x}{\partial t} = \partial_t x(\tilde{x}, t) = \partial_t \tilde{\boldsymbol{\xi}}(\tilde{x}, t). \tag{4.1.4}$$

Note that the particle system viewpoint used to describe the evolution of the continuum $\Omega_s(t)$ is the *Lagrangian coordinate system*. Figure. 4.1 illustrates the dynamics of such a system. The particles $\tilde{x}$ follow a certain path $\tilde{\boldsymbol{\xi}}(\tilde{x}, t)$ over time. This approach is typically used in structural mechanics where particles in the reference system are closely linked to each other. From a practical point of view, the numerical study of a physical system requires a spatial discretization of the system and the mesh used for this purpose is deformable, meaning that the nodes of the mesh are attached to the material volumes defined by the discretization.

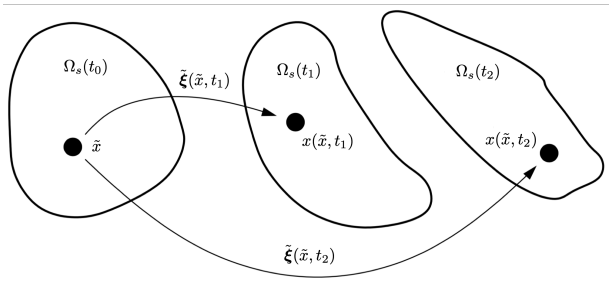

Figure 4.1: Schematic of a Lagrangian reference system.

The deformation gradient is a fundamental quantity in the study of continuum mechanics, It is a tensor that relates the initial and final configurations of a material volume and expresses how much a body has deformed under a given loading,

$$\tilde{\mathbf{F}}(\tilde{x}, t) = \mathbf{I} + \tilde{\nabla}\tilde{\boldsymbol{\xi}}(\tilde{x}, t), \tag{4.1.5}$$

where $\mathbf{I}$ is the identity matrix and $\tilde{\nabla}$ is the nabla operator applied to the deformation in the reference configuration. Using the deformation gradient, the strain tensor describing the relative length change of location of a material point can be defined as,

$$\tilde{\mathbf{E}} = \frac{1}{2}(\tilde{\mathbf{F}}^T\tilde{\mathbf{F}} - \mathbf{I}), \tag{4.1.6}$$

where $\tilde{\mathbf{E}}$ is the *Green-Lagrange strain tensor* which does not contain rigid body deformations. The strain therefore measures the difference of the squared length of a line-segment under deformation. The term $\tilde{\mathbf{F}}^T\tilde{\mathbf{F}}$ is called the *right Cauchy-Green tensor* and is denoted by $\tilde{\mathbf{C}}$. This tensor is symmetric and positive definite. In addition, both tensors $\tilde{\mathbf{C}} = \tilde{\mathbf{F}}^T\tilde{\mathbf{F}}$ and $\tilde{\mathbf{E}} = \frac{1}{2}(\tilde{\mathbf{C}} - \mathbf{I})$ are non-linear functions that can be expressed in terms of the deformaton gradient,

$$\tilde{\mathbf{C}} = \mathbf{I} + \tilde{\nabla}\tilde{\boldsymbol{\xi}} + \tilde{\nabla}\tilde{\boldsymbol{\xi}}^T + \tilde{\nabla}\tilde{\boldsymbol{\xi}}\tilde{\nabla}\tilde{\boldsymbol{\xi}}^T, \quad \tilde{\mathbf{E}} = \frac{1}{2}(\tilde{\nabla}\tilde{\boldsymbol{\xi}} + \tilde{\nabla}\tilde{\boldsymbol{\xi}}^T + \tilde{\nabla}\tilde{\boldsymbol{\xi}}\tilde{\nabla}\tilde{\boldsymbol{\xi}}^T). \tag{4.1.7}$$

If the deformations are assumed to be small ($\left\|\tilde{\nabla}\tilde{\boldsymbol{\xi}}\right\| << 1$), the non-linear term $\tilde{\nabla}\tilde{\boldsymbol{\xi}}\tilde{\nabla}\tilde{\boldsymbol{\xi}}^T$ can be dropped and the linearized strain tensor is obtained,

$$\mathbf{c} = \mathbf{I} + \tilde{\nabla}\tilde{\boldsymbol{\xi}} + \tilde{\nabla}\tilde{\boldsymbol{\xi}}^T, \quad \boldsymbol{\epsilon} = \frac{1}{2}(\tilde{\nabla}\tilde{\boldsymbol{\xi}} + \tilde{\nabla}\tilde{\boldsymbol{\xi}}^T). \tag{4.1.8}$$

Generally speaking, the *Green-Lagrange strain tensor* is sufficient to describing non-linear structural deformations, while the linearized version of this tensor, $\boldsymbol{\epsilon}$, is adequate to approximate linear deformations.

Deformation and strain are kinematic principles that describe the motion and amount of deformation of a solid body without considering the forces that cause the deformation. Stress on the other hand is not a kinematic principle, it measures the internal forces within a material that arise when it is subject to an external force or load and is defined as the force per unit area that a material experiences. There exist different approaches to describe the stress in a material and Cauchy's stress theorem implies that there exists a unique second order tensors σ_s and $\tilde{\mathbf{P}}$ so that,

$$\vec{t}_s(x, t, \vec{n}_s) = \sigma_s(x, t)\vec{n}_s, \quad \tilde{\vec{t}}_s(\tilde{x}, t, \tilde{\vec{n}}_s) = \tilde{\mathbf{P}}(\tilde{x}, t)\vec{n}_s. \tag{4.1.9}$$

where $\vec{n}_s$ is the unit normal vector acting on a surface and pointing outward. The tensor σ_s is symmetric and called the Cauchy stress tensor. It describes the stress in the current or deformed configuration. In matrix form, and using Einstein's notation, the three dimensional form of σ_s can be written as:

$$\sigma_s = \begin{pmatrix} \sigma_{ii} & \sigma_{ij} & \sigma_{ik} \\ \sigma_{ji} & \sigma_{jj} & \sigma_{jk} \\ \sigma_{ki} & \sigma_{kj} & \sigma_{kk} \end{pmatrix}, \tag{4.1.10}$$

where the normal and shear stresses constitute the diagonal and off-diagonal terms respectively. The stress tensor is useful when describing simple linear elasticity models. Note that the first Piola-Kirchhoff stress tensor, $\tilde{\mathbf{P}}$, is a more useful quantity than the Cauchy stress tensor in some cases, such as when analyzing non-linear material behavior, large deformations, and problems involving coordinates that are not orthogonal. The second order tensor $\tilde{\mathbf{P}}$ is usually not symmetric and consists of nine independent entries. There exists a relationship between this tensor and the Cauchy stress tensor,

$$\sigma_s \vec{n}_s d\Omega_s = \tilde{\mathbf{P}}\tilde{\vec{n}}_s d\tilde{\Omega}_s. \tag{4.1.11}$$

Note that it is often convenient for numerical purposes to define a symmetric stress tensor $\tilde{\mathbf{S}}$ that relates the *Green-Lagrange* strain tensor to the *Cauchy* stress tensor. This tensor is called the *second Piola-Kirchhoff* stress tensor and is expressed as,

$$\tilde{\mathbf{S}} = det(\tilde{\mathbf{F}})\tilde{\mathbf{F}}^{-1}\tilde{\sigma_s}\tilde{\mathbf{F}}^{-T}. \tag{4.1.12}$$

For the sake of simplicity, the structure solver to be developed hereafter is limited to hyperelastic solid models for which the stress-strain relationship is based on the Saint-Venant-Kirchhoff model so only geometric non-linearities are considered. The *second Piola-Kirchhoff* stress tensor $\tilde{\mathbf{S}}$ then writes:

$$\tilde{\mathbf{S}} = \lambda_s tr(\tilde{\mathbf{E}})\mathbf{I} + 2\mu_s\tilde{\mathbf{E}}. \tag{4.1.13}$$

In this last expression, the non-dimensional Lamé coefficients are related to the Poisson ratio, ν_s, which is a measure of the material's compressibility, as well as the Young's modulus, E_s, which is a measure of the material's stiffness,

$$\lambda_s = \frac{E_s \nu_s}{(1+\nu_s)(1-2\nu_s)}, \quad \mu_s = \frac{E_s}{2(1+\nu_s)}. \tag{4.1.14}$$

Again, if deformations are assumed to be small ($\left\|\tilde{\nabla}\tilde{\boldsymbol{\xi}}\right\| << 1$), linearizing this tensor yields,

$$\tilde{\mathbf{S}} = \tilde{\boldsymbol{\sigma}}_s = \mathbf{c} : \boldsymbol{\epsilon}, \tag{4.1.15}$$

where the Cauchy stress tensor becomes equal to the second Piola-Kirchhoff stress tensor. In other words, for linear problems, the two stress measures are equivalent. Ultimately, the *first Piola-Kirchhoff* stress tensor $\tilde{\mathbf{P}}$ can be used to relate the force acting on the current configuration $\Omega_s(t)$ to the surface element in the reference configuration $\Omega_s(t_0)$. This tensor is written as a function of the *second Piola-Kirchhoff* stress tensor $\tilde{\mathbf{S}}$ so that,

$$\tilde{\mathbf{P}} = \tilde{\mathbf{F}}\tilde{\mathbf{S}}. \tag{4.1.16}$$

Having defined the behavior o a material, one of the most fundamental conservation principles in the context of fluid dynamics and structural mechanics to be used are the conservation of mass and momentum. The former states that mass can neither be created nor destroyed, whereas the latter implies that the change in momentum is equal to the sum of external forces. Note that, a distinction has to be made in the case of compressible and incompressible solids. In the current framework, the assumption of a uniform solid density ρ_s is adopted in absence of external forces acting on the solid body. When a certain load is applied, the density varies in compressible materials according to the following relation:

$$\rho_s(t) = \tilde{J}\rho_s(t_0), \tag{4.1.17}$$

where $\tilde{J} = det\,\tilde{\mathbf{F}}$ is the deformation gradient determinant that measures the volumetric change of a solid. For incompressible materials that conserve the same density over time, the volumetric change is zero so,

$$\tilde{J} = 1. \tag{4.1.18}$$

For $t \geq 0$, the Reynolds Transport Theorem is then used to derive the conservation of mass and the conservation of momentum equations. For a certain material volume $\Omega_s(t)$, let $\boldsymbol{\Phi(x,t)}$ be a sufficiently smooth scalar function defined on $\Omega_s(t)$, the transport theorem then writes,

$$\frac{d}{dt}\int_{\Omega_s(t)} \boldsymbol{\Phi}(x,t) d\Omega_s = \int_{\Omega_s(t)} \frac{\partial \boldsymbol{\Phi}(x,t)}{\partial t} d\Omega_s + \int_{d\Omega_s(t)} \boldsymbol{\Phi(x,t)} \frac{\partial \boldsymbol{\xi}}{\partial t}(x,t) \cdot \vec{n}_s dS \tag{4.1.19}$$

Note that $\Omega_s(t)$ is bounded by a closed regular surface $d\Omega_s$ with outward normal $\vec{n}_s$.

Making use of the Transport Theorem, the law of Mass Conservation writes for the scalar value $\Phi(x,t) = \rho_s(x,t)$:

$$\int_{\Omega_s(t)} \frac{\partial \rho_s}{\partial t} + \nabla \cdot (\rho_s \frac{\partial \boldsymbol{\xi}}{\partial t}) \Omega_s = 0. \tag{4.1.20}$$

Assuming that the term under the integral is continuous which is a valid assumption for the physical property of a solid, the following equation holds,

$$\frac{\partial \rho_s}{\partial t} + \nabla \cdot (\rho_s \frac{\partial \boldsymbol{\xi}}{\partial t}) = 0. \tag{4.1.21}$$

Similarly, the **conservation of momentum** equation derived for the scalar value $\boldsymbol{\Phi}(x,t) = \rho_s(x,t)\frac{\partial \boldsymbol{\xi}}{\partial t}(x,t)$ and combined with the mass-conservation equation yields:

$$\rho_s \frac{\partial^2 \boldsymbol{\xi}}{\partial t^t} + \rho_s(\frac{\partial \boldsymbol{\xi}}{\partial t} \cdot \nabla)\frac{\partial \boldsymbol{\xi}}{\partial t} = \rho_s \mathbf{f} + \nabla \cdot (\sigma_s). \tag{4.1.22}$$

The above equation is the non-conservative form of the momentum equation where $\mathbf{f}$ is the external body force and σ_s is the Eulerian stress tensor. These conservation equations are valid in the Eulerian framework.

As discussed at the beginning of this section, it is better to describe the dynamics of a structure in a Lagrangian framework. Transforming equation (4.1.22) to the Lagrangian coordinate system and finding the exact form of the Piola Kirchhoff stress tensor in this reference system, the momentum equations becomes,

$$\rho_s \frac{\partial^2 \tilde{\xi}}{\partial t^2} = \tilde{\nabla} \cdot \tilde{\mathbf{P}} + \rho_s \tilde{\mathbf{f}}. \tag{4.1.23}$$

This last expression is the so-called elastodynamic equation which describes the behavior of a structure in response to external forces. It expresses the fact that the acceleration of a material point is given by the second derivative of its displacement which is equal to the change in momentum due to the internal stresses that develop in the material as it deforms, plus the external forces that act on the material from the outside, such as gravity or applied loads. Note that the convective term in the conservation of momentum equation (4.1.22) has been dropped, this is due to the change of Eulerian to Lagrangian coordinates. The reader can refer to (Richter (2017)) for the complete derivation of this equation.

4.2 Numerical methods and solid mechanics

While the derivation of the governing equations are not unduly difficult, finding their exact solution with existing mathematical methods is often challenging due to geometric and physical parameter complexities. To circumvent this difficulty, there exists numerical methods and as for other fields of physics, the finite difference approximation, finite volume method, spectral methods can be used. In structural mechanics however, the finite element method (FEM) has been widely used for the design and analysis of a variety of structures. Indeed, its flexibility and efficiency have proven to be applicable to a wide range of structural problems, from simple beams to complex three-dimensional structures. In addition to being computationally efficient, FEM can handle large-scale problems as it allows for the use of parallel processing techniques to reduce the time required for solving large-scale problems. The mathematical theory behind the finite element method is out

of the scope of this work and readers can refer to the books of J N Reddy (2005), Sadd (2009) and Becker & Becker (2004) for more details. The basic idea of this method is to approximate the solution of a partial differential equation by dividing the problem domain into a finite number of smaller regions known as *finite elements*. Then, polynomials or piecewise polynomial functions are used to approximate the solution over each element. These functions are typically defined by a set of nodal values, which are determined by imposing boundary conditions and matching the solutions at the interfaces between neighboring elements. This process is known as *meshing* or *discretization*. The equations for each element are then assembled into a global system of equations that describes the behavior of the entire structure which can be solved numerically to obtain the nodal values of the solution.

To break down these steps into a coherent example, only one finite element is considered below. Assuming a continuous function $u(x, y)$ within an isolated element Ω_e possessing a certain number of nodes n, the general form of the polynomial function u_h^e used to approximate u takes the form,

$$u(x, y) \approx u_h^e = \sum_{a=1}^{n} u_a^e N_a^e(x, y) \quad over \quad \Omega_e, \tag{4.2.1}$$

where u_a^e is the nodal value of u at node a within element e and N_a is the interpolation function associated to node a. The interpolation function is also called *shape function* in the literature and verifies the two following properties,

$$\begin{cases} N_a^e(x, y, z) = 1, \\ N_a^e(x, y, z) = 0, \quad a \neq b. \end{cases} \tag{4.2.2}$$

This property implies that these functions are continuous piecewise affine and are equal to 1 on one node of a mesh and 0 on all others. The number of nodes or positions where unknowns are to be obtained in an element depends on its geometry and the polynomial order. In our context and for simplicity, one retains $2D$ triangular and $3D$ tetrahedral elements. Regarding the polynomial order, only first order P_1 and second-order P_2 elements will be considered as recommended by the literature. These are also known as **linear elements** and **quadratic elements**. Figure 4.2 shows two $2D$ triangular finite elements used in this work and highlight the notion of order of a polynomial in each. The number of nodes in each element equals the number of parameters required to define a certain order of a polynomial. These elements are defined using *Pascal's triangle*, whereas for $3D$ tetrahedral elements, a *Pascal's pyramid* is used. Assuming a $2D$ Cartesian coordinate system (x, y), a $P1$ element is defined using three terms: a constant a, b for the x dependency and c for the y dependency. Subsequently, the corresponding shape function is generated over the discretized domain or the so called *reference elements*. For each vertex u^a, the first-order polynomial function N_a is thus given by,

$$N_a = a_a + b_a x + c_a y. \tag{4.2.3}$$

where a_a, b_a and c_a are constants to be determined while constructing the system of equations that satisfies each shape function N_a. In particular, for N_1 the corresponding

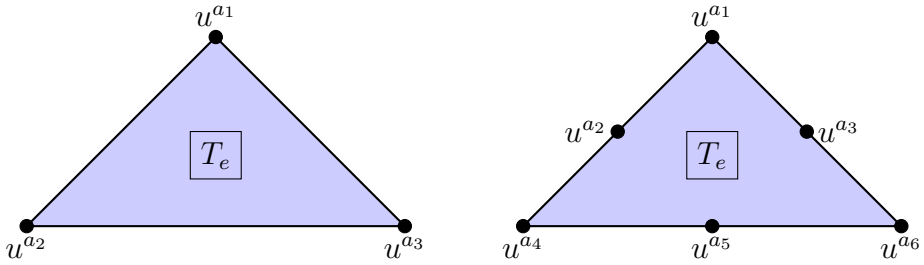

(a) $P1$ degree of freedom on triangle T_e

(b) $P2$ degree of freedom on triangle T_e

Figure 4.2: $2D$ triangular finite elements .

requirements are formulated to be,

$$\begin{cases} N_1(x_1, y_1) = a_1 + b_1 x_1 + c_1 y_1 = 1, \\ N_1(x_2, y_2) = a_1 + b_1 x_2 + c_1 y_2 = 0, \\ N_1(x_3, y_3) = a_1 + b_1 x_3 + c_1 y_3 = 0, \end{cases} \tag{4.2.4}$$

where N_1 is considered to be the home node for which $u^{a_1}(x_1, y_1) = 1$ and N_2 and N_3 are the distant nodes. This system of equations is then solved to retrieve the three unknowns a_1, b_1 and c_1. That is,

$$a_1 = \frac{x_2 y_3 - x_3 y_2}{2A_e}, \quad b_1 = \frac{y2 - y3}{2A_e}, \quad c_1 = \frac{x_3 - x_2}{2A_e}, \tag{4.2.5}$$

where A_e is the area of the triangular element that can be obtained using,

$$A_e = \frac{1}{2} det \begin{vmatrix} 1 & x_1 & y_1 \\ 1 & x_2 & y_2 \\ 1 & x_3 & y_3 \end{vmatrix} = \frac{1}{2}[(x_2 y_3 - x_3 y_2) + (y_2 - y_3)x_1 + (x_3 - x_2)y_1] \tag{4.2.6}$$

Substituting Eq. (4.2.5) into the system of Eq. (4.2.4), N_1 can be re-written as:

$$N_1 = \frac{1}{2A_e}[(y_2 - y_3)(x - x_2) + (x_3 - x_2)(y - y_2)]. \tag{4.2.7}$$

The same procedure can be applied to the remaining shape functions N_2 and N_3. For the sake of conciseness, the shape functions are summarized below in the following form:

$$\begin{aligned} N_i &= a_i + b_i x + c_i y, \\ a_i &= \frac{1}{2A_e}(x_j y_k - x_k y_j), \\ b_i &= \frac{1}{2A_e}(y_j - y_k), \\ c_i &= \frac{1}{2A_e}(x_k - x_j), \end{aligned} \tag{4.2.8}$$

where the subscript i varies from 1 to 3, and j and k are determined by the cyclic permutation in the order of i, j, k. The methodology developed for the design of Linear Lagrange elements can be extrapolated to quadratic elements. A $P2$ element however requires 6 parameters to be defined, explaining the 6 nodes shown on Fig. 4.2. The shape function describing such an element is made of second-order polynomials defined using the following expression,

$$N_a = a_a + b_a x + c_a y + d_a x^2 + e_a xy + f_a y^2. \tag{4.2.9}$$

The same derivation procedure as before requires that for any node a of an element, the corresponding shape function N_a is equal to unity at this node and zero at the remaining nodes. The shape function is then generated. Note that $3D$ tetrahedral elements used in this thesis are defined using *Pascal's pyramid*. Their derivation is not provided here due to the lengthy procedure.

4.2.1 Steady-state linear elasticity problem

In this section, the particular case of solving numerically the steady-state elasticity problem is first detailed. Since the problem is no longer time dependent, the elastodynamic Eq. (4.1.23) reduces to,

$$-\tilde{\nabla} \cdot \tilde{\mathbf{P}} = \rho_s \tilde{\mathbf{f}}. \tag{4.2.10}$$

In addition, and as a first step towards solving this equation, small deformations are assumed so that only the steady-state linear elasticity equation is addressed. That is,

$$-\tilde{\nabla} \cdot \tilde{\sigma}_s = \rho_s \tilde{\mathbf{f}}. \tag{4.2.11}$$

To complete the problem formulation, this partial differential equation needs to come with appropriate boundary conditions. To do so, the boundary of the solid domain $\tilde{\Gamma}_s = \partial\tilde{\Omega}_s$ is split into a Dirichlet boundary $\tilde{\Gamma}_s^D = \partial\tilde{\Omega}_s^D$ and a Neumann boundary on segment $\tilde{\Gamma}_s^N = \partial\tilde{\Omega}_s^N$ so that $\tilde{\Gamma}_s = \tilde{\Gamma}_s^D \cup \tilde{\Gamma}_s^N$. On the Dirichlet boundary, the following condition is enforced for the deformation,

$$\tilde{\boldsymbol{\xi}} = \tilde{\boldsymbol{\xi}}^D \quad on \quad \tilde{\Gamma}_s^D. \tag{4.2.12}$$

Contrarly, the Neumann condition implies the specification of boundary stresses to be,

$$\tilde{\boldsymbol{\sigma}}_s \cdot \vec{n}_s = \mathbf{g}_s \quad on \quad \tilde{\Gamma}_s^N, \tag{4.2.13}$$

where $\mathbf{g}_s$ is the normal force applied on $\tilde{\Gamma}_s^N$.

The equations and assumptions listed above result in a system of equations that describe the stead-state linear elasticity problem:

$$\begin{cases} -\tilde{\nabla} \cdot \tilde{\sigma}_s = \rho_s \tilde{\mathbf{f}} & in \quad \tilde{\Omega}_s, \\ \tilde{\sigma}_s = \lambda_s tr(\boldsymbol{\epsilon})\mathbf{I} + 2\mu_s(\boldsymbol{\epsilon}) & in \quad \tilde{\Omega}_s, \\ \tilde{\boldsymbol{\xi}} = \tilde{\boldsymbol{\xi}}^D & on \quad \tilde{\Gamma}_s^D, \\ \tilde{\boldsymbol{\sigma}}_s \cdot \vec{n}_s = \mathbf{g}_s & on \quad \tilde{\Gamma}_s^N. \end{cases} \tag{4.2.14}$$

This system of equations is often referred to as the **strong form** of the linear elasticity equation.

As stated earlier, exact mathematical methods are often impractical to solve partial differential equations. As discussed previously, an alternative technique consists in constructing approximation functions including piecewise functions and the notion of the variational method, also called the **weak form** of a PDE. This context is obtained by multiplying the strong form by a test function and integrating over the domain. This mathematical manipulation leads to a set of integral equations involving integrals of the functions themselves as well as their derivatives. The weak form is a more general statement of the problem that requires weaker assumptions on the regularity of the function and offers several advantages that will be revealed shortly after. There are several types of weak form methods that can be then used to solve partial differential equations (PDEs), e.g. the Ritz, Galerkin, colocation, least-squares, weighted-residual methods... These methods differ in the choice of the test functions and in the way they approximate the solution of the PDE. In particular, the Galerkin method used in this chapter introduces test functions and basis functions to be the same to approximate the solution of the PDE. This method leads to a symmetric, positive definite system of linear equations for the problem at hand. Before proceeding to the derivation of the weak form, it is however necessary to define an appropriate test function.

To do so, let $\tilde{\boldsymbol{\psi}}_s$ be a test function from the function space $\tilde{\boldsymbol{\mathcal{U}}}_s = \{\tilde{\boldsymbol{\psi}}_s \in \mathcal{H}^1(\tilde{\Omega}_s), \tilde{\boldsymbol{\psi}}_s = \mathbf{0}$ on $\tilde{\Gamma}_s^D\}$ with $\mathcal{H}^1(\tilde{\Omega}_s)$ being the space of continuous functions such as $\mathcal{H}^1(\Omega) = \{\tilde{\boldsymbol{\xi}} \in \boldsymbol{\mathcal{L}}^2(\Omega) : \nabla\tilde{\boldsymbol{\xi}} \in \boldsymbol{\mathcal{L}}^2(\Omega)\}$ where $\boldsymbol{\mathcal{L}}^2(\Omega)$ is the Hilbert space. The weak form of the steady-state linear elasticity equation can then be formulated as,

$$\begin{aligned}
\int_{\tilde{\Omega}_s} \tilde{\mathbf{f}} \cdot \tilde{\boldsymbol{\psi}}_s &= \int_{\tilde{\Omega}_s} -\tilde{\nabla} \cdot \tilde{\sigma}_s(\tilde{\boldsymbol{\xi}}) \cdot \tilde{\boldsymbol{\psi}}_s \,, \\
&= \int_{\tilde{\Omega}_s} \tilde{\sigma}_s(\tilde{\boldsymbol{\xi}}) : \nabla\tilde{\boldsymbol{\psi}}_s - \int_{\tilde{\Gamma}_s^N} \tilde{\boldsymbol{\psi}}_s \cdot \mathbf{g}_s \,, \\
&= \int_{\tilde{\Omega}_s} \tilde{\sigma}_s(\tilde{\boldsymbol{\xi}}) : \boldsymbol{\epsilon}(\tilde{\boldsymbol{\psi}}_s) - \int_{\tilde{\Gamma}_s^N} \tilde{\boldsymbol{\psi}}_s \cdot \mathbf{g}_s \,, \\
&= \int_{\tilde{\Omega}_s} \lambda_s \nabla(\tilde{\boldsymbol{\xi}}) \nabla(\tilde{\boldsymbol{\psi}}_s) + \int_{\tilde{\Omega}_s} 2\mu_s \boldsymbol{\epsilon}(\tilde{\boldsymbol{\xi}}) : \boldsymbol{\epsilon}(\tilde{\boldsymbol{\psi}}_s) - \int_{\tilde{\Gamma}_s^N} \tilde{\boldsymbol{\psi}}_s \cdot \mathbf{g}_s \,.
\end{aligned} \tag{4.2.15}$$

This weak form has several advantages compared to the strong form. First, it enables the use of discontinuous or non-smooth functions as solutions, which is not possible for the strong form where solutions must be at least twice differentiable. The order of differentiation of the dependent variable $\tilde{\boldsymbol{\xi}}$ is furthermore reduced in the weak form. This feature makes it easier to numerically solve the partial differential equations, since higher-order derivatives are often difficult to approximate accurately. The weak form also allows for a more natural incorporation of the boundary conditions. These can be included as part of the weight function, which simplifies the problem formulation.

The above equation holds for any test function $\tilde{\boldsymbol{\psi}}_s$ for the solution of the model PDE to be found. However, to actually solve this equation, an infinite number of test functions $\tilde{\boldsymbol{\psi}}_s \in \tilde{\boldsymbol{\mathcal{U}}}_s$ is required since $\tilde{\boldsymbol{\mathcal{U}}}_s$ is an infinite-dimensional space. Instead of tackling this infinite-dimensional problem, it is sufficient to use a finite number of

test functions, provided they form a complete subset of the solution space $\mathcal{H}^1(\tilde{\Omega}_s)$. Therefore if one defines $\tilde{\sqcap}_s$ a finite-dimensional space such that $\tilde{\sqcap}_s \in \tilde{\boldsymbol{\mathcal{U}}}_s$, this allows the definition of a finite element basis $\{N_1, N_2, ..., N_N\}$ of $\tilde{\sqcap}_s$ to exist. The Galerkin approach consists in taking the weak form of the problem and replace the dependent variable $\tilde{\boldsymbol{\xi}}$ by its approximation $\tilde{u_h} = \sum_{a=1}^{N} \tilde{u}_a N_a$ over the solid domain $\tilde{\Omega}_s$. The Lagrange shape function N is in particular used as test function. The resulting equation hence reduces to,

For each $i = 0, 1... N$,

$$\begin{aligned}
&\int_{\tilde{\Omega}_s} \lambda_s \nabla(\tilde{\mathbf{u_h}}) \nabla(\tilde{\mathbf{N_i}}) d\Omega + \int_{\tilde{\Omega}_s} 2\mu_s \boldsymbol{\epsilon}(\tilde{\mathbf{u_h}}) : \boldsymbol{\epsilon}(\tilde{\mathbf{N_i}}) d\Omega = \int_{\tilde{\Gamma}_s^N} \tilde{\mathbf{N_i}} \cdot \mathbf{g}_s d\Gamma + \int_{\tilde{\Omega}_s} \tilde{\mathbf{f}} \cdot \tilde{\mathbf{N_i}} d\Gamma \,, \\
&\sum_{a=1}^{N} [(\lambda_s \int_{\tilde{\Omega}_s} \nabla(\tilde{\mathbf{N}}_a) \nabla(\tilde{\mathbf{N_i}}) + 2\mu_s \int_{\tilde{\Omega}_s} \boldsymbol{\epsilon}(\tilde{\mathbf{N}}_a) : \boldsymbol{\epsilon}(\tilde{\mathbf{N_i}})) \tilde{u}_a] = \int_{\tilde{\Gamma}_s^N} \tilde{\mathbf{N_i}} \cdot \mathbf{g}_s + \int_{\tilde{\Omega}_s} \tilde{\mathbf{f}} \cdot \tilde{\mathbf{N_i}} \,.
\end{aligned} \tag{4.2.16}$$

Note that the last algebraic relationship can be recast in a compact matrix form so,

$$\sum_{a=1}^{n} \tilde{\mathbf{K}}_{ia} \tilde{u}_a = \tilde{\mathbf{F}}_i \quad for \quad n = 1, 2, ..., N \,, \tag{4.2.17}$$

where,

$$\begin{aligned}
\tilde{\mathbf{K}}_{ia} &= [(\lambda_s \int_{\tilde{\Omega}_s} \nabla(\tilde{\mathbf{N}}_a) \nabla(\tilde{\mathbf{N_i}}) + 2\mu_s \int_{\tilde{\Omega}_s} \boldsymbol{\epsilon}(\tilde{\mathbf{N}}_a) : \boldsymbol{\epsilon}(\tilde{\mathbf{N_i}})) \tilde{u}_a] \,, \\
\tilde{\mathbf{F}}_i &= \int_{\tilde{\Gamma}_s^N} \tilde{\mathbf{N_i}} \cdot \mathbf{g}_s + \int_{\tilde{\Omega}_s} \tilde{\mathbf{f}} \cdot \tilde{\mathbf{N_i}} \,,
\end{aligned} \tag{4.2.18}$$

or,

$$\begin{pmatrix}
K_{11} & K_{12} & \cdots & K_{1a} & \cdots & K_{1n} \\
K_{21} & K_{22} & \cdots & K_{2a} & \cdots & K_{2n} \\
\vdots & & & & & \vdots \\
K_{a1} & K_{a2} & \cdots & K_{aa} & \cdots & K_{an} \\
\vdots & & & & & \vdots \\
K_{n1} & K_{n2} & \cdots & K_{na} & \cdots & K_{nn}
\end{pmatrix}
\begin{Bmatrix} u_1 \\ u_2 \\ \vdots \\ u_a \\ \vdots \\ u_n \end{Bmatrix} =
\begin{Bmatrix} F_1 \\ F_2 \\ \vdots \\ F_a \\ \vdots \\ F_n \end{Bmatrix} .$$

The most compact form being,

$$\{\tilde{\mathbf{K}}\}\{\tilde{u}\} = \{\tilde{\mathbf{F}}\} \,, \tag{4.2.19}$$

where $\{\tilde{\mathbf{K}}\}$ is the **stiffness matrix** and $\{\tilde{\mathbf{F}}\}$ is the **force vector** representing the external forces acting on the structure. To incorporate the Dirichlet boundary conditions, a matrix penalization is usually applied to the stiffness matrix, adding a large value to the diagonal terms K_{aa} if the node a is on the boundary and a zero value otherwise.

The full methodology to derive and solve the steady-state linear elasticity equation using the finite element method has been presented. There exists however some cases that involve large structure deformations. These cases cannot be addressed using the linear elasticity theory, instead the full non-linear elasticity equation must be solved. In such cases, the following is to be considered.

4.2.2 Steady-state non-linear problem

The final linear system is valid only for small strains as stated at the beginning of this section. For large deformations, the non-linear term issued bu the Green-Lagrange strain tensor must be taken into account. Subsequently, the non-linear problem is formulated by transforming Eq. (4.2.10) into a minimization problem (a type of optimization) where the goal is to find the minimum value of a given function subject to certain constraints. In this particular case, one seeks the displacement $\tilde{\boldsymbol{\xi}}(u_x, u_y)$ minimizing a certain objective function $\mathcal{F}$. In mathematical terms, the problem writes as,

For $g \in \mathcal{C}^2$;

$$min\ \mathcal{J}(\tilde{\boldsymbol{\xi}}) = \int_{\tilde{\Omega}_s} g(\mathcal{F}) d\Omega - \int_{\tilde{\Gamma}_s^N} \tilde{\mathbf{f}} u_2 dS\,, \tag{4.2.20}$$

where $\mathcal{F} = \mathcal{A}(\tilde{\mathbf{E}}(\tilde{\boldsymbol{\xi}}), \tilde{\mathbf{E}}(\tilde{\boldsymbol{\xi}}))$ and $\mathcal{A}$ is a bilinear symmetric positive function that takes two matrices as input and returns a scalar value.

To do so, if one let $\tilde{\mathbf{v}}(v_x, v_y)$ and $\tilde{\mathbf{w}}(w_x, w_y)$ be two auxiliary displacement functions used to compute the first and second differentials of the bilinear form $\mathcal{F}$, taking the first and second derivatives of $\mathcal{J}(\tilde{\boldsymbol{\xi}})$ yields,

$$\begin{aligned} D\mathcal{J}(\tilde{\boldsymbol{\xi}})(\mathbf{v}) &= \int_{\tilde{\Omega}_s} D\mathcal{F}(\tilde{\boldsymbol{\xi}})(\mathbf{v}) g'(\mathcal{F}(\tilde{\boldsymbol{\xi}})) d\Omega - \int_{\tilde{\Gamma}_s^N} \tilde{\mathbf{f}} v_2 dS\,, \\ D^2\mathcal{J}(\tilde{\boldsymbol{\xi}})((\mathbf{v}),(\mathbf{w})) &= \int_{\tilde{\Omega}_s} D\mathcal{F}(\tilde{\boldsymbol{\xi}})(\mathbf{v}) D\mathcal{F}(\tilde{\boldsymbol{\xi}})(\mathbf{w}) g''(\mathcal{F}(\tilde{\boldsymbol{\xi}})) d\Omega \\ &\quad + \int_{\tilde{\Omega}_s} D^2\mathcal{F}(\tilde{\boldsymbol{\xi}})((\mathbf{v}),(\mathbf{w})) g'(\mathcal{F}(\tilde{\boldsymbol{\xi}})) d\Omega\,, \end{aligned} \tag{4.2.21}$$

where $D^2\mathcal{F}(\tilde{\boldsymbol{\xi}})((\mathbf{v}),(\mathbf{w})) = 2\mathcal{A}(D^2\tilde{\mathbf{E}}[\tilde{\boldsymbol{\xi}}](\mathbf{v},\mathbf{w}), \tilde{\mathbf{E}}[\tilde{\boldsymbol{\xi}}])) + 2\mathcal{A}(D\tilde{\mathbf{E}}[\tilde{\boldsymbol{\xi}}](\mathbf{v}), D\tilde{\mathbf{E}}[\tilde{\boldsymbol{\xi}}](\mathbf{w})))$ and $D^2\tilde{\mathbf{E}}$ is the second differential of $\tilde{\mathbf{E}}$. The first derivative of $\mathcal{J}$ gives insight on the direction which changes $\mathcal{J}$ the most for a small perturbation $\mathbf{v}$ of the displacement field $\tilde{\boldsymbol{\xi}}$ while the second order differential of $\mathcal{J}$, also called the Hessian of $\mathcal{J}$, measures the curvature of $\mathcal{J}$ at the point $\tilde{\boldsymbol{\xi}}$ in the directions $\mathbf{v}$ and $\mathbf{w}$. This curvature provides information about the stability of the minimizer of $\mathcal{J}$ at $\tilde{\boldsymbol{\xi}}$. If $D^2\mathcal{J}(\tilde{\boldsymbol{\xi}})((\mathbf{v}),(\mathbf{w}))$ is positive, then $\tilde{\boldsymbol{\xi}}$ is a local minimum of $\mathcal{J}$ in the direction of $\mathbf{v}$ and $\mathbf{w}$, and hence a stable minimizer. If it is negative, then $\tilde{\boldsymbol{\xi}}$ is a local maximum and hence an unstable minimizer. If it is zero, then further analysis is needed to determine the nature of the minimizer. Given the gradient and Hessian of $\mathcal{J}$, a Newton minimization method can be applied to find the displacement field $\tilde{\boldsymbol{\xi}}$ that minimizes $\mathcal{J}$. Such a Newton method involves iteratively solving the linear system:

$$D^2\mathcal{J}(\tilde{\boldsymbol{\xi}}_k)(d\tilde{\boldsymbol{\xi}}) = D\mathcal{J}(\tilde{\boldsymbol{\xi}}_k)\,, \tag{4.2.22}$$

where $\tilde{\boldsymbol{\xi}}_k$ is the current estimate of the displacement field, $d\tilde{\boldsymbol{\xi}}$ is the displacement update, while $D^2\mathcal{J}(\tilde{\boldsymbol{\xi}}_k)$ and $D\mathcal{J}(\tilde{\boldsymbol{\xi}}_k)$ are the Hessian and gradient evaluated at $\tilde{\boldsymbol{\xi}}_k$ respectively. The solution of this linear system gives the displacement update $d\tilde{\boldsymbol{\xi}}$ that is added to the current estimate $\tilde{\boldsymbol{\xi}}_k$ to obtain a new estimate $\tilde{\boldsymbol{\xi}}_{k+1}$. This process is then repeated until convergence is achieved, *i.e.*, when the norm of the gradient $D\mathcal{J}(\tilde{\boldsymbol{\xi}})$ becomes smaller than a certain tolerance. Figure 4.3 illustrates a Newton optimization problem. In this case,

the Newton update step can be interpreted as creating a quadratic approximation of F around point x. Note that second-order optimization methods tend to converge faster and with greater accuracy than first-order methods because they take into account the curvature of the function. However, they are more computationally expensive since they require the computation of the second derivative. In some cases, quasi-Newton methods can be used as an alternative to approximate the Hessian matrix without explicitly computing it. In that case, such methods are first-order methods and only require the value of the error function and its gradient with respect to the parameters.

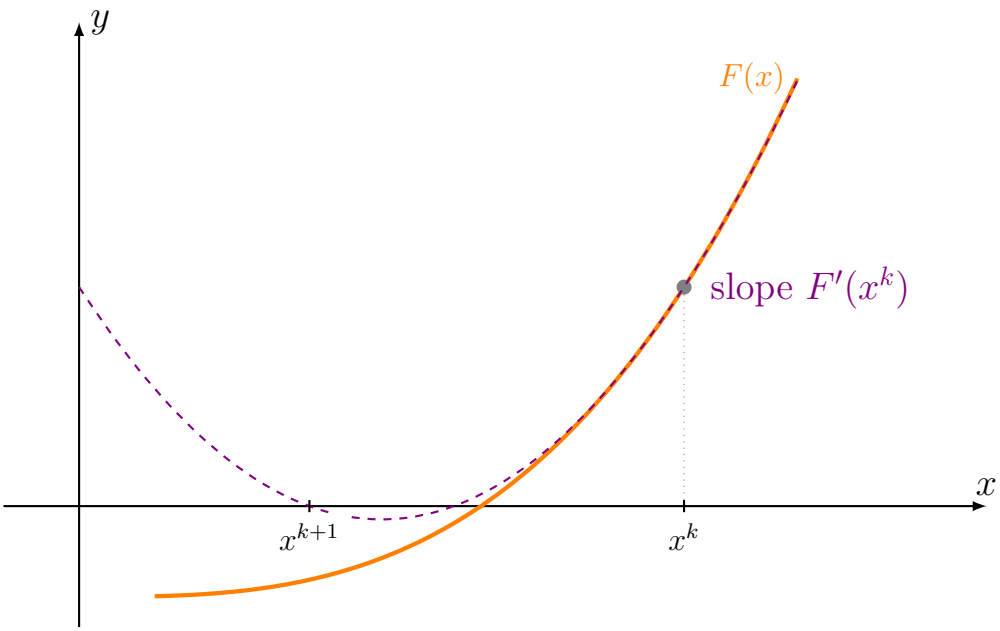

Figure 4.3: Illustration of the Newton minimization method.

While the stead-state elasticity theory can retrieve the correct displacements when dealing with static loads, it will fail to model cases involving dynamic or time dependent problems. This is owed to the fact that the time component is not present in the equation. To address this issue, and to model dynamic problems, the transient elasticity equation is solved in space and time as detailed in the next section.

4.2.3 Dynamic or time dependent problems

In this section, the elastodynamic equation derived section 4.1 in both space and time using the finite element method and a direct numerical integration. To do so, the equation is written in the form of a n-DOF mechanical system with viscous damping. That is,

$$\mathbf{M}\ddot{\mathbf{u}} + \mathbf{C}\dot{\mathbf{u}} + \mathbf{K}\mathbf{u} = \mathbf{F}\,, \tag{4.2.23}$$

where $\mathbf{M}$, $\mathbf{C}$ and $\mathbf{K}$ are the mass, damping and stiffness matrices; $\mathbf{F}$ is the vector of externally applied loads; and $\ddot{\mathbf{u}}$, $\dot{\mathbf{u}}$, $\mathbf{u}$ are the discrete acceleration, velocity and displacement vectors. The idea behind a direct integration method is to assume a variation of

displacements, velocities, and accelerations within a time interval. To do so, suppose that the displacement, velocity, and acceleration vectors at time t_0 denoted by $u_{(0)}$, $\dot{u}_{(0)}$ and $\ddot{u}_{(0)}$ are known so the solution of Eq. (4.2.23) advances this state from time t_0 to time T. To achieve this, the time interval of interest is divided into equal sub-intervals Δt and the integration scheme employed provides a solution approximations at times Δt, $2\Delta t$,...,t,$t + \Delta t$,...,T. As the solution at each instant is calculated based on the solutions at the previous times, the algorithms are derived by assuming that the solutions at times 0, Δt...,t are known, and that the solution at time $t + \Delta t$ is required next. A simple widely used numerical resolution method is in this context the central difference scheme in which Eq.(4.2.23) is discretized as,

$$\mathbf{M}\frac{1}{\Delta t^2}(\mathbf{u}^{t-\Delta t} - 2\mathbf{u}^t + \mathbf{u}^{t+\Delta t}) + \mathbf{C}\frac{1}{2\Delta t}(\mathbf{u}^{t-\Delta t} + \mathbf{u}^{t+\Delta t}) + \mathbf{K}\mathbf{u}^t = \mathbf{F}^t\,, \tag{4.2.24}$$

from which one can solve for $\mathbf{u}^{t+\Delta t}$. This method is effective for very small time steps which is why it is said to be conditionally stable. Indeed, the scheme can become unstable for a time step larger than a certain critical value that can be calculated for a given problem. Another disadvantage is that the solution might yield spurious oscillations. The reader can refer to the book of Bathe (2014) for more details on this method and other integration schemes.

Implicit integration schemes can also be used to solve the dynamic elasticity equation. These methods are unconditionally stable meaning that the choice of the time step does not affect the stability of the scheme. The first of such integration scheme used to solve the above described problem is the Newmark-beta method. This approach is a type of implicit integration scheme that is commonly used for time integration of dynamic systems. It was first introduced by Newmark (1959) and has since become one of the most widely used time integration methods in the field of structural dynamics. The Newmark-beta method is a two-parameter family of algorithms that allows for adjustable levels of numerical damping, which can improve the stability and accuracy of the solution. One of the main strength of this scheme is its ability to handle problems that involve stiff differential equations or use large time steps. This makes it particularly useful in the analysis of structures subject to transient and impulsive loads. The Newmark integration scheme uses the following estimates for the acceleration and velocity,

$$\begin{aligned}\ddot{\mathbf{u}}_{t+\Delta t} &= m_1(\mathbf{u}_{t+\Delta t} - \mathbf{u}_t) - m_2\dot{\mathbf{u}}_t - m_3\ddot{\mathbf{u}}_t\,,\\ \dot{\mathbf{u}}_{t+\Delta t} &= c_1(\mathbf{u}_{t+\Delta t} - \mathbf{u}_t) - c_2\dot{\mathbf{u}}_t - c_3\ddot{\mathbf{u}}_t\,,\end{aligned} \tag{4.2.25}$$

where,

$$\begin{cases} m_1 = \dfrac{1}{\alpha \Delta t^2}\,, \\ m_2 = \dfrac{1}{\alpha \Delta t}\,, \\ m_3 = \dfrac{1}{2\alpha} - 1\,, \\ c_1 = \dfrac{\delta}{\alpha \Delta t}\,, \\ c_2 = \dfrac{\delta}{\alpha} - 1\,, \\ c_3 = \dfrac{\Delta t}{2}(\dfrac{\delta}{\alpha} - 2)\,, \end{cases} \tag{4.2.26}$$

and α and β are Newmark integration parameters that can be determined to obtain integration accuracy and stability. These parameters must meet the following criteria,

$$\begin{cases} \alpha \geq \dfrac{1}{4}(\dfrac{1}{2} + \delta)^2\,, \\ \delta \geq \dfrac{1}{2}. \end{cases} \tag{4.2.27}$$

When $\alpha = \frac{1}{6}$ and $\delta = \frac{1}{2}$, relations (4.2.25) correspond to the linear acceleration method. Newmark initially proposed an unconditionally stable scheme called the constant-average acceleration method, also called the trapezoidal rule for which $\alpha = \frac{1}{4}$ and $\delta = \frac{1}{2}$. In addition to Eq. (4.2.25), to solve for the displacement at $t+\Delta t$ the equilibrium Eq. (4.2.23) is expressed through,

$$\mathbf{M}\ddot{\mathbf{u}}_{t+\Delta t} + \mathbf{C}\dot{\mathbf{u}}_{t+\Delta t} + \mathbf{K}\mathbf{u}_{t+\Delta t} = \mathbf{F}_{t+\Delta t}. \tag{4.2.28}$$

Considering the trapezoidal rule and replacing Eq. (4.2.25) in Eq. (4.2.23) yields,

$$(m_1\mathbf{M}+c_1\mathbf{C}+\mathbf{K})\mathbf{u}_{t+\Delta t} = \mathbf{M}(m_1\mathbf{u}+m_2\dot{\mathbf{u}}_t+a_3\ddot{\mathbf{u}}_t)+\mathbf{C}(c_1\mathbf{u}_t+c_2\mathbf{u}_t+c_3\ddot{\mathbf{u}}_t)+\mathbf{F}_{t+\Delta t}. \tag{4.2.29}$$

This last equation is then solved at every iteration to retrieve $\mathbf{u}_{t+\Delta t}$. In such a case, velocity and acceleration vectors are computed using Eq. (4.2.25).

The Newmark-beta method is commonly used along with the finite element methods for fluid-structure interaction applications. But it has some disadvantages that make it less desirable in some cases. To circumvent these issues, several alternatives have been proposed. One significant drawback of the Newmark method is that it does not allow for the introduction of numerical damping when $\delta = \frac{1}{2}$. It results in high-frequency modes or in the predicted dynamics of such systems, motions that have no physical meaning, resulting in large phase errors. Using other values for α and δ induces non-zero numerical damping that suppresses such high-frequency noise but then care is needed. The Hilber-Hughes-Taylor (HHT) time integration procedure, for example, is a variation of the Newmark method that effectively damps high-frequency noise especially for structural dynamics problems. Another effective numerical scheme is the Generalized-alpha

algorithm. Chung & Hulbert (1993) introduced this method to solve hyperbolic equations that arise in structural dynamics. It has become widely used in engineering and sciences due to its second-order accuracy in time, unconditional stability and user control of high-frequency numerical dissipation. The generalized-alpha method involves solving the dynamic evolution equation at an intermediate time between t and $t+1$ noted as,

$$\mathbf{M}\ddot{\mathbf{u}}_{t+\Delta t-\alpha_m} + \mathbf{C}\dot{\mathbf{u}}_{t+\Delta t-\alpha_f} + \mathbf{K}\mathbf{u}_{t+\Delta t-\alpha_f} = \mathbf{F}_{t+\Delta t-\alpha_f}\,, \tag{4.2.30}$$

where

$$\begin{cases} \ddot{\mathbf{u}}_{t+\Delta t-\alpha_m} = (1-\alpha_m)\ddot{\mathbf{u}}_{t+\Delta t} + \alpha_m \ddot{\mathbf{u}}_t\,, \\ \dot{\mathbf{u}}_{t+\Delta t-\alpha_f} = (1-\alpha_f)\dot{\mathbf{u}}_{t+\Delta t} + \alpha_f \dot{\mathbf{u}}_t\,, \\ \mathbf{u}_{t+\Delta t-\alpha_f} = (1-\alpha_f)\mathbf{u}_{t+\Delta t} + \alpha_f \mathbf{u}_t\,, \\ \mathbf{F}_{t+\Delta t-\alpha_f} = (1-\alpha_f)\mathbf{F}_{t+\Delta t} + \alpha_f \mathbf{F}_t. \end{cases} \tag{4.2.31}$$

Complementarily, the approximations for the displacement and velocity at $t+\Delta t$ should hold so,

$$\begin{aligned} \ddot{\mathbf{u}}_{t+\Delta t} &= m_1(\mathbf{u}_{t+\Delta t} - \mathbf{u}_t) - m_2\dot{\mathbf{u}}_t - m_3\ddot{\mathbf{u}}_t\,, \\ \dot{\mathbf{u}}_{t+\Delta t} &= c_1(\mathbf{u}_{t+\Delta t} - \mathbf{u}_t) - c_2\dot{\mathbf{u}}_t - c_3\ddot{\mathbf{u}}_t\,, \end{aligned} \tag{4.2.32}$$

where:

$$\begin{cases} m_1 = \dfrac{1-\alpha_m}{\alpha\Delta t^2}\,, \\ m_2 = \dfrac{1-\alpha_m}{\alpha\Delta t}\,, \\ m_3 = \dfrac{1-\alpha_m}{2\alpha} - 1\,, \\ c_1 = \dfrac{(1-\alpha f)\delta}{\alpha\Delta t}\,, \\ c_2 = \dfrac{(1-\alpha_f)\delta}{\alpha} - 1\,, \\ c_3 = \dfrac{(1-\alpha_f)\Delta t}{2}(\dfrac{\delta}{\alpha} - 2). \end{cases} \tag{4.2.33}$$

It can be seen that these constraints are equivalent to the relations of the Newmark method. The latter is therefore obtained for a particular case $\alpha_m = \alpha_f = 0$. After plugging these relations into the evolution Eq. (4.2.32), the problem can be formulated in terms of the unknown displacement at $t+\Delta t$ as,

$$\begin{aligned} &(m_1\mathbf{M} + c_1\mathbf{C} + (1-\alpha_f)\mathbf{K})\mathbf{u}_{t+\Delta t} = \\ &\qquad \mathbf{M}(m_1\mathbf{u} + m_2\dot{\mathbf{u}}_t + a_3\ddot{\mathbf{u}}_t) + \mathbf{C}(c_1\mathbf{u}_t + c_2\mathbf{u}_t + c_3\ddot{\mathbf{u}}_t) + (1-\alpha_f)\mathbf{F}_{t+\Delta t} + \alpha_f\mathbf{F}_t - \alpha_f\mathbf{K}\mathbf{u}_t. \end{aligned} \tag{4.2.34}$$

Following the same paradigm as for the Newmark method, the displacement field $U_{t+\Delta t}$ can be solved iteratively and the new velocity and acceleration are computed using the previous formulae.

4.2.4 Direct vs iterative methods

Partial differential equations describing complex problems are often solved by discretizing them in time and space as detailed in the previous sections. This process typically involves solving a linear system of size $\mathcal{N} >> 1$, which can be done once or at multiple successive instants. When using a finite element discretization, the problem is usually sparse, with few non-zero matrix entries. When it comes to inverting these linear systems of equations, two broad categories of methods are viable: direct and indirect methods, also known as iterative methods. Direct methods are algorithms that compute the exact solution to the linear system of equations by performing a finite sequence of mathematical operations. These methods work well for small to moderate-sized problems and are typically used when accuracy is of utmost importance. Nowadays there are many packages available to invert such systems, like MUMPS, SUPERLU and PETSc. PETSc (Portable, Extensible Toolkit for Scientific computing), for example, is a software library for parallel numerical computation that provides a range of solvers and preconditioners for linear and nonlinear systems of equations. It includes several direct solvers for solving sparse linear systems of equations such as: LU factorization, Cholesky factorization, QR factorization, Schur complement. For instance PETSc can use the LU factorization to solve linear systems of the form $\mathbf{Ax} = \mathbf{b}$, where $\mathbf{A}$ is a square sparse matrix. The LU decomposition factorizes the matrix into a lower triangular matrix $\mathbf{L}$ and an upper triangular matrix $\mathbf{U}$, so that the original matrix can be represented as the product of these two matrices: $\mathbf{A} = \mathbf{LU}$. The factorization is then performed using partial pivoting to ensure stability. Partial pivoting involves selecting the pivot element in each column as the element with the largest magnitude. If necessary, the rows of the matrix are interchanged to place the pivot element on the diagonal. Once the LU factorization is complete, the solver uses forward substitution to solve the lower triangular system $\mathbf{Ly} = \mathbf{b}$, followed by a backward substitution to solve the upper triangular system $\mathbf{Ux} = \mathbf{y}$. These steps yield the solution $\mathbf{x}$ to the original linear system $\mathbf{Ax} = \mathbf{b}$. Direct methods are able to find the exact solution of a problem while computationally efficient for small to moderate-sized problems. However, they can be computationally expensive for large-scale problems and require significant amounts of memory. Indeed, the LU decomposition scales barely better than $\mathcal{O}(\mathcal{N}^3)$ operations, making it unsuitable for large-scale problems. For this purpose, iterative methods such as conjugate gradient (CG), generalized minimal residual (GMRES) and bi-conjugate gradient stabilized (BiCGSTAB) are often used instead for large-scale problems where the memory requirements of direct methods are considered a bottleneck. These methods involve calculating a sequence of vectors that, under certain conditions, converge towards the solution for the linear system so that,

$$\mathbf{x}^{k+1} = \mathbf{F}(\mathbf{A}, \mathbf{x}^k)\mathbf{b}^k. \tag{4.2.35}$$

The convergence of these schemes depends on the distribution of the eigenvalue matrix $\mathbf{A}$. In general, the more eigenvalues are clustered, the better the convergence. To clusterize those eigenvalues and accelerate the convergence rate of these iterative techniques, preconditioning is typically used. Preconditioning can be applied to a system by re-expressing it into,

$$(\mathbf{M_L}^{-1}\mathbf{A}\mathbf{M_R}^{-1})(\mathbf{M_R}\mathbf{x}) = \mathbf{M_L}^{-1}\mathbf{b}\,, \tag{4.2.36}$$

where $\mathbf{M_L}$ and $\mathbf{M_R}$ are the left and right preconditioning matrices. If $\mathbf{M_L} = \mathbf{I}$, right preconditioning applies and the residuals of Eq. (4.2.36) is preserved,

$$\mathbf{r} \equiv \mathbf{b} - \mathbf{A}\mathbf{x} = \mathbf{b} - \mathbf{A}\mathbf{M_R}^{-1}\mathbf{M_R}\mathbf{x}. \tag{4.2.37}$$

In contrast, for the left part, if $\mathbf{M_R} = \mathbf{I}$ the residual becomes,

$$\mathbf{r_L} \equiv \mathbf{M_L}^{-1}\mathbf{b} - \mathbf{M_L}^{-1}\mathbf{A}\mathbf{x} = \mathbf{M_L}^{-1}\mathbf{r}. \tag{4.2.38}$$

4.2.5 Code implementation and validation

As said before, for the purpose of the present Ph.D work, a structural mechanics code is needed as a preliminary demonstrator and applicability of the proposed numerical resolution strategy. To do so, the steady and dynamic elasticity equations are developed using FreeFEM++ Hecht (2012). It is an open-source finite element software package specifically designed for solving partial differential equations (PDEs) numerically. It provides a high-level programming language allowing the definition and resolution of a wide range of PDE problems using the finite element method. Both problems are then validated separately in the next sections. In addition, linear and quadratic elements are assessed to evaluate their accuracy and impact for such numerical tools. Finally, a comparative study of direct and iterative methods is conducted to determine their performance with respect to the problem size.

4.2.6 Steady state problem validation

In the following and in order the ensure the correct derivation and implementation of the steady-state linear elasticity solver, a simple $2D$ test case is considered. This test consists in computing the deformation of an elastic beam subject to a gravitational field $\mathbf{g}_s = 2\ m/s^2$ as proposed by Turek & Hron (2007) and referred to as CSM1. For this problem, note that the geometry is identical to the one used in fluid-structure interaction benchmark cases for which a laminar incompressible flow interacts with a beam clamped to the back of a fixed cylinder.

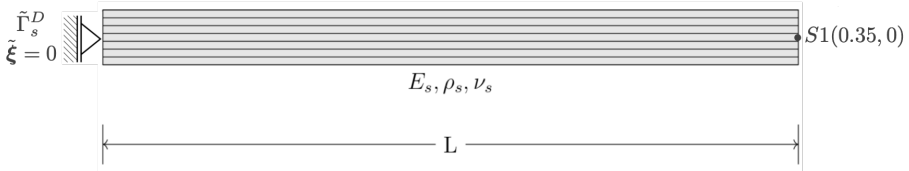

Figure 4.4: Sketch of the $2D$ elastic beam used by Turek & Hron (2007) (Figure not to scale).

All the geometric parameters and material properties are shown on Fig. 4.4. The structure consists of a $L \times H = 0.35\ m \times 0.02\ m$ beam fixed at one end and free to deform elsewhere. The material is characterized by a Young modulus of $E_s = 1.4\ MPa$, a density of $\rho_s = 1000\ Kg/m^3$ and a Poisson's ratio of $\nu_s = 0.4$. For validation, computations are

carried out using three meshes, all composed of triangular elements as shown by Fig. 4.5. Note also that both types of elements $P1$ and $P2$ are used to verify their impact and accuracy on obtained results.

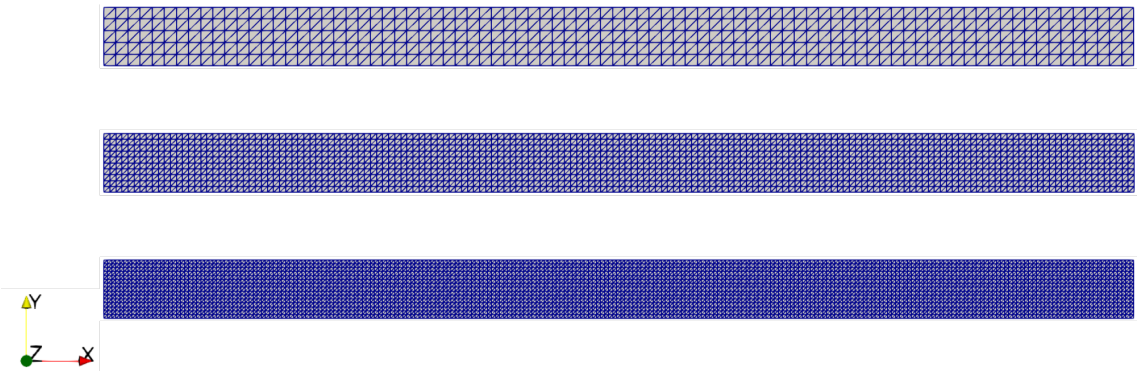

Figure 4.5: Triangular meshes used for mesh convergence study. From top to bottom, the mesh cell size is respectively 0.004 m, 0.002 m and 0.0013 m.

The problem is solved separately using the linear and non-linear methods. The former employs Eq. (4.2.15) while the latter uses Eq. (4.2.20). Figure 4.6 displays the deformation magnitude of the structure using $P1$ elements. As expected, the structure deflects downward in the direction of the gravitational field. The results obtained for the different meshes and methods are compiled in Tab. 4.1. For the non-linear problem, six Newton iterations are necessary for the solution to converge for mesh 1, whereas five iterations are required for the remaining meshes. Convergence is achieved when the residuals of the deformation magnitude becomes smaller than the tolerance set to be 10^{-10}. The two components of the displacement $\tilde{\boldsymbol{\xi}}(\tilde{\mathbf{u}}_x, \tilde{\mathbf{u}}_y)$ are recorded through the numerical probe $S1(0.35, 0)$ and the associated error is determined using the actual displacement magnitude and the reference displacement magnitude from the benchmark case CSM1: where $\tilde{\boldsymbol{\xi}}(\tilde{\mathbf{u}}_x, \tilde{\mathbf{u}}_y) = (-0.007187, -0.066)$. A significant error difference is found for the first mesh which then decreases as the mesh becomes finer. Note that the additional mesh refinement of mesh 3 does not improve results, indicating that mesh convergence is attained. Although the error computed for the linear method is relatively small compared to the non-linear method, a discrepancy is found between the magnitude of the transverse deformation. This is explained by the axial deflection of the beam where the displacement is large but the strains are small. The linear theory is thus sufficient to capture the correct deformation. The deformation of the structure in the transverse direction is however more important indicating that a non-linear method is necessary to retrieve the correct deformation.

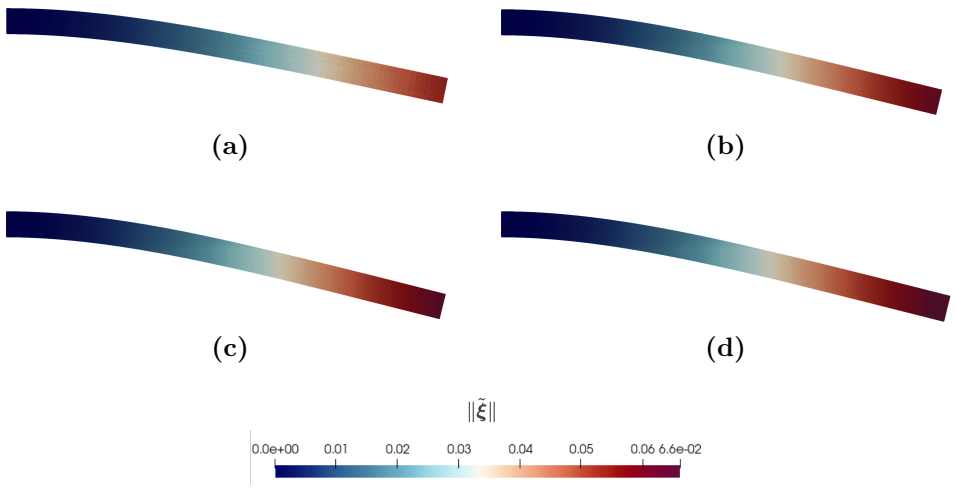

Figure 4.6: Steady state problem solved using **P1 elements**. Structures are colored by magnitude of the deformation. (*a*) Mesh 1, (*b*) Mesh 2, (*c*) Mesh 3, (*d*) Mesh 3 (linear assumption).

mesh	N_{cells}	$\tilde{\mathbf{u}}_x[m]$	$\tilde{\mathbf{u}}_y$ $[m]$	Linear/Non-linear	Error $\left\|\tilde{\boldsymbol{\xi}}\right\|$ (%)
Mesh 1	850	-0.00483	-0.0542	non-linear	22.12%
Mesh 2	3400	-0.00638	-0.0622	non-linear	6.19%
Mesh 3	7650	-0.00675	-0.0640	non-linear	3.18%
Mesh 3	7650	-0.0000014	-0.0657	linear	0.99%

Table 4.1: Results obtained using triangular **P1 Elements** .

Simulations are reconducted using $P2$ elements, the corresponding structural deformations being shown on Fig. 4.7 and Tab. 4.2. In this case, results are more accurate compared to the previous simulations where triangular linear $P1$ elements were used. Since quadratic $P2$ elements introduce higher degrees of freedom, the correct deformation is captured for the same mesh sizes. Good agreement is found for all the different meshes, although the relative error decreases as the mesh becomes finer. The linear method exhibits the same behavior as before, with an underestimation of the transverse deformation $\tilde{\mathbf{u}}_x$ and an accurate prediction of the axial deformation $\tilde{\mathbf{u}}_y$. While both triangular linear $P1$ and quadratic $P2$ elements are able to predict the correct deformations, quadratic $P2$ elements provide more accurate results, albeit with a higher computational cost.

4.2.7 Dynamic problem validation

In the current study, the discretized unsteady elasticity equation is evaluated using both direct and indirect approaches to determine their capabilities. The former employs a classical LU decomposition, while the latter involves two Krylov subspace methods based

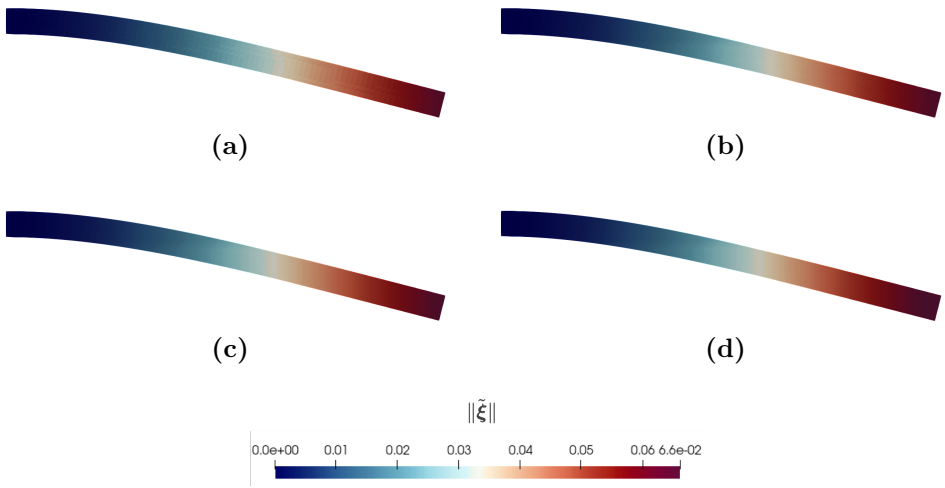

Figure 4.7: Steady state problem solved using **P2 elements**. Structures are colored by magnitude of the deformation. (*a*) Mesh 1, (*b*) Mesh 2, (*c*) Mesh 3, (*d*) Mesh 3 (linear assumption).

mesh	N_{cells}	$\tilde{\mathbf{u}}_x[m]$	$\tilde{\mathbf{u}}_y$ $[m]$	Linear/Non-linear	Error $\left\|\tilde{\boldsymbol{\xi}}\right\|$ (%)
Mesh 1	850	-0.00707	-0.0655	non-linear	0.83%
Mesh 2	3400	-0.00708	-0.0653	non-linear	0.73%
Mesh 3	7650	-0.00708	-0.0655	non-linear	0.7%
Mesh 3	7650	-0.0000012	-0.0657	linear	1.53%

Table 4.2: Results obtained using triangular **P2 Elements**.

on GMRES with left preconditioning and conjugate gradient. In the next section, the performance of each method is discussed.

The dynamic problem resolution procedure is verified through a test case proposed by Helfer *et al.* (2020) and solved in FEniCS (Alnaes *et al.* (2015); Logg *et al.* (2012)), a popular open-source software framework for solving partial differential equations (PDEs) numerically. This solver is based on the generalized alpha scheme and is analyzed by Erlicher *et al.* (2002).

For this validation and test case, the geometry consists of a $3D$ $L \times B \times H = 1\ m \times 0.1\ m \times 0.5\ m$ rectangular beam that is fixed on one end and is subject to a time-dependent loading, $\mathbf{F}$, at the other extremity. Body forces are equal to zero and the imposed loading consists of a uniform vertical traction applied at the right extremity as shown on Fig. 4.8. The total simulation time is $T = 10\,s$ and the loading amplitude varies linearly from 0 to 1 over the time interval $[0; t_c = 0.8]$ where t_c is the cut-off duration, meaning that at this time the loading is removed. When the loading $\mathbf{F}$ is removed the beam is free to oscillate around its initial position and a numerical probe, $S2$ identified on Fig. 4.8, is used to track the trajectory of the beam. The material is characterized by a Young modulus of $E_s = 1000\ Pa$, a density of $\rho_s = 1\ Kg/m^3$ and a Poisson's ratio of $\nu_s = 0.3$.

For the simulation, three meshes composed of tetrahedral elements as shown on Fig. 4.9 are generated with different cell sizes and both linear $P1$ and quadratic $P2$ elements are tested. All mesh properties are given in Table 4.3.

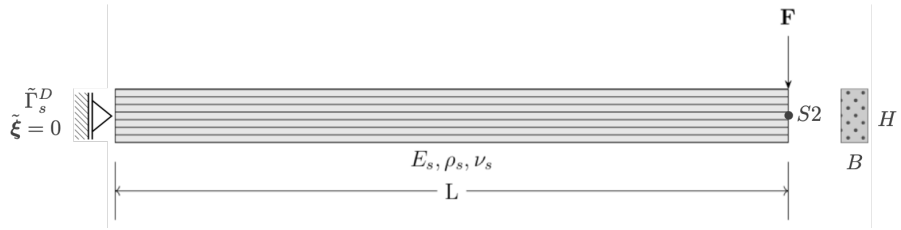

Figure 4.8: Sketch of the $3D$ elastic beam (Figure not to scale).

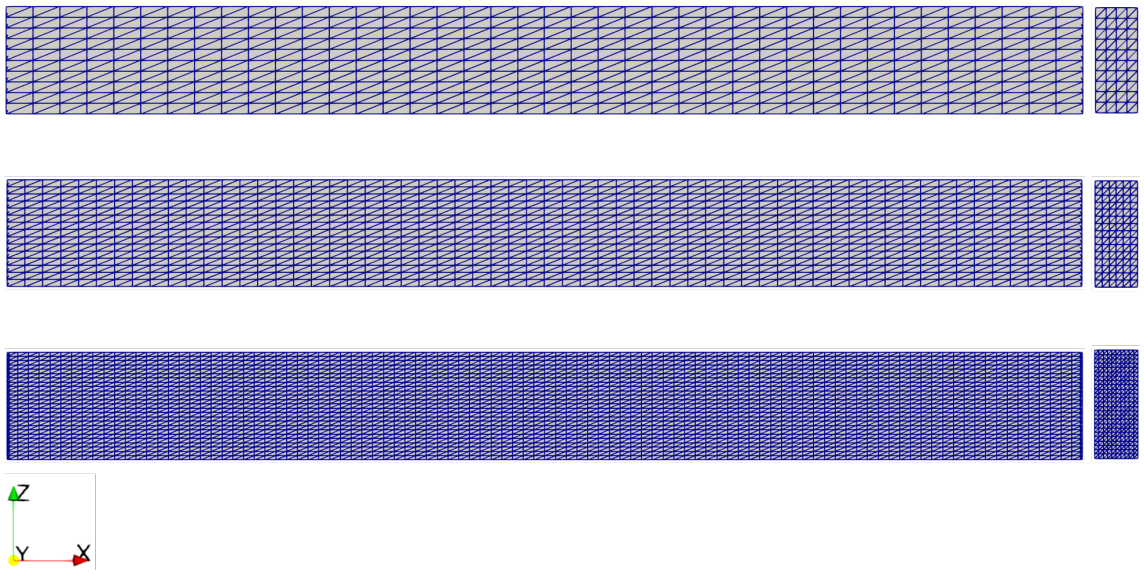

Figure 4.9: Tetrahedral meshes used for mesh convergence study. From top to bottom, the mesh cell size is respectively 0.01 m, 0.0067 m and 0.004 m.

	Mesh 1	**Mesh 2**	**Mesh 3**
Δz [m]	0.01	0.0067	0.004
N_{cells}	9600	32400	150000
N_{nodes} $(P1)$	2255	6832	28886
N_{nodes} $(P2)$	15309	48763	215271

Table 4.3: Characteristics of the three meshes shown on Fig. 4.9.

Simulations are carried using the Generalized alpha method for a total time of $T = 10s$ and a fixed time-step of $\Delta t = 0.08s$. For now, the structure is assumed to be undamped, hence the elastodynamic equation reduces to two left hand side terms that are the mass

and stiffness matrices. Figure 4.10 shows the time evolution of the axial displacement of the beam for point $S2$ and for the three different meshes. Excellent agreement is found between the two solvers for all meshes with $P1$ elements. As expected, once the traction loading is released, the beam starts to oscillate about its initial position with a constant amplitude since external forces and damping are not present. The amplitude attained varies according to the mesh size, the displacement being underestimated for a coarse mesh. Table 4.4 provides a comparative summary of the results obtained by

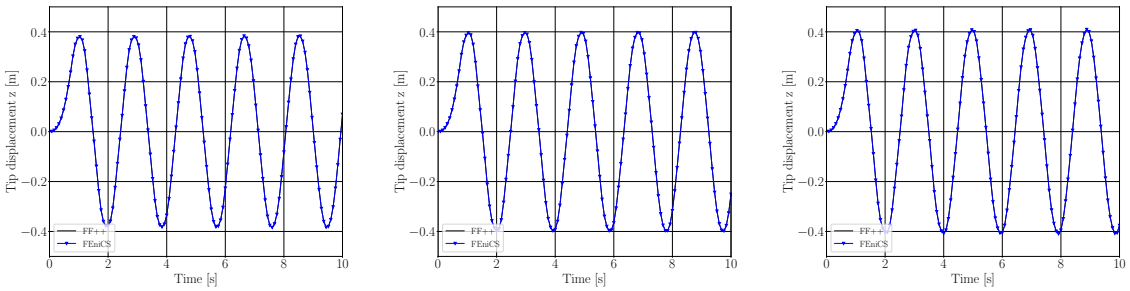

Figure 4.10: Time evolution of the tip displacement $S2$ of the beam obtained with different tetrahedral $P1$ meshe: (a) Mesh 1, (b) Mesh 2, (c) Mesh 3.

the two solvers FreeFEM++ and FEniCS. The error is very low for all cases considered indicating that the correct deformation has been captured. Note however that mesh convergence does not seem to be achieved for this $P1$ based simulation as highlighted by the differences of the transverse component of the deformation $\tilde{\mathbf{u}}_x$ across the three meshes. This is explained by the fact that this case exhibits complex large deformations, linear $P1$ elements failing to capture the correct strains as well as the underlying stresses even for very fines meshes. Subsequently, higher order elements are used specifically to capture this specific dynamics.

mesh	Amp. $\tilde{\mathbf{u}}_x[m]$	Amp. $\tilde{\mathbf{u}}_y$ $[m]$	Amp. $\tilde{\mathbf{u}}_x[m]$(Ref)	Amp. $\tilde{\mathbf{u}}_y[m]$(Ref)	Error $\left\|\tilde{\boldsymbol{\xi}}\right\|$ (%)
Mesh 1	0.00057	0.383	0.00053	0.382	0.26%
Mesh 2	0.00025	0.396	0.00025	0.397	0.25%
Mesh 3	0.00011	0.405	0.00012	0.406	0.25%

Table 4.4: Results obtained using tetrahedral **P1 Elements**.

To do so, computations are performed again using $P2$ elements and results are highlighted in Tab. 4.5. The global behavior of the structure remains almost unchanged as shown on Fig. 4.11. However, mesh convergence can be noticed with the first mesh. The higher degree of freedoms of $P2$ elements enables an accurate computation of the deformation as indicated by the axial and transverse components. Such results clearly illustrate the

need for quadratic elements to have better results compared to linear elements even for a smaller size mesh cells. This confirms their efficiency when dealing with complex large deformations.

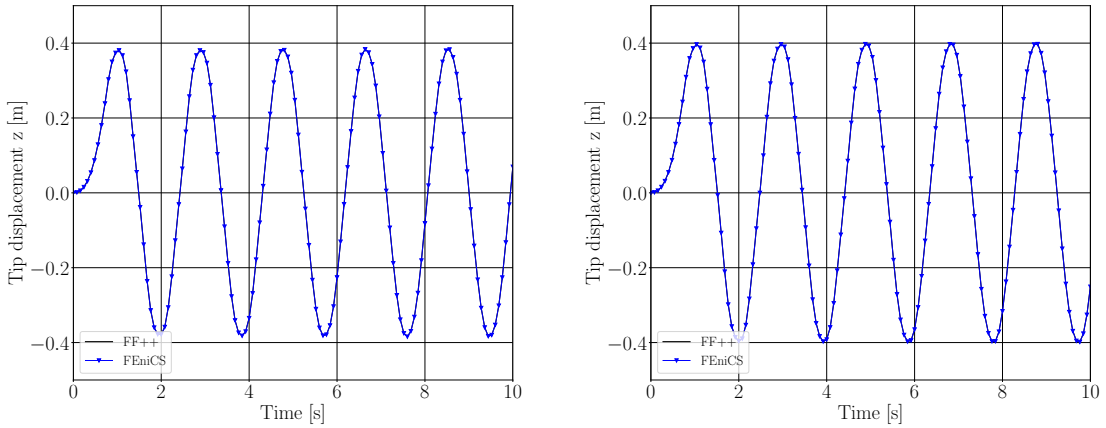

Figure 4.11: Time evolution of the tip displacement $S2$ of the beam obtained with different tetrahedral $P2$ meshes: (a) Mesh 1, (b) Mesh 2, (c) Mesh 3.

mesh	Amp. $\tilde{\mathbf{u}}_x[m]$	Amp. $\tilde{\mathbf{u}}_y\ [m]$	Amp. $\tilde{\mathbf{u}}_x[m]$(Ref)	Amp. $\tilde{\mathbf{u}}_y[m]$(Ref)	Error $\left\|\tilde{\boldsymbol{\xi}}\right\|$ (%)
Mesh 1	1.36×10^{-6}	0.413	1.3×10^{-6}	0.412	0.24%
Mesh 2	1.34×10^{-6}	0.413	1.28×10^{-6}	0.412	0.24%

Table 4.5: Results obtained using triangular **P2 Elements**.

Until now the effect of damping was disregarded. Adding the damping matrix $\mathbf{C}$ for a given material can be however a challenging task. The method called Rayleigh damping is often used to model such specifities of materials. This method consists in using a linear combination of the mass and stiffness matrices so that the damping matrix is expressed as,

$$\mathbf{C} = \eta_M \mathbf{M} + \eta_K \mathbf{K}\,, \tag{4.2.39}$$

where η_M and η_K are two positive parameters that can be fitted against experimental data, usually by measuring the damping ratio of two natural modes of vibration (Chopra (1995); Chopra (2007)).

Based on the results obtained earlier, and to evaluate the effect of damping on the structure motion, Rayleigh damping is added to the initial problem with $\eta_K = \eta_M = 0.01$. A direct consequence of such a change is a structure that exhibits a new dynamic behavior as shown by Fig. 4.12. The amplitude of motion is no longer constant and as expected

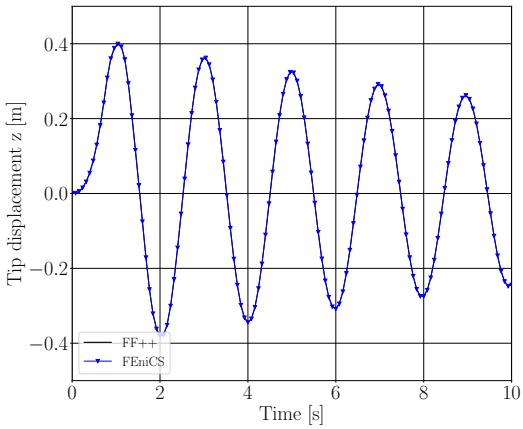

Figure 4.12: Time evolution of the tip displacement $S2$ of the beam obtained with mesh 1 ($P2$ elements) with Rayleigh damping.

decays in time since the structure is now dissipating energy. To further understand the effect of damping on the whole system, various energies can be computed on the fly during simulations. However, the total energy of the system should be conserved so the sum of kinetic E_{kin}, elastic E_{elas} and damping energies E_{damp} which follow,

$$E_{tot} = E_{kin} + E_{elas} + E_{damp}\,, \tag{4.2.40}$$

should hold at any instant with the definitions,

$$\begin{aligned} E_{kin} &= \int_{\tilde{\Omega}_s} \frac{1}{2}\rho_s \dot{\mathbf{u}} \cdot \dot{\mathbf{u}}\; d\Omega\,, \\ E_{elas} &= \int_{\tilde{\Omega}_s} \frac{1}{2}\sigma_s(\mathbf{u}) : \epsilon(\mathbf{u})\; d\Omega\,, \\ E_{damp} &= \eta_M \int_{\tilde{\Omega}_s} \frac{1}{2}\rho_s \dot{\mathbf{u}} \cdot \dot{\mathbf{u}}\; d\Omega + \eta_K \int_{\tilde{\Omega}_s} \frac{1}{2}\sigma(\mathbf{u}) : \epsilon(\mathbf{u})\; d\Omega. \end{aligned} \tag{4.2.41}$$

The evolution of these energies as a function of time is shown on Fig. 4.13. In the absence of Rayleigh damping, the kinetic and elastic energies oscillate between zero and a certain maximal value. When the maximum displacement amplitude is reached by $S2$, the kinetic energy of the beam is zero since at that point the structure switches to the opposite direction so its axial velocity is zero. In contrast, the elastic energy follows the opposite behavior: it reaches its maximum value when $S2$ reaches its peak displacement value and is equal to zero when $S2$ passes through the initial position. When Rayleigh damping is added to the system, the damping energy is seen to increase with time at the expense of the elastic and kinetic energies. Looking at the total energy of the system, although it should be conserved at every time step, it appears to slightly decrease with time at a very slow rate indicative of numerical damping.

Recall that when setting the generalized alpha parameters to zero ($\alpha_m = \alpha_f = 0$), the Newmark beta scheme is recovered. In such a case, the scheme is known to be

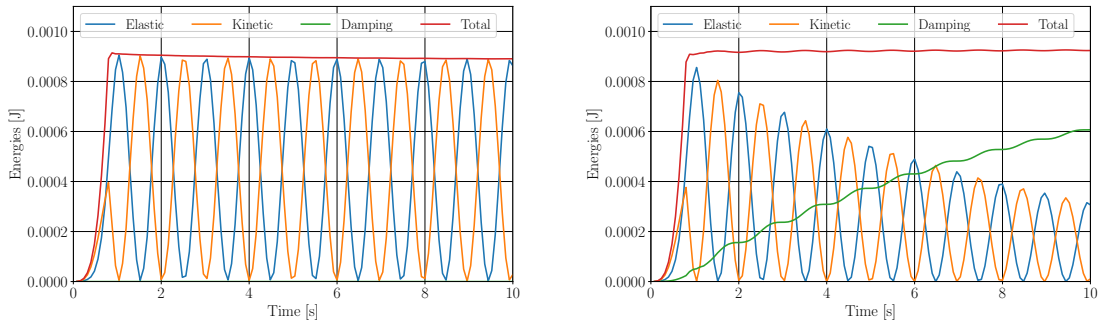

(a) **(b)**

Figure 4.13: Variation of the elastic, kinetic, damping and total energy in function of time. (*a*) undamped, (*b*) damped. (**Generalized alpha**)

conservative as highlighted by the constant total energy that remains constant in time and corresponds to the value reached when the loading is removed (se Fig. (4.14). In both cases the scheme is unconditionally stable and these differences disappear when decreasing the simulation time step.

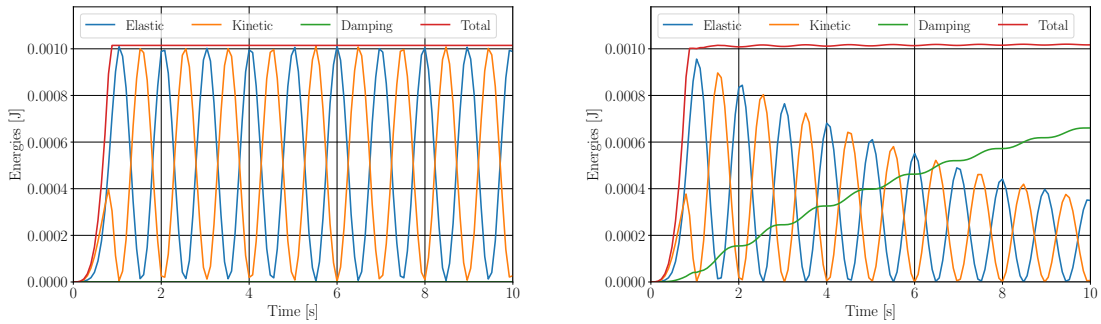

(a) **(b)**

Figure 4.14: Variation of the elastic, kinetic, damping and total energy in function of time. (*a*) undamped, (*b*) damped. (**Newmark Beta scheme**)

It is worth noting that these simulations have been carried out using a direct decomposition method. In order to justify the choice of this method, a comparative study is conducted between a direct LU decomposition and an iterative Krylov method. The ultimate aim is to select an appropriate solver that would optimize the performance of the code. Performance is measured by calculating the number of iterations required for each solving method. Figure. 4.15 shows the computational speed of both direct (LU decomposition) and iterative (GMRES and CG) methods measured in terms of number of iterations per second as a function of the mesh used for $P1$ and $P2$ elements. As the number of unknowns in the problem increases, the computational speed naturally decreases for all methods used. Furthermore, for the same mesh, there is a tenfold decrease

in performance from $P1$ to $P2$ elements, regardless of the method employed. However, the performance of each solver differs from one another for the same number of elements. Indeed, in the current test case, the LU decomposition has the fastest solving time for both linear and quadratic elements. The performance gap between direct and indirect solvers decreases as the mesh became finer since this method is suitable for small-scale problems. It can be observed that the breaking point is reached for mesh 3 when LU attains a similar solving time as the other indirect solvers. Regarding the iterative methods used, both conjugate gradient (CG) and generalized minimal residual (GMRES) methods exhibit similar performances, with CG outperforming GMRES slightly. This gain in performance is attributed to the nature of the problem itself, where all matrices solved are symmetric and positive definite. In fact CG is designed specifically for such problems, whereas GMRES is a more general algorithm that can also solve non-symmetric or positive definite matrices. The choice of solver is hence highly dependent on the nature of the problem and the size of the domain. Therefore, one must try different solvers and/or preconditioners to achieve the desired performance.

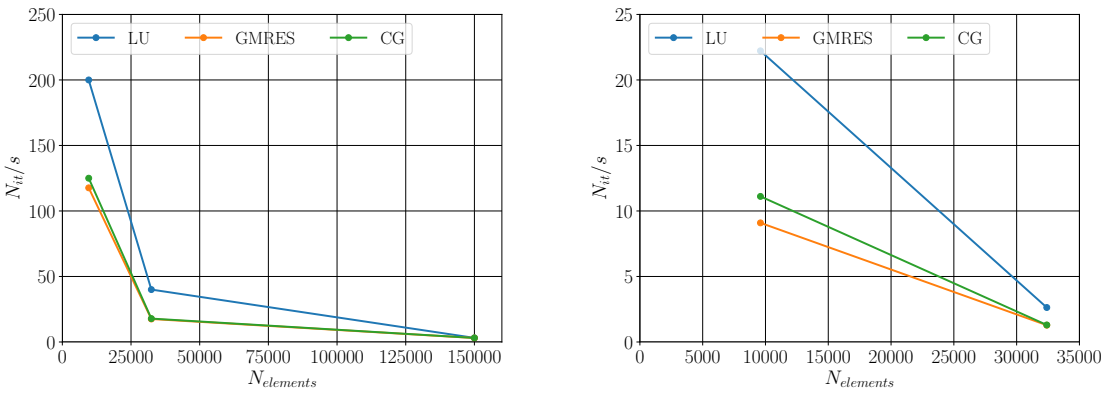

Figure 4.15: Performance of direct and indirect solvers obtained with the different meshes used: (a) $P1$ **elements** (b) $P2$ **elements**.

4.3 Conclusion

This chapter focuses on the numerical development of a structural mechanics solver, which is a crucial step towards developing a fully coupled fluid-structure interaction solver. This tool is capable of solving both the steady and transient elasticity equations. Additionally, it can handle the elastodynamic equation for a rotating structure, similar to the equation used in Chap. 2, where it is solved in the frequency domain. In this case, Coriolis and centrifugal effects are considered in the calculations due to the rotation, and the equation is solved using the polar coordinate reference frame. Such a feature allows the calculation of the dynamic response of rotating components such as turbine blades or discs, which is important in the context of turbomachinery applications. However, due to the lack of validation cases for rotating structure, the solver has been verified using available test cases found in the literature.

Chapter 5

Development of a numerical fluid-structure interaction coupling chain

Contents

A self-excited vibration is a flow induced-vibration that involves a complex, two-way interaction between a fluid and a solid. This multiphysical phenomenon is challenging to model due to the interplay of multiple physical effects. While simple aeroelastic problems can be solved analytically, large-scale fluid-structure interaction problems pose significant challenges in terms of mathematical modeling, numerical discretization, and solution techniques, even with today's advanced computer architectures. Commercial computational fluid dynamics (CFD) and computational structural mechanics packages have made progress and simulating industry relevant fluid-structure interaction (FSI) problems is possible today but it primarily relies on steady or quasi-steady CFD approaches such as RANS or URANS. The aim of this chapter is to develop a numerical fluid-structure interaction framework using Large Eddy Simulation (LES) along with the structural dynamics code to tackle complex multiphysical problems as encountered in turbomachinery devices. To do so, the framework must be computationally efficient, able to run on parallel computer systems and capable of high-resolution simulations. To achieve this, the structural mechanics code presented in the previous chapter is coupled to the LES solver using a Multiple Program Multiple Data (MPMD) approach through the library CWIPI resulting in a partitioned solver that combines the strengths of both codes. Two test cases are then considered to demonstrate the capabilities of the framework: an immersed beam in a still fluid, and a Vortex Induced Vibration (VIV) case. The first case shows that a vibrating beam in a still fluid eventually returns to its equilibrium position due to the damping effect of fluid viscosity. The second case successfully captures the eigenmode and amplitude of vibration of a thin elastic plate, demonstrating that fluid-structure modes can be captured using LES.

5.1 Introduction

From the flap of a bird's wings to a flying aircraft, a fundamental physical phenomenon takes place which is of considerable and technological interest in a broad spectrum of disciplines such as aerodynamics, civil engineering, biomedical engineering, etc. This phenomenon is known as Fluid Structure Interaction or FSI. Simply put, FSI studies the interaction between a deformable structure with a surrounding or internal flow. This multiphysical phenomenon involves more than one physical effect hence rendering its complexity rather challenging to model. Indeed, the motion and the deformation of solid structures are the results of the surrounding fluid stress, while the fluid flow in return is influenced by the solid movement. The fluid-structure interface is as a result and very often complex and time-dependent. Given that the interaction is instantaneous and continuous, representing such a complex interface accurately and efficiently is also difficult. As a result, the numerical modeling of FSI problems is everything but an easy task and the reliability of such simulations, the underlying errors and models are still at the center of many research activities. It is clear that the design of robust and efficient solvers to solve the resulting non-linear systems still have to be dealt with and

remains a priority for many engineering problems. The problem at hand is furthermore exacerbated by the fact that unsteady CFD is to be used. In this context and although LES is not well established in the FSI context, especially for complex rotating flows, it still remains the most reliable CFD modeling context since intrinsically unsteady. While recent advancements around the use of LES for FSI problems has gained some success, steady CFD became a major tool in the middle of the 90's (Wolf & Brakkee (1996), Bathe *et al.* (1995), Lesoinne & Farhat (1996), Maman & Farhat (1995)). The reason for this misuse is owed to the computational complexity and cost when moving from steady CFD like RANS to an unsteady approach like LES.

Note also that the methods and underlying models used to treat fluid-structure interaction problems vary in their complexity. The simplest model is probably the well known "piston theory" (Holt & Garabed (1956)) which is used to analyze the behavior of a rigid body moving through a fluid. In this approach one assumes that the fluid moves around the body without affecting its shape or motion while the body generates pressure waves in the fluid. Although useful for some engineering applications, this piston theory is limited: the fluid must be inviscid, incompressible and does not affect the shape or motion of the body. The body is rigid and moves at a constant speed without causing any turbulence or disturbance in the fluid and the pressure waves generated by the body move at the speed of sound in the fluid. These assumptions simplify the problem and make it easier to analyze the interaction between the fluid and the body, but they also limit the applicability of the model to certain scenarios. A non-linear version of the piston theory exists. It is still however bounded by the frequency or Mach number range of the application. The full-potential flow theory is a natural extension to consider but it requires the solution of a non-linear wave equation for the velocity potential. However, if one assumes that the solid body is small and the profile is thin, the linear convected-wave equation can be obtained for the velocity potential. The solution of this equation is the basis of many FSI problems and has been extensively used for the flutter or other phenomena of aircraft (Dowell (2014)). Sophisticated models based on the Euler or Navier-Stokes equations provide higher fidelity simulations but require substantial computer resources. Note also that the solid models should handle all sort of deformations. For the solid part, the models are usually classified depending on the deformation of the structure *i.e.*, a linear stress-strain relationship can account for rigid body deformation whereas non-linear models are needed to account for large body deformations.

Figure 5.1 shows the different developments applied to fluid-structure interaction problems and classified according to the complexity of the solid and fluid models. Typically, the spring-mounted wing flutter analysis (a) is a dynamic analysis that is used to study the flutter phenomenon of aircraft wings. In this case, the wing is modeled as a flexible structure and its motion is coupled to the airflow around it. To do so, the wing is mounted on a support structure with a spring and a damper allowing for the wing's motion to be simulated. This method can also take into account more sophisticated solid models like a beam model (d) or a membrane model (e). In the vortex method (b), the deformable structure is represented by a mesh of discrete points or elements, and the fluid is modeled using a set of discrete vortices. The motion of the fluid or of the structure are calculated separately and their interaction is accounted for through a coupling

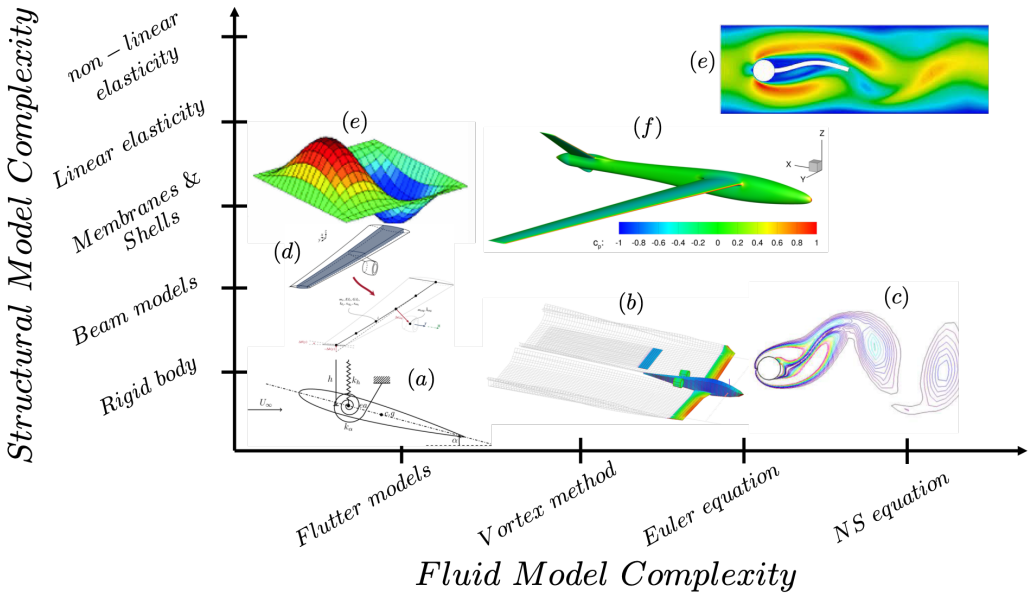

Figure 5.1: Fluid-structure interaction models classified according to the structure and fluid model complexity. The example shown include (a) academic spring-mounted wing flutter problem (Heinrich (1956)), (b) simulation of an airplane using the vortex lattice method (VLM), (c) vortex-induced vibrations of a spring-mounted cylinder in a Navier-Stokes flow (Nguyen *et al.* (2014)),(d) low-order physics-based flutter model using beam theory (Opgenoord *et al.* (2019)), (e) aeroelastic investigation on the flutter properties of supersonic panel using supersonic piston theory for the fluid and thin plate theory for the solid (Song & Li (2014)), (f) CFD-Based Aeroelastic simulation of an aircraft in Euler flow (Rozov *et al.* (2019)), (g) Vortex induced vibration of an elastic plate attached to a fixed cylinder (Turek & Hron (2007)).

term that transfers forces between the two. The method is particularly well-suited for problems involving large deformations and complex geometries as it allows the fluid and the structure to move independently of each other. This makes it possible to simulate the behavior of flexible structures such as membranes, cables, and flags in a flow, which can be difficult or impossible to model using other techniques. Sophisticated CFD-based aeroelastic simulations are used on an aircraft using Euler flow (f) in addition to two vortex induced vibration cases involving a spring-mounted rigid cylinder (c), and an elastic plate attached to a rigid cylinder (e) simulated by coupling the Navier-Stokes equations to a non-linear elasticity model.

A third axis can be added to describe the type of coupling between these models. The choice of coupling depends on the strength of interaction between the solid and the fluid. For example, the coupling between a fluid represented by the piston theory and an elastic solid would fail to reproduce the actual physics involved and the time-delay effect between the two. On the other hand, turbomachinery components such as blades and discs interact weakly with a turbulent flow around them. Generally speaking, the more refined the models are, the more feedback loops are required between the fluid and the

solid, and the interaction becomes more significant.

In this thesis, a general modeling approach is adopted with no restriction on the complexity of the fluid or solid models. The objective is to develop a fluid-structure interaction solver specifically tailored to turbomachinery applications. This means that complex unsteady fluid phenomena are modeled using Large Eddy Simulation (LES), while the structural components are modeled using a linear or non-linear finite element model. This chapter details the numerical coupling strategy developed to meet this purpose. It is organized as follows: first, the coupled FSI problem is thoroughly described with all necessary details on the theory and equations used. Second, a review of the state-of-the-art on coupling methods available in the literature is provided, along with the choice adopted for this work. Interface management and mesh adaptation are also discussed as part of the coupling. To finish, two coupled cases are presented to validate the coupling framework and tools.

5.2 Coupled FSI problem

Unlike the structure, the motion of the fluid is described using a Eulerian framework where the change of quantities of interest (temperature, pressure, velocity...) are observed at spatially fixed locations. The fluid problem is described using the Navier-Stokes and continuity equations derived in Chap. 2. These equations can be recast in the following compact form:

$$\begin{cases} \dfrac{\partial(\rho_f \mathbf{u}_f)}{\partial t} + (\mathbf{u}_f - \mathbf{w}) \cdot \nabla(\rho_f \mathbf{u}_f) - \nabla \cdot \boldsymbol{\sigma}(\mathbf{u}_f, p) = \mathbf{0}, \quad in \quad \Omega_f, \\ \nabla \cdot \mathbf{u}_f = 0, \quad in \quad \Omega_f, \end{cases} \tag{5.2.1}$$

where σ_f is the fluid stress tensor that contains the normal and shear stresses and $\mathbf{w}$ is the grid velocity. The uncoupled fluid-structure system of equations then writes,

$$\begin{cases} \dfrac{\partial(\rho_f \mathbf{u}_f)}{\partial t} + (\mathbf{u}_f - \mathbf{w}) \cdot \nabla(\rho_f \mathbf{u}_f) - \nabla \cdot \boldsymbol{\sigma}(\mathbf{u}_f, p) = \mathbf{0}, \quad in \quad \Omega_f, \\ \nabla \cdot \mathbf{u}_f = 0, \quad in \quad \Omega_f, \\ \rho_s \dfrac{\partial^2 \tilde{\xi}}{\partial t^2} = \tilde{\nabla} \cdot \tilde{\mathbf{P}} + \rho_s \tilde{\mathbf{f}}, \quad in \quad \tilde{\Omega}_s, \end{cases} \tag{5.2.2}$$

where each of the fluid and solid problems are solved separately in a Eulerian and Lagrangian reference systems respectively. In order to construct the link between these two reference systems and hence to couple the fluid and the solid problems, the Arbitrary Lagrangian Eulerian method introduced in Chap. 3 is used. The ALE viewpoint allows for the mesh to move with the material while retaining the ability to track the motion of the fluid. In addition, ALE ensures that the fluid and solid domains never overlap nor separate, and the flow velocity at the interface must be equal to the solid boundary velocity (*no-slip* condition). These two properties of ALE represent the kinematic requirement that imposes equal displacements and velocities at the wet interface. That is,

$$\mathbf{x}_f = \xi, \qquad \mathbf{w} = \frac{\partial \xi}{\partial t}, \qquad on \quad \Gamma\,. \tag{5.2.3}$$

ALE also enforces an equilibrium requirement at the interface where Γ is the common wet interface: *i.e.*, the location where the solid domain and fluid domain are in contact. This equilibrium states that the forces acting on the fluid and the structure must be balanced. More specifically, the forces acting on the fluid must be equal and opposite to the forces acting on the structure (see Fig. 5.2). This is because any unbalanced forces would cause the fluid and/or the structure surfaces to accelerate, which would violate the requirement of equilibrium and continuity. Mathematically, this requirement can be expressed using the equation,

$$\boldsymbol{\sigma} \cdot \vec{n}_f = \mathbf{P} \cdot \vec{n}_s, \quad on \quad \Gamma. \tag{5.2.4}$$

where $\vec{n}_f$ and $\vec{n}_s$ are the unit normal vectors acting on the fluid and solid surfaces

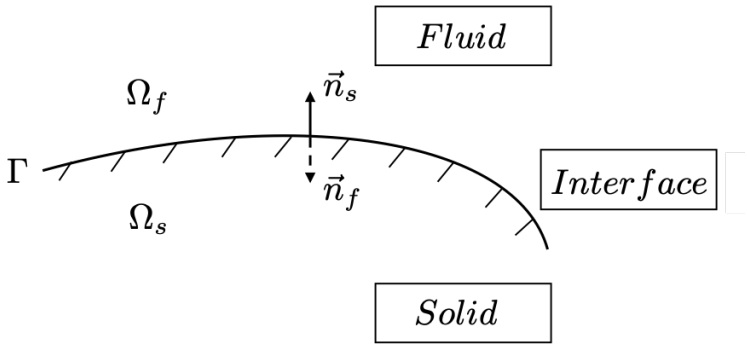

Figure 5.2: Schematic drawing of the fluid-structure interface highlighting the different domains and the outer normals of the fluid and structure.

respectively and pointing outward. Note that despite the choice detailed above, numerous alternatives have been proposed to handle fluid-structure equations on moving domains. The Immersed Boundary Method (IBM) proposed by Peskin (1977) for example, is a numerical technique where the fluid flow equations are solved on a fixed grid, and the motion of the immersed solid boundaries is represented through a forcing term in the fluid equations. The IBM approach involves two main steps: interpolating the fluid properties to the solid interface, and imposing the boundary conditions using the immersed boundary method. The interpolation step involves assigning the fluid properties at the grid points near the solid boundary based on the properties of the fluid in the surrounding grid points. This is typically done using a weighted interpolation scheme such as the distance-weighted interpolation approach. In the second step, the force exerted by the solid object on the fluid is represented as a source term in the Navier-Stokes equations. This forcing term is determined based on the displacement and deformation of the solid object. The resulting modified Navier-Stokes equations are then solved numerically on the fixed grid to obtain the fluid flow. A similar technique has been used to solve FSI problems and is called the Fictitious Domain Method (FDM) (Glowinski *et al.* (1994)). Here the fluid equations are solved on a fixed grid and the solid boundaries are represented as a continuous distribution of forces and velocities, rather than explicitly modeling the solid geometry. The FDM approach involves adding an additional term to the Navier-Stokes equations that represents the forces exerted by the solid boundaries on the fluid.

This term is derived based on the distribution of forces and velocities within the solid, which is typically determined using a constitutive relation. Both of these techniques are referred to as *non-conforming* because the mesh nodes on the fluid and solid sides of the interface do not coincide, meaning that there is no one-to-one correspondence between the mesh elements on either side. This type of mesh is less accurate than conforming mesh approaches because it introduces numerical errors at the interface that can affect the stability of the simulation.

The ALE method can be considered a mesh conforming technique even though it is somewhat hybrid in nature. The mesh is moved in such a way that it is always conforming to the deforming structure, and the governing equations are formulated in a reference frame that moves with the mesh. This allows the method to capture large deformations of the solid domain while maintaining the accuracy of a conforming mesh. One requirement that comes with the ALE method is that node motions should not distort the mesh too much for computational accuracy. As a consequence, a supplementary equation must be introduced to propagate efficiently the deformation of the solid boundary into the fluid domain. There exists many mathematical models that can be used to handle mesh deformation. These models vary in robustness and efficiency and the choice is usually based on the application itself and the level of compromise between the two. Typically, some methods are suitable for large mesh deformations and others are preferred when dealing with small deformations. The most common methods used in FSI problems are the mesh connectivity based methods. These can be classified in an increasing order of efficiency or decreasing order of robustness. For example,

- The linear spring analogy presented by Batina (1990). The idea is to assimilate the edges of the mesh to linear springs. The resulting system is a linear set of equations that models a network of springs subject to a deformation on its boundary. The latter is then solved using iterative methods such as Jacobi or Gauss Seidel.

- The pseudo solid approach is based on the idea of introducing an artificial solid-like behavior into the fluid mesh. This is achieved by applying the classical laws of structural mechanics which model the elastic response of the fluid mesh deformation (Stein *et al.* (2003); Stein *et al.* (2004)). The Pseudo-Solid term is based on the constitutive equations for linear elasticity, and it depends on the deformation gradient of the fluid mesh. Mathematically this translates to:

$$\begin{aligned} \nabla^2\mathbf{w} + \frac{1}{1-2\nu}\frac{\partial}{\partial x}\boldsymbol{\nabla}\cdot\mathbf{w} = 0\,, \\ \nabla^2\mathbf{w} + \frac{1}{1-2\nu}\frac{\partial}{\partial y}\boldsymbol{\nabla}\cdot\mathbf{w} = 0\,, \\ \nabla^2\mathbf{w} + \frac{1}{1-2\nu}\frac{\partial}{\partial z}\boldsymbol{\nabla}\cdot\mathbf{w} = 0. \end{aligned} \tag{5.2.5}$$

  with $\mathbf{w}$ being the vector field of displacement of the nodes of the mesh and ν_s is the Poisson's ratio of the solid considered. The main advantage of this method compared to the linear spring analogy method is its inherent ability to avoid drastic

cell compression. Its major flaw is the associated computational cost. In fact, it is almost never used in a crude manner to meshes composed of several million elements. To circumvent this problem, (Lefrançois (2008)) proposes the Moving Submesh Approach (MSA). It is based on the division of the computational domain into zones (or super-elements) in which deformations are computed before being interpolated on the original mesh. Another solution has been recently proposed by Fabbri (2022) to improve this method by adjusting the Young's Modulus of cells according to their quality. This way the method handles large cell deformations while trying to maintain a minimal skewness.

- Another possible approach consists in simplifying the pseudo-solid relation, Eq. (5.2.5), to reduce the computational cost by removing the coupling term and therefore only solving the Laplacian term:

$$\nabla^2 \mathbf{w} = 0. \tag{5.2.6}$$

  This is known as the Laplacian smoothing method and belongs to the family of elliptic smoothing methods. The basic idea is to adjust the position of each vertex based on the positions of its neighbors, so that the resulting mesh is smoother and more regular. The Laplacian operator is a differential operator that measures the amount of curvature at a point on a surface. In the context of mesh processing, the Laplacian operator is applied to each vertex of the mesh to calculate a new position that minimizes the amount of curvature

- Biharmonic operators (Helenbrook (2003)) are more sophisticated versions of the Laplacian smoothing method. The basic idea is to minimize the curvature of the mesh by smoothing any abrupt change in direction. To do so, the biharmonic operator, which is a linear differential operator defined as,

$$\nabla^4 \mathbf{w} = 0\,, \tag{5.2.7}$$

  is usually used.

  One advantage of the biharmonic operator over other mesh smoothing techniques is that it tends to preserve sharp features of meshes, such as edges and corners, while still producing smoother overall surfaces. However, it can be computationally expensive and may require careful tuning of its parameters to avoid over-smoothing or under-smoothing meshes.

In the current study, the Laplacian smoothing method is adopted as a compromise between robustness and efficiency. It is furthermore noted that this elliptic method converges fast in cases of small deformations which makes it an interesting approach for turbomachinery applications. The method is applied to the nodal displacements of the mesh: *i.e.*, each vertex i is moved to the centroid of its surrounding vertices j so that,

$$x_i = x_i + \frac{1}{n}\sum_{j=1}^{n}(x_j - x_i). \tag{5.2.8}$$

The Laplacian smoothing problem is then formulated as a set of equations $\mathbf{Ax} = \mathbf{b}$ and solved using a standard conjugate gradient approach. Rather than explicitly calculating the matrix $\mathbf{A}$, only the matrix-vector product $\mathbf{Ax}$ is effectively computed. Note also that the conjugate gradient method is never fully converged but instead is looped until the residual has been reduced by a factor specified by the user. This approach ensures that the mesh node displacements caused by the moving boundaries are effectively propagated throughout the entire mesh. Doing so avoids the appearance of highly deformed cells next to the moving boundary which would require more frequent re-meshing.

Now that the fluid and solid sub-problems have been coupled using the ALE and mesh smoothing methods (here based on the Laplacian approach), the coupled fluid-structure system of equations can be formulated as,

$$\begin{cases} \dfrac{\partial(\rho_f \mathbf{u}_f)}{\partial t} + (\mathbf{u}_f - \mathbf{w}) \cdot \nabla(\rho_f \mathbf{u}_f) - \nabla \cdot \boldsymbol{\sigma}(\mathbf{u}_f, p) = \mathbf{0}, & in \quad \Omega_f, \\ \nabla \cdot \mathbf{u}_f = 0, & in \quad \Omega_f, \\ \rho_s \dfrac{\partial^2 \tilde{\xi}}{\partial t^2} = \tilde{\nabla} \cdot \tilde{\mathbf{P}} + \rho_s \tilde{\mathbf{f}}, & in \quad \tilde{\Omega}_s, \\ \mathbf{x}_f = \xi, & on \quad \Gamma, \\ \mathbf{w} = \dfrac{\partial \xi}{\partial t}, & on \quad \Gamma, \\ \boldsymbol{\sigma} n_f - \mathbf{P} n_s = 0, & on \quad \Gamma, \\ \nabla^2 \mathbf{w} = 0, & in \quad \Omega_f. \end{cases} \tag{5.2.9}$$

In order to solve this coupled system of equations, there exists two major approaches that are distinguished based on how many solvers are used to solve the system: the *monolithic approach* or the *partitioned approach*.

5.3 Monolithic coupling approach

The *monolithic approach* is a fully coupled FSI approach, where the fluid and structural equations are solved together in a single solver. This approach involves solving the Navier-Stokes equations for the fluid and the equations of motion for the structure simultaneously. In addition, the coupling between the fluid and structure is accounted for in the equations. The monolithic coupling discretization of a fluid-structure interaction problem yields a system of equations of the form,

$$\mathbf{A}(\mathbf{y}_{\mathcal{F}}, \mathbf{y}_{\mathcal{S}}, \mathbf{y}_{\mathcal{I}}) = 0\,, \tag{5.3.1}$$

where $\mathbf{A}$ is a matrix that contains discrete flow variables $\mathbf{y}_{\mathcal{F}}$, discrete structural variables $\mathbf{y}_{\mathcal{S}}$ and coupling variables $\mathbf{y}_{\mathcal{I}}$ related to both the fluid and the structure. Since this system of equations is usually non-linear, a common approach to seek a numerical solution is to apply Newton's based algorithm. This results in the repeated solution of the problem,

$$\boldsymbol{\mathcal{J}}^k \begin{bmatrix} \Delta \mathbf{y}_{\mathcal{F}} \\ \Delta \mathbf{y}_{\mathcal{S}} \\ \Delta \mathbf{y}_{\mathcal{I}} \end{bmatrix} = -\boldsymbol{\mathcal{R}}^k \tag{5.3.2}$$

where $\boldsymbol{\mathcal{J}}^k$ stands for the Jacobian, or an approximation of the Jacobian of the coupled non-linear operator applied to $(\mathbf{y}_\mathcal{F}, \mathbf{y}_\mathcal{S}, \mathbf{y}_\mathcal{I})$ and $\boldsymbol{\mathcal{R}}^k$, the vector of residuals such that,

$$\boldsymbol{\mathcal{J}}^k = \begin{pmatrix} \boldsymbol{\mathcal{J}}_\mathcal{F}(\mathbf{y}_\mathcal{F}) & 0 & \boldsymbol{\mathcal{J}}_\mathcal{F}(\mathbf{y}_\mathcal{F}) \\ 0 & \boldsymbol{\mathcal{J}}_\mathcal{S}(\mathbf{y}_\mathcal{S}) & \boldsymbol{\mathcal{J}}_\mathcal{S}(\mathbf{y}_\mathcal{S}) \\ \boldsymbol{\mathcal{J}}_\mathcal{I}(\mathbf{y}_\mathcal{I}) & \boldsymbol{\mathcal{J}}_\mathcal{I}(\mathbf{y}_\mathcal{I}) & 0 \end{pmatrix}, \qquad \boldsymbol{\mathcal{R}}^k = \begin{bmatrix} r_\mathcal{F} \\ r_\mathcal{S} \\ r_\mathcal{I} \end{bmatrix}. \tag{5.3.3}$$

After solving this linear system, the following update procedure applies,

$$\begin{bmatrix} \mathbf{y}_\mathcal{F}^{k+1} \\ \mathbf{y}_\mathcal{S}^{k+1} \\ \mathbf{y}_\mathcal{I}^{k+1} \end{bmatrix} = \begin{bmatrix} \mathbf{y}_\mathcal{F}^{k} \\ \mathbf{y}_\mathcal{S}^{k} \\ \mathbf{y}_\mathcal{I}^{k} \end{bmatrix} + \begin{bmatrix} \Delta\mathbf{y}_\mathcal{F}^{k} \\ \Delta\mathbf{y}_\mathcal{S}^{k} \\ \Delta\mathbf{y}_\mathcal{I}^{k} \end{bmatrix}. \tag{5.3.4}$$

The main difficulty in solving such systems lies in the evaluation of the Jacobian matrix and more specifically the evaluation of the cross derivative terms that arise form its application. Therefore, variations of the Newton method that deal with Jacobian approximations have been used to deal with such problems. For example, Turek *et al.* (2010) solved this problem using a damped Newton method. This approach greatly improves the robustness of the solver when the current approximation $\mathbf{y}^k$ is not close enough to the final solution. In this case, the Jacobian matrix is approximated using a finite difference of the residual vector $\boldsymbol{\mathcal{R}}^k$. Inexact methods have also been used by Heil (2004) where sub-blocks of $\boldsymbol{\mathcal{J}}^k$ are neglected using block-triangular approximations. Doing so, the resulting block-triangular matrix is shown to be an efficient preconditionner for the solution of the linearized system. Other Newton-based iteration methods have been investigated by Tezduyar *et al.* (2006). These include direct, quasi-direct and block-iterative techniques. The direct method uses the exact Jacobian to solve the coupled system. Contrarily, in the block-iterative method, the coupling terms are completely neglected which leads to a partitioned-like solution algorithm. This method is particularly suitable for FSI computations where the structure is light, meaning that the structural response is very sensitive to small changes in the fluid rendering convergence rather difficult to achieve. In the quasi-direct approach, the coupling terms are partially evaluated by keeping them in the system without considering the effect of the coupled structural terms on the mesh motion. This method is also suitable for problems where the solid to fluid feedback is important. Overall, the coupled monolithic approach results in a very accurate and efficient solution to FSI problems as it solves the flow equations and structure equations simultaneously and the interface conditions are implicit in the model. It is thus able to handle a higher amount of coupling instabilities (Degroote *et al.* (2009); Heil *et al.* (2008)). Nonetheless, such an approach can be computationally expensive, especially for large-scale FSI problems. It furthermore requires a robust numerical scheme to ensure stability and accuracy. This is thus typically used only for cases where the fluid and structure are tightly coupled.

5.4 Partitioned coupling approach

The *partitioned approach* treats the fluid and solid domains as two distinct computational fields, with their respective meshes as well as solvers that solve each problem separately.

This approach offers more versatility in the construction of the FSI solver since two different codes are used for the fluid and solid. These codes exchange all the necessary data, such as fluid forces and structural displacements at the interface which implies that the flow is unchanged while the solution of the structural equations is calculated and vice versa (Degroote *et al.* (2009)). The fluid is generally solved with the ALE description as explained in the previous section allowing to compute the flow variables on a moving grid. For the solid, the finite element method is most widely used with some variations regarding the type of application; *i.e.*, beam models, membranes and shells, non-linear elasticity, etc. The specificity is here due to the fact that boundary values are exchanged between the fluid and structure interfaces. The partitioned approach therein requires the use of a third module in addition to the fluid and structure solvers to ensure the communication of the information between interfaces. This specific coupling module will be described later in a dedicated section.

The goal of the partitioned approach is to be as accurate as its monolithic counterpart while providing flexibility in the choice of the solvers and robustness to deal with a wide range of FSI problems. To achieve those objectives, multiple coupling schemes exist. They are divided into two categories: *implicit (strong)* and *explicit (weak) coupling schemes*. The idea behind the first set of these coupling schemes is that fluid and solid equations are solved multiple times for every time step until a convergence criteria is attained so the obtained solution at this time step is strongly coupled. Conversely, when the fluid and solid equations are solved only once for every time step that is without convergence check, the coupling scheme is said weakly coupled. The last approach is numerically much faster than the former but less stable in some cases. Indeed, an important issue arising in the partitioned approach concerns the stability of the scheme due to the significant lag in the transmission of the information at the wet interface. This lag is owed to the fact that the fluid and structure solutions are solved successively and not simultaneously which violates the conservation of kinetic and kinematic conditions at the interface. In the monolithic approach, the coupling terms being implicitly solved by the fluid and solid equations, such a difficulty is inherently treated. This may not be the case in the partitioned approach; it depends on the type of coupling used. In weakly coupled problems, this numerical issue may cause the velocity at the interface to diverge. Under the same condition, strongly coupled problems exhibit convergence problems along with an increase in sub-iterations. However, there exist some criteria that have to be met in order for this instability to occur notably when the density of the structure approaches the density of the fluid and when the structure is particularly slender (Causin *et al.* (2005)). For this reason, the density ratio $\boldsymbol{\mathcal{M}} = \rho_s/\rho_f$ that dictates the strength of inertia between the structure and the fluid is often used as indicator to determine the type of interaction between the fluid and structure. When $\boldsymbol{\mathcal{M}} >> 1$ the interaction is weak, whereas if $\boldsymbol{\mathcal{M}} \approx 1$ the interaction is strong. Subsequently, this non-dimensional parameter gives insight on which coupling should be used for a given application. A low density ratio requires the use of a strongly coupled or implicit approach whereas a high density ratio problem can be solved using a weakly coupled or explicit approach.

In the present study, the development of a coupled numerical chain based on a com-

pressible LES solver (AVBP) and a structural mechanics code aims at investigating multiphysical phenomena in turbomachinary components. In this context, the mass ratio is relatively high and the structure is usually bulky. Therefore, a weakly coupled approach is preferred as it can capture aeroelastic effects in addition to alleviating the computational cost of such simulations compared to a strongly coupled approach. A brief overview of the implicit and explicit coupling schemes are discussed hereafter followed by a thorough description of the coupling scheme developed during this Ph.D.

5.4.1 Implicit coupling schemes

As said previously, partitioned models can solve the FSI problem using an iterative approach at every time step in order to satisfy a certain convergence criterion and result in an implicit coupling scheme. This is done to enforce exactly the kinematic and dynamic conditions, Eq. (5.2.3-5.2.4), at the wet interface and consequently to prevent any numerical stability. In such a case if $\boldsymbol{\mathcal{F}}$ and $\boldsymbol{\mathcal{S}}$ denote the partitioned operators for the fluid and solid solvers respectively, the computed solution at the wet interface by each solver at every time step is obtained such that,

$$\begin{aligned} \mathbf{f}_{n+1} &= \boldsymbol{\mathcal{F}}(\mathbf{d}_n), \\ \mathbf{d}_{n+1} &= \boldsymbol{\mathcal{S}}(\mathbf{f}_{n+1}), \end{aligned} \tag{5.4.1}$$

where $\mathbf{f}_{n+1}$ represents the kinematic variables (stresses or forces) computed by the fluid solver using the displacement $\mathbf{d}_n$ (*i.e.*, from the previous iteration) and $\mathbf{d}_{n+1}$ is the new displacement computed by the structure solver using the kinematic variables $\mathbf{f}_{n+1}$. Figure 5.3 shows a typical diagram of such an implicit coupling algorithm. Note that the algorithm operates by first solving the fluid equations and then transfers the kinematic variables at the interface to the structure solver. The dynamic variables are then computed and passed to the acceleration block. This step is essential to ensure that the solution at the interface converges before closing the feedback loop. It functions as a sub-iterative block, whereby the fluid and solid equations are solved multiple times to satisfy a specific criterion. This sub-iterative block is a crucial component of strongly coupled schemes. Various methods exist to stabilize such schemes which can still be numerically unstable: *i.e.*, introducing under-relaxation methods and Newton methods for example.

One way of stabilizing a coupled fluid-structure iteration is to perform an under-relaxation on the computed displacement $\mathbf{d}_{n+1}$ so that,

$$\tilde{\mathbf{d}}_{n+1}^{k+1} = \omega \mathbf{d}_{n+1}^{k+1} + (1-\omega)\mathbf{d}_{n+1}^{k}. \tag{5.4.2}$$

$\tilde{\mathbf{d}}_{n+1}^{k+1}$ in Eq. (5.4.2) is the relaxed displacement at the next time step and k represents the sub-iteration index of the acceleration block and the under-relaxation factor is noted ω. This last value can either be a constant (in the range $0 < \omega < 1$) or can be computed at every sub-iteration. A value close to 1 is preferred but can cause the computation to diverge whereas a value close to 0 makes the computation more stable at the expense of a larger number of sub-iterations. Alternatively, a dynamic relaxation can be used to

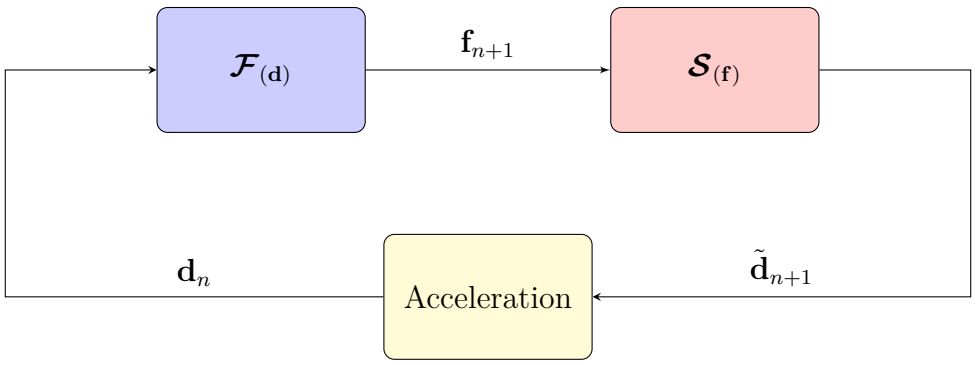

Figure 5.3: Implicit coupling scheme

accelerate the convergence of the sub-iterations which is known as the Aitken Relaxation method. In this approach, the relaxation factor ω is computed at every sub-iteration using the two previously computed displacements via linear extrapolation (Aitken (1927)). Under-relaxation methods are direct and intuitive approaches that stabilize most coupled fluid-structure problems. There exists, however, a set of implicit schemes that outperform the under-relaxation method when this latter diverges. These schemes fall under the Newton-Raphson type schemes or more specifically the quasi-Newton type methods. For the Newton scheme consists in applying a fixed point iteration to the partitioned fluid-structure problem. This is done by first defining the fluid residual operator $\boldsymbol{\mathcal{R}}_{\mathcal{F}}(\mathbf{f},\mathbf{d})$ and the solid residual $\boldsymbol{\mathcal{R}}_{\mathcal{S}}(\mathbf{f},\mathbf{d})$ such that,

$$\begin{aligned}\boldsymbol{\mathcal{R}}_{\mathcal{F}}(\mathbf{f},\mathbf{d}) &= \mathbf{f} - \boldsymbol{\mathcal{F}}_{(\mathbf{d})} = 0\\ \boldsymbol{\mathcal{R}}_{\mathcal{S}}(\mathbf{f},\mathbf{d}) &= \mathbf{d} - \boldsymbol{\mathcal{S}}_{(\mathbf{f})} = 0\end{aligned} \tag{5.4.3}$$

Using these equations, the block Newton iteration problem can be expressed as,

$$\begin{pmatrix}\boldsymbol{\mathcal{J}}_{\boldsymbol{R}_{\mathcal{F}}}(\mathbf{f}^k) & \boldsymbol{\mathcal{J}}_{\boldsymbol{R}_{\mathcal{F}}}(\mathbf{d}^k)\\ \boldsymbol{\mathcal{J}}_{\boldsymbol{R}_{\mathcal{S}}}(\mathbf{f}^k) & \boldsymbol{\mathcal{J}}_{\boldsymbol{R}_{\mathcal{S}}}(\mathbf{d}^k)\end{pmatrix}\begin{bmatrix}\Delta\mathbf{f}^k\\ \Delta\mathbf{d}^k\end{bmatrix} = -\begin{bmatrix}\boldsymbol{\mathcal{R}}_{\mathcal{F}}(\mathbf{f}^k,\mathbf{d}^k)\\ \boldsymbol{\mathcal{R}}_{\mathcal{S}}(\mathbf{f}^k,\mathbf{d}^k)\end{bmatrix} \tag{5.4.4}$$

along with the update variables,

$$\begin{bmatrix}\mathbf{f}^{k+1}\\ \mathbf{s}^{k+1}\end{bmatrix} = \begin{bmatrix}\boldsymbol{f}_k\\ \boldsymbol{d}_k\end{bmatrix} + \begin{bmatrix}\Delta\boldsymbol{f}_k\\ \Delta\boldsymbol{d}_k\end{bmatrix} \tag{5.4.5}$$

In such an approach the residual vectors are first obtained using Eqs. (5.4.3) after communicating the fluid and solid variables. If the Jacobian of the matrix is known, a Newton iteration can be performed using Eqs. (5.4.4) and the variables can be updated using Eqs. (5.4.5). The major issue is that the Jacobian matrix is either not known for a given problem or numerically expensive to calculate. Subsequently, matrix-free methods have been developed to account for this difficulty and the approaches become *quasi-Newton methods*. For instance, the *Interface Block Quasi-Newton Method* (IBQN-LS) features reduced order models for the fluid and structure solvers to get rid of the Jacobian matrix and hence increase the speed of convergence of the coupled iterations (Vierendeels *et al.* (2007)). In such a case, the block Newton system is formulated such that,

$$\begin{pmatrix} \hat{\boldsymbol{\mathcal{F}}}' & -\mathbf{I} \\ -\mathbf{I} & \hat{\boldsymbol{\mathcal{S}}}' \end{pmatrix} \begin{bmatrix} \Delta\tilde{\mathbf{f}} \\ \Delta\tilde{\mathbf{d}} \end{bmatrix} = \begin{bmatrix} \boldsymbol{\mathcal{R}}_{\mathcal{F}}(\mathbf{f},\mathbf{d}) \\ \boldsymbol{\mathcal{R}}_{\mathcal{S}}(\mathbf{f},\mathbf{d}) \end{bmatrix}, \tag{5.4.6}$$

where $\hat{\boldsymbol{\mathcal{F}}}'$ and $\hat{\boldsymbol{\mathcal{S}}}'$ are linear reduced order models for the fluid and solid Jacobians. The key feature of this scheme is that the fluid and solid variables are not directly computed. Instead, intermediate variables $\tilde{\mathbf{f}}$ and $\tilde{\mathbf{d}}$ are computed at every sub-iteration. That said, $\Delta\tilde{\mathbf{f}}$ and $\Delta\tilde{\mathbf{d}}$ are output coupling values that are used to form a matrix containing the corresponding change in stress or force distribution at the interface, and the corresponding change in displacement respectively. To construct the fluid solver interface Jacobian, the input coupling variables $\Delta\mathbf{d}$ and the output coupling variables $\Delta\tilde{\mathbf{f}}$ are used to form two distinct vector matrices $\mathbf{V}_{\mathcal{F}}$ and $\mathbf{W}_{\mathcal{F}}$. The new input change in displacement $\Delta\mathbf{d}$ is then approximated by a linear combination of the previously computed input displacements as,

$$\Delta\mathbf{d} \approx \beta_{\boldsymbol{\mathcal{F}}}\mathbf{V}_{\mathcal{F}}\,, \tag{5.4.7}$$

with $\beta_{\boldsymbol{\mathcal{F}}}$ being the vector of coefficients. The corresponding change in stress distribution $\Delta\mathbf{f}$ can thus be approximated by,

$$\Delta\mathbf{f} \approx \beta_{\boldsymbol{\mathcal{F}}}\mathbf{W}_{\mathcal{F}}. \tag{5.4.8}$$

To solve for $\beta_{\boldsymbol{\mathcal{F}}}$, a least square problem is usually obtained by minimizing $\|\Delta\mathbf{d} - \beta_{\boldsymbol{\mathcal{F}}}\mathbf{V}_{\mathcal{F}}\|$. Its solution yields $\beta_{\boldsymbol{\mathcal{F}}} = (\mathbf{V}_{\mathcal{F}}{}^{T}\mathbf{V}_{\mathcal{F}})^{-1}\mathbf{V}_{\mathcal{F}}{}^{T}\Delta\mathbf{d}$, so that $\Delta\mathbf{f} = \hat{\boldsymbol{\mathcal{F}}}'\Delta\mathbf{d}$ with $\boldsymbol{\mathcal{F}} = \mathbf{W}_{\mathcal{F}}(\mathbf{V}_{\mathcal{F}}{}^{T}\mathbf{V}_{\mathcal{F}})^{-1}\mathbf{V}_{\mathcal{F}}{}^{T}$.

Similarly, the solid solver interface Jacobian is constructed using the same procedure except that the inputs are the change in stresses $\Delta\mathbf{f}$ and the outputs are the intermediate change in displacement $\Delta\tilde{\mathbf{d}}$. These values are then stored in two distinct vector matrices $\mathbf{V}_{\mathcal{S}}$ and $\mathbf{W}_{\mathcal{S}}$. Once the least square problem is solved to obtain the optimal coefficients $\beta_{\boldsymbol{\mathcal{S}}}$, the resulting reduced order model for the solid problem becomes,

$$\hat{\boldsymbol{\mathcal{S}}}' = \mathbf{V}_{\mathcal{S}}(\mathbf{W}_{\mathcal{F}}{}^{T}\mathbf{W}_{\mathcal{S}})^{-1}\mathbf{W}_{\mathcal{S}}{}^{T} \tag{5.4.9}$$

There exists similar algorithm like the one described above. For example, the Interface Quasi-Newton Method (IQN-ILS) which relies on one reduced order model for the inverse of the overall interface Jacobian matrix of the Newton system of Eq. (5.4.4). This is done to avoid solving the Jacobian at every Newton-raphson iteration (Degroote *et al.* (2009)). Other algorithms like the block-Newton (Matthies & Steindorf (2002)) or inexact Newton (Gerbeau & Vidrascu (2003)) have also been used in partitioned approaches. However, their description goes beyond the scope of this work and a complete description can be found in the thesis of Gatzhammer (2015).

5.4.2 Explicit coupling schemes

Explicit schemes do not try to enforce a balance of kinetic and kinematic values at the interface like implicit methods. Instead, an approximation of the monolithic and implicit coupled problem, Eq. (5.3.2), is done by solving the partitioned problem using

Eq. (5.4.1) for a fixed number of iterations per time step (usually once) hence simplifying the coupling algorithm to two blocks as depicted on Fig. 5.4. This coupling strategy however yields good results in aeroelastic simulations only if the interaction between the fluid and the solid is weak: in other words the mass ratio of the problem is very high (Farhat *et al.* (2006)). Different algorithms have been developed to solve explicit coupling schemes such as the conventional serial staggered (CSS) (Piperno *et al.* (1995)), improved serial staggered (ISS) (Lesoinne & Farhat (1998)), conventional parallel staggered (CPS) (Farhat (2000)), improved parallel staggered (IPS) (Farhat (2000)). These algorithms have been tested in the framework of compressible flow simulations making them good candidates for the current application.

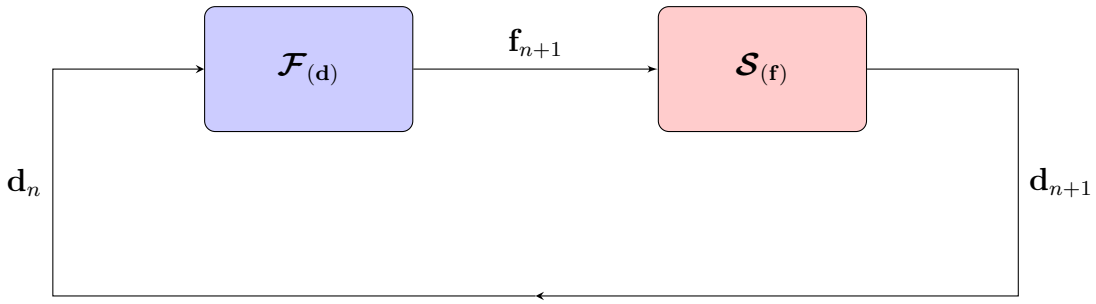

Figure 5.4: Implicit coupling scheme

The conventional serial staggered algorithm (CSS) (Piperno *et al.* (1995)) has been developed and implemented in the present work where the fluid and solid variables are computed once for every iteration. The time iteration n hence begins with the computation of the fluid time step, Δt_f, determined by the acoustic Courant Friedrichs Lewy number (CFL). Thanks to the unconditional stability feature of the Generalized alpha scheme, the fluid time step, Δt_f, can be passed to the structure solver since the coupling time step simply becomes $\Delta t_c = \Delta t_f = \Delta t_s$. AVBP then computes the normal and shear stresses on the coupled surfaces and transfers them to the structure solver. The calculated displacement by the structure solver is then sent back to AVBP to first move the mesh interface so it coincides with the new position of the solid interface and then calculate the new stresses at the next time step. Figure 5.5 shows a typical diagram of the CSS procedure highlighting two fluid-structure interaction iterations.

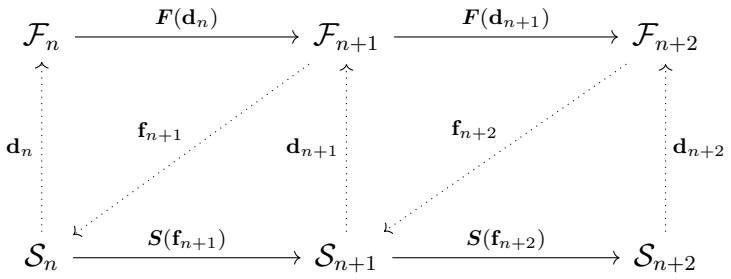

Figure 5.5: Diagram representing the Conventional serial staggered (CSS) algorithm.

It is worth noting that subcycling has also been implemented in this context. The time step in compressible flow simulations being small compared to the incompressible flow application, the use of such a small time step for both the fluid and structure components can be computationally expensive, especially for simulations involving complex geometries and high Reynolds numbers. Subcycling is in such a case useful to overcome the limitation by allowing the fluid and structure subsystems to advance using different time steps Δt_f and Δt_s (Piperno *et al.* (1995)). In this context, the fluid time step Δt_f is smaller than the structure time step Δt_s, so the solid solver time step can be divided into multiple of such sub-steps k so the run-time of the fluid solver before an exchange with the solid solver is equal to $k\Delta t_f$. During each sub-step, no exchange of data between the two solvers takes place. Once the fluid solver has achieved a full run-time cycle, the fluid and structure solvers are re-synchronized so that $\Delta t_s = k\Delta t_f$. Nevertheless, this technique does not enforce a conservation of energy at the interface at every time step, instead the energy transferred becomes directly proportional to the time step itself rising stability issues and errors. For this reason, and to compensate the time lag between the fluid and structure solvers, the generalized conventional staggered (GCSS) (Farhat & Lesoinne (1996)) procedure has been implemented in the FSI solver. This procedure works exactly as the CSS algorithm except that it incorporates a predictor operation for the structural displacement. The estimated displacement at $n+1$ is evaluated using the prediction,

$$\mathbf{d}_{n+1}^{p} = \mathbf{d}_n + \alpha_0 \Delta t_c \mathbf{v}_n + \alpha_1 \Delta t_c (\mathbf{v}_n - \mathbf{v}_{n-1}), \tag{5.4.10}$$

where α_0 and α_1 are real coefficients and $\mathbf{v}$ is the solid velocity. The combination of $\alpha_0 = 1$ and $\alpha_1 = 0$ yields a first order linear extrapolation whereas for $\alpha_0 = 1$ and $\alpha_1 = 0.5$, a quadratic extrapolation is obtained. The full GCSS procedure is hence decomposed as follows:

1. Compute the normal and shear stresses on the coupled surfaces and send them to the structure solver.

2. If $\Delta t_f \neq \Delta t_s$ subcycle the fluid solver until $\Delta t_f = \Delta t_s$ then calculate the corresponding structural displacement and velocity.

3. Predict the structural displacement at time t^{n+1} using Eq. (5.4.10).

4. Update the position of the fluid mesh according to the predicted displacement d_p^{n+1} then compute the normal and shear stresses to advance to the next time step.

Piperno & Farhat (2001) conducted an energy analysis of the various instances of partitioned procedures that can be obtained for the different values of α_0 and α_1 in Eq. (5.4.10). They concluded that if $d_{n+1}^{p} = d^n$ and $\alpha_0 = \alpha_1 = 0$, the CSS algorithm is recovered and always lead to a first-order energy-accurate method at the fluid-structure interface. By setting $\alpha_0 = 1$ and $\alpha_1 = 0$ the GCSS algorithm is recovered that is a second order energy accurate CSS and for $\alpha_0 = 1$ and $\alpha_1 = 0.5$ the GCSS algorithm is also recovered but it is a third order energy accurate CSS. Hence by using a simple predictor for the structure displacement the conservation of energy at the interface can be improved.

5.5 Implementation, construction and validation of the LES based FSI solver

So far, the coupled system of fluid-structure equations has been derived and the method used to solve such a system have been detailed. As stated previously, the weak coupling is preferred in the current framework since the density ratio is high. Note that this partitioned approach requires a third module that enables data transfer between the fluid and structure solvers. Its role is to communicate all the necessary data at the wet interface on the fly during calculations. Furthermore, for the purpose of validating the FSI solver, mesh adaptation is needed to improve the quality of the mesh whenever Laplacian smoothing fails to do so. This section is thus structured as follows: first, the coupling tool implemented in the current work is presented followed by the mesh adaptation procedure. Finally, two test cases are presented to validate the coupling.

5.5.1 Interface management and data transfer: CWIPI

The partitioned approach adopted uses a conforming mesh method (ALE) but it is not node-to-node coincident. Thus, it is crucial to ensure a correct data transfer between the interface nodes at every time step since the fluid and the solid meshes have different local refinements. The data transfer procedure allows the exchange of the coupling variables at the interface,

$$\begin{cases} \mathbf{w}_{n+1} = \dfrac{\mathbf{d}_{n+1} - \mathbf{d}_n}{\Delta t_c}\,, \\ \mathbf{f}_{n+1} = \displaystyle\int_\Gamma (\mu \frac{\partial \mathbf{u}_{n+1}}{\partial n} + \mathbf{p}_{n+1}\mathbf{n}_f) d\Gamma\,, \end{cases} \tag{5.5.1}$$

where $\mathbf{w}$ is the fluid mesh velocity that is equal to the rate of change of the solid boundary displacement and $\mathbf{f}$ represents the fluid forces obtained by integrating the pressure and wall shear stresses at the interface. The data transfer is ensured by the coupling library CWIPI (Coupling With Interpolation Parallel Interface). The CWIPI interface library provides a set of APIs and tools that enable the coupling of multiple software components or applications into a larger, integrated system. The APIs are coded in both Fortran and python and must be used at appropriate locations inside the codes that need to be coupled. Note that, a new API has been developed specifically for FreeFEM++ to handle the data exchange from the structure solver side. The great advantage of this library is that it allows the exchange of data between parallel codes based on unstructured meshes by interpolating them on the fly during calculations. Moreover, CWIPI can handle meshes composed of different element types such as segments for 1D elements, triangles for $2D$ elements, tetrahedra for $3D$ elements and many others. Figure 5.6 shows a simplified schematic highlighting the data exchanged between the two coupled solvers AVBP and FreeFEM++. In this example, the fluid mesh is much finer than its solid counterpart, and hence, the fluid solver runs on a higher number of processors ($m > n$). The communication between the coupled solvers is handled by the MPI protocol which must be launched in the same MPI environment. During initialization, CWIPI determines this intra-communicator for each solver. When creating the coupling, CWIPI also creates

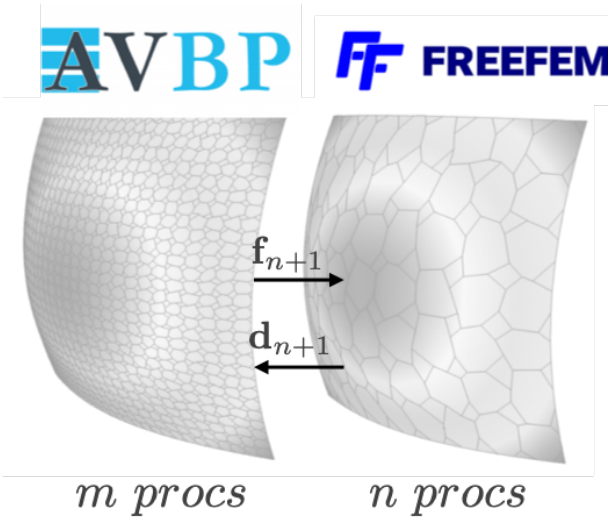

Figure 5.6: Schematic drawing of the coupling data exchange process between AVBP and FreeFEM++.

inter-communicators that link all processes of the two codes and constructs the communication graph used for exchanges through the geometric interface. Since each process contains only part of the global mesh interface whether it is the fluid or solid part, once the mesh interface has been defined and partitioned across all processors, CWIPI locates the nodes required to interpolate the exchanged information. After completing this step, CWIPI performs field interpolation by allocating weights based on the barycentric coordinates of the point within the localized mesh. The process of locating and computing barycentric coordinates is performed at the end of every coupled time step to ensure that the two meshes are always conforming and to avoid missing nodes that might otherwise induce accuracy errors.

5.5.2 Mesh adaptation

As explained earlier, the ALE method allows the mesh interface to deform in the fluid domain after receiving the corresponding displacements from the structure solver. The motion of the interface is then propagated in the whole fluid domain using a Laplacian smoothing method. However, even with a mesh smoothing approach, limitations are reached when deformations become large. The only solution to overcome this problem is as of today re-meshing techniques. Re-meshing consists in performing one or several operations such as refinement, coarsening and swapping to improve the quality of a mesh. Refinement operations are employed when certain elements of a mesh become too coarse, *i.e.*, an edge becomes too long or an element volume becomes too large. These operations are important to maintain a minimum mesh density to adequately capture the flow physics in a specific mesh region. Usually refinement is performed by splitting the longest edge in an element by adding a new node at its midpoint. Coarsening on the other hand is employed when the mesh becomes too fine, *i.e.*, an edge becomes too short or an element

volume falls below a certain threshold. This operation is important to avoid the presence of small cell volumes which will then decrease the time step of the simulation and hence increase the overall simulation time. Coarsening is usually performed through an edge collapse operation: where the two nodes forming an edge are collapsed to a single node consequently eliminating small cell volumes. The swapping operation does not involve any suppression or addition of new elements, instead it affects the local connectivity of an element. It involves replacing certain edges to satisfy a certain criterion such as skewness or the maximum tolerated dihedral angle. The current mesh adaptation technique used in the present work relies on the triangular ($2D$) and tetrahedral ($3D$) fully automatic MMG library (Dobrzynski & Frey (2008); Dapogny *et al.* (2014)). Re-meshing is however not performed at every iteration. Instead the user can trigger it based on a certain metric. The user can also limit the resulting gradient in mesh size after application of the metric if necessary. Figure 5.7 illustrates an adapted mesh when a cell volume near the interface fells below a certain threshold. Once the re-meshing is triggered, the field values are interpolated on the new mesh and the simulation is carried on.

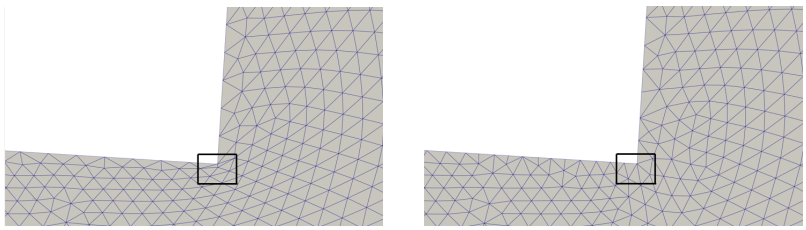

Figure 5.7: Mesh adaptation using MMG. (a) old mesh, (b) improved mesh.

5.5.3 Oscillating beam immersed in a fluid at rest

Case presentation

The aim of this first test case is to evaluate the mechanical equilibrium of an elastic plate immersed in a static fluid by varying the structure's density and/or the viscosity of the fluid. The idea is similar to the test case studied by Sigüenza *et al.* (2016) which was used to validate their fluid-structure interaction coupling based on the immersed thick boundary method. In this problem, the $2D$ plate is defined by its length L and width l as shown on Fig. 5.8. It is fixed at one end: *i.e.*, the bottom of the fluid domain and free to deform elsewhere. The fluid domain consists of a rectangular $20L \times 200l$ box containing a still fluid. A $t = 0s$, a time dependent loading is applied to the structure consisting of a body force $\vec{F}_x$ normal to its initial position. During this period, the coupling between the fluid and the structure is not active, only mesh deformation is active. Once the loading is removed, the coupling is activated and the beam starts to oscillate. In the absence of structural damping, the beam should oscillate indefinitely. The presence of a viscous fluid however acts as a damping force

on the motion of the structure bringing the latter back to its initial position after some time. Although it may seem trivial, this test presents a significant challenge to verify the operation of the fluid-structure interaction and coupling. The oscillating beam indeed perturbs the initially still fluid, generating vortices and strong pressure gradients that, in turn, interact with the moving structure. The objective is here first to assess the mechanical equilibrium of the beam since for any fluid/structure parameters, the vibrating beam should eventually return to its equilibrium position. The dynamics of the structure is then analyzed by varying the density of the structure and the viscosity of the fluid.

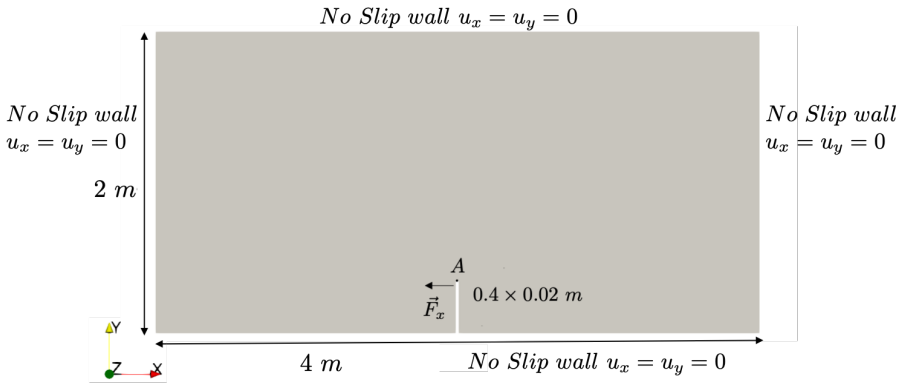

Figure 5.8: Geometrical parameters of the fluid domain and elastic beam. The force F_x is applied over all the left surface of the beam.

Numerical model

The fluid mesh is generated based on Fig. 5.8. It is a fully unstructured and composed of tetrahedra as shown on Fig. 5.9. It is made of 11 630 elements, with a minimum cell resolution of $h_{min} = 0.0017\,m$ near the moving walls. The structure is on the other hand meshed using 250 triangular elements with a constant resolution of $h = 0.002\,m$ resulting in a fluid to solid node resolution ratio of 3 at the interface. Regarding the numerical boundary treatments, a no-slip boundary condition is applied on all walls on the fluid side. Note also that the ALE description is active for these moving walls. For the fluid simulation, the third order convective (Colin & Rudgyard (2000*a*)) finite-element scheme based on a two steps Taylor-Galerkin (TTGC) formulation is used. The timestep Δt_f is evaluated on the fly following the Courant-Friedrichs-Levy (CFL) constraint of 0.7 to ensure numerical stability. This leads to a time step value around $1.5 \times 10^{-5} s$. Once the coupling is activated, this time-step is passed to the structure solver so that $\Delta t_f = \Delta t_s = \Delta t_c$. Recall that the structure is fixed to the bottom of the channel by its lower extremity. This translates mathematically into $\boldsymbol{\xi} = 0$ and $\frac{\partial \boldsymbol{\xi}}{\partial t} = 0$ at this surface. The structure dynamics is modeled using the elastodynamic equation (4.1.23) discretized in time using the Generalized alpha scheme with $\alpha = 0.25$ and $\delta = 0.5$. Since the size of the solid domain is relatively small, a direct method based on

LU decomposition is used to speed up calculations.

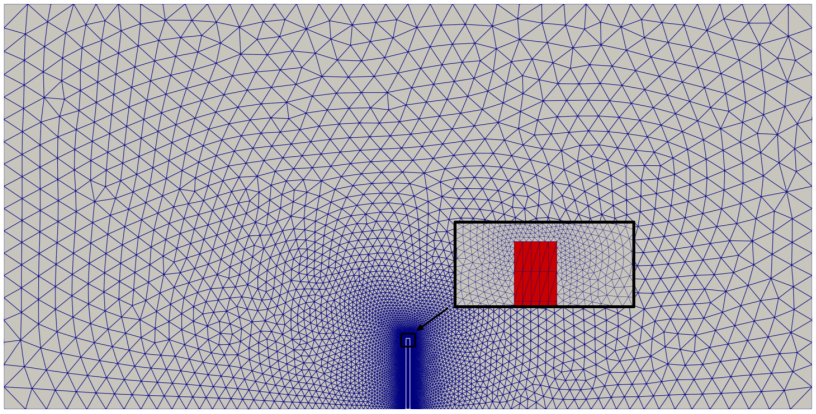

Figure 5.9: Fluid-structure domain and its associated mesh.

Different simulations are now carried out. Three cases named **Case** 1, **Case** 2 and **Case** 3 are discussed. These differ only by the density of the structure and the dynamic viscosity of the fluid as detailed in Tab. 5.1. The Young's modulus and the Poisson's ratio of the structure remain fixed and equal to $1.4\,MPa$ and 0.4 respectively. As said before, at time $t = 0$, a time dependent loading $\vec{F}_x$ is applied to the structure for the interval $[0; t_c]$. After that the loading is removed, so the fluid-structure coupling is activated at $t = t_c = 0.1\,s$. The initial position at the beginning of the coupling ($t = t_c$) is the same for all cases.

	Case 1	**Case 2**	**Case 3**
ρ_s [Kg/m^3]	100	50	100
μ [Pa.s]	3.716×10^{-3}	3.716×10^{-3}	7.42×10^{-3}

Table 5.1: Parameters used for the different test cases.

Figures 5.10 and 5.11 show a series of instantaneous snapshots of the pressure field and mesh respectively, for **Case 1** starting at the moment when coupling is activated. At the time of release ($t = t_c$), a pressure gradient forms around the beam as it is pushed away from its initial position. This pressure gradient results from the force exerted by the beam on the fluid which is set in motion. Once the mechanical force is released, the beam has stored the maximum amount of potential energy that will then be converted into kinetic energy. In simple terms, the beam will oscillate around its equilibrium position dissipating its kinetic energy by transferring it to the fluid. It is worth to note that re-meshing is not needed in this application, the Laplacian smoothing method is able to handle mesh deformation. Note also that while oscillating, vortices are formed near the free end of the beam indicating an important fluid-structure interaction activity. Figure 5.12 illustrates such a formation of vorticies near the tip of the structure where the displacement is the most significant.

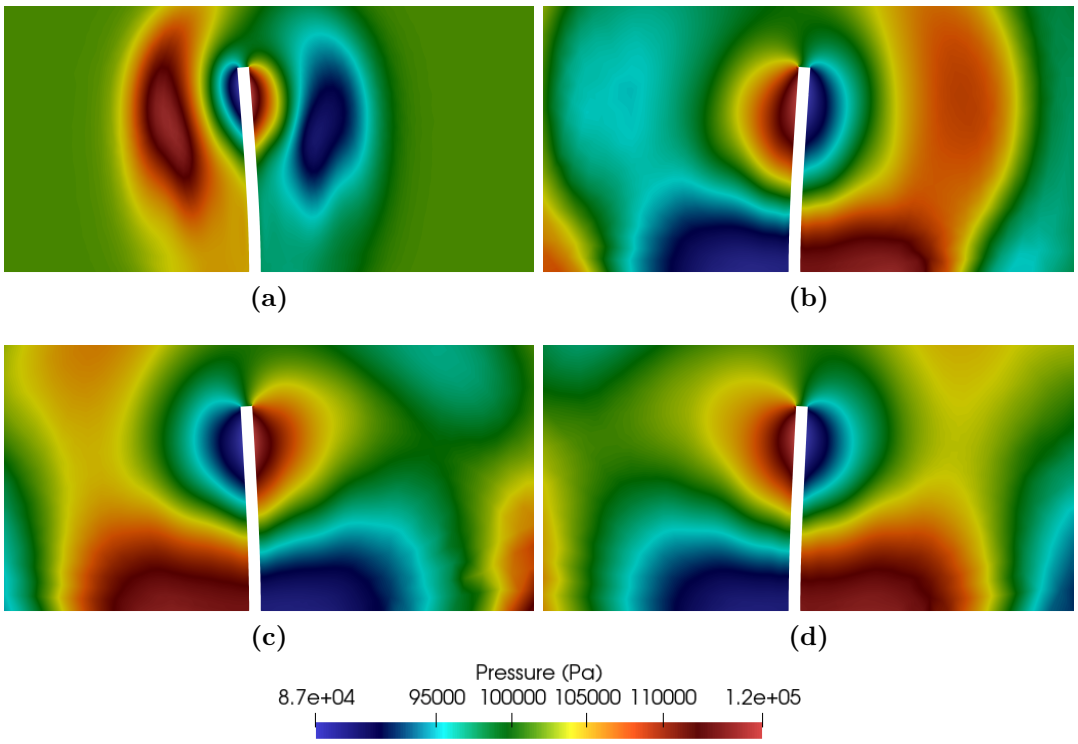

Figure 5.10: Instantaneous snapshots of the pressure field after release: (a) t_c (b) t_c+$T/2$ (c) $t_c + 3T/2$.

As the distance from the beam increases, the magnitude of the activity within the fluid decreases. This phenomenon occurs in all three cases, although the dynamics of the fluid and the structure differ due to the changes in density and dynamic viscosity. These differences result in different behaviors in each case, which can be further analyzed by looking at the dynamic response of the structure or the fluid respectively.

For all cases, the temporal evolution of the tip displacement of the beam is recorded for all cases using a numerical probe attached to the beam tip and results are depicted on Fig. 5.13. All cases demonstrate an oscillatory behavior where the displacement fluctuates between a certain minimum and maximum values. From such a diagnostic, the beam needs approximately $7s$ to regain its equilibrium position for Case 1. In contrast, the equilibrium position is attained after only $5s$ in Case 2. Indeed, when decreasing the density of the structure, this latter carries more momentum and dissipates its kinetic energy faster to the fluid, hence reaching the equilibrium position in a shorter amount of time. Note that varying the density does not affect the displacement of the beam, it is strictly linked to the strength of inertia of the structure. An increase in structural density yields a lower acceleration and hence lower velocity, conversely a lower structural density leads to a higher acceleration and velocity such as in this case. Case 3 is seen to have a similar behavior as for Case 1 with larger oscillations than for Case 2. However, since the fluid viscosity has increased, damping effects become more important leading to a faster convergence towards the initial position. Overall and in all cases, the structure

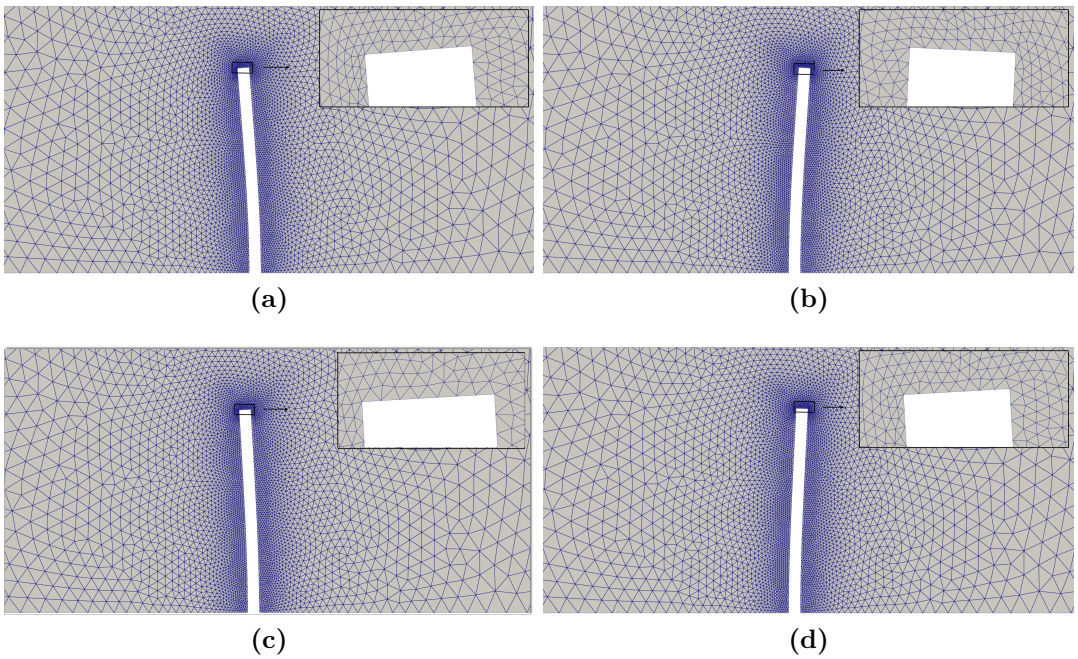

Figure 5.11: Instantaneous snapshots of the mesh after release: (a) t_c (b) $t_c + T/2$ (c) $t_c + 3T/2$.

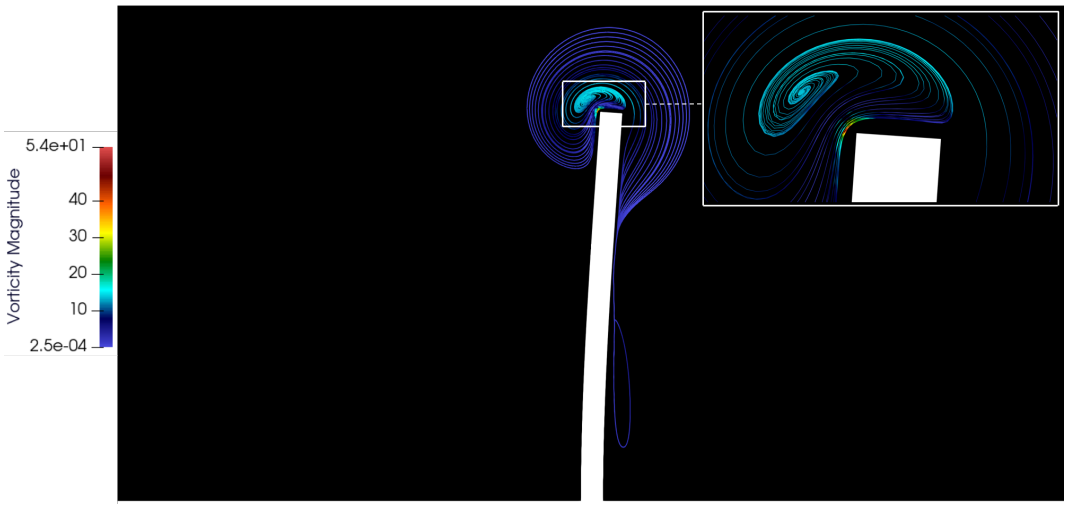

Figure 5.12: instantaneous vorticity streamlines at $t = t_c + T/2$.

is able to re-gain its initial position and shape for various coupling conditions replicating the expected physical behavior.

As a complement to the previous discussion, flow dynamics can also be analyzed in time by looking at the volume averaged kinetic energy of the fluid, Fig. 5.14. Again, large fluctuations are present at the beginning when the kinetic energy reaches its maximum value due to the imposed force and beam deflection. Just like the plate which reaches its initial equilibrium, the fluid returns at rest with time and the kinetic energy

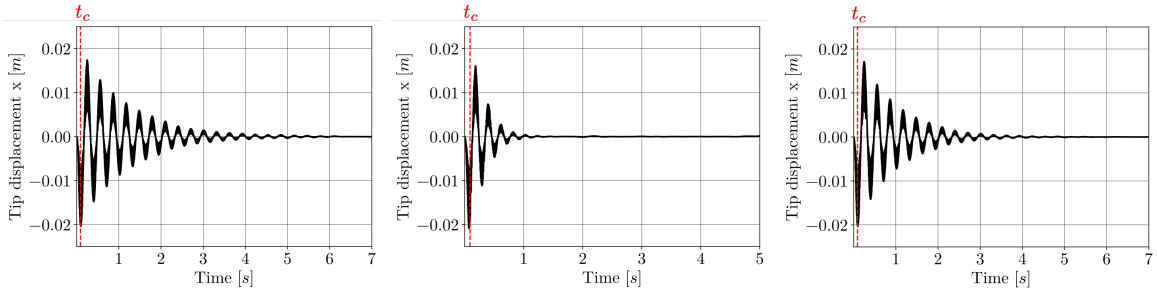

Figure 5.13: Time evolution of the tip displacement recorded at point A for **Case 1** (a), **Case 2** (b) and **Case 3** (c)

falls back to zero. The time needed for the fluid to return to rest is influenced by the same aforementioned structural and flow parameters. Indeed, when the flow viscosity is increased the kinetic energy stabilizes faster as indicated by Case 3. On the other hand, Case 2 highlights large kinetic energy fluctuations compared to the other two cases. This phenomenon is due to the higher momentum carried by the beam as stated previously. Since a higher momentum implies a beam higher velocity (mass is conserved in this case), and since the walls push the fluid, a stronger activity is observed and the fluid needs more time to go to rest which explains the higher frequency of the fluctuating kinetic energy.

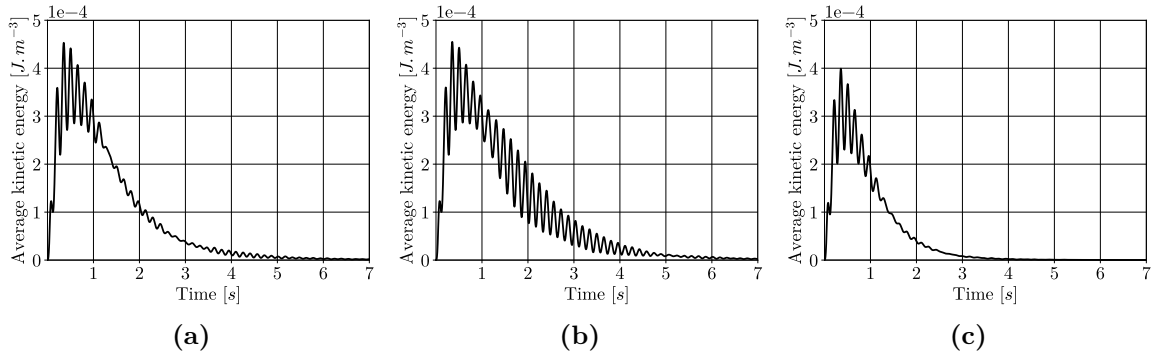

Figure 5.14: Time evolution of the total average volumetric kinetic energy for **Case 1** (a), **Case 2** (b) and **Case 3** (c)

This first test case confirms that the mechanical equilibrium of a displaced beam immersed in a still fluid can be retrieved using the developed FSI tool. More specifically, it provides a clear validation of the numerical coupling developed in this work. The physical aspects involved in this application are however relatively limited as the Laplacian smoothing technique is known to be inadequate for handling significant deformations. To address these limitations, a second application is considered where vortex-induced vibration causes a thin elastic plate to oscillate with large amplitudes.

5.5.4 Vortex induced vibration of a thin elastic plate

Case presentation

This second test case was originally proposed by Wall & Ramm (1998) to investigate the coupling between incompressible unsteady flow phenomena and large structure deformations of a thin elastic plate. It has been since then extensively used to validate various FSI approaches: a monolithic coupling based on a hybrid Eulerian-ALE method (Schott *et al.* (2018)), a monolithic coupling based on space-time finite elements method (Hübner *et al.* (2004)), a weak coupling partitioned approach (Debrabandere *et al.* (2012)) and strong coupling partitioned approach (Uyttersprot (2014)). The configuration consists of a thin elastic cantilever beam clamped to the back of a rigid square cylinder. All dimensions and boundary conditions are shown on Fig. 5.15. The beam density, Young's modulus and Poisson's ratio of the structure are given by $\rho_s = 2000\ Kg/m^3$, $E = 2 \times 10^5\ Pa$ and $\nu_s = 0.35$. The Density and dynamic viscosity of the fluid are also given: $\rho_f = 1.18\ Kg/m^3$ and $\mu = 1.82 \times 10^{-5}\ Pa.s$. This results in a Reynolds number of $Re = 204$ and a mass ratio of $\mathcal{M} = 1700$. At this Reynolds number, the flow is laminar and undergoes a Hopf bifurcation causing von Kármán vortices to shed from the corner of the cylinder and eventually a vortex induced vibration phenomenon. Vortex Induced Vibration (VIV) is a phenomenon that may occur when

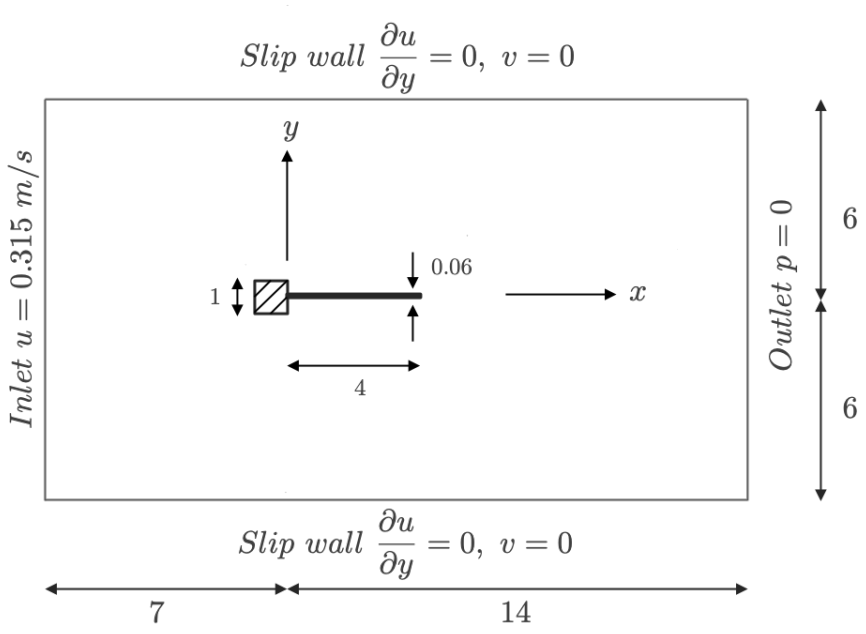

Figure 5.15: Geometric setup and boundary conditions for the vortex induced vibration beam (dimensions are in *cm*).

an object, such as an elastic plate, is placed in a fluid flow. When the fluid flows past the rigid square, vortices are shed from the corners of the square, causing fluctuations in pressure and velocity around the square. These fluctuations can cause the plate to

vibrate in the direction perpendicular to the flow, which is known as vortex-induced vibration.

In terms of setup, the computation for this process is divided into two parts. First, the fluid problem is considered independently by computing the flow field until the von Kármán vortex street develops behind the square. During this phase, there is no coupling between the fluid and the structure, the latter remaining rigid. Once the flow field is established, the coupling between the fluid and the structure is activated, so the structure is allowed to deform.

Fluid only problem

Flow computations are first carried out on the geometric configuration presented earlier and corresponding to Fig. 5.15. To do so, the geometry is meshed with 22 000 triangular elements with a minimum cell resolution $h_{min} = 1 \times 10^{-3}$ near the rigid square and beam. In addition to the boundary conditions indicated on the schematic of Fig. 5.15, a no-slip condition is applied on all walls of the rigid square and beam. In this simulation, the third order convective Colin & Rudgyard (2000*a*) finite-element scheme based on a two steps Taylor-Galerkin (TTGC) formulation is used. The timestep Δt_f is computed following the Courant-Friedrichs-Levy (CFL) convective time step constraint to 0.7 to ensure numerical stability. Note that since the test case considers an incompressible flow, and a Mach number that is very small (≈ 0.00014), a pressure gradient scaling (PGS) method is used to speed up the simulation by artificially reducing the speed of sound in order to impose a Mach number of $Ma = 0.2$ for a velocity $U_\infty = 0.315\ m/s$. Note that the new Mach number is chosen such that compressibility effects are negligible. This yields a ten folds increase of the time step of the resulting simulation and a value around $0.4 \times 10^{-4} s$.

Figure 5.16 shows instantaneous solutions over one shedding period of the pressure fields issued by AVBP for this problem. Vortex shedding clearly occurs periodically at the edges of the rigid square. One shedding period is characterized by the appearance of two vortices on one side of the beam and a large vortex on the other side. The spatial organization of these vortices then alternates sides with respect to the beam, creating an alternating pressure differential. As a result of this distribution, if the beam is allowed to deform, a vortex-induced vibration phenomenon is expected. The vortex shedding frequency is determined using pressure data collected from a numerical probe placed near the square wake. The resulting spectrum displayed on Fig. 5.17 clearly indicates that the shedding frequency obtained is equal to $f_F = 3.6Hz$. Overall, findings are consistent with the simulations of Hübner *et al.* (2004) where a similar periodic vortex shedding behavior is observed at a frequency of $3.7Hz$.

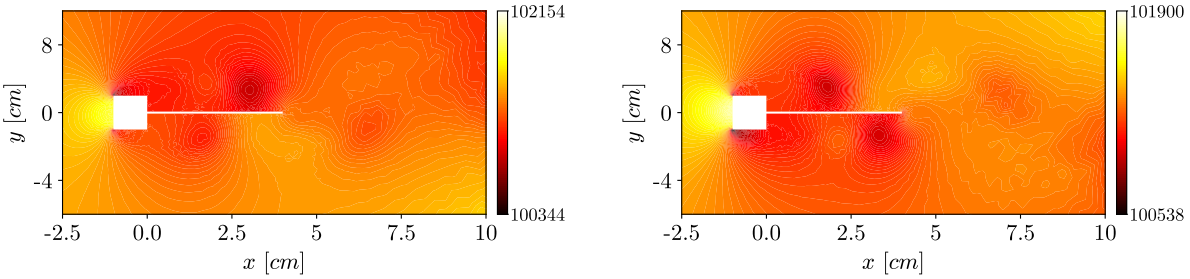

Figure 5.16: Pressure distribution field over one shedding period.

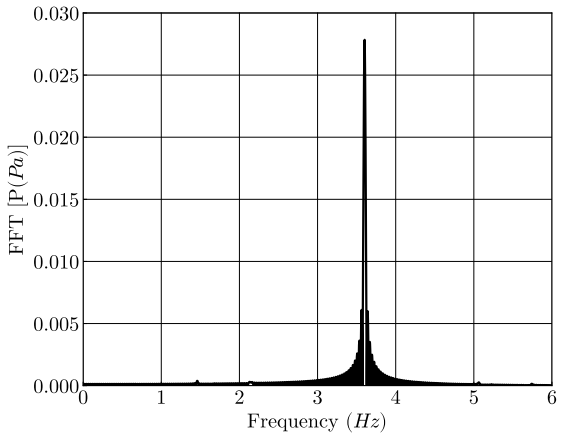

Figure 5.17: Magnitude of the fast Fourier transform performed using collected pressure data near the square wake.

FSI problem

In the following the beam is allowed to deform starting with the previously obtained fluid only result. To do so, the ALE description is added to the no-slip boundary condition to allow the motion of the nodes of the corresponding wall and the coupling is activated. The numerical domain involving both the fluid and structure is shown on Fig. 5.18. The beam is meshed using 216 triangular elements resulting in a fluid to solid node ratio of 4 at the interface. Recall that all nodes at the left extremity of the beam are fixed so $\boldsymbol{\xi} = 0$ and $\frac{\partial \boldsymbol{\xi}}{\partial t} = 0$. The remaining surface nodes of the beam and present on its surfaces compose the exchange interface and are shared by the fluid and solid domains. The time integration scheme used to model the dynamic response of the structure is again the Generalized alpha scheme with direct preconditioning applied to solve for the assembled matrices. When it comes to the fluid solver parameters, they are unchanged and correspond to the fluid only simulation.

As anticipated earlier, the vortex street observed in the fluid only problem produces pressure changes on the surface of the flexible structure, which in turn generates forces that accelerate the structure and cause vibrations of increasing amplitude. Figure 5.19 shows the time evolution of the tip displacement at the flow limit cycle and as recorded

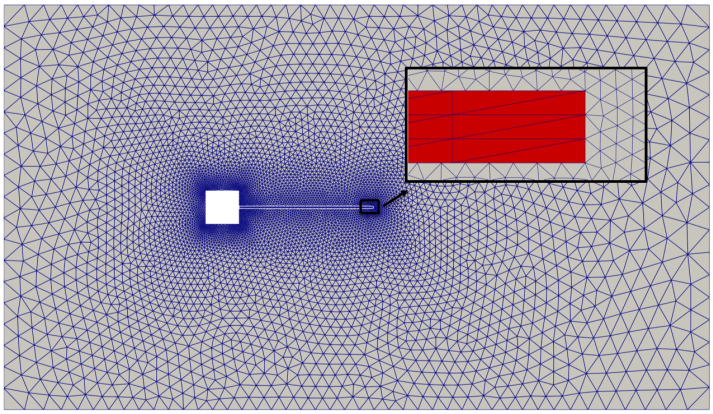

Figure 5.18: Fluid-structure numerical domain

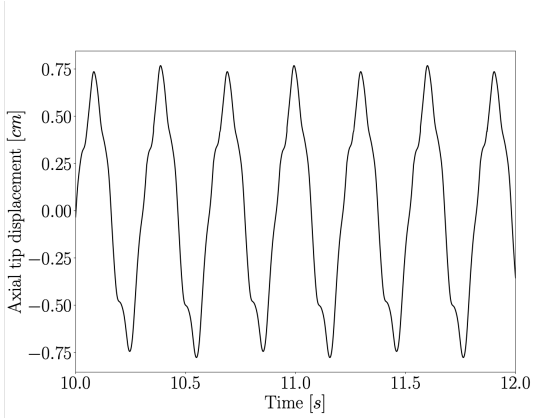

Figure 5.19: Time evolution of the axial tip displacement at the flow limit cycle.

using a numerical probe placed on the free end of the beam. The maximum amplitude attained is $\mathbf{u}_y = 0.77\,cm$ and the obtained coupled fluid-structure frequency $f_c = 3.2Hz$. Note that this FSI frequency differs from the fluid vortex shedding frequency which was $f = 3.6Hz$. Such results and observations are in agreement with the findings of Hübner *et al.* (2004), who also observed an amplitude of vibration $\mathbf{u}_y = 0.8\,cm$ and a coupled motion frequency at $f_c = 3.1\,Hz$. Note that depending on the ratio of the vortex frequency to the natural frequencies of the structure, different structural deformations can be expected. These deformations can in turn affect the vortex frequency or, more generally, the dynamic parameters of the flow. Such a complex interaction is at the root of FSI tools. Wall & Ramm (1998) demonstrated that the change in the modulus of elasticity or a change in the structure's density lead to a shift in the coupled structural response from its second to its first eigenmode. Similarly, Debrabandere *et al.* (2012) obtained the structure first eigenmode response, albeit at a smaller Reynolds number. Multiple coupling methods have been used in the literature to simulate this test case. In that respect, Table 5.2 provides a comprehensive summary of results obtained using different codes and coupling types. For almost all reported cases, the coupling software MpCCI

Codes	**Structure Model**	**Amp. $\mathbf{u}_y$ $[cm]$**	**Coupling type**
Fluent-MSC Marc	Plane-strain	0.6	partitioned (weak)
Fluent-Nastran	Plane-stress	0.8	partitioned (weak)
Fluent-ANSYS	Plane-stress	0.65	partitioned (weak)
Fluent-Abaqus	Plane-strain	0.6	partitioned (weak)
FEM (Hübner *et al.* (2004))	Plane-stress	0.8	monolithic
AVBP-FreeFEM++	Plane-stress	0.77	partitioned (weak)

Table 5.2: Comparison between different solvers and coupling methods .

(SCAI (2007)) was used to couple the fluid solver fluent with various Structure solvers. These partitioned weakly coupled simulations hence differ only in the method used to model the response of the structure. MSC Marc and Abaqus solvers make use of the plane-strain model whereas Nastran and Ansys use a plain-stress model for the structure. The plain-stress assumption implies that the three stress tensor components related to the in-plane direction (z in this case) are zero. It is an adequate approximation for thin plates but it is only correct when the thickness approaches zero. Conversely, the plain-strain formulation does not contain any approximation and refers to a condition where an object is constrained in the z direction meaning that the displacements or equivalently strains are null in this direction. Subsequently, the plain-strain model is stiffer than the plain-stress model which explains the discrepancy in the maximum amplitude recorded by the different models. To further understand the dynamic response of the structure, instantaneous snapshots are illustrated on Fig. 5.16. These solutions constitute one full period of vibration of the beam. From such a view, the series of vortices identified in the rigid case are observed to behave differently in the coupled simulation. Indeed, as these vortices exert a pressure force on the beam, the latter deforms and the vortices follow this deformation in a "roll-off" fashion as highlighted by Wall & Ramm (1998). Their trajectory is hence impacted and so is the force on the beam. It is worth noting that re-meshing has been used here since the Laplacian smoothing technique was not able to compensate for such large mesh deformations. Figure 5.21 shows snapshots of the mesh at the same instants as the solutions of Fig. 5.20. On average, a total of three mesh adaptations were needed per period of vibration.

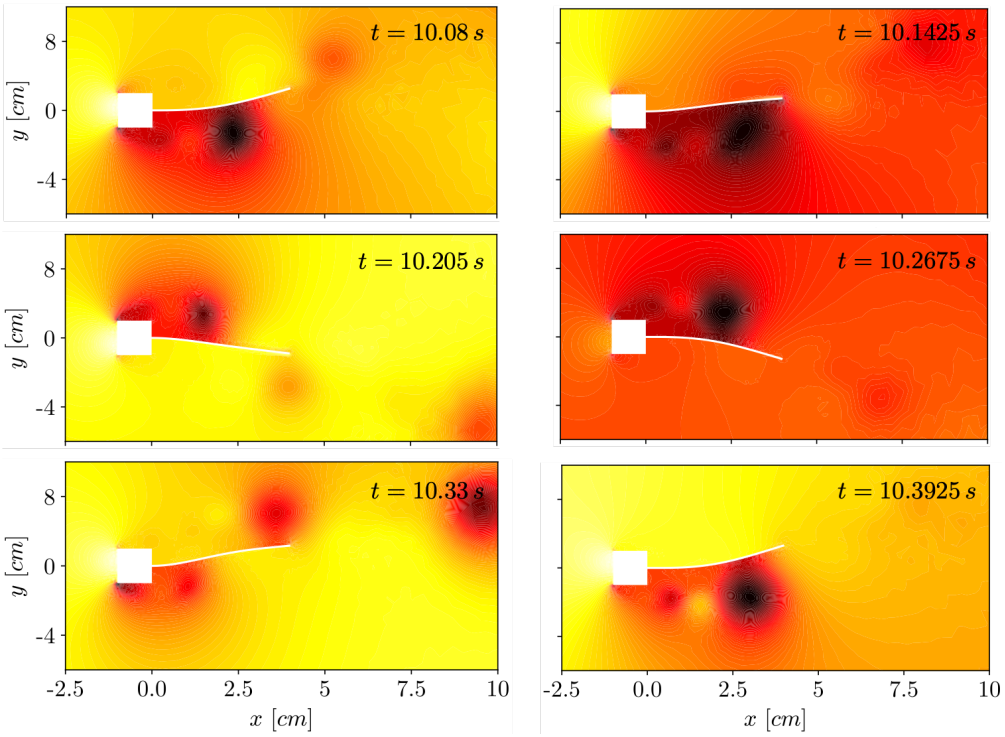

Figure 5.20: Instantaneous snapshots of the pressure field over one period of vibration.

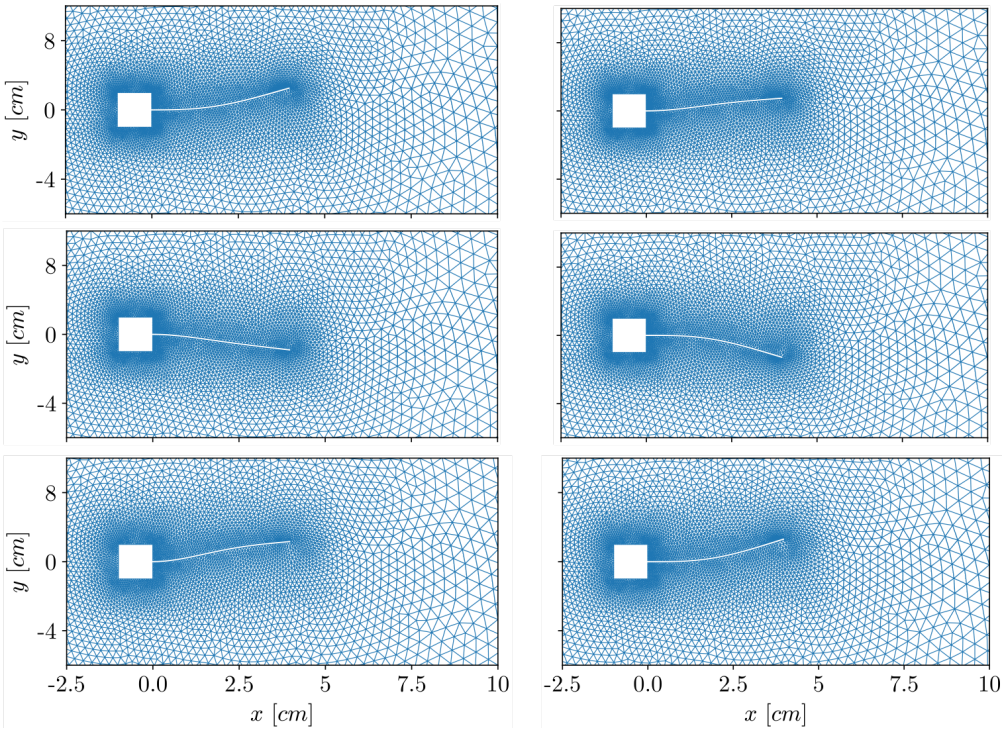

Figure 5.21: Mesh snapshots corresponding to Fig. 5.20.

5.6 Conclusion

Overall, observed flow dynamics is correctly retrieved if compared to literature results for the VIV problem. Similarly, the correct structure dynamics an flow behavior is observed for the first test case. Note nonetheless that the two test cases evaluated here are $2D$ models with relatively low Reynolds numbers. In the next chapter, FSI computations are carried out on a complex $3D$ case at a high Reynolds number to demonstrate the capabilities of the coupling tool assembled in this thesis work and if applied to a real life industrial problem.

Chapter 6

Investigation of the coupled fluid-structure phenomena of the first stage rotodynamic pump

Contents

The second chapter has highlighted the capacity of Large Eddy Simulation (LES) to retrieve the dynamics of the flow inside a first stage rotodynamic pump, and in particular, the underlying flow instabilities causing strong pressure fluctuations. This chapter is a follow-up to this study where a numerical fluid-structure investigation is carried out in order to identify potential multiphysical phenomena that are responsible for the detrimental vibration levels of the turbopump. The primary goal of this investigation is to assess the capacity of LES coupled to the structural dynamics solver to retrieve coupled fluid-structure interaction modes. These modes are highly sensitive to geometrical parameters, boundary conditions, operating point of the turbopump, etc.. In addition, the physical properties of structural components play a major role in determining the vibration response of the system. Results show that the flow dynamics retrieved by LES is attributed to a coupled fluid-structure mode that causes the fluid and structure to oscillate at an identical frequency that is close to the natural frequency of the rotor. Finally, this coupled mode is found to match the acoustic frequency of the cavity leading to a vibroacoustic phenomenon between the fluid, rotor disk and cavity.

6.1 Introduction

The design of rocket engines remains to this day a formidable challenge to engineers. Each component must be precisely designed, manufactured and tested due to the tremendous thermal and dynamic stress levels it should withstand. Moreover, the complex nature of the fluid mechanisms and their interaction with various components only exacerbate the task at hand. Flow instabilities responsible for pressure fluctuations inside a first stage rotodynamic pump have been successfully captured by LES in conjunction to other predictive numerical strategies as demonstrated in Chap. 2. This unsteady CFD approach has also proved to be a reliable tool in capturing the *pressure band* phenomenon inside a first stage turbine cavity of a turbopump. For instance, Bridel-Bertomeu (2016*a*) and Queguineur (2020) have retrieved the modal content of the flow inside such industrial devices through LES and subsequently proved that contrary to RANS, LES is able to identify this phenomenon. Nevertheless, the fluid analysis alone is not enough to fully understand the occurrence of multiphysical phenomena that take place within space turbopumps. Indeed, as stated earlier in this thesis, flow instabilities can couple to the surrounding structure creating fluid-structure modes of vibration and hence generating major risks for the operation of the turbopump. To address this particular issue, a coupled fluid-structure interaction simulation is carried out on the cavity introduced in Chap. 2. The focal point of this study is to evaluate the stability of the Axial Balancing System (ABS) under certain working conditions. The ABS is self-balanced meaning that the axial position of the rotor is determined through pressure equilibrium on its faces. However, if the rotor oscillates near its natural frequency it exhibits large amplitude of vibrations. More importantly, since the flow is compressible, if the natural acoustic frequency of the cavity is close to the natural frequency of the rotor, a three way coupling

between the fluid, the structure and the cavity may appear resulting in an unbalanced system. Brunier-Coulin *et al.* (2022) described this type of dynamical system using the following third order differential equation with $\mathbf{u}$ being the variation of the rotor axial displacement with respect to its equilibrium position:

$$\dddot{\boldsymbol{u}} + \lambda_2 \ddot{\boldsymbol{u}} + \omega_a^2 \dot{\boldsymbol{u}} + \lambda_0 \mathbf{u} = 0 \tag{6.1.1}$$

with ω_a the acoustic pulsation of the cavity, and λ_0 and λ_2 two parameters which depend on the pressure loss mechanisms inside the cavity so that,

$$\begin{aligned} \omega_a &= k_d^2 \sqrt{\frac{G}{\rho_s}} \\ \lambda_0 &= (\omega_a^2 \frac{\partial Q}{\partial P}|_u - \frac{1}{\mu} \frac{\partial Q}{\partial \boldsymbol{u}}|_P) f(\omega_c) \\ \lambda_2 &= (\frac{\partial Q}{\partial P})_u f(\omega_c) \end{aligned} \tag{6.1.2}$$

where k_d is the axial wavenumber of the disk of shear modulus G and ρ_s the density. λ_0 and λ_2 are the upstream and downstream pressure loss coefficients that characterize the stiffness of the upper valve. These coefficients are defined in function of the flow rate Q passing through the cavity, the rotor displacement $\mathbf{u}$ and the pressure loss P. ω_c finally represents the coupled fluid-structure pulsation frequency. The third and first order terms in Eq. (6.1.1) represent the Helmholtz oscillator while the two remaining terms represent the upper valve oscillator. The stability of the ABS is thereby dictated by the competition between two oscillators. In other words, the rotor deformation and the pressure readjustment control the stability of the system. In order to determine if such system is stable or not, the Routh-Hürwitz criterion is usually applied. It states that a dynamical system is stable if all the roots of its characteristic equation lie on the left-half of the complex plane (*i.e.*, have negative real parts). In this case, the solution is stable if and only if $\omega_d^2 > \lambda_0/\lambda_2$, meaning that the ABS is stable if the characteristic time of the rotor displacement is smaller than the pressure readjustment in the cavity. Solving Eq. (6.1.1) yields a solution defining the critical flow rate above which the system becomes unstable for a given acoustic frequency ω_a and valve clearance a that is the sum of the initial valve clearance a_0 and the axial displacement of the rotor $\mathbf{u}$ (see Fig. 6.1).

Such an analytical approach, although very powerful, is valid only if certain assumptions are satisfied. These assumptions state that the rotor disk considered should be very thin ($H << R$), the Mach number must be small ($Ma << 1$), the axial flow rate between the disk and the cavity is uniform and the acoustic waves are isentropic. Subsequently, the analytical model alone is not reliable enough to determine accurately the critical flow rate of a real life application. To overcome this limitation, Deneuve *et al.* (2020) and Brunier-Coulin *et al.* (2022) conducted numerical and experimental tests to calculate the critical mass flow rate as a function of the upper valve clearance. To do so, five different initial upper valve clearances were tested: $45\mu m$, $65\mu m$, $95\mu m$, $135\mu m$ and $175\mu m$. For each clearance, the flow rate was increased progressively from $0\,m^3/h$ to $35\,m^3/h$ to determine the critical limit. Results show that for a given upper valve clearance, increasing

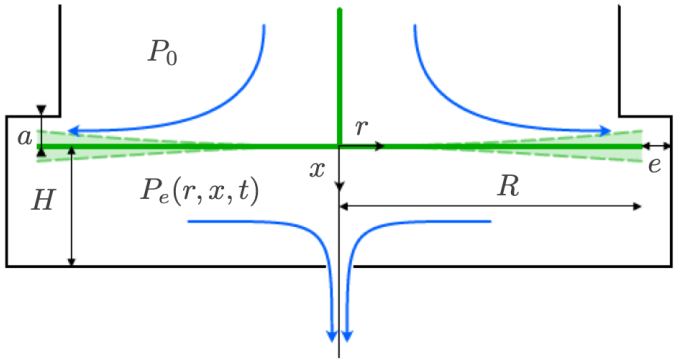

Figure 6.1: Schematic drawing of the cavity and rotor. The rotor disk is vibrating at its $0ND$ mode.

the flow rate beyond the critical threshold causes an exponential increase of the vibration levels. Furthermore, this allowed the classification of the different operating points according to their stability. In parallel to these theoretical and experimental studies, a numerical fluid-structure interaction investigation has been carried out on the cavity and rotor disk. In this case, RANS and URANS computations have been performed for the same operating points to detect unstable fluid-structure modes. Although the results are in agreement with the experimental approach, the FSI computations were limited to a modal approach where the $0ND$ structural mode is computed beforehand and the eventual coupled response is evaluated. In the current study, a fluid-structure interaction simulation is carried out on the cavity introduced in Chap. 2 with no assumption on the fluid or modal response of the structure. The objective is to assess the capacity of the developed numerical coupling chain between AVBP and the structural solver to retrieve the flow limit cycle corresponding to the correct coupled mode of vibration and damping rate for this configuration. This step is crucial from a manufacturer's point of view to determine the amount of damping required to stabilize this system. In a second step, the unstable response of the axial balancing system is investigated when damping is removed to confirm the condition of stability of the ABS.

6.2 Numerical model

The geometric model consists of both the cavity and rotor disk as shown on Fig. 6.2. The rotor disk is created using a 1° axisymmetric cut of the complete configuration, similar to the cavity, so that the shared boundaries coincide. The rotor is made of steel with a density $\rho_s = 7720\,Kg/m^3$ and a Young's Modulus $E = 2 \times 10^{11}\,Pa$ yielding a solid to fluid mass ratio of $\mathcal{M} \approx 6550$ and Lamé coefficients $\lambda_s = 1.15 \times 10^{11}\,Pa$ and $\mu_s = 7.7 \times 10^{10}\,Pa$. All the characteristic parameters of the cavity and disk presented in Chapter 2 hold for this simulation. Regarding the fluid numerical domain, Mesh 1 is used to discretize the cavity. The rotor disk section is meshed using 3500 tetrahedral elements

Figure 6.2: CAD model of the cavity (grey) and rotor disk (red).

which was found sufficient to reach mesh convergence of the solid solution. Three nodes are placed in the azimuthal direction across all faces of the rotor to correctly capture the shear and normal stresses where interactions are important (see Fig. 6.3). Note that subcycling is not activated in the simulation to be discussed as to avoid the potential energy loss at the interface that would affect the accuracy of the results. The rotor is fixed at the hub and free to deform elsewhere in all directions. All shared boundaries in the fluid domain are treated with the ALE description in order to account for the mesh velocity. In addition, the Laplacian smoothing technique is activated to efficiently propagate the deforming cells near the interface. All the numerical parameters used for the fluid simulation are valid for this case. Concerning the structural part computational details, the generalized alpha scheme with direct LU factorization of matrices is used.

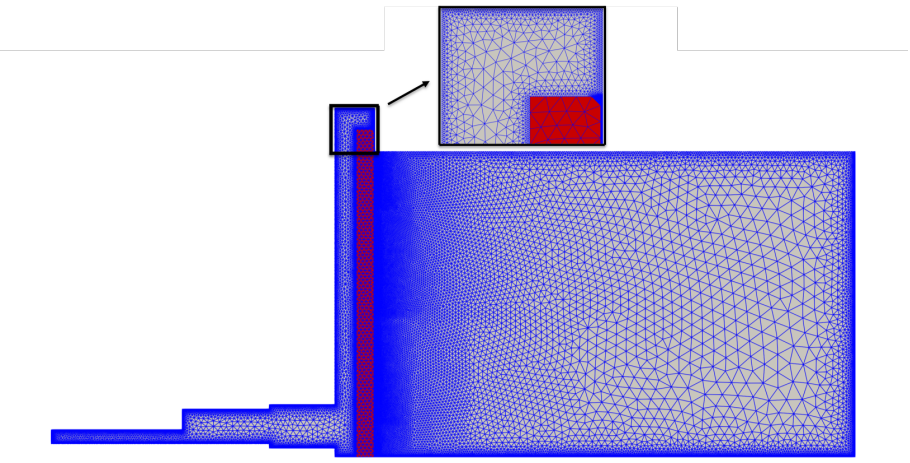

(a)

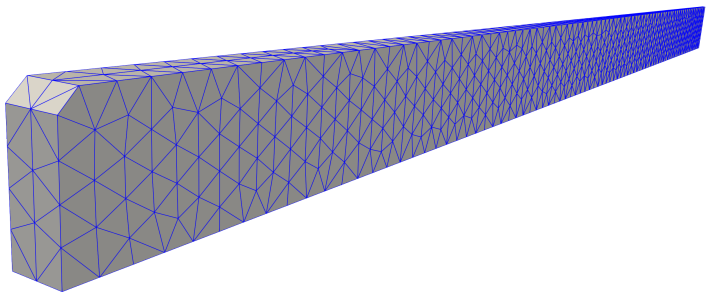

(b)

Figure 6.3: (*a*) fluid-structure domain and its associated mesh , (*b*) rotor disk component.

6.3 Results and discussion

Computations are initialized from a converged solution obtained from the fluid only simulation. Pressure forces are computed at the beginning of each iteration and sent to the structure solver, the latter then computes the corresponding velocity and displacement and sends them back to the fluid solver to advance to the next time step. Figure 6.4 shows the fluid-structure interface along with two of the exchanged variables: pressure and axial displacement. At the start of the simulation, the fluid exiting the first cavity exerts a pressure on the upper face of the rotor that is greater than the pressure exerted at the back of the rotor. Indeed, since the rotor constitutes an "obstacle" for the fluid between the first and second cavities, this leads to a pressure build-up on its upper face. This pressure differential across its two faces creates a net positive force oriented downward which leads to an axial displacement of the rotor in the same direction. The axial displacement increases radially till it reaches its maximum value at the rotor circumference

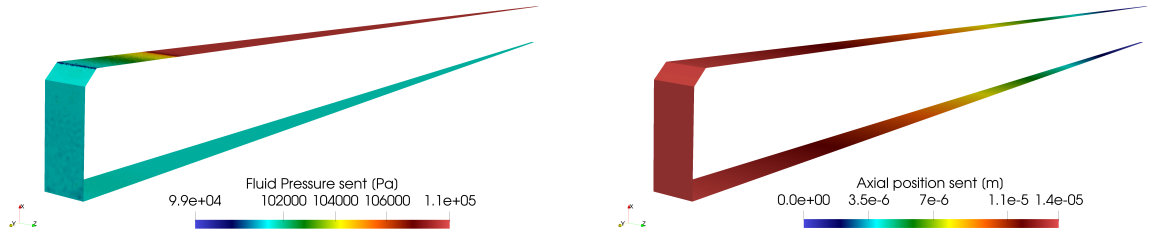

(a) **(b)**

Figure 6.4: two of the exchanged variables at the fluid-structure interface: (a) presssure and (b) axial tip displacement.

then switches direction. Figure 6.5 shows snapshots of the disk axial displacement over one period of vibration. The whole structure is indeed to be in a dynamic motion (except the right extremity that is fixed to the hub) with a maximum displacement recorded at the left free end. As illustrated here, the structure does not exhibit any nodal value along its diameter during the vibration cycle which means that the disk is vibrating at its $0ND$ mode. To verify this claim, the $0ND$ mode of the rotor section is calculated separately

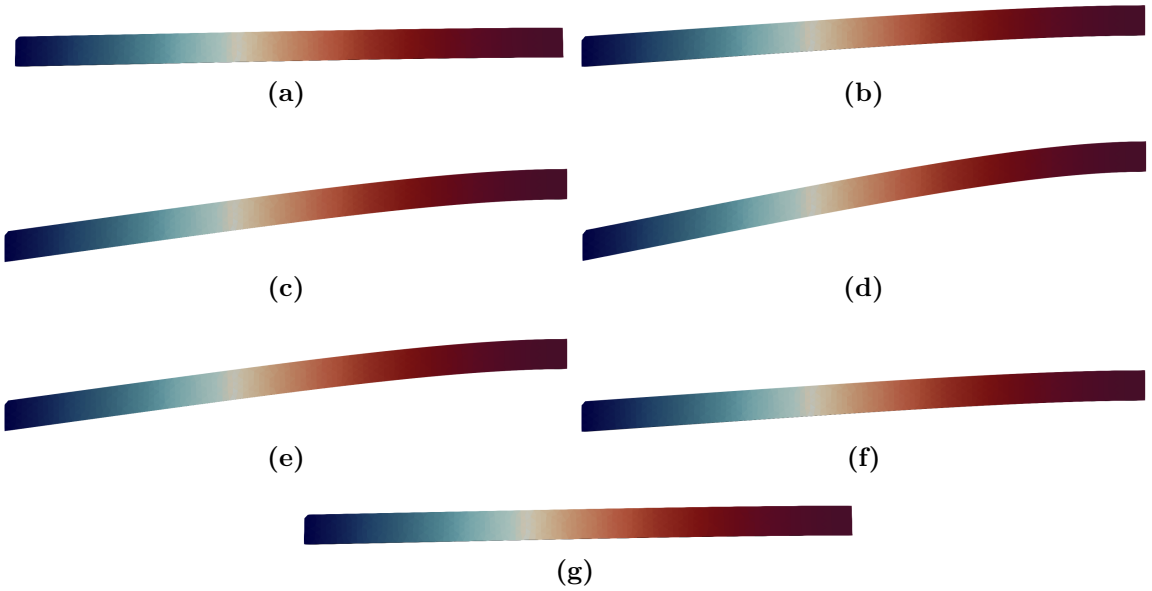

(a) **(b)** **(c)** **(d)** **(e)** **(f)** **(g)**

Figure 6.5: Snapshots of the rotor disk axial displacement magnified by a factor of 10^4 over one period of vibration.

via the developed modal analysis tool and is superposed on the axial velocity of the fluid mesh as shown on Fig. 6.6. The mode shape matches exactly the movement of the fluid grid axial displacement indicating that the $0ND$ mode does indeed respond to the fluid excitation.

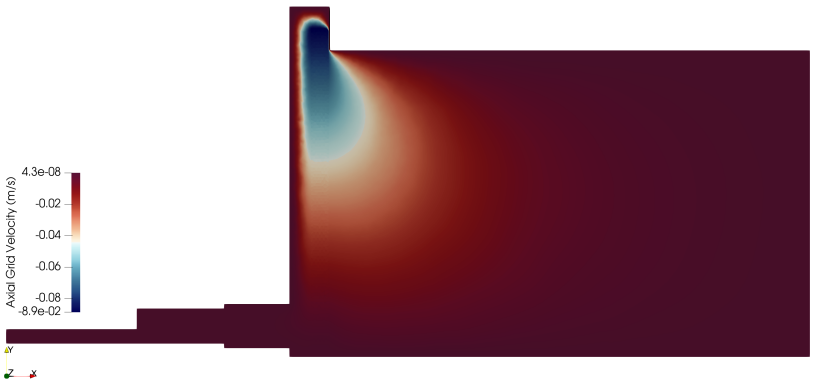

Figure 6.6: rotor mode shape matching the axial grid velocity.

Regarding mesh management and deformation, re-meshing was not necessary as the Laplacian smoothing method was able to handle the small amplitude of vibration without compromising the quality of the mesh. Figure 6.7 shows snapshots of the mesh quality near the upper valve clearance where the amplitude of vibration is important. In this case, the mesh quality is evaluated based on the cell aspect ratio that is calculated by dividing the length of the longest edge for a given cell by the length of the shortest edge of this cell. This criterion measures how stretched or distorted a tetrahedral element is. For a good-quality mesh, it is desirable to have tetrahedral elements with aspect ratios as close to 1 as possible. A value of 1 indicates that the tetrahedron is as close to a regular tetrahedron (equilateral) as possible, and the element is not distorted. In this case more than 90 % of cells maintain an aspect ratio below 2.5 over one period of vibration. This means that this quality is maintained between the initial disc position and the maximum amplitude of vibration indicating that mesh distortion is seen to be negligible. Further away from the shroud and towards the hub, the cells barely deform and are intact at the fixed extremity.

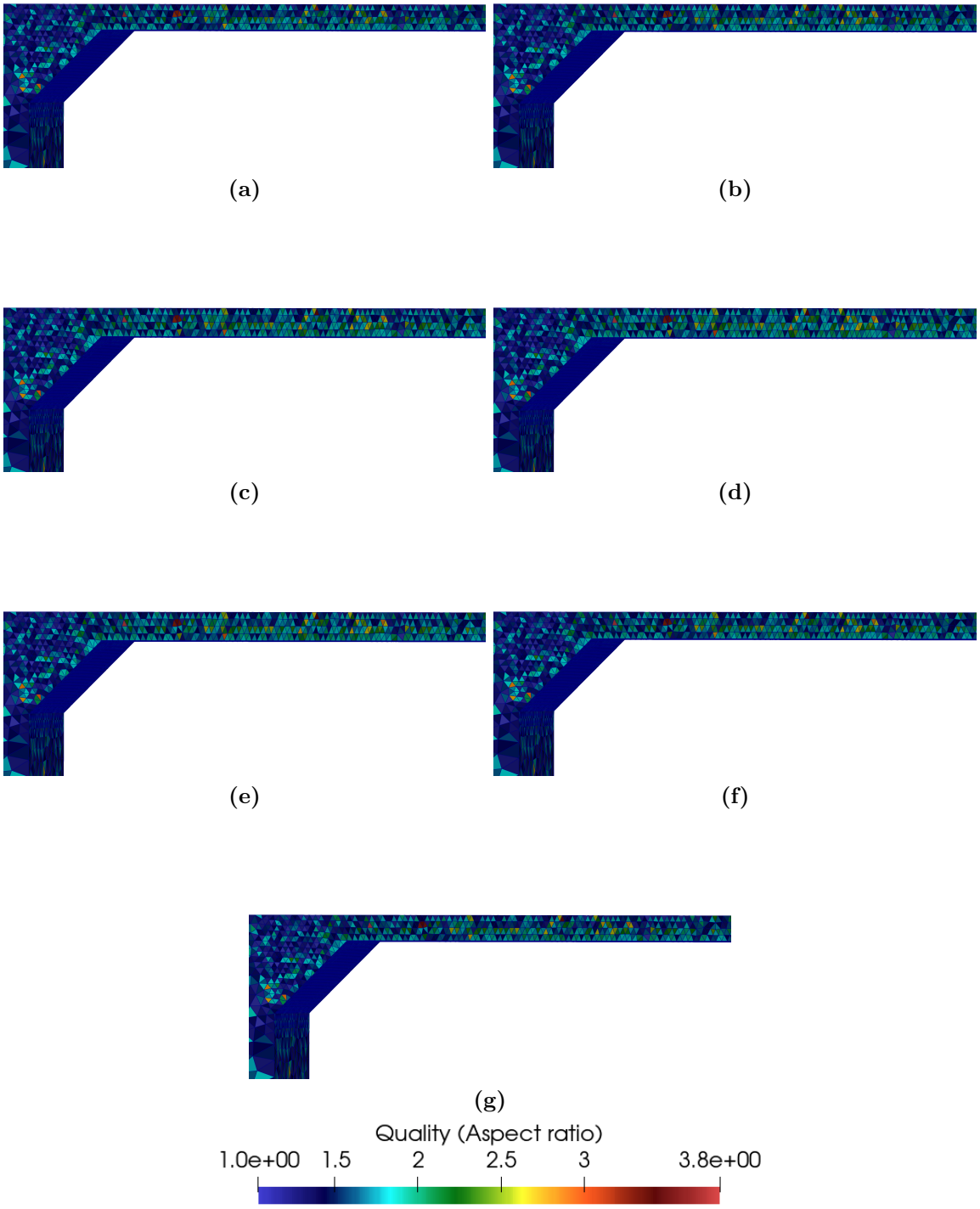

Figure 6.7: Snapshots of the mesh deformation near the upper valve over one period of disk vibration .

It is worth noting that in the current geometry the radial and azimuthal displacements are negligible compared to the axial displacement. Similar to the previous simulations, the evolution of the axial tip displacement is recorded at the flow limit cycle and shown on Fig. 6.8. As hinted previously, the axial disk displacement oscillates around its mean deflection between a maximal $U_{R(max)}$ and minimal value $U_{R(min)}$. For the current operating conditions, a frequency of vibration is found to be equal to the first natural frequency of the rotor disk $f^*_{d_{0ND}}$. Recall that here the amplitude of vibration is stabilized by calculating the amount of material dissipation required by the disk. This damping rate was determined via trial and error while estimating the appropriate damping stiffness matrix coefficient η_k. A damping rate of 2.25% was found to be required to stabilize the axial balancing system. Note that a slightly lower rate of 2.1% was obtained by Brunier-Coulin *et al.* (2022) during ping test experiments.

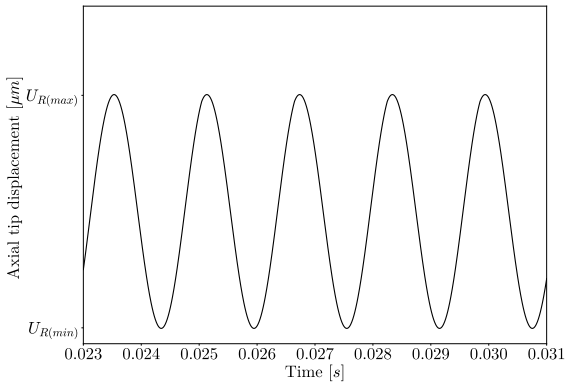

Figure 6.8: Time evolution of the axial tip displacement of the rotor disk with damping.

Before investigating the undamped process, a close focus is given on the effect of disk vibration on the flow dynamics. Recall that in the fluid only simulation where the disk is fixed, the radial component of the flow velocity is constant at the flow limit cycle since the gap opening is held constant yielding a constant mass flow rate crossing the upper valve clearance. For the current setting, the disk vibration leads to a fluctuation of the mass flow rate that is proportional to the gap opening. This phenomenon is then observed to alter the flow dynamics that is entering the housing. To investigate the effect of rotor vibration on the flow, instantaneous snapshots of the velocity streamlines over one period of disc vibration are highlighted on Fig. 6.9. The formation of vortices near the upper valve and housing are present in this case. However, unlike the fluid only simulation (Fig. 2.13), the vortices do not seem to interact meaning that only one instability is present and it is pulsating at a single frequency. To backup this observation, the pressure field is monitored through the same numerical probes as used in the fluid only simulation and a power spectral density is performed using the pressure discrete signals. Results are displayed on Fig. 6.10 showing one dominant frequency $f^* = 1$ across all spectra recorded near the upper valve and housing indicating that the flow oscillates as a whole at a frequency nearly equal the vibration frequency of the rotor confirming the fluid-structure coupling at $f^*_c = f^*_{0_{ND}}$ where f^*_c is the coupled fluid-structure mode frequency.

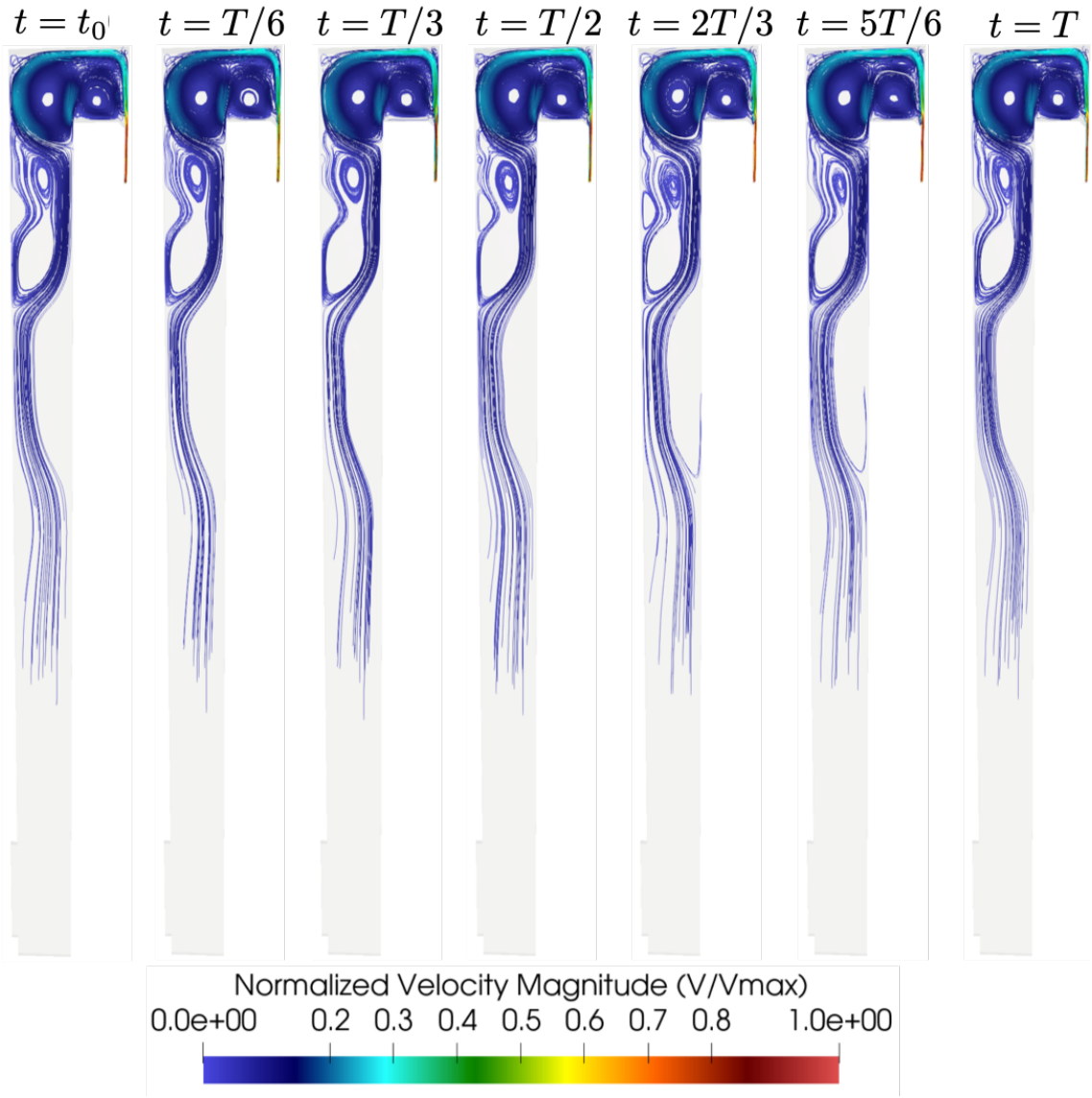

Figure 6.9: Snapshots of the velocity stream plot constituting one period of disk vibration.

It is also noted that the identified fluid-structure mode f_c^* has a frequency equal to the first acoustic mode of the cavity, $f_{ac_1}^*$ evaluated in Chap. 2. This indicates the likelihood of a vibroacoustic phenomenon created by the disk oscillation and the acoustic wave pulsation of the cavity at . To determine the frequency of oscillation that stems from the acoustic pulsation of the flow, a Fast Fourier transform is performed on the discrete pressure fluctuation signal P' that is obtained by subtracting the mean flow pressure from the instantaneous flow pressure. In such a case and to specifically target acoustics, the pressure time data is recorded at two points widely separated from the housing toward the hub and further downstream close to the outlet when the flow limit cycle has already

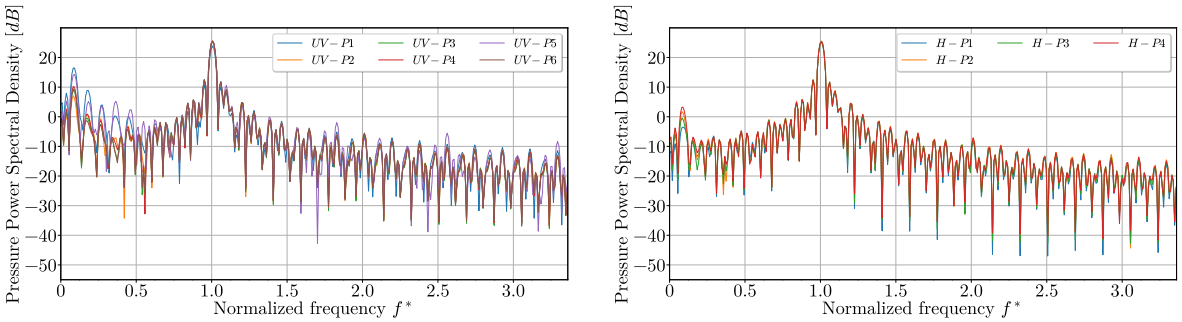

(a) **(b)**

Figure 6.10: Pressure power spectral densities computed at (a) upper valve and (b) housing.

been attained. Results are shown on Fig. 6.11. Two dominant frequencies are clearly identified in both spectra and are both equal to 1: *i.e.*, the frequency of the first natural acoustic mode of the cavity, $f^*_{ac_1}$, confirming the coupling between the hydraulic oscillator created by the upper valve and the acoustic pulsation of the cavity.

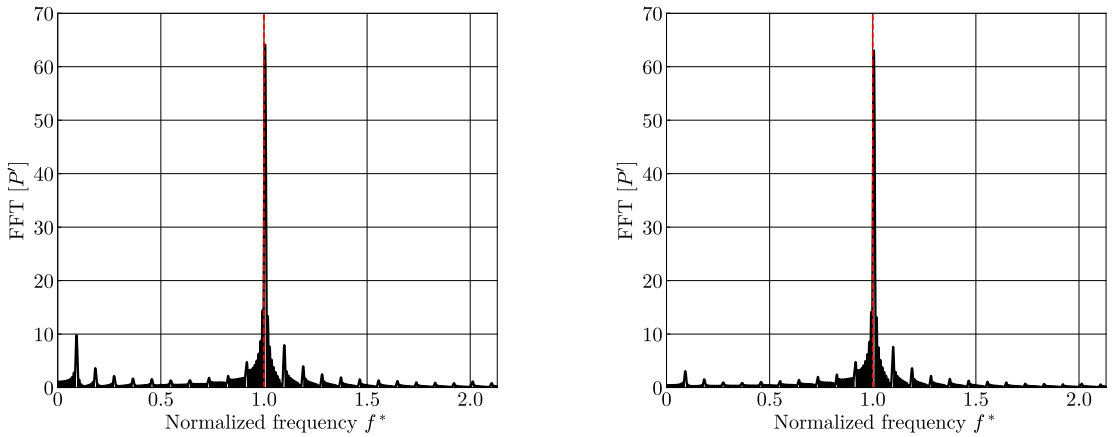

(a) **(b)**

Figure 6.11: FFT performed on the pressure fluctuation P' in the housing near (a) the hub and (b) near the outlet. (The dashed red line represents the first natural acoustic frequency of the cavity).

This acoustic mode can be further illustrated by performing a DMD on a set of instantaneous solutions P' sampled from the converged signal. Figure 6.12 shows the DMD extraction with real and imaginary parts of the DMD mode at $f^* = 1$. The two fields are shown to be identical to the pressure magnitude and phase shapes of the natural acoustic frequency of the cavity. This confirms that the acoustic pulsation has been excited by the coupled fluid-structure mode.

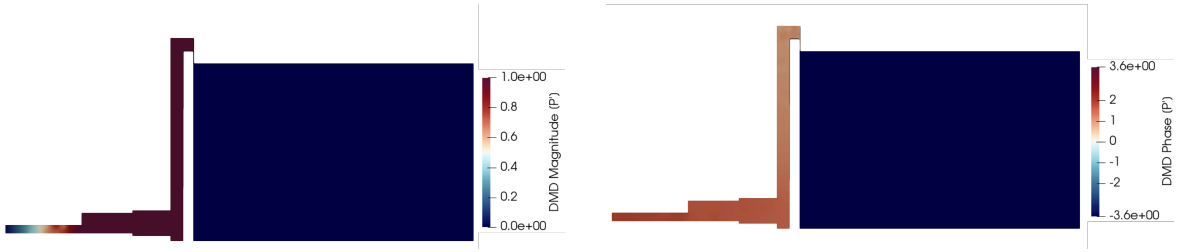

(a) **(b)**

Figure 6.12: Dynamic mode decomposition performed on P'. (a) Magnitude and (b) Phase

Note that all results to this point have been obtained for vibration levels that are controlled: *i.e.*, with the presence of damping. This allowed the identification of the correct flow limit cycle with the $0ND$ mode recovered for the disk and forming a fluid-structure mode causing the disk to vibrate at its natural frequency which coincides with the natural acoustic frequency of the cavity. Note that in this study, the initial upper valve clearance and the inlet mass flow rate are not varied. The inlet mass flow rate is however known to be a crucial parameter that dictates the stability the axial balancing system. Based on the experiments of Brunier-Coulin *et al.* (2022) and URANS simulations of Deneuve *et al.* (2020), it is possible to determine the critical mass flow rate as a function of the upper valve clearance corresponding to the mean axial deflection of the disk. This critical mass flow rate indeed constitutes a threshold beyond which the system becomes unstable. Figure 6.13 summarizes the evolution of the critical mass flow rate values for each valve opening determined via experiments. All eventual operating points that lie above the critical mass flow rate curve constitute an unstable configuration, conversely all the operating points that lie below the critical mass flow rate curve lead to a stable configuration. URANS and LES operating points for the current case are also added and are observed to be in close proximity. These two points correspond to damped cases even though they lie above the experimentally obtained critical mass flow rate curve.

To investigate an unstable operation of this configuration, a simulation is detailed for which damping is suppressed. To do so, at approximately $t = 0.0315\,s$ of the previous prediction, damping is removed. Figure 6.14 illustrates the corresponding response which clearly indicates that the amplitude of the vibration starts amplifying in time when the structure is undamped. This unsteady process will subsequently alter the axial gap height which can also affect the unsteady loop (unsteady forces leading to unsteady disk vibration). Such a scenario shares similarities with the labyrinth seal aeroelastic instability described by Abbott (1981). Indeed, Alford (1965) pointed out that this phenomenon could also introduce energy into the vibrating system and cause fatigue and eventually failure. The gradual increase of the disk axial tip displacement beyond its previously reached maximum amplitude will eventually lead in this case to a contact with the housing. Such a destabilization of the axial balancing system is in fact expected since

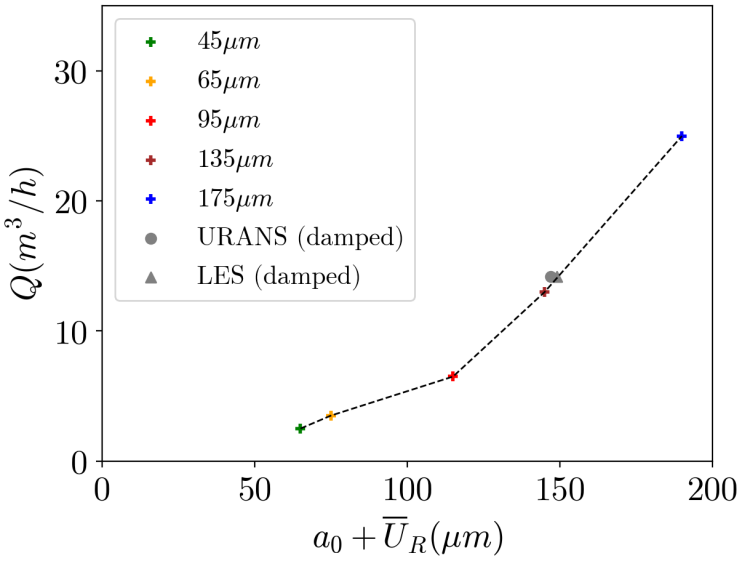

Figure 6.13: Scatter plot highlighting the critical mass flow rate for each upper valve clearance determined by the experiments of Brunier-Coulin *et al.* (2022). Each color represent an initial valve clearance. Data points marked in (+) correspond to experiments while (△) and (•) correspond to damped LES and URANS simulations.

no damping is present and the critical flow rate for this configuration $Q_{crit} = 0.37 Q_{max}$ is below the current inlet flow rate set to $Q_{in} = 0.40 Q_{crit}$. This explains the unstable behavior of the rotor disk. It is thus critical to well estimate such quantities and their effect on flows.

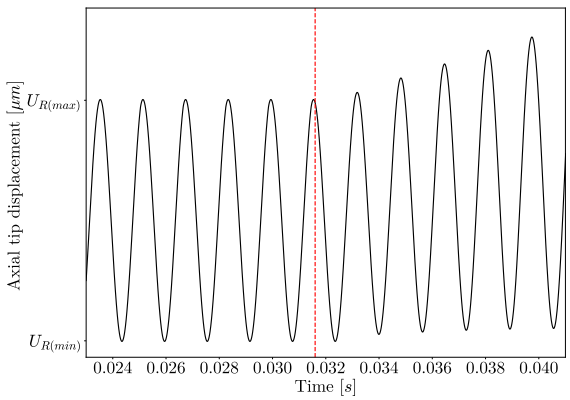

Figure 6.14: Time evolution of the axial tip displacement of the rotor disk (the dashed red line indicates the time at which damping is removed).

6.4 Conclusion

This chapter presents the significant impact of rotor disk vibration on the axial balancing system of a first-stage rotodynamic pump. It also emphasizes the crucial need to simulate multiphysical phenomena to accurately capture such flow and structure dynamics. The study also demonstrates the capability of the developed FSI solver to handle complex turbomachinery applications, particularly in the context of the present LES tool. In terms of industrial use, such a capability allows for the evaluation of the structural damping rate, a vital parameter in structural design to prevent resonance or potential mode coupling with the flow. Using the new FSI tool, the study identifies a vibroacoustic phenomenon as the source of the instability of the axial balancing system. To mitigate this phenomenon, one can shift the natural frequency of the structure away from the natural acoustic frequency of the cavity. One approach could be to adjust the disk thickness, among other ways. However, this adjustment may lead to disk vibrations at higher nodal diameters which should then be checked to avoid coinciding with the natural acoustic modes of the cavity. It's worth noting that in such specific cases, simulating the complete rotodynamic pump geometry is necessary since the absence of axisymmetry (the $0ND$ node is axisymmetric) prohibits the use of periodic boundary conditions. Consequently, these cases become computationally expensive and fall beyond the scope of the present work but can be considered for a future study.

Chapter 7

Mode identification through a global linear stability analysis

Contents

Understanding and predicting flow instabilities are vital for designing efficient and stable fluid systems. Flow instabilities refer to deviations from a smooth and predictable fluid motion, often leading to complex and turbulent flow patterns. The transition from a laminar to a turbulent flow is a common type of instability, occurring when fluid velocity exceeds critical thresholds or encounters disturbances. This transition is characterized by the formation of eddies, vortices, and fluctuations in velocity and pressure as seen in LES of the fluid flow of the rotodynamic pump. Rotating enclosed cavity flows at high Reynolds numbers however exhibit different forms of instabilities that are intrinsically three dimensional and more complex. These furthermore dominate the cavity with the potential apparition of multiple frequencies. Fluid flows can also exhibit self-sustained oscillations whose origin may differ from previously discussed ones. Typically, fluid-structure interaction often yields vortex-induced vibrations seen for example in axial balancing systems. The present chapter details a global linear stability framework that provides a mean to identify hydrodynamic instabilities that arise at the flow limit cycle of the aforementioned applications. Results obtained by the global linear stability analysis confirm the retrieved dynamics by LES and DMD.

7.1 Historical perspectives around instabilities

Hydrodynamics stability has been recognised as one of the most complex and fundamental subject in fluid mechanics. The laminar flow breakdown, development and eventual transition to turbulence intrigued scientists for more than a century to this date. Flow stability has many applications in engineering, meteorology, astrophysics.. . The core problem of hydrodynamic stability was formulated and analyzed notably by Helmholtz, Kelvin, Rayleigh and Reynolds. The latter is famously known for the "Reynolds experiment" Reynolds (1883) where a set of experiments shows that the laminar flow inside a pipe breaks down when V_a/ν exceeds a certain critical value where V_a is the fluid velocity and ν is the kinematic viscosity of the fluid (see Fig. 7.1(a)). This non-dimensional number is known as the Reynolds Number. Other instabilities were later identified by scientists. For instance, two fluids flowing at different velocities and densities, one stream above the other can create a shear velocity leading to an instability (Fig. 7.1(b)). Indeed, Helmholtz (1868) remarked that "every perfect geometrically sharp edge by which a fluid flows must tear it asunder and establish a surface of separation, however slowly the rest of the fluid may move". This type of instability was initially posed and solved by Kelvin (1871) and it is now known as Kelvin-Helmholtz instability. Similarly, such an instability can occur at the interface between two fluids of different densities (Fig. 7.1(c)). In such a case, the instability is driven by the interplay of buoyancy and acceleration and can lead to the mixing and a transition to turbulence of the fluids. This instability is known as the Rayleigh-Taylor instability (Rayleigh (1883)), named after Lord Rayleigh and G. I. Taylor, who independently studied and described the phenomenon.

The hydrodynamic instability of interest to the present thesis is the transition oc-

(a) **(b)** **(c)**

Figure 7.1: Example of hydrodynamic instabilities: (a) The Reynolds experiment, (b) Kelvin-Helmholtz instability, (c) Rayleigh-Taylor instability.

curring in the so-called oscillator flows for which modes of oscillations can be identified. Figure 7.2 displays two such forms of this instabilities. For instance, in Fig. 7.2(a) the conditional stability of a flow around a rigid circular cylinder is determined by its flow Reynolds number. Indeed, it is now known that a bifurcation occurs at $Re \approx 47$ with an unsteady von Kármán vortex wake, below this Reynolds number, the flow being steady. Such a transition occurs also in rotodynamic pump housings when the flow exiting the upper valve clearance becomes unsteady with the creation of large vortex structures along with fluctuations of velocity and pressure. Rotating flow instabilities occur at high Reynolds numbers and such instabilities can be observed in galactic spirals as well as in flows above rotating discs. The transition in these type of flows is governed by instabilities that arise within the rotating boundary layer and are usually identified by three-dimensional spirals and/or concentric vortices.

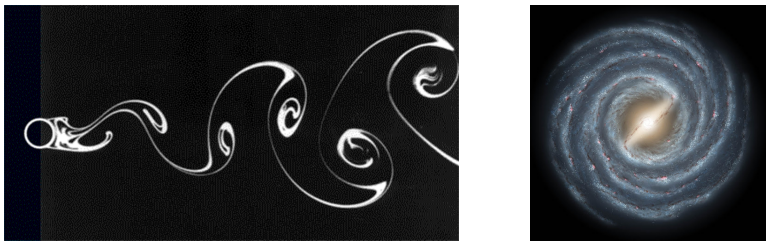

(a) **(b)**

Figure 7.2: (a) von Kármán vortex street forming behind a rigid circular cylinder at $Re = 140$ (Gedikli (2014)), (b) Rotational instability observed in galaxies.

Elastic solids can also be subject to instabilities under certain conditions. These arise due to the interplay between the material properties, geometrical factors and external loading. Instabilities of elastic solids usually refer to situations where the equilibrium state of the solid becomes unstable and small perturbations can cause significant changes in the material's behavior. One common example of such an instability is buckling. Buckling occurs when a slender structure, such as a column or beam, is subject to compressive forces and undergoes sudden, uncontrollable lateral deflection. The critical buckling load is typically lower than the load required to cause material failure in compression. The reader can refer to the book of Timoshenko & Gere (2012) for a complete review about

this phenomenon. Another example is the wrinkling or folding of thin elastic sheets under compressive or shear forces. This phenomenon is often observed in materials like paper or metal foils. Wrinkling can occur when the applied forces exceed the material's resistance to bending or stretching, leading to the formation of localized deformations and instability in the sheet. The behavior of elastic solids and the occurrence of instabilities can be analyzed using various mathematical and computational methods. For example, finite element and stability analysis, all can help predict and understand the response of these materials under different loading conditions. Note that solid instabilities tend to be easier to analyse compared to flow instabilities and can be easily identified.

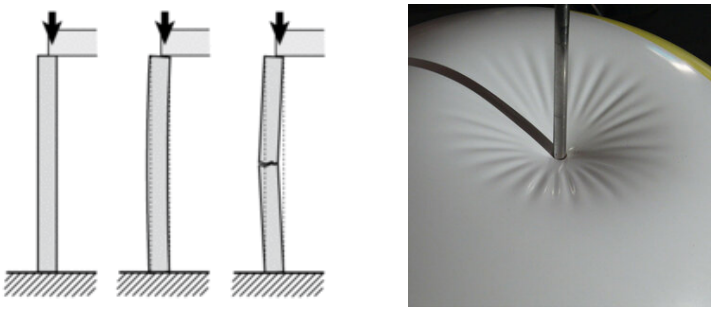

(a) **(b)**

Figure 7.3: (a) Structure failure due to buckling, (b) Wrinkling of an elastic shell due to applied pressure.

When a flow interacts with a deformable structure, Fluid-structure instabilities may occur. Contrarily to previously discussed cases, these instabilities arise due to the coupling between the fluid and structure, the fluid exerting forces on the structure causing its deformations which in turn deform the fluid flow. Note that in such a coupled multiphysics problem, even if the flow and the deformable structure do not express any unstable behavior for the respective individual conditions, their interaction may yield a coupled instability. The multiphysics aspect of such instability can occur in various forms. One of these is the Vortex-Induced Vibrations (VIV) as seen in the FSI case of the elastic plate attached to the rigid square application and the homogeneous energy harvesting device of Fig. 7.4(a). As vortices shed from the structure in the wake region, they create alternating lift and drag forces that cause the structure to vibrate. When it comes to engineering applications, one of the most classical example of aeroelastic instability that arises in aerodynamic applications is flutter (Fig. 7.4(b)). It occurs when the coupling between the fluid forces and the structural deformations leads to self-excited, limit cycle oscillation which often cause structural damage or even catastrophic failure if not properly controlled.

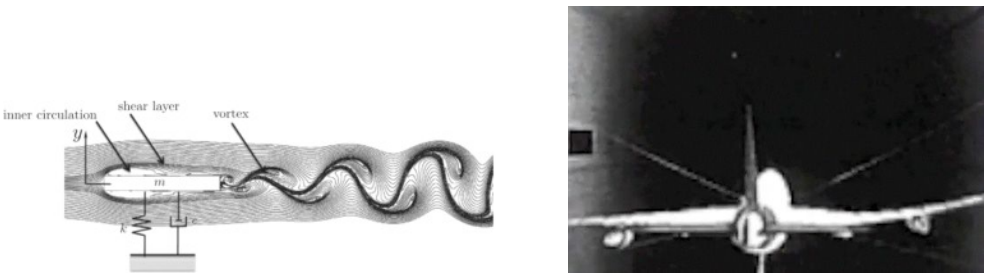

(a) **(b)**

Figure 7.4: (*a*) Energy harvesting device via vortex-induced vibration, (*b*) Wing flutter test of an airplane model.

7.2 Mathematical framework

A dynamical system can be described by a set of equations that govern the evolution of its variables over time. In such cases, if one lets $\boldsymbol{q}(\boldsymbol{x}, t)$ be a state vector function of time t and the space coordinate $\boldsymbol{x}$, while $\boldsymbol{F}$ is a non-linear operator, the dynamic system can be simply described by,

$$\frac{\partial \boldsymbol{q}}{\partial t} = \boldsymbol{F}(\boldsymbol{q}), \tag{7.2.1}$$

In the context of fluid dynamics, the state vector is the vector comprising the Navier-Stokes variables, *i.e.*, density, velocity components and flow pressure. For such problems, the first step is the evaluation of the equilibrium state of the system. That is to compute the base state vector $\boldsymbol{Q}$ which is solution of Eq. (7.2.1), with,

$$\boldsymbol{F}(\boldsymbol{Q}) = 0, \tag{7.2.2}$$

Then by using small-amplitude pertubations that are also solution to Eq. (7.2.1), the state vector $\boldsymbol{q}$ can be decomposed into a steady term $\boldsymbol{Q}$ and a fluctuation term $\boldsymbol{q}'$ such that,

$$\boldsymbol{q}(\boldsymbol{x}, t) = \boldsymbol{Q}(\boldsymbol{x}) + \epsilon \boldsymbol{q}'(\boldsymbol{x}, t), \tag{7.2.3}$$

ϵ being an infinitesimal term ($\epsilon \ll 1$). Injecting this decomposition into the non-linear evolution Equation (7.2.1), a linearized version can be obtained,

$$\frac{\partial \boldsymbol{q}'}{\partial t} = \boldsymbol{F}'(\boldsymbol{Q} + \boldsymbol{q}'), \tag{7.2.4}$$

where $\boldsymbol{F}'$ is the linearized non-linear operator around the base state $\boldsymbol{Q}$ that is approximated as,

$$\boldsymbol{F}(\boldsymbol{Q} + \boldsymbol{q}') = \boldsymbol{F}(\boldsymbol{Q}) + \nabla \boldsymbol{F}(\boldsymbol{Q}) \cdot (\boldsymbol{q} - \boldsymbol{Q}) + \mathcal{O}(\|\boldsymbol{q}\|^2). \tag{7.2.5}$$

Neglecting higher order terms, Eq. (7.2.5) can be approximated by,

$$\boldsymbol{F}(\boldsymbol{Q} + \boldsymbol{q}') \approx \nabla \boldsymbol{F}(\boldsymbol{Q}) \cdot \boldsymbol{q}', \tag{7.2.6}$$

so the final linearized form of Eq. (7.2.1) becomes,

$$\frac{\partial \boldsymbol{q}'}{\partial t} = \nabla \boldsymbol{F}'(\boldsymbol{Q}) \cdot \boldsymbol{q}'. \tag{7.2.7}$$

which can be recast into the following compact form,

$$\boldsymbol{B}\frac{\partial \boldsymbol{q}'}{\partial t} = \boldsymbol{J}\boldsymbol{q}'. \tag{7.2.8}$$

In (7.2.8) $\boldsymbol{B}$ is a matrix and $\boldsymbol{J}$ is the Jacobian operator. Note that Eq. (7.2.8) describes the evolution of an infinitesimal perturbation in time and the problem can be solved if appropriate initial and boundary conditions are provided. That is,

$$\begin{cases} \boldsymbol{q}'(\boldsymbol{x}, t=0) = \boldsymbol{q}'_0, \\ \mathcal{L}\boldsymbol{q}'(\boldsymbol{x}_0, t) = 0 \in \partial\mathcal{D}. \end{cases} \tag{7.2.9}$$

The stability analysis around the base flow can be achieved by the mean of different methods depending on the nature of the base flow used: A local stability analysis that uses the parallel flow assumption or global linear stability analysis that is used for $2D$ and $3D$ flows with a non-parallel flow assumption. The linearization process of the equations involved are presented in the upcoming sections followed by a brief description of the two theories. Note that these equations describe only the fluid problem since the study is limited to flow modes. Nevertheless, several case studies already discussed in the thesis including forced flow problems and fluid structure interaction are considered within the framework of global stability theory, which is the main scope of this chapter.

7.2.1 flow linearized equations

The linearization process of the incompressible Navier-Stokes equations is considered in this section. This process relies on the decomposition of the flow quantities into a steady part, usually called base flow, and an unsteady part such that,

$$\begin{cases} \boldsymbol{u}(\boldsymbol{x}, \boldsymbol{y}, \boldsymbol{z}, t) &= \boldsymbol{U}(\boldsymbol{x}, \boldsymbol{y}, \boldsymbol{z}) + \boldsymbol{u}'(\boldsymbol{x}, \boldsymbol{y}, \boldsymbol{z}, t), \\ p(\boldsymbol{x}, t) &= P(\boldsymbol{x}, \boldsymbol{y}, \boldsymbol{z}) + P'(\boldsymbol{x}, \boldsymbol{y}, \boldsymbol{z}, t). \end{cases} \tag{7.2.10}$$

In Eq. (7.2.10) P and $\boldsymbol{U}$ stand for the base flow solutions of the steady Navier-Stokes equations while p' and $\boldsymbol{u}'$ represent respectively the pressure and velocity perturbations. Injecting Eqs. (7.2.10) into the Navier-Stokes and continuity equations one obtains,

$$\begin{cases} \nabla \cdot (\mathbf{U} + \mathbf{u}') = 0, \\ \dfrac{\partial(\mathbf{U} + \mathbf{u}')}{\partial t} + [(\mathbf{U} + \mathbf{u}') \cdot \nabla](\mathbf{U} + \mathbf{u}') = -\nabla(P + p') + \dfrac{1}{Re}\Delta(\mathbf{U} + \mathbf{u}'). \end{cases} \tag{7.2.11}$$

Developing this system of equations, one obtains the base flow which satisfies the steady Navier-Stokes and continuity equations and read,

$$\begin{cases} \nabla \cdot \mathbf{U} = 0, \\ (\mathbf{U} \cdot \nabla)\mathbf{U} = -\nabla P + \dfrac{1}{Re}\Delta\mathbf{U}. \end{cases} \tag{7.2.12}$$

The remaining part composes the perturbed Navier-Stokes and continuity equations. That is,

$$\begin{cases} \nabla \cdot \mathbf{u}' = 0, \\ \dfrac{\partial \mathbf{u}'}{\partial t} + (\mathbf{U} \cdot \nabla)\mathbf{u}' + (\mathbf{u}' \cdot \nabla)\mathbf{U} = -\nabla p' + \dfrac{1}{Re}\Delta \mathbf{u}' + (\mathbf{u}' \cdot \nabla)\mathbf{u}'. \end{cases} \tag{7.2.13}$$

Assuming an infinitesimal perturbation, the second-order term $(\mathbf{u}' \cdot \nabla)\mathbf{u}'$ can be dropped and the Linearized Navier-Stokes equations results,

$$\begin{cases} \nabla \cdot \mathbf{u}' = 0, \\ \dfrac{\partial \mathbf{u}'}{\partial t} + (\mathbf{U} \cdot \nabla)\mathbf{u}' + (\mathbf{u}' \cdot \nabla)\mathbf{U} = -\nabla p' + \dfrac{1}{Re}\Delta \mathbf{u}'. \end{cases} \tag{7.2.14}$$

Governing equations for a three dimensional flow

Recasting the linearized Navier-Stokes equations (7.2.15) in the normal coordinate system $(\mathbf{x}, \mathbf{y}, \mathbf{z})$, one obtains the following scalar equations,

$$\begin{cases} \dfrac{\partial u_x'}{\partial x} + \dfrac{\partial u_y'}{\partial y} + \dfrac{\partial u_z'}{\partial z} = 0 \\ \dfrac{\partial u_x'}{\partial t} + U_x\dfrac{\partial u_x'}{\partial x} + U_y\dfrac{\partial u_x'}{\partial y} + U_z\dfrac{\partial u_x'}{\partial z} + u_x'\dfrac{\partial U_x}{\partial x} + u_y'\dfrac{\partial U_x}{\partial y} + u_z'\dfrac{\partial U_x}{\partial z} = -\dfrac{\partial p'}{\partial x} + \dfrac{1}{Re}\Delta u_x' \\ \dfrac{\partial u_y'}{\partial t} + U_x\dfrac{\partial u_y'}{\partial x} + U_y\dfrac{\partial u_y'}{\partial y} + U_z\dfrac{\partial u_y'}{\partial z} + u_x'\dfrac{\partial U_y}{\partial x} + u_y'\dfrac{\partial U_y}{\partial y} + u_z'\dfrac{\partial U_y}{\partial z} = -\dfrac{\partial p'}{\partial y} + \dfrac{1}{Re}\Delta u_y' \\ \dfrac{\partial u_z'}{\partial t} + U_x\dfrac{\partial u_z'}{\partial x} + U_y\dfrac{\partial u_z'}{\partial y} + U_z\dfrac{\partial u_z'}{\partial z} + u_x'\dfrac{\partial U_z}{\partial x} + u_y'\dfrac{\partial U_z}{\partial y} + u_z'\dfrac{\partial U_z}{\partial z} = -\dfrac{\partial p'}{\partial z} + \dfrac{1}{Re}\Delta u_z' \end{cases} \tag{7.2.15}$$

Governing equations for a three dimensional rotating flow

Rotating flow problems are treated in the (r, θ, z) coordinate system. Their corresponding governing equations are constructed following the same procedure as the previous section. Assuming infinitesimal perturbations, instantaneous flow quantities are decomposed into the sum of the steady state and deviation so,

$$\begin{cases} \boldsymbol{u}(\boldsymbol{r}, \boldsymbol{z}, t) & = \boldsymbol{U}(\boldsymbol{r}, \theta, \boldsymbol{z}) + \boldsymbol{u}'(\boldsymbol{r}, \boldsymbol{\theta}, \boldsymbol{z}, t), \\ p(\boldsymbol{r}, \boldsymbol{\theta}, \boldsymbol{z}, t) & = P(\boldsymbol{r}, \boldsymbol{\theta}, \boldsymbol{z}) + P'(\boldsymbol{r}, \boldsymbol{\theta}, \boldsymbol{z}, t). \end{cases} \tag{7.2.16}$$

where p and $\mathbf{u}' = (\mathbf{u}_\mathbf{r}', \mathbf{u}_\theta', \mathbf{u}_\mathbf{z}')$ represent respectively the pressure and velocity perturbations while $\mathbf{U} = (\mathbf{U}_\mathbf{r}, \mathbf{U}_\theta, \mathbf{U}_\mathbf{z})$ stands for the base flow solution of the Navier-Stokes equations.

After linearizing the Navier-Stokes equations around the base flow and injecting the above decomposition, the following systems of equations in the cylindrical-polar coordi-

nates (r, θ, z) is obtained:

$$\begin{cases} \frac{1}{r}\frac{\partial r u_r'}{\partial r} + \frac{1}{r}\frac{\partial u_\theta'}{\partial \theta} + \frac{\partial u_z'}{\partial z} = 0 \\ \frac{\partial u_r'}{\partial t} + U_r\frac{\partial u_r'}{\partial r} + \frac{U_\theta}{r}\frac{\partial u_r'}{\partial \theta} + U_z\frac{\partial u_r'}{\partial z} + u_r'\frac{\partial U_r}{\partial r} + \frac{u_\theta'}{r}\frac{\partial U_r'}{\partial \theta} + u_z'\frac{\partial U_r}{\partial z} - \frac{2U_\theta u_\theta'}{r} = \\ -\frac{1}{\rho}\frac{\partial p'}{\partial r} + \nu(\frac{\partial^2 u_r'}{\partial z^2} + \frac{\partial^2 u_r'}{\partial r^2} + \frac{1}{r^2}\frac{\partial^2 u_r'}{\partial \theta^2} + \frac{1}{r}\frac{\partial u_r'}{\partial r} - \frac{u_r'}{r^2} - \frac{2}{r^2}\frac{\partial u_\theta'}{\partial \theta}) \\ \frac{\partial u_\theta'}{\partial t} + U_r\frac{\partial u_\theta'}{\partial r} + \frac{U_\theta}{r}\frac{\partial}{\partial u_\theta'} + U_z\frac{\partial u_\theta'}{\partial z} + u_r'\frac{\partial U_\theta}{\partial r} + \frac{u_\theta'}{r}\frac{\partial U_\theta}{\partial \theta} + u_z'\frac{\partial U_\theta}{\partial z}\frac{U_r u_\theta'}{r} + \frac{u_r' V_b}{r} = \\ -\frac{1}{r\rho}\frac{\partial p'}{\partial \theta} + \nu(\frac{\partial^2 u_\theta'}{\partial z^2} + \frac{\partial^2 u_\theta'}{\partial r^2} + \frac{1}{r^2}\frac{\partial^2 u_\theta'}{\partial \theta^2} + \frac{1}{r}\frac{\partial u_\theta'}{\partial r} - \frac{u_\theta'}{r^2} - \frac{2}{r}\frac{\partial u_\theta'}{\partial \theta}) \\ \frac{\partial u_z'}{\partial t} + U_r\frac{\partial u_z'}{\partial r} + \frac{U_\theta}{r}\frac{\partial u_z'}{\partial \theta} + U_z\frac{\partial u_z'}{\partial z} + u_r'\frac{\partial U_z}{\partial r} + \frac{u_\theta'}{r}\frac{\partial U_z}{\partial \theta} + u_z'\frac{\partial U_z}{\partial z} = \\ -\frac{1}{\rho}\frac{\partial p'}{\partial z} + \nu(\frac{\partial^2 u_z'}{\partial z^2} + \frac{\partial^2 u_z'}{\partial r^2} + \frac{1}{r}\frac{\partial u_z'}{\partial r} + \frac{1}{r^2}\frac{\partial^2 u_z'}{\partial \theta^2}) \end{cases} \quad (7.2.17)$$

the set of equations can be reformulated in the following linear problem,

$$\mathbf{B}\frac{\partial \hat{\mathbf{q}}}{\partial t} = \mathbf{J}\hat{\mathbf{q}}, \quad (7.2.18)$$

where $\mathbf{B}$ and $\mathbf{J}$ are a matrix and the Jacobian operator respectively and $\hat{\mathbf{q}} = (\mathbf{u}, p)^T$ is a vector containing all the perturbed Navier-Stokes variables. The stability analysis around the base flow $\mathbf{U}$ is then given by the spectrum of eigenvalues of the matrix $\mathbf{J}$. In general, the solution vector $\hat{\mathbf{q}}$ is assumed to be harmonic. This means that a Fourier decomposition in the complex space is possible. Note that for $3D$ problems, it is possible to calculate $3D$ eigenmodes but it is computationally expensive. That said, if the base flow is planar *i.e.*, invariant in the z direction, a Fourier decomposition can be applied in the cross-stream direction z. Similarly, for an axisymmetric rotating flow, a Fourier decomposition can be applied along θ since the base flow is invariant in the azimuthal direction. More details on this decomposition in given in the following sections.

7.3 Different types of stability analyses

In this section, the two most prominent flow stability analyses are discussed: Local stability analysis and global stability analysis. The normal mode or Fourier decomposition associated to the flow perturbation variables is dependent on the analysis to be conducted. Indeed, the base flow and infinitesimal perturbation spatial dimensions are directly linked to the type of linear stability analysis applied as detailed hereafter.

7.3.1 Local stability analysis

Local stability analysis is valid under the parallel flow assumption or when the flow varies slowly in a given spatial direction (Kleiser & Zang (1991)): *i.e.*, the fluid flows along a

given path or through a system along parallel streamlines, meaning that there is no crossflow or significant mixing between adjacent streamlines. This assumption is often applied in cases where the flow velocities are low to moderate, and the dimensions of the system are much larger compared to the characteristic length scale of the flow. Under such an assumption, the base flow takes the form of $\mathbf{U} = (U(y), 0, 0)$ (in the normal coordinate system (x, y, z)). Introducing an infinitesimal perturbation around such base flow, the following global decomposition can be applied,

$$\begin{cases} \boldsymbol{u}(\boldsymbol{x}, \boldsymbol{y}, \boldsymbol{z}, t) & = \boldsymbol{U}(\boldsymbol{x}) + \boldsymbol{u}'(\boldsymbol{x}, \boldsymbol{y}, \boldsymbol{z}, t), \\ p(\boldsymbol{x}, t) & = P(\boldsymbol{x}) + P'(\boldsymbol{x}, \boldsymbol{y}, \boldsymbol{z}, t). \end{cases} \tag{7.3.1}$$

The resulting linearized Navier-Stokes equations is hence highly simplified and can be solved by applying the normal mode expansion of the perturbation so that,

$$[u'_x, u'_y, u'_z, p']^T = [\hat{u_x}, \hat{u_y}, \hat{u_z}, \hat{p}]^T(y) e^{i(\alpha x + \beta z) + \omega t}. \tag{7.3.2}$$

In Eq. (7.3.2) α and β are real parameters (wavenumbers) along the streamwise and spanwise directions respectively and $\omega = \omega_r + \omega_i$ is the complex frequency of the normal mode considered. Recasting the linearized Navier-Stokes equations with the above normal mode expansion yields a dispersion relation of the form,

$$D_L(\omega, \alpha, \beta, \hat{q}) = 0 \tag{7.3.3}$$

Which characterizes the local stability of modes. This approach has been widely used well over a century (Drazin & Reid (1982); Rayleigh (1894)) since it involves few hundreds degrees of freedom. Based on this approach, several types of analyses can be conducted.

Temporal stability analysis

The temporal stability analysis consists of finding the evolution of an infinitesmal perturbation in the flow due to a prescribed spatial excitation. In other words the wavevector $k = \alpha \boldsymbol{x} + \beta \boldsymbol{z}$ is fixed for a set of streamwise and spanwise wavenumbers along the unit vectors $\boldsymbol{x}$ and $\boldsymbol{z}$ respectively. In this context, the sought complex eigenvalue is ω. The corresponding problem is usually simplified using Squire's theorem (Squire & Southwell (1933)),

$$\omega \mathbf{B} \hat{\mathbf{q}} = \boldsymbol{J} \hat{\mathbf{q}}, \tag{7.3.4}$$

In this case, the linear stability of the base flow is dictated by the sign of $\mathfrak{Re}(\omega)$:

- If $\mathfrak{Re}(\omega) < 0$, the perturbation has a negative growth rate hence the base flow is linearly stable.
- If $\mathfrak{Re}(\omega) > 0$, the perturbation has a positive growth rate hence the base flow is linearly unstable.
- If $\mathfrak{Re}(\omega) = 0$, the perturbation is marginally stable and does not change in time.

The temporal analysis is of a great importance when dealing with parallel shear flows with no spatial evolution. The problem is furthermore cheap in terms of computational cost due to the reduced size eigenvalue problem.

Spatial stability analysis

Unlike the temporal stability analysis, the assumption of a fixed wavenumber is relaxed here. In this context, the solution of the linearized Navier-Stokes equations is sought by prescribing a real frequency ω, treating α as the complex eigenvalue hence dropping β. From a numerical point of view, the resulting problem can be recast into a non-linear eigenvalue problem in α such that,

$$\boldsymbol{A}\hat{\mathbf{q}} + \alpha\boldsymbol{B}\hat{\mathbf{q}} + \alpha^2\boldsymbol{C}\hat{\mathbf{q}} = 0, \tag{7.3.5}$$

where $\boldsymbol{A}$, $\boldsymbol{B}$ and $\boldsymbol{C}$ are matrices containing the terms that stem from the linearized Navier-Stokes equations (the reader can refer to the thesis of Loiseau (2014) for the complete derivation). Since the eigenvalue problem (7.3.5) is quadratic in α, solving it is numerically and computationally expensive. To overcome this issue, the problem is instead re-written in the following form,

$$\mathbf{B} = \begin{pmatrix} \mathbf{A} & \mathbf{B} \\ 0 & 1 \end{pmatrix} \begin{pmatrix} \hat{\mathbf{q}} \\ \alpha\hat{\mathbf{q}} \end{pmatrix} = \alpha \begin{pmatrix} 0 & -\mathbf{C} \\ 1 & 0 \end{pmatrix} \begin{pmatrix} \hat{\mathbf{q}} \\ \alpha\hat{\mathbf{q}} \end{pmatrix}. \tag{7.3.6}$$

Again the stability of the perturbation is determined by looking at the sign of the obtained $\mathfrak{Re}(\alpha)$. If $\mathfrak{Re}(\alpha) > 0$ else if $\mathfrak{Re}(\alpha) < 0$ the perturbation decays in space.

Spatio-temporal stability analysis

In the previous two analyses the flow stability was assessed based on an infinitesimal perturbation that grows either in time or space respectively. Nevertheless, there exists some instances where spatially evolving flows develop self-excited modes without external forcing. In this case, both α and ω can be complex so the perturbations are allowed to grow or decay in both time and space. The review of Huerre & Monkewitz (1990) presents a comprehensive reading of this context. They pointed to the different types of instabilities that are obtained using this analysis:

- A flow is said to be convectively unstable if the perturbation generated grows upstream or downstream from a specific region.
- A flow is absolutely unstable if the impulse response propagates upstream and downstream.

Mathematically speaking, a convective instability is characterized by positive temporal growth rate for certain wavenumbers or spatial modes, but there is a critical wavenumber beyond which the temporal growth rate becomes negative. This critical wavenumber represents the fastest-growing mode. Note that, the temporal growth rate of perturbations associated with an absolute instability is positive for all wavenumbers or spatial modes while large wavenumbers modes usually decay in time. This means that all perturbations, regardless of their wavelength or spatial scale, will grow and amplify over time if absolutely unstable, leading to a completely unstable flow.

The eigenvalue problem sought is therein constructed as follows,

$$\begin{cases} \omega_n \mathbf{B}\hat{\mathbf{q}} = \mathbf{J}\hat{\mathbf{q}}, \\ \dfrac{\partial \omega_n}{\partial \alpha} = 0. \end{cases} \tag{7.3.7}$$

where ω_n is the eigenvalue solution of the problem for a given complex wavenumber α. Subsequently, the flow is said to be convectively unstable if $\mathfrak{Im}(\omega_n) < 0$ and absolutely unstable if $\mathfrak{Im}(\omega_n) > 0$. Extensive details about this method and the associated mathematical procedure is provided by Chomaz *et al.* (1991*a*,*b*). Note that, the local stability analysis have been the core work of the Ph.D theses of Queguineur (2020) and Bridel-Bertomeu *et al.* (2016*b*) who extensively studied the origin and development of intrinsic enclosed rotating flows instabilities which lead to the current work. The extension of the method to the present work leads to the so-called *global linear stability analysis* which is the main focus of this chapter. In this context, the parallel flow assumption is relaxed to take into account non-parallel flows that are present in most applications. This approach enables the investigation of $2D$ and $3D$ instability mechanisms of strongly non-parallel flows.

7.3.2 Global linear stability analysis

In a global linear stability analysis, the dynamics of a small amplitude perturbations around the base flow is analyzed while relying on the weakly parallel flow assumption of Theofilis (2011) and Pierrehumbert, R & Widnall (1982). According to Lyapunov (1992), a fluid system can be considered stable if infinitesimal perturbations around the base flow remain infinitesimal over time without growth, or if the perturbed flow remains close to the base flow. It is important to note that linear stability analysis can also provide information about the physical characteristics of these small perturbations such as their frequency and growth rate. These characteristics differ from the ones obtained from a local stability analysis. Indeed, in such approach the complex frequency ω correspond to the global characteristics of a certain global mode. Furthermore, the wavenumber describing a perturbation is strictly a real number meaning that a spatial analysis is not possible with the global approach. The base flow represents the solution of the Navier-Stokes equations modeling a specific system. For instance, analytical solutions can be obtained for simple hydrodynamic problems. Tollmien (1931) and Schlichting (1933) defined the analytical solutions of the Orr-Sommerfeld equations that are derived from the full Navier-Stokes equations by making several simplifying assumptions. One such assumption is that a flat plate boundary layer can be approximated as a parallel flow. If the analytical solution is difficult to obtain, several numerical approaches can be used to calculate the base flow of an unstable configuration like the Selective Frequency Damping method (SFD) proposed by Åkervik *et al.* (2006). For complex flow problems, the mean flow solutions (*i.e.*, time averaged CFD predictions) have emerged as useful alternatives to base flow solutions. In such case, flow non-linearities and the structure of the fluctuations can be predicted by linear stability analyses. Although the mean flow is a statistical construct without inherent meaning, substantial research has been conducted to predict

unsteady features of turbulent flows using the mean flow. Indeed, Zielinska *et al.* (1997) demonstrated that in the present of flow non-linearities, the mean flow becomes significantly different from the base flow rendering the linear stability around the base flow incapable of retrieving flow unsteadiness. As a result, many articles have shown for instance that the mean flow can substitute the base flow under such circumstances (Pier (2002*a*); Mittal (2008); Barkley (2006)). Furthermore, in the case of flow around a cylinder, Pier (2002*b*) showed a very good prediction of the vortex shedding frequency, even far from the critical Reynolds number by using the mean flow. Regarding axisymmetric rotating flows, Queguineur (2020) also succeeded in performing a global local linear stability analysis using the mean flow of an academic rotor/stator cavity. Good agreement was found between the modes predicted by linear stability analysis and the frequencies extracted by large eddy simulation.

Governing equations

Assuming a three dimensional base flow and perturbation vector solutions of the linearized Navier-Stokes equations (7.2.15), a general normal mode decomposition can be applied,

$$[u'_x, u'_y, u'_z, p'] = [\hat{u_x}, \hat{u_y}, \hat{u_z}, \hat{p}]e^{\omega t}. \tag{7.3.8}$$

with $[\hat{u_x}, \hat{u_y}, \hat{u_z}, \hat{p}]$ being the normal mode vector that represents the spatial organization of each mode in the three dimensional space (x, y, z) and ω is its complex frequency such that $\omega = \omega_r + \omega_i$ where ω_r and ω_i represent the real and imaginary parts respectively. If the base flow is strongly dependent on two spatial dimensions and is homogeneous in the third dimension, the global stability analysis can be performed a $2D$ cross section plane containing all three velocity components. Hence, the solution of the linearized Navier-Stokes equations can still be sought in the form of normal modes,

$$[u'_x, u'_y, u'_z, p'] = [\hat{u_x}, \hat{u_y}, \hat{p}]e^{ikz+\lambda t}. \tag{7.3.9}$$

with $[\hat{u_x}, \hat{u_y}, \hat{p}]$ being the normal mode in the $2D$ plane (x, y) and k is its spanwise wavenumber. Injecting this decomposition into the linearized Navier-Stokes equations, a linear generalized eigenvalues problem in ω if formed,

$$\omega \mathbf{B}\hat{\mathbf{q}} = \mathbf{J}\hat{\mathbf{q}}. \tag{7.3.10}$$

In Eq. (7.3.10), $\mathbf{B}$ and $\mathbf{J}$ are a matrix and the Jacobian operator respectively given by,

$$\mathbf{B} = \begin{pmatrix} 1 & 0 & 0 & 0 \\ 0 & 1 & 0 & 0 \\ 0 & 0 & 1 & 0 \\ 0 & 0 & 0 & 0 \end{pmatrix} \tag{7.3.11}$$

, and

$$\mathbf{J} = \begin{pmatrix} -\frac{\partial U_x}{\partial x} - (\mathbf{U}\cdot\nabla) + \frac{1}{Re}\Delta & -\frac{\partial U_x}{\partial y} & 0 & -\frac{\partial}{\partial x} \\ -\frac{\partial U_y}{\partial x} & -\frac{\partial U_y}{\partial x} - (\mathbf{U}\cdot\nabla) + \frac{1}{Re}\Delta & 0 & -\frac{\partial}{\partial y} \\ 0 & 0 & -(\mathbf{U}\cdot\nabla) + \frac{1}{Re}\Delta & -ik \\ \frac{\partial}{\partial x} & \frac{\partial}{\partial y} & ik & 0 \end{pmatrix} \tag{7.3.12}$$

.

Note that, for an axisymmetric rotating flow, the same procedure applies except that in this case the normal decomposition satisfies the linearized Navier-Stokes equation in the cylindrical polar coordinate system (r, θ, z). In this case, the set of equations are homogeneous in the azimuthal direction, hence the normal decomposition writes,

$$[u_r, u_\theta, u_z, p] = [\hat{u}_r, \hat{u}_\theta, \hat{u}_z, \hat{p}](z)e^{(im\theta+\omega t)}. \tag{7.3.13}$$

The normal modes $[u_r, u_\theta, u_z, p]$ are represented by their spatial organization $[\hat{u}_r, \hat{u}_\theta, \hat{u}_z, \hat{p}]$ in the (r, z) plane and by a pair of parameters (m, ω) where m denotes the azimuthal wavenumber that is inherent to cylindrical problems or flows. If the mode is axisymmetric then $m = 0$, if the mode exhibits spiral arms then m corresponds to the number of the spiral pattern identified. ω is a complex frequency so that $\omega = \omega_r + \omega_i$ where ω_r and ω_i represent the real and imaginary parts respectively. The eigenvalue sought is hence obtained by solving the linear eigenvalue problem (7.3.10) for every value of m where $\mathbf{B}$ and $\mathbf{J}$ are a matrix and the Jacobian operator given by,

$$\mathbf{B} = \begin{pmatrix} 1 & 0 & 0 & 0 \\ 0 & 1 & 0 & 0 \\ 0 & 0 & 1 & 0 \\ 0 & 0 & 0 & 0 \end{pmatrix} \tag{7.3.14}$$

, and

$$\mathbf{J} = \begin{pmatrix} -\frac{\partial U_r}{\partial r} - (\mathbf{U}\cdot\nabla) + \nu\Delta & -\frac{\partial U_r}{\partial \theta} & 0 & -\frac{1}{r}\frac{\partial}{\partial r} \\ -\frac{\partial U_\theta}{\partial r} & -\frac{\partial U_\theta}{\partial r} - (\mathbf{U}\cdot\nabla) + \nu\Delta & 0 & -\frac{1}{r}\frac{\partial}{\partial \theta} \\ 0 & 0 & -(\mathbf{U}\cdot\nabla) + \nu\Delta & -im \\ \frac{1}{r}\frac{\partial}{\partial r} & \frac{1}{r}\frac{\partial}{\partial \theta} & im & 0 \end{pmatrix} \tag{7.3.15}$$

. The full linearized system of equations is given in App.B. Note that in both cases, the stability analysis around the base flow $\mathbf{U}$ is given by the spectrum of eigenvalues of the matrix $\mathbf{J}$. The asymptotic time evolution of the perturbation vector $\hat{\boldsymbol{q}}$ is hence dictated by the sign of $\mathfrak{Re}(\omega)$:

- If $\mathfrak{Re}(\omega) < 0$, all the disturbances in the flow decay over time and the base flow returns eventually to its original state becoming globally stable.

- If $\mathfrak{Re}(\omega) > 0$, there exists at least one disturbance that grows in time and destabilizes the flow and the base flow is considered globally unstable leading to significant changes in the flow behavior.

- If $\mathfrak{Re}(\omega) = 0$, the perturbations are neither growing nor decaying over time. This condition is known as "neutral stability."

Global stability flow solver

The linearized Navier-Stokes equations as expressed before constitute a set of partial differential equations that need to be spatially discretized to be solved numerically. In order to achieve this discretization and subsequently tackle the linear eigenvalue problem, a solver called GIFIE is used in this Ph.D. work. This code has been initially developed by Bridel-Bertomeu *et al.* (2016*b*) and further advanced by Queguineur (2020) throughout his Ph.D. The code is implemented using FreeFEM++ (Hecht (2012)), a partial differential equation solver based on the finite element method. The approach involves transforming the partial differential equations into their weak formulation and then discretizing them via the finite element method. The resulting block matrices are assembled and solved in the same solver. Given that these equations are generally sparse and the matrix dimensions are notably substantial, indirect techniques are employed to solve such problems. Specifically, the GMRES method from the PETSc library (Balay *et al.* (2019)) is used in conjunction to the library SLEPc (Roman *et al.* (2019)) to solve the linear eigenvalue problem based on the shift-invert spectral transformation method which facilitates the extraction of a set of eigenvalues in close proximity to a specified complex shift. The advantage of these libraries is that they can efficiently solve problems on large clusters by leveraging parallelism and distributing computations. It is worth highlighting that this solver accommodates computations for both incompressible and compressible scenarios across $2D$, $3D$, and $2D$ asymmetric flows. Additionally, the solver can also handle the computations of adjoint modes.

Note that the code has been enhanced to incorporate structural modal analysis for both fixed and rotating structures, a development stemming from the present thesis. For fixed structures with constant or no damping, the modal analysis procedure is rather simple compared to flow problems since the equation involved is linear. The validation of this part is detailed in App. A. Conversely, for rotating structures, the equation involved is non-linear as seen in the case of the rotating disc in Chap. 2. Furthermore, The scope of work extends to encompassing flow stability analysis for fluid-structure problems. This also entails for resolving the fully coupled fluid-structure problem to extract aeroelastic modes.

7.4 Applications and analysis

7.4.1 Flow around a $2D$ circular cylinder

The first case involves a flow around a cylinder *i.e.*, the same test case studied in Chap. 3 for a fixed cylinder for $Re_D = 40$ and $Re_D = 100$ using the same computational domain. This classical problem has been used in multiple modal analyses and dynamics or control studies (Sipp *et al.* (2010); Marquet *et al.* (2008)). It involves an oscillator flow exhibiting an unsteadiness once the flow undergoes a bifurcation at $Re_D \approx 47$. The unsteadiness is due to the presence of an unstable global mode. The objective hereafter is to evaluate the presence of global modes via a global linear stability analysis. To do so, first, the $2D$ mean flow is computed. Then a linear stability analysis is performed around this mean flow.

Mean flow computation

The mean flow is obtained from the LES by taking the temporal and spatial average of the flow at its limit cycle. Figure 7.5 shows the obtained mean flows for $Re_D = 40$ and $Re_D = 100$. As expected, both cases exhibit a streamwise symmetric pattern with respect to the cylinder. For $Re_D = 40$, the flow is stable and does not show any significant unsteadiness. The wake is characterized by an elongated re-circulation zone with a strong vorticity gradient near the cylinder wall that then decreases downstream. The boundary layer near the cylinder's surface remains attached along the entire length of the cylinder. For $Re_D = 100$, a shorter re-circulation zone is noted with larger spanwise vorticity contours. Such differences in spatial distributions are due to the unsteady nature of the second case.

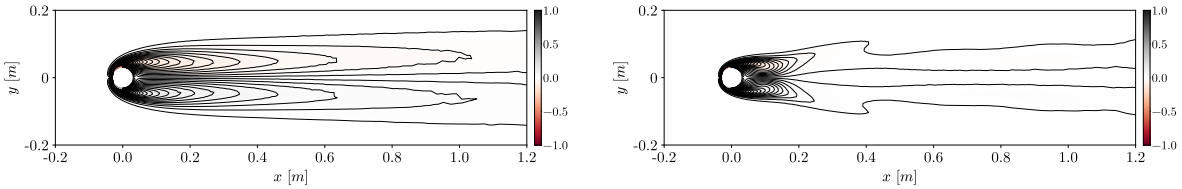

(a) **(b)**

Figure 7.5: Mean vorticity plots for (a) $Re_D = 40$ and (b) $Re_D = 100$.

Normal modes

The $2D$ normal mode approach is desired by solving the simplified eigenvalue problem given in Eq. (7.3.10). Figure 7.6 shows the mapping of frequencies obtained for both mean flows *i.e.*, $Re_D = 40$ and $Re_D = 100$ with their corresponding growth rates. For $Re_D = 40$ the most unstable mode found has a negative growth rate which indicates that the flow is stable and remains steady whatever the perturbation injected

($Re_D < Re_c$). By increasing the Reynolds number above Re_c, a mode appears on the positive part of the real plane and its imaginary part settles at the vortex shedding frequency $f_s = 138.5\,Hz$ ($\mathbf{Im}(\omega/2\pi)$).

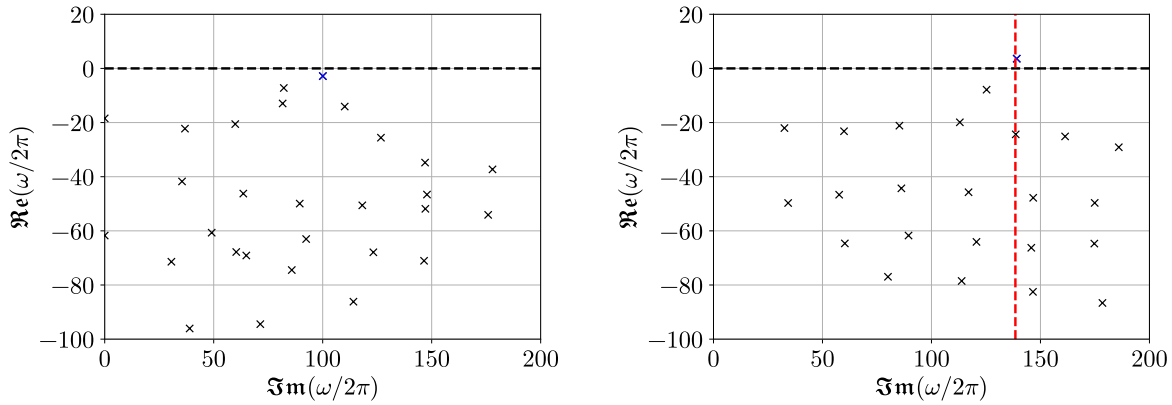

Figure 7.6: Scatter plot of the temporal growth rate and frequency obtained for (a) $Re_D = 40$ and (b) $Re_D = 100$. (the dashed red line indicates the frequency obtained by LES).

The spatial organization of both most unstable modes is reconstructed and depicted on Fig. 7.7. As seen, the modes express as a series of zones of alternating sign.

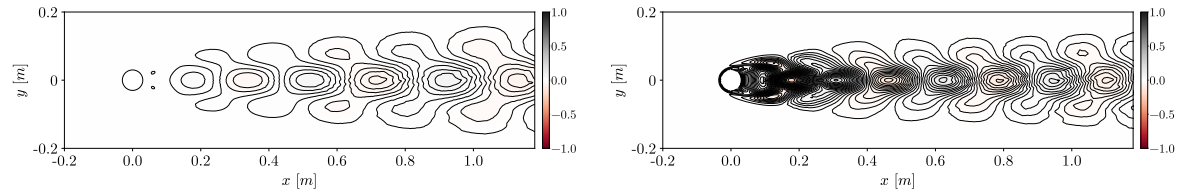

Figure 7.7: Spatial organization of the vorticity of the most unstable modes for (a) $Re_D = 40$ and (b) $Re_D = 100$.

7.4.2 Forced flows in an enclosed rotor/stator cavity

In this section, the global stability analysis of the academic rotor/stator cavity studied in Chap. 3 is discussed. In this case, global modes are sought for forced flow cases to gain more insight about the underlying dynamics of the flow and the stability of the new dominant modes inside such a system. The objective is hence to evaluate the response of the hydrodynamic modes when the flow is subject to a forcing. Recall that two cases were considered: Case 1 and Case 2 for the LES predictions were respectively obtained by forcing the flow cavity at the frequency of the rotor vibration equal the two most

unstable modes in the cavity and found in the unforced case (refer to section 3.5.3). Note that this study has been published in Noun *et al.* (2021).

Mean flow computation

The mean field is obtained using AVBP and computing the temporal and azimuthal averages of the flow prediction considering the average axial position of the rotor at the flow limit cycle. Figure 7.8 shows the normalized averaged radial velocity component for Case 1 and Case 2 in the (r, z) plane. It is clearly seen that the radial velocity field is positive in the rotor boundary layer and negative in the stator as expected. These boundary layers flows correspond to a *Von Kármán* and a *Bödewadt* boundary layer respectively as retrieved in the non-forced case (Queguineur (2020)). Forcing the flow however alters the mean flow. For both cases the mean field is affected in different ways. For the rotor boundary layer, the hub and the shroud, the effect seems to have a stronger influence on the organization for Case 2. The imposed higher frequency of vibration generates stronger gradients of the flow contours in those regions for $0.071 < r < 0.8$ and $0.22 < r < 0.25$. The two statoric boundary layers also seem affected. The most notable difference of the base flow organization of the two cases appears for $0.16 < r < 0.24$. In this region, the mean radial velocity component separates from the stator in Case 2. This separation is not seen in the first case. Note that this specific zone has been shown to have the maximum structural sensitivity for the non-forced case (Queguineur (2020)). It is the triggering location of a global mode of the system and modifications of the flow/geometry at this location leads to the largest drift of the eigenvalues (Giannetti & Luchini (2007)).

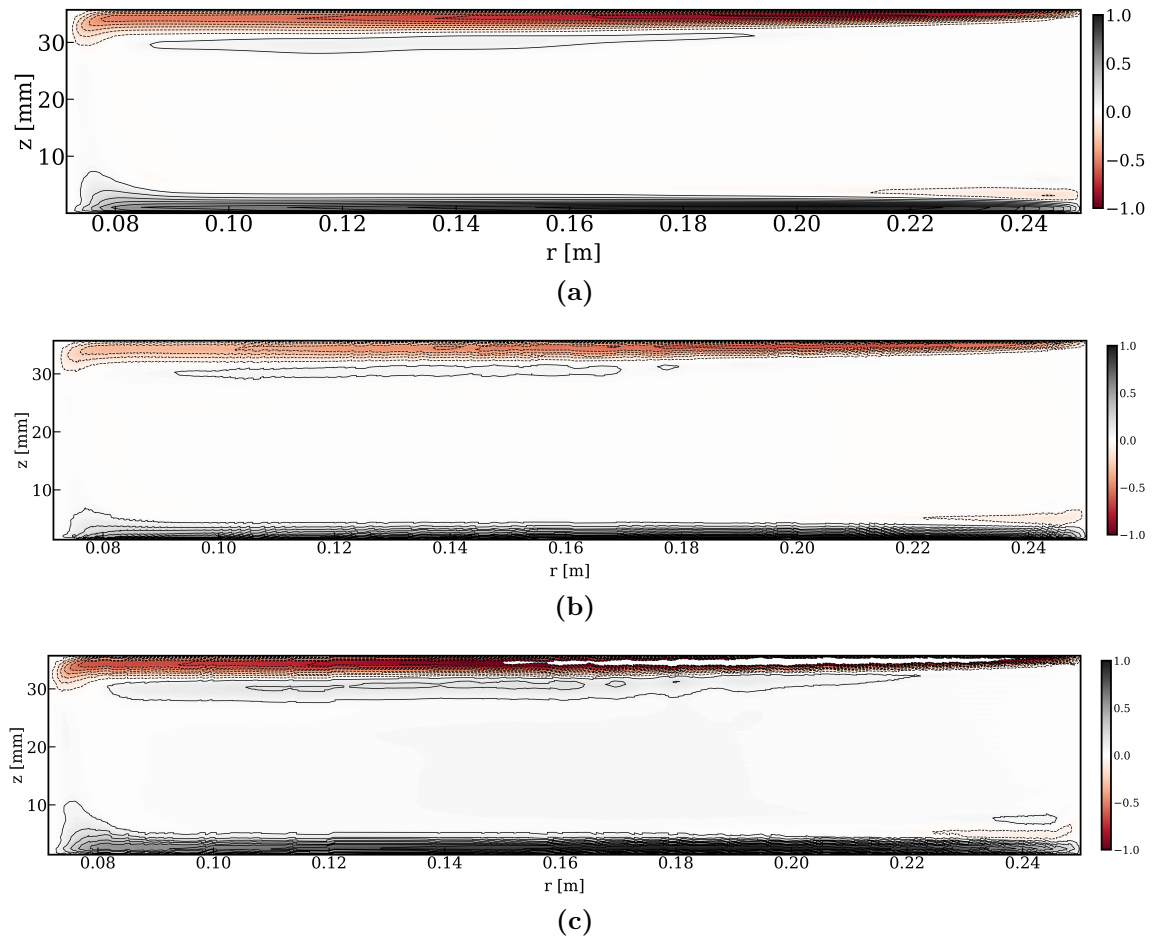

Figure 7.8: Mean flow contours of the time and azimuthal averaged radial velocity component U_r normalized by its maximum magnitude for (a) Non forced case (b) **Case** 1 and (c) **Case** 2. (The stator is located at the top and the rotor at the bottom).

GLSA results

Using previously obtained mean fields, the eigenvalue problem (7.3.10) can be solved for each case to obtain all the modes along with their frequencies and amplifications at each wavenumber m. Figure 7.9 shows a plot of the frequency and growth rate of the most unstable modes at each wavenumber m for Case 1. Four distinct regions can be identified in such views. The most unstable mode of the first branch corresponds to the axisymmetric mode $m = 0$ and has a frequency of $4.71F_0$. Mode $m = 28$ can be identified in the fourth branch and has a frequency of $3.6F_0$. Even though it does not have the highest growth rate, it is the only mode that imposes its spatial organization in the stator boundary layer as shown previously by LES. Similarly for Case 2 (see Fig. 7.10), the axisymmetric mode $m = 0$ is the most unstable one for the first branch and has a frequency of $3.3F_0$. The second mode with the wavenumber $m = 30$ is retrieved and has the highest amplification rate in the system for a frequency of $4.92F_0$. These modes obtained clearly reflect the presence of the two distinct rotational instabilities identified

by LES and DMD in Chap. 3. To go further and understand the results obtained by the global linear stability analysis, the spatial organization of these modes are presented and compared to a Dynamic Mode Decomposition (DMD) where each mode is projected on its corresponding wavenumber. This projected DMD method consists in decomposing the flow mode shapes according to their azimuthal wavenumber in $2D$ (in the (r, z) plane) instead of computing them in $3D$ which is more expensive in terms of data storage and numerically. Thanks to this step, the characterization of modes according to their complex frequency and wavenumber allows a direct comparison with the obtained mode shapes from linear stability analysis which is not feasible with classical DMD.

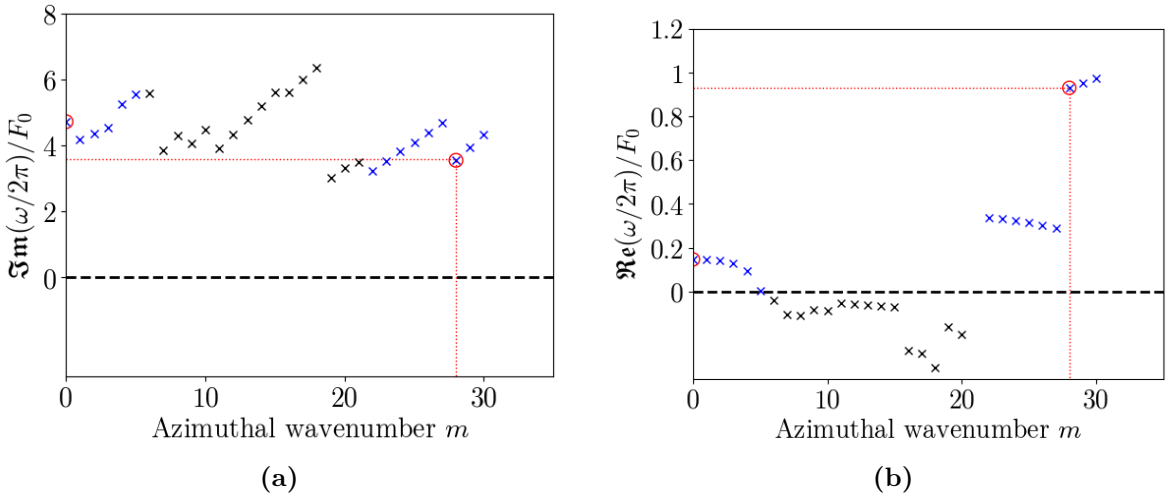

(a) **(b)**

Figure 7.9: Scatter plots of the (a) frequency and (b) growth rate versus the azimuthal wavenumber m of the linear global modes obtained for **Case** 1. (The values are normalized by the rotational frequency of the rotor F_0).

Figure 7.11 shows the spatial organization of the $2D$ axisymmetric axial velocity modes for the wavenumbers $m = 0$ and $m = 28$ of Case 1. Good agreement is found between DMD and the global linear stability. For mode $m = 0$, the annular vortices identified by LES and DMD on the circular cuts are highlighted in this region. The impact of the observed re-circulation zone on the forced mean flow is identified clearly here near the hub and throughout the cavity. Mode $m = 28$ is expressed through spiral arms located at $0.13 < r < 0.21$ in the stator boundary layer as shown by Fig. 7.11(b). Indeed, this mode appears to be dominant within the stationary disc only, which is confirmed by the global stability analysis and the DMD projection for this specific wavenumber. Table 7.1 provides a comparative summary of the results obtained by DMD and GLSA for Case 1. Note that all other frequencies are quite similar as well if comparing DMD to GLSA but these were found to be of lesser interest.

For Case 2, Fig. 7.12, the $2D$ mode shape of the axial velocity mode $\hat{u}_z$ obtained by the global linear stability analysis and DMD also coincide. The spatial organization of mode $m = 0$ seems to comply except for the region near the rotor where GLSA yields a higher mode amplitude. Retrieved frequencies remain however similar: $3.3F_0$ and $3.24F_0$.

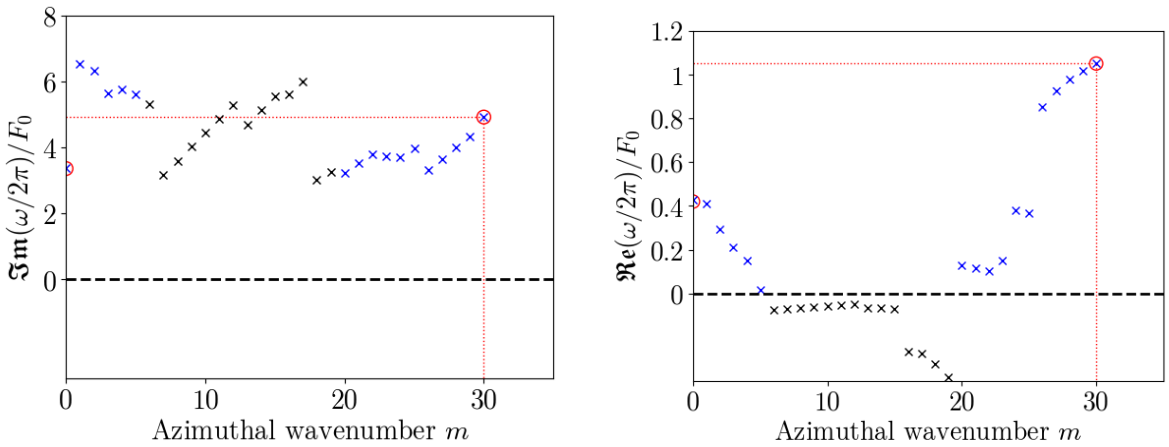

(a) **(b)**

Figure 7.10: Scatter plots of the (a) frequency and (b) growth rate versus the azimuthal wavenumber m of the linear global modes obtained for **Case** 2. (The values are normalized by the rotational frequency of the rotor F_0).

Case 1	**DMD**	**GLSA**
Mode $m = 0$	$4.64F_0$	$4.71F_0$
Mode $m = 28$	$3.64F_0$	$3.6F_0$

Table 7.1: Comparison between the modes obtained by DMD and GLSA for **Case** 1.

Both spatial distributions furthermore agree with the fact that for this mode, the region with the highest level of fluctuations results from circular vortices concentrated near the stationary disc: $0.071 < r < 0.12$ and near the hub at very low radii. Note that this mode has also been found by Queguineur *et al.* (2018) in local and global stability analyses. The second mode pulsates at $4.92F_0$ for a wavenumber $m = 30$ again, close to the one found by DMD, $5F_0$. Its presence is essentially found near the stationary disc for $0.13 < r < 0.20$ where spiral vortices manifest. All modes retrieved by DMD and GLSA for Case 2 are summarized in Tab. 7.2.

To conclude, just like the stationary case of Queguineur (2020), the global linear stability analysis (GLSA) and Dynamic Mode Decomposition (DMD) offer a mean to

Case 2	**DMD**	**GLSA**
Mode $m = 0$	$3.26F_0$	$3.3F_0$
Mode $m = 30$	$5F_0$	$4.92F_0$

Table 7.2: Comparison between the modes obtained by DMD and GLSA for **Case** 1.

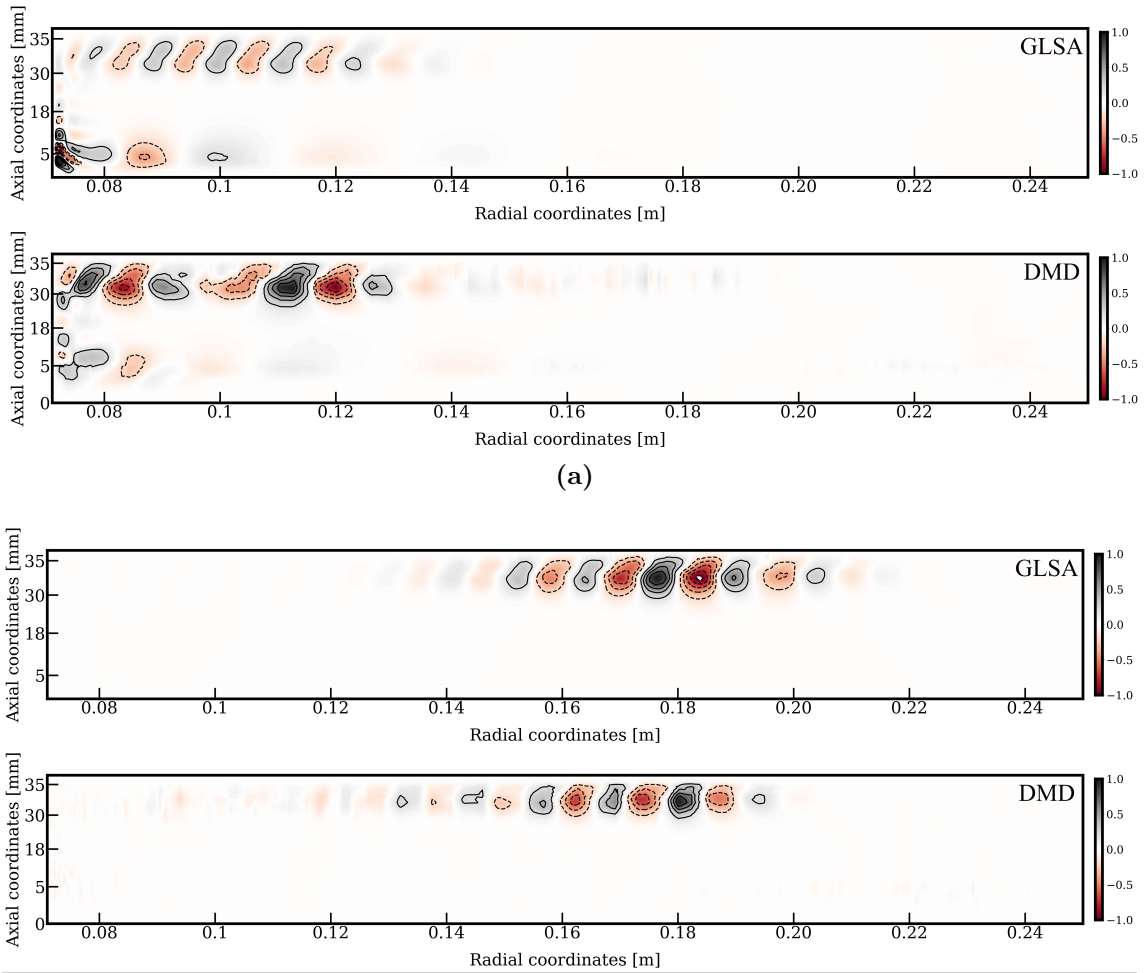

Figure 7.11: $2D$ shapes of the axial velocity mode $\hat{u}_z$ obtained by GLSA and compared with the DMD predictions for the two wavenumbers (a) $m = 0$ and (b) $m = 28$ for **Case** 1.

access flow modes populating a limit-cycle even in forced conditions. Note that the forcing frequency for both cases is retrieved by the stability analysis. However the study is here restricted to the fluid modes only.

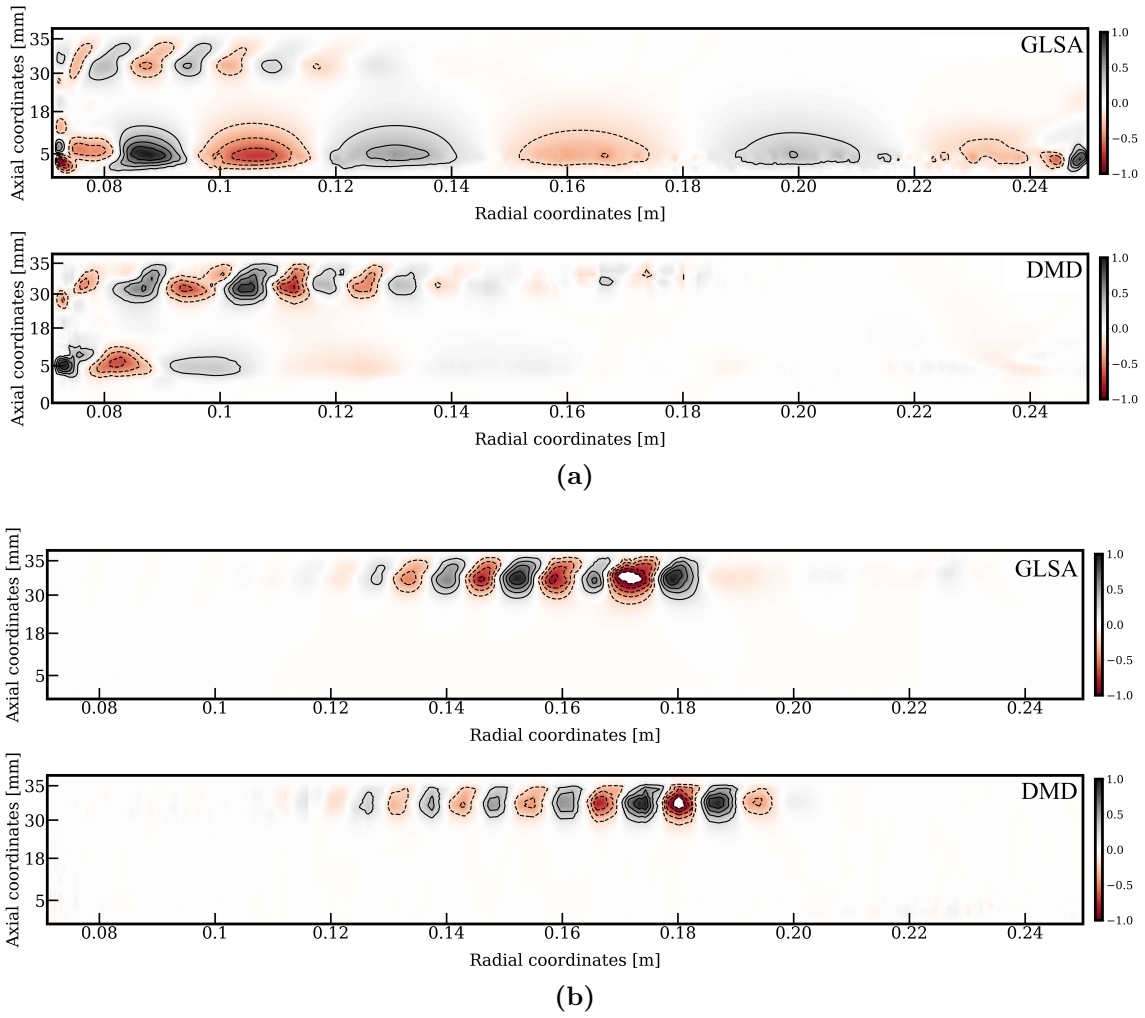

Figure 7.12: $2D$ shapes of the axial velocity mode $\hat{u}_z$ obtained by GLSA and compared with the DMD predictions for the two wavenumbers (a) $m = 0$ and (b) $m = 30$ for **Case** 2.

7.4.3 Flow stability of the first stage rotodynamic pump

Fluid only simulation

Focus is now brought to the underlying axial instabilities observed in the reduced scale rotodynamic pump studied in Chap. 2. Recall that through LES, two instabilities have been identified. The first one stems from a pulsating vortex at a frequency $f_1^* = 0.157$ near the upper valve clearance while the second one corresponds to a set of vortices that originate from the initial vortex but shed downstream in the housing and at a frequency $f_2^* = 0.314$. Although both instabilities seem to be mutually exclusive, the second mode f_2^* appears to be the primary instability inside the cavity as evidenced by DMD. A linear stability analysis is conducted therein on the fluid only simulation of the reduced scale

rotodynamic pump to investigate the presence of these instabilities and compare them to the previously obtained numerical simulations.

Mean flow

The mean flow in this case is obtained by computing the temporal and azimuthal averages of the macroscopic flow properties from the non-coupled simulation. Figure 7.18 shows a $2D$ slice illustrating the distributions of the mean axial velocity and the mean vorticity within the cavity. In the upper cavity as well as in the upper valve clearance the flow does not depict any particular spatial organization. However, the flow mainly evolves at the entrance of the housing. Indeed, the mean axial velocity contour plot (Fig. 7.18(a)) reveals two high-magnitude structures of opposing signs at the housing inlet followed by similar but smaller patterns further downstream. This suggests the presence of a strong re-circulation zone that is confirmed by looking at the mean vorticity field of Fig. 7.18(b). A large vortical structure indeed forms just at the inlet of the housing followed by two elongated structures of opposite signs further downstream. This flow organization then dissipates as the flow section decreases.

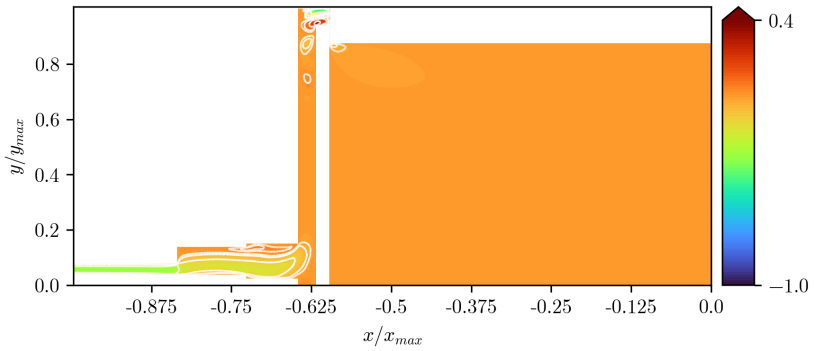

(a)

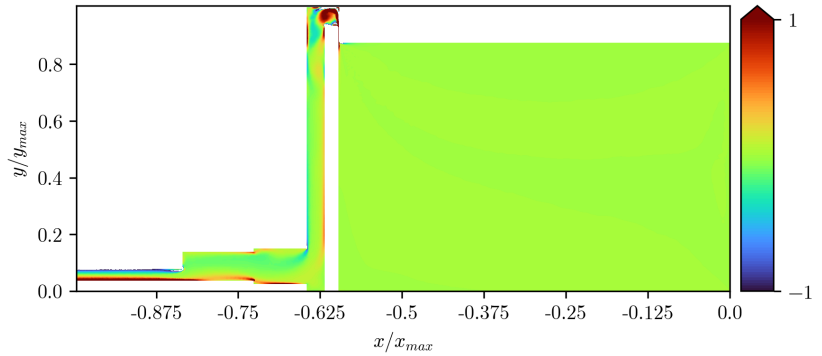

(b)

Figure 7.13: Mean fields of the fluid only simulation: (a) axial velocity and (b) vorticity.

Normal modes

The linearized eigenvalue problem of Eq. (7.3.10) is then solved for a fixed azimuthal number at $m = 0$ due to the absence of azimuthal dependency observed in the LES prediction. In the present scenario, the rotor disc remains stationary through non-linearities and the flow Reynolds number remains low, consequently simplifying the problem into a fully axisymmetric flow configuration.

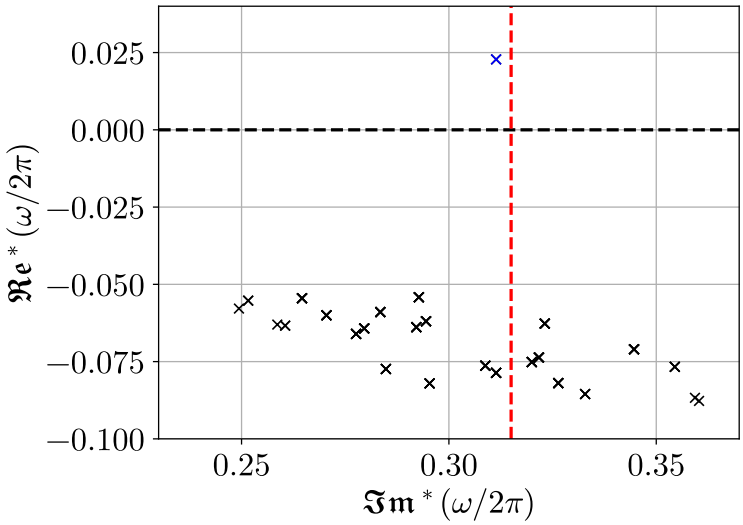

Figure 7.14: Scatter plot of the temporal growth rate and frequency obtained for the fluid only simulation. (the dashed red line indicates the frequency obtained by LES).

Figure 7.14 shows a scatter plot of the growth rates and frequencies obtained via such a linear stability analysis. One unstable mode is found at $f^* = 0.308\,Hz$, in agreement with the second mode observed in LES ($f_2^* = 0.314$). Note that the mode f_1^* of LES is not retrieved by the linear analysis (the secondary instability). This outcome reaffirms that f_2^* is indeed the driving mechanism within the cavity, f_1^* being most likely a recombination of the f_2^* activity. As anticipated, the spatial shape of this mode, Fig. 7.15, predominantly mark at the housing inlet, with alternating patches that indicate a spatial propagation of the structure downstream.

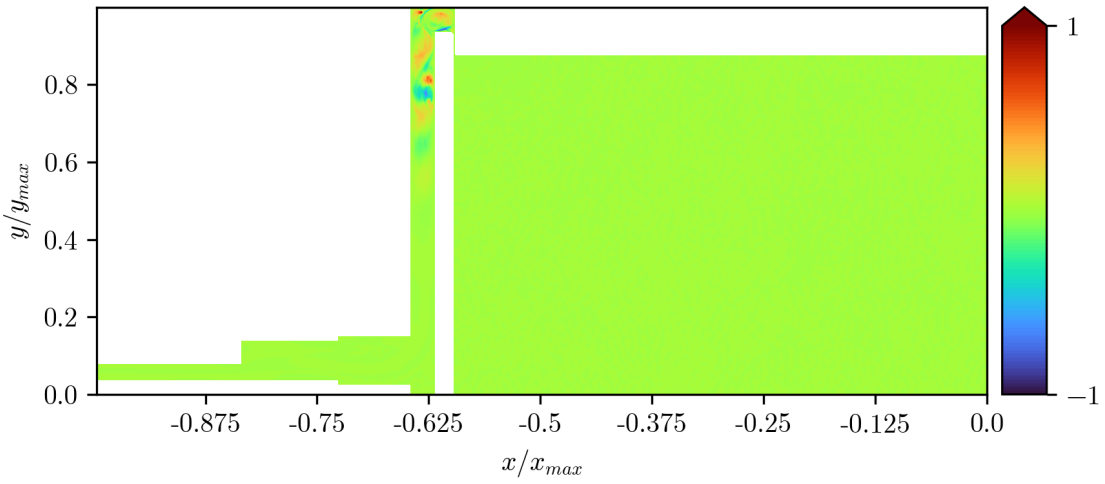

Figure 7.15: Real part of the axial velocity mode shape obtained by GLSA.

Fluid-structure simulation

Regarding the fluid-structure simulation, attention is directed towards the hydrodynamic mode responsible for the fluid-structure instability found in the rotodynamic pump (refer to chap. 6). Recall that through the FSI simulation, one fluid-structure instability has been identified pulsating at around $f_c^* = 1$. The aim of this analysis is to identify this mode from a purely hydrodynamic perspective and compare it to the mode found in the fluid only simulation.

Mean flow

The mean flow is obtained following the same procedure as in the fluid only simulation except that for this problem the rotor disk motion must be taken into account. In this scenario, the mean field is obtained by taking the temporal and azimuthal average of the flow quantities that correspond to the mean static deflection of the rotor disc. the mean flow field is hence obtained by averaging the macroscopic quantities across a sequence of azimuthal cross-sections in the (x, y) plane and projected onto the domain corresponding to the mean static deflected rotor. This specific situation is obtained by applying the mean resultant force: *i.e.*, over multiple oscillation cycles to the rotor. This specific approach ensures consistency for the mean fluid-structure solution and the principles of linear stability analysis theory. Figure 7.16 shows a $2D$ cross-section of the mean axial velocity component $\bar{u}_x$ and the mean vorticity field. Similar to the non coupled case, the upper cavity exhibits no distinct activity. The housing entrance, however exhibit the presence of two structures of opposite axial velocity values that are larger than the one found in the fluid-only simulation. This observation aligns with the prior findings of Chap. 6 while examining instantaneous snapshots of velocity magnitude. Overall, a similar trend persists when inspecting the mean vorticity field. Notably, a

substantial vortex structure materializes just beyond the upper valve, extending along the shroud and lower section of the housing. Although differing in shape if compared to the fluid only solution, this re-circulation zone also exhibits a more pronounced vorticity magnitude compared to the uncoupled case.

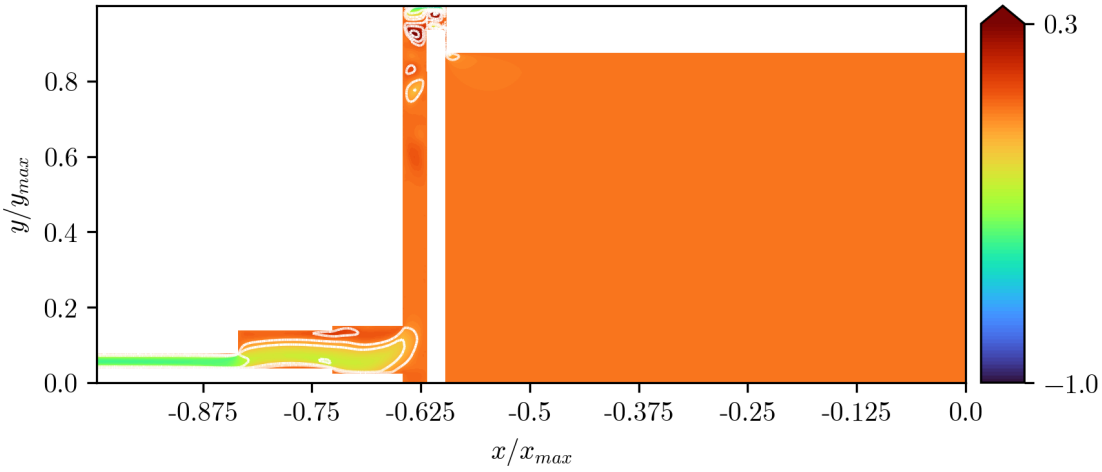

(a)

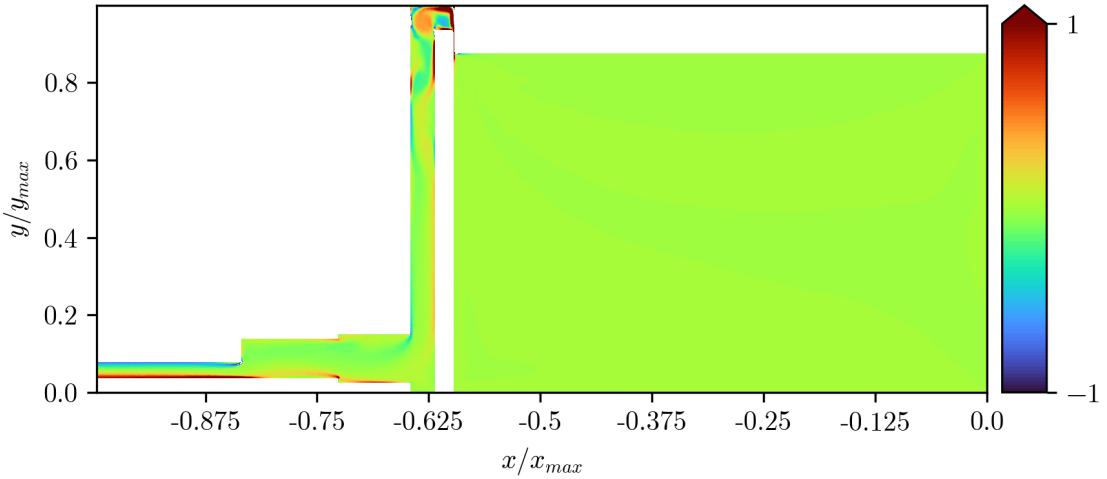

(b)

Figure 7.16: Mean fields of the fluid-structure simulation: (*a*) axial velocity and (*b*) vorticity.

Normal modes

The same procedure as before is then applied for solving the eigenvalue problem in the absence of rotation for $m = 0$. Figure 7.17 shows the retrieved scatter plot of the temporal growth rates and frequencies thereby obtained. One unstable mode is retrieved

at $f^* = 1.01$ that is close to the frequency obtained by PSD in the corresponding LES suggesting that this hydrodynamic mode originates from the fluid-structure coupling and is indeed different from the one found in the fluid only simulation.

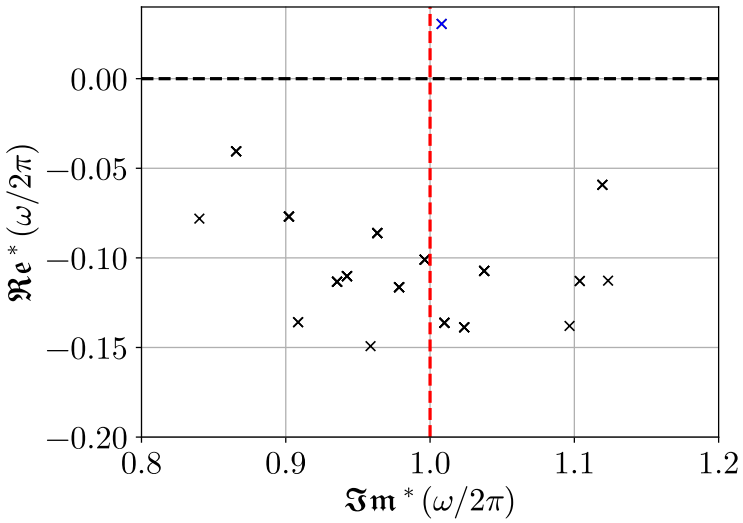

Figure 7.17: Scatter plot of the temporal growth rate and frequency obtained for the fluid only simulation. (the dashed red line indicates the frequency obtained by LES).

The mode shape of this mode is visualized on Fig. 7.18. Its spatial organization also differs from the mode retrieved on the fluid only simulation. Indeed, two re-circulation zones can be evidenced, a small one near the the upper valve and a larger one just beneath it both pulsating at the same frequency $f^* = 1.01$. This spatial organization is similar to the one retrieved by LES confirming the dynamics of the flow in coupled conditions.

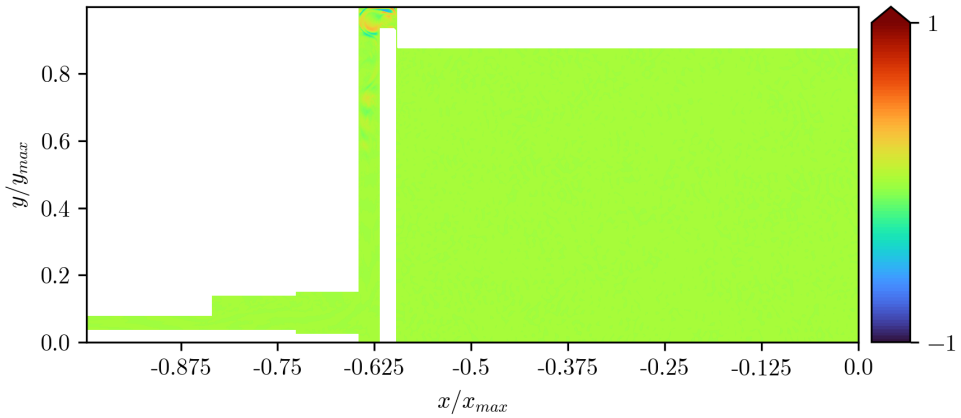

Figure 7.18: Real part of the axial velocity mode shape obtained by GLSA.

7.5 Conclusion

In this chapter, the global linear stability analysis has been performed on fluid problems, forced vibration problems, as well as fluid-structure interaction problems. The mean flow is computed separately using LES and the appropriate linearized eigenvalue is solved separately. Results are compared with the spectral content of LES and Dynamic Mode Decomposition whereby confirming that this predictive numerical tool can retrieve hydrodynamic modes even in forced or coupled conditions. The key in this context is to have the appropriate mean flow issued from the right simulation. This opens the door to adjoint based methods to measure the flow sensitivity and qualify its robustness to changes in order to design efficient control strategies. Nevertheless, to fully investigate multiphysics modes, a coupled fluid-structure linear stability analysis is necessary. To do so, the fully coupled system of equations must be linearized and solved around the mean field. This allows the recovery of coupled fluid-structure modes revealing the mode shapes of the fluid as well as the structure. Additionally, adjoint method can be used in this case to optimize the fluid-structure system by modifying the fluid and/or the structure characteristics allowing the passive control of fluid-structure instabilities.

Chapter 8

Conclusion

Vibration problems in rocket turbopumps are notorious for reducing their lifespan and compromising the structural integrity of the entire engine. This undesirable phenomenon results from the self-sustained oscillatory motion of the working fluid, commonly referred to as "pressure bands", which can couple with the solid structure posing a significant risk to the operation of the turbopump. Given the inherently intricate and three-dimensional nature of these flow instabilities especially when encountered within complex configurations, a numerical approach is preferred to address the problem. Specifically, Large Eddy Simulation, an unsteady Computational Fluid Dynamics (CFD) based approach, has been proven to accurately model these hydrodynamic instabilities in contrast to steady-state simulations. Nevertheless, this method alone is not enough to investigate multiphysics problems hence multiple numerical tools have been developed in this thesis to investigate forced vibration and self-induced vibration problems.

In this numerical framework, the first type of machine vibration, forced vibration, is addressed. A simple test case is first considered that consists of a $2D$ cylinder which oscillates transversely to the incoming flow stream at a fixed Reynolds number. By varying the amplitude and frequency of vibration within a specified range, various vortex shedding patterns are observed. The resulting wake characteristics are then analyzed using time series data of aerodynamic coefficients. The results indicate that under specific combinations of predetermined frequency and amplitude of vibration, a "lock-in" phenomenon occurs, where the vortex shedding frequency matches the imposed frequency. This application serves also to validate the use of the moving mesh technique ALE as well as the imposed cylinder displacement law under forced conditions. Subsequently, those tools are used in a second study where an annular rotor/stator cavity subject to imposed rotor oscillations is investigated. This academic cavity has been the focal point of numerous numerical and experimental studies due to its approximation to real-life industrial turbomachines making it an appealing research subject. Previous investigations have revealed that the flow within such a cavity exhibits inherent three-dimensionality and, due to the high Reynolds number of the rotating flow, hydrodynamic instabilities manifest at three distinct azimuthal wavenumbers. These instabilities dominate the stator, rotor, and mid-cavity regions, taking the form of annular and/or spiral vortices. Predictive numerical techniques such as Dynamic Mode Decomposition (DMD) and Power Spectral Density (PSD) analysis have provided evidence of the presence of these unstable modes. The critical question arising from this issue is as follows: How do these hydrodynamic modes respond when the rotor starts oscillating at the same frequency as one of these modes, essentially replicating a resonance phenomenon? To address this question, two Large Eddy Simulation (LES) predictions are conducted. In the first instance, the imposed vibration frequency is matched with the stator mode, while in the second instance, it is matched with the mid-cavity mode, both of which are the most dominant modes within the cavity. The results reveal that the imposed vibration indeed has an impact on the primary modes within the cavity. In the non-forced scenario, these leading modes either shift to new frequencies and mode shapes or completely vanish.

Self-induced vibration constitutes the second category of machine vibration addressed in this thesis. To investigate this multiphysics aspect, a structural mechanics solver is first developed that is able to perform modal analyses as well as elastodynamic calculations.

The solver is verified first using a steady approach, followed by verification of the transient elasticity equation. Results demonstrate excellent alignment with existing literature, affirming the capability of the developed tool to accurately capture structural modes, static deformations, and dynamic responses. The structural solver is then coupled to the LES solver AVBP using a Multiple Program Multiple Data (MPMD) approach. This allows the exchange of information between the two solver on the fly during calculation. The resulting partitioned fluid-structure solver adopts a weak coupling strategy, which proves adequate for simulating scenarios involving high solid-to-fluid density ratios as commonly encountered in turbomachinery applications. To validate this coupling, two distinct test cases are examined. The first case consists of a vibrating beam immersed a closed fluid domain. This test case demonstrates that regardless of the fluid and structural parameters employed, the structure ultimately returns to its equilibrium position after a specific duration. The time required to reach equilibrium is influenced by the density of the structure and the viscosity of the fluid. Both parameters are varied one at a time and results show that by increasing the solid density or fluid viscosity the time needed to reach equilibrium increases. Conversely by decreasing those parameters equilibrium is attained faster. The second test case involves a vortex-induced vibration phenomenon of an elastic plate clamped behind a rigid cylinder. This complex test case serves to validate the coupling under more intricate conditions where vortices shed at the cylinder's corners induce substantial amplitude vibrations of the plate. Results reveal that the vortex shedding frequency resulting from the coupling differs from that obtained in a fluid-only simulation where the plate remains fixed. The coupled frequency and amplitude of vibration are then compared to results that stem from other coupling strategies from the existing literature, demonstrating a high degree of agreement with the findings.

This point leads us to the application of the developed FSI solver to an industrial turbomachinery application. The involved configuration represents a first stage rotodynamic pump. The primary objective is to simulate the axial balancing system and assess its stability under specific operating conditions. Structure and acoustic modal analyses showed that the natural frequency of the rotor disk coincide with the first acoustic frequency of the cavity indicating a potential vibroacoustic phenomenon. To tackle this problem, an LES prediction is conducted on the reduced scale hydrogen turbopump to investigate the flow dynamics in non coupled conditions. Results show that the flow dynamics in the second part of the cavity are driven by two leading hydrodynamic modes that interact with each other. However, their frequencies do not align with either the structural disk mode or the cavity acoustic mode, suggesting that this approach alone is insufficient for capturing multiphysics phenomena. Consequently, a fluid-structure interaction simulation is performed on the same configuration by allowing the rotor disk to deform. As anticipated, the disk vibrates at its $0ND$ mode close to its natural frequency, thus confirming the likelihood of a vibroacoustic phenomenon as observed in experiments and the capability of the developed tools to predict the phenomenon. Moreover, the coupled solver allows the calculation of the structural damping ratio required to stabilize this configuration. Therefore, the designer must strategically adjust the natural frequency of the rotor disk, accounting for material damping, under specific operating conditions of the turbopump.

Finally, a more in-depth investigation is conducted on the configurations of interest to identify the hydrodynamic instabilities responsible for the flow dynamics. Within this context, a comprehensive global linear stability analysis (GLSA) framework is established to analyze oscillating flows in fluid problems, encompassing forced vibration and fluid-structure interaction scenarios. The key here is to obtain the right mean flow for each application, meaning that the flow macroscopic quantities are linearized around the base flow obtained using LES . This methodology enables the identification of vortex shedding modes for flow problems, such as flow past a fixed rigid cylinder, as well as hydrodynamic instabilities in axial driven flows in the rotodynamic pump. In the case of forced flow problems, two primary unstable modes are identified in each of the forced cases within the academic rotor/stator cavity, thereby corroborating the LES predictions and findings from techniques like DMD and PSD. Additionally, this method facilitates the identification of the unstable fluid mode resulting from the fluid-structure coupling between the rotor disk and axial flow. All those application prove that such a method is able to retrieve flow modes even in forced or coupled scenarios. Furthermore it lays the foundation for performing control and sensitivity studies to understand the origin of these fluid modes and suppress them if necessary. However, it is important to note that the GLSA has inherent limitations in capturing all the dynamics within multiphysics problems. This limitation is expected since the equations primarily model the behavior of the fluid alone (Navier-Stokes and continuity equations). To fully comprehend fluid-structure modes, ongoing efforts have been initiated to linearize the fully coupled fluid-structure system of equations. This extension aims to identify coupled and non coupled fluid-structure modes in both $2D$ open flows and $2D$ axisymmetric flows. This next step in research expands the GLSA framework to encompass fluid-structure problems, enabling the exploitation of self-sustained coupled instabilities and subsequently control fluid and/or solid modes responsible for the coupling.

Bibliography

Abbott, D. R. 1981 Advances in Labyrinth Seal Aeroelastic Instability Prediction and Prevention. *Journal of Engineering for Power* **103** (2), 308–312. (Cited on page 143.)

Aitken, A. C. 1927 Xxv.—on bernoulli's numerical solution of algebraic equations. *Proceedings of the Royal Society of Edinburgh* **46**, 289–305. (Cited on page 111.)

Åkervik, Espen, Brandt, Luca, Henningson, Dan S., Hœpffner, Jérôme, Marxen, Olaf & Schlatter, Philipp 2006 Steady solutions of the Navier-Stokes equations by selective frequency damping. *Physics of Fluids* **18** (6), 2006–2009. (Cited on pages 11 and 157.)

Alford, Joseph S. 1965 Protecting turbomachinery from self-excited rotor whirl. *Journal of Engineering for Power* **87**, 333–343. (Cited on page 143.)

Alnaes, Martin S., Blechta, Jan, Hake, Johan, Johansson, August, Kehlet, Benjamin, Logg, Anders, Richardson, Chris N., Ring, Johannes, Rognes, Marie E. & Wells, Garth N. 2015 The FEniCS project version 1.5. *Archive of Numerical Software* **3**. (Cited on page 91.)

Anagnostopoulos, P. 2000 Numerical study of the flow past a cylinder excited transversely to the incident stream. part 1: Lock-in zone, hydrodynamic forces and wake geometry. *Journal of Fluids and Structures* **14** (6), 819–851. (Cited on page 52.)

Balay, Satish, Abhyankar, Shrirang, Adams, Mark F., Brown, Jed, Brune, Peter, Buschelman, Kris, Dalcin, Lisandro, Dener, Alp, Eijkhout, Victor, Gropp, William D., Karpeyev, Dmitry, Kaushik, Dinesh, Knepley, Matthew G., May, Dave A., McInnes, Lois Curfman, Mills, Richard Tran, Munson, Todd, Rupp, Karl, Sanan, Patrick, Smith, Barry F., Zampini, Stefano, Zhang, Hong & Zhang, Hong 2019 PETSc users manual. *Tech. Rep.* ANL-95/11 - Revision 3.11. Argonne National Laboratory. (Cited on page 160.)

Barkley, D 2006 Linear analysis of the cylinder wake mean flow. *Europhys. Lett.* **75** (5), 750–756. (Cited on page 158.)

Barkley, D. & Henderson, R.D. 1996 Three-dimensional floquet stability analysis of the wake of a circular cylinder. *J. Fluid Mech.* **322**. (Cited on page 42.)

Batchelor, G K 1951 Note on a class of solutions of the navier-stokes equations representing steady rotationally-symmetric flow. *Q. J. Mech. Appl. Math.* **4** (1), 29–41. (Cited on page 55.)

Bathe, K.J. 2014 *Finite element procedures*. K.J. Bathe. (Cited on page 84.)

Bathe, K.J., Nitikitpaiboon, C. & Wang, X. 1995 A mixed displacement-based finite element formulation for acoustic fluid-structure interaction. *Computers Structures* **56** (2), 225–237, nonlinear Finite Element Analysis and ADINA Proceedings of the 10th ADINA Conference. (Cited on page 101.)

Batina, John T. 1990 Unsteady euler airfoil solutions using unstructured dynamic meshes. *AIAA Journal* **28** (8), 1381–1388. (Cited on page 105.)

Baumgartner, M., Kameier, F. & Hourmouziadis, J. 1995 *Twelfth International Symposium on Airbreathing Engines* . (Cited on page 10.)

Beaudan, P. & Moin, P. 1994 Numerical experiments on the flow past a circular cylinder at sub-critical reynolds number. *Report No. TF-62* pp. Department of Mechanical Engineering, Stanford University. (Cited on pages 42 and 43.)

Becker, A.A. & Becker, A.A. 2004 *An Introductory Guide to Finite Element Analysis*. Professional Engineering. (Cited on page 77.)

Bernard, H. 1908 Formation de centres de giration à l' arrière d' un obstacle en mouvement. *C. R. Acad. Sci* **147**. (Cited on page 42.)

Bödewadt, U T 1940 Die Drehstr{ö}mung {ü}ber festem Grunde. *Zeitschrift f{ü}r Angew. Math. und Mech.* **20** (5), 241–253. (Cited on page 54.)

Bridel-Bertomeu, Thibault 2016*a* Investigation of unsteady phenomena in rotor/stator cavities using large eddy simulation. *PhD thesis Institut National Polytechnique de toulouse* **(Umr 5563), 118**. (Cited on pages 11, 53, 54, 56, 61, and 132.)

Bridel-Bertomeu, Thibault 2016*b* Investigation of unsteady phenomena in rotor/stator cavities using Large Eddy Simulation. *Ph.d.thesis Institut National Polytechnique de toulouse* (Umr 5563), 118. (Cited on page 60.)

Bridel-Bertomeu, T., Gicquel, L. & Staffelbach, G. 2016*a* Wall modeled LES and its impact on rotor/stator cavity unsteady features. *Proceedings of ASME Turbo Expo 2016* . (Cited on page 57.)

Bridel-Bertomeu, Thibault, Gicquel, Laurent & Staffelbach, Gabriel 2016*b* Wall modeled LES and its impact on rotor/stator cavity unsteady features. *ASME Turbo Expo 2016* . (Cited on pages 157 and 160.)

Bridel-bertomeu, Thibault & Gicquel, L Y M 2017 Large scale motions of multiple limit-cycle high Reynolds number annular and toroidal rotor / stator cavities Large scale motions of multiple limit-cycle high Reynolds number annular and (July 2018). (Cited on page 54.)

Brouzet, D., Haghiri, A., Talei, M, Brear, M. J., Schmidt, O. T., Rigas, G. & Colonius, T. 2020 Role of coherent structures in turbulent premixed flame acoustics. *AIAA Journal* **58** (6), 2635–2642. (Cited on page 37.)

Brunier-Coulin, Florian, Vandenberghe, Nicolas, Verhille, Gautier & Le Gal, Patrice 2022 Fluid–structure instabilities in the axial balancing system of a turbo-pump. *Journal of Sound and Vibration* **538**, 117–193. (Cited on pages 19, 26, 133, 140, 143, and 144.)

Causin, P., Gerbeau, J.F. & Nobile, F. 2005 Added-mass effect in the design of partitioned algorithms for fluid–structure problems. *Computer Methods in Applied Mechanics and Engineering* **194** (42), 4506–4527. (Cited on page 109.)

CERFACS 2008 The AVBP HandBook . (Cited on page 29.)

Chomaz, J-M, Huerre, P & Redekopp, L G 1991*a* A frequency selection criterion in spatially developing flows. *Stud. Appl. Math.* **84**, 119–144. (Cited on page 157.)

Chomaz, J M, Huerre, P & Redekopp, L G 1991*b* A frequency selection criterion in spatially developing flows. *Stud. Appl. Math* . (Cited on page 157.)

Chopra, Anil K 1995 Dynamics of structures: Theory and applications to earthquake engineering, prentice hall. *Inc., Upper Saddle River, NJ* . (Cited on page 94.)

Chopra, Anil K 2007 *Dynamics of structures*. Pearson Education India. (Cited on page 94.)

Chung, J. & Hulbert, G. M. 1993 A Time Integration Algorithm for Structural Dynamics With Improved Numerical Dissipation: The Generalized- Method. *Journal of Applied Mechanics* **60** (2), 371–375. (Cited on page 86.)

Colin, Olivier 2000 Simulations aux Grandes Echelles de la Combustion Turbulente Prémélangée dans les Statoreacteurs. PhD thesis. (Cited on pages 31 and 59.)

Colin, O. & Rudgyard, M. 2000*a* Development of high-order taylor-galerkin schemes for unsteady calculations. *Journal of Computational Physics* **162** (2), 338–371. (Cited on pages 59, 118, and 124.)

Colin, O. & Rudgyard, M. 2000*b* Development of high-order taylor–galerkin schemes for les. *J. Comput. Phys.* **2**, 338–371. (Cited on pages 31, 44, and 59.)

Daily, J W & Nece, R E 1960 Chamber dimension effects on induced flow and frictional resistance of enclosed rotating disks. *J. Fluids Eng.* **82** (1), 217–230. (Cited on page 54.)

D'Angelo, C. & Mote, C.D. 1993 Natural frequencies of a thin disk, clamped by thick collars with friction at the contacting surfaces, spinning at high rotation speed. *Journal of Sound and Vibration* **168** (1), 1–14. (Cited on page 20.)

Dapogny, C., Dobrzynski, C. & Frey, P. 2014 Three-dimensional adaptive domain remeshing, implicit domain meshing, and applications to free and moving boundary problems. *Journal of Computational Physics* **262**, 358–378. (Cited on page 117.)

Debrabandere, F., Tartinville, B., Hirsch, Ch. & Coussement, G. 2012 Fluid–Structure Interaction Using a Modal Approach. *Journal of Turbomachinery* **134** (5), 051043. (Cited on pages 123 and 126.)

Degroote, Joris, Bathe, Klaus-Jürgen & Vierendeels, Jan 2009 Performance of a new partitioned procedure versus a monolithic procedure in fluid–structure interaction. *Computers Structures* **87** (11), 793–801, fifth MIT Conference on Computational Fluid and Solid Mechanics. (Cited on pages 108, 109, and 112.)

Deneuve, Ariane, Seive, Martin, Testa, David, Yvain, Thierry, Fiore, Giuseppe, Vieille, Bruno, Prevost, Lilian, Gicquel, Laurent Y M, Brunier-coulin, Florien, Verhille, Gauthier, Gal, Pascal Le, Vandenberghe, Nicolas & Eddy, Large. 2020 Arianegroup R & T activities on fluid structure interaction (FSI) for space turbomachinery. *Space Propulsion* . (Cited on pages 19, 20, 22, 133, and 143.)

Dobrzynski, C. & Frey, P. 2008 Anisotropic delaunay mesh adaptation for unsteady simulations pp. 177–194. (Cited on page 117.)

Dowell, Earl H. 2014 A modern course in aeroelasticity. **217**. (Cited on page 101.)

Drazin, P. & Reid, W. 1982 Hydrodynamic stability. *Journal of Fluid Mechanics* **124**, 529–532. (Cited on page 155.)

Edeline, Emmanuel, Fonteyn, Patrice, Frocot, Manuel, Dehouve, Jérôme & Fayolle, Patrice 2002 Tptech, a technological demonstrator for future rocket engine turbopump. *Fourth International Conference on Launcher Technology, Liège, Belgium,Dec. 3–6.* . (Cited on page 19.)

Edeline, Emmanuel, Fonteyn, Patrice, Frocot, Manuel, Dehouve, Jérôme & Fayolle, Patrice 2004 Development and testing of a fluid film bearing lh2 turbopump demonstrator. *40th AIAA/ASME/SAE/ASEE Joint Propulsion Conference and Exhibit* . (Cited on page 19.)

Ekman, Vagn Walfrid 1905 On the influence of the Earth's rotation on ocean currents. *Ark. f{ö}r Mat. Astron. och Fys.* **2**, 1–53. (Cited on page 54.)

Erlicher, Silvano, Bonaventura, Luca & Bursi, O. 2002 The analysis of the generalized - method for non-linear dynamic problems. *Computational Mechanics* **28**, 83–104. (Cited on page 91.)

Fabbri, Thomas 2022 Development of a high fidelity fluid-structure interaction solver: towards flexible foils simulation. PhD thesis, Ph.D. thesis Université Grenoble Alpes. (Cited on page 106.)

Farhat, Charbel & Lesoinne, M. 1996 On the accuracy, stability, and performance of the solution of three-dimensional nonlinear transient aeroelastic problems by partitioned procedures. *37th Structure, Structural Dynamics and Materials Conference* (April). (Cited on page 114.)

Farhat, C., Zee, van der, K.G. & Geuzaine, P. 2006 Provably second-order time-accurate loosely-coupled solution algorithms for transient nonlinear computational aeroelasticity. *Computer Methods in Applied Mechanics and Engineering* **195** (17-18), 1973–2001. (Cited on page 113.)

Farhat, C; Lesoinne, Midelsohn Sergio R (Editor); ONATE Eugenio (Editor); BUGEDA Gabriel (Editor) ; International Association for Computational Mechanics International (Funder/Sponsor); Argentinean Association for Computational Mechanics Argentina (Funder/Sponsor); Spanish Society for Numerical Methods in Engineering Spain (Funder/Sponsor)International Association for Computational Mechanics International (Funder/Sponsor); Argentinean Association for Computational Mechanics Argentina (Funder/Sponsor); Spanish Society for Numerical Methods in Engineering Spain (Funder/Sponsor) 2000 Two efficient staggered algorithms for the serial and parallel solution of three-dimensional nonlinear transient aeroelastic problems. *Computer methods in applied mechanics and engineering* . (Cited on page 113.)

Favre, Alexandre 1983 Turbulence: Space-time statistical properties and behavior in supersonic flows. *Physics of Fluids* **26** (10), 2851–2863. (Cited on page 27.)

Fey, U., König, M. & Eckelmann, H. 1998 A new strouhal–reynolds-number relationship for the circular cylinder in the range 47 $<$ re $<$ 2×10^5.$Physicsof Fluids$**10**, 1547 − −1549.($Citedonpage$ 43.)

Fransen, Rémy, Vial, Laurence & Gicquel, Laurent Y M 2013 Large Eddy Simulation of Rotating Ribbed Channel. *ASME Turbo Expo 2013: Turbine Technical Conference and Exposition* (GT2013-95076). (Cited on page 44.)

Gatzhammer, Bernhard 2015 Efficient and flexible partitioned simulation of fluid-structure interactions . (Cited on page 112.)

Gedikli, Ersegun 2014 Experimental investigation of low mode number cylinders subjected to vortex-induced vibrations. PhD thesis. (Cited on page 149.)

Gerbeau, Jean-Frédéric & Vidrascu, Marina 2003 A Quasi-Newton Algorithm Based on a Reduced Model for Fluid-Structure Interaction Problems in Blood Flows. *ESAIM: Mathematical Modelling and Numerical Analysis* **37** (4), 631–647. (Cited on page 112.)

Giannetti, Flavio & Luchini, Paolo 2007 *Structural sensitivity of the first instability of the cylinder wake*, , vol. 581. (Cited on page 163.)

Glowinski, R., Pan, T. & Periaux, J. 1994 A fictitious domain method for Dirichlet problem and applications. *Computer Methods in Applied Mechanics and Engineering* **111** (3-4), 283–303. (Cited on page 104.)

Goddard, Robert H. 1920 A method of reaching extreme altitudes. *Nature* **105** (2652), 809–811. (Cited on pages 3 and 6.)

Gourdain, N, Gicquel, L, Staffelbach, G, Vermorel, O, Duchaine, F, Boussuge, J-F & Poinsot, T 2009 High performance parallel computing of flows in complex geometries: I. Methods. *Comput. Sci. Discov.* **2**. (Cited on pages 30, 44, and 59.)

Hecht, F 2012 New development in freefem ++. *Journal of Numerical Mathematics* **20** (3), 251–265. (Cited on pages 24, 88, 160, and 199.)

Heil, Matthias 2004 An efficient solver for the fully coupled solution of large-displacement fluid-structure interaction problems. *Computer Methods in Applied Mechanics and Engineering* **193**, 1–23. (Cited on page 108.)

Heil, Matthias, Hazel, Andrew & Boyle, Jonathan 2008 Solvers for large-displacement fluid-structure interaction problems: Segregated versus monolithic approaches. *Computational Mechanics* **43**, 91–101. (Cited on page 108.)

Heinrich, H. 1956 Raymond l. bisplinghoff, holt ashley und robert l. halfman, aeroelasticity. ix + 860 s. m. 306 abb. cambridge 1955. addison-wesley publishing company, inc. preis geb. 14.50$. *ZAMM - Journal of Applied Mathematics and Mechanics / Zeitschrift für Angewandte Mathematik und Mechanik* **36** (7-8), 316–316. (Cited on page 102.)

Helenbrook, Brian T. 2003 Mesh deformation using the biharmonic operator. *International Journal for Numerical Methods in Engineering* **56** (7), 1007–1021. (Cited on page 106.)

Helfer, Thomas, Bleyer, Jeremy, Frondelius, Tero, Yashuk, Ivan, Nagel, Thomas & Naumov, Dmitri 2020 The MFrontGenericInterfaceSupport project. *Journal of Open Source Software* **5** (48). (Cited on page 91.)

Helmholtz, H. 1868 Über discontinuirliche flüssigkeitsbewegungen. *Monatsbericht Akad. Wiss. Berlin* **23**. (Cited on page 148.)

Henderson, Ronald D. 1997 Nonlinear dynamics and pattern formation in turbulent wake transition. *Journal of Fluid Mechanics* **352**, 65–112. (Cited on page 47.)

Hirt, C. W., Amsden, a. a. & Cook, J. L. 1974 An arbitrary Lagrangian-Eulerian computing method for all flow speeds. *Journal of Computational Physics* **14** (3), 227–253. (Cited on pages 44 and 57.)

Hoffman, J. & Johnson, C. 2006 A new approach to computational turbulence modeling. *Computer Methods in Applied Mechanics and Engineering* **195** (23), 2865–2880, incompressible CFD. (Cited on page 29.)

Holt, A. & Garabed, Z. 1956 Piston theory-a new aerodynamic tool for the aeroelastician. *Journal of the Aeronautical Sciences* **23** (12), 1109–1118. (Cited on page 101.)

Huerre, Patrick & Monkewitz, Peter a. 1990 Local and Global Instabilities in Spatially Developing Flows. (Cited on page 156.)

Hübner, Björn, Walhorn, Elmar & Dinkler, Dieter 2004 A monolithic approach to fluid–structure interaction using space–time finite elements. *Computer Methods in Applied Mechanics and Engineering* **193** (23), 2087–2104. (Cited on pages 123, 124, 126, and 127.)

Itoh, Motoyuki, Yamada, Yutaka, Imao, Shigeki & Gonda, Masahiro 1992 Experiments on turbulent flow due to an enclosed rotating disk. *Exp. Therm. Fluid Sci.* **5** (3), 359–368. (Cited on page 56.)

J N Reddy, D. 2005 *An Introduction to the Finite Element Method*. McGraw-Hill Education. (Cited on page 77.)

Kameier, Frank 1994 *Experimentelle Untersuchung zur Entstehung und Minderung des Blattspitzen-Wirbellärms axialer Strömungsmaschinen*, als ms. gedr. edn. Düsseldorf: VDI-Verl. (Cited on page 11.)

Kameier, F. & Neise, W. 1997 Rotating Blade Flow Instability as a Source of Noise in Axial Turbomachines. *Journal of Sound Vibration* **203** (5), 833–853. (Cited on page 11.)

Kang, Namcheol & Raman, Arvind 2004 Aeroelastic flutter mechanisms of a flexible disk rotating in an enclosed compressible fluid. *Journal of Applied Mechanics-transactions of The Asme - J APPL MECH* **71**. (Cited on page 20.)

Karman, T.V. 1921 Überlaminareundturbulentereibung.zeitschriftfürangew. *Math.undMech* **4**. (Cited on page 54.)

Kelvin, W.T. 1871 Hydrokinetic solutions and observations. *Philosophical Magazine* **42**. (Cited on page 148.)

Kleiser, L & Zang, T A 1991 Numerical simulation of transition in wall-bounded shear flows. *Annual Review of Fluid Mechanics* **23** (1), 495–537. (Cited on page 154.)

Kolmogorov 1991 The local structure of turbulence in incompressible viscous fluid for very large Reynolds numbers. *Proceedings of the Royal Society of London. Series A: Mathematical and Physical Sciences* **434** (1890), 9–13. (Cited on page 26.)

Koopman, G-H. 1967 The vortex wakes of vibrating cylinders at low reynolds numbers. *J. Fluid Mech.* **28** (3). (Cited on pages 48 and 49.)

Kármán, T. Von 1911 Über den mechanismus des flüssigkeits- und luftwiderstandes. *Göttinger Nachrichten, Math.-Phys* **509**. (Cited on page 42.)

Lance, G. N., Rogers, M. H. & Howarth, Leslie 1962 The axially symmetric flow of a viscous fluid between two infinite rotating disks. *Proceedings of the Royal Society of London. Series A. Mathematical and Physical Sciences* **266** (1324), 109–121. (Cited on page 54.)

Lefrançois, Emmanuel 2008 A simple mesh deformation technique for fluid–structure interaction based on a submesh approach. *International Journal for Numerical Methods in Engineering* **75**, 1085 – 1101. (Cited on page 106.)

Lesoinne, Michel & Farhat, Charbel 1996 Geometric conservation laws for flow problems with moving boundaries and deformable meshes, and their impact on aeroelastic computations. *Computer Methods in Applied Mechanics and Engineering* **134** (1), 71–90. (Cited on page 101.)

Lesoinne, M. & Farhat, C. 1998 Higher-order subiteration-free staggered algorithm for nonlinear transient aeroelastic problems. *AIAA Journal* **36** (9), 1754–1757. (Cited on page 113.)

Lilly, D 1967 Representation of small scale turbulence in numerical simulation experiments pp. 195–210. (Cited on page 29.)

Lilly, Douglas K 1966 On the Instability of Ekman Boundary Flow. (Cited on page 31.)

Logg, Anders, Mardal, Kent-Andre, Wells, Garth N. *et al.* 2012 *Automated Solution of Differential Equations by the Finite Element Method*. Springer. (Cited on page 91.)

Loiseau, J.-C. 2014 Dynamics and global stability analysis of three dimensional flows . (Cited on page 156.)

Lopez, Juan M, Marques, Francisco, Rubio, Antonio M & Avila, Marc 2009 Crossflow instability of finite Bo ¨ dewadt flows : Transients and spiral waves Crossflow instability of finite Bödewadt flows : Transients and spiral waves (November). (Cited on page 60.)

Lyapunov, A. M. 1992 The general problem of the stability of motion. *International Journal of Control* **55** (3), 531–534. (Cited on page 157.)

Maman, N. & Farhat, C. 1995 Matching fluid and structure meshes for aeroelastic computations: A parallel approach. *Computers Structures* **54** (4), 779–785. (Cited on page 101.)

Marquet, Olivier, Sipp, Denis & Jacquin, Laurent 2008 Sensitivity analysis and passive control of cylinder flow. *Journal of Fluid Mechanics* **615**, 221–252. (Cited on page 161.)

Martin, Seive, Jean-Michel, Nguyen Duc & Fonteyn, Patrice 2022 Stability of Hydrogen Turbopump Rotor Shaft Axially Self-Balanced. *Journal of Fluids Engineering* **144** (9), 1–11. (Cited on page 19.)

Matthies, Hermann G. & Steindorf, Jan 2002 Partitioned but strongly coupled iteration schemes for nonlinear fluid–structure interaction. *Computers Structures* **80** (27), 1991–1999. (Cited on page 112.)

Meirovitch, L. 1967 *Analytical Methods in Vibrations*. Macmillan. (Cited on page 197.)

Misdariis, A 2015 Schémas cinétiques réduits et couplage thermique pour les simulations aux grandes échelles du cliquetis dans les moteurs à piston. PhD thesis, INP Toulouse. (Cited on page 44.)

Mittal, Sanjay 2008 Global linear stability analysis of time-averaged flows. *International Journal for Numerical Methods in Fluids* **58** (1), 111–118. (Cited on page 158.)

Mittal, S. & Kumar, V. 2001 Flow-induced vibrations of a light circular cylinder at reynolds numbers 103to 104. *Journal of Sound and Vibration* **245** (5), 923–946. (Cited on page 53.)

Morkovin, M.V. 1964 Flow around a circular cylinder-kaleidoscope of chal- lenging fluid phenomena. *Proceedings of ASME Symposium on Fully Separated Flows, Philadelphia* **(unpublished)**, 102–119. (Cited on page 42.)

Moureau, Vincent, Lartigue, G., Sommerer, Y., Angelberger, C., Colin, O. & Poinsot, T. 2005 Numerical methods for unsteady compressible multi-component reacting flows on fixed and moving grids. *Journal of Computational Physics* **202** (2), 710–736. (Cited on pages 44 and 57.)

Newmark, NM. 1959 *A Method of Computation for Structural Dynamics.*. American Society of Civil Engineers. (Cited on page 84.)

Nguyen, L., Tuan, T. & Temarel, P. 2014 Numerical simulation of an oscillating cylinder in cross-flow at a reynolds number of 10,000: Forced and free oscillations. *Proceedings of the International Conference on Offshore Mechanics and Arctic Engineering - OMAE* **2**. (Cited on page 102.)

Nicoud, Franck, Benoit, Laurent, Sensiau, Claude & Poinsot, Thierry 2007 Acoustic Modes in Combustors with Complex Impedances and Multidimensional Active Flames. *AIAA Journal* **45** (2), 426–441. (Cited on page 21.)

Nicoud, Franck & Ducros, F 1999 Subgrid-scale stress modelling based on the square of the velocity gradient tensor. *Flow, Turbul. Combust.* **62** (3), 183–200. (Cited on page 29.)

Nobari, M.R.H. & Naderan, H. 2006 A numerical study of flow past a cylinder with cross flow and inline oscillation. *Computers Fluids* **35**, 393–415. (Cited on page 53.)

Norberg, C. 1987 Effects of reynolds number and a low-intensity free-stream turbulence on the flow around a circular cylinder. *Publication No. 87/2* pp. Department of Applied Thermodynamics and Fluid Mechanics, Chalmers University of Technology. (Cited on pages 42 and 43.)

Noun, M., Gicquel, L. & Staffelbach, G 2021 Global Stability Analysis of an Academic Rotor/Stator Cavity Subject to Periodic and Simple Wall Oscillations. *ASME TURBO EXPO 2021, Gas Turbine Technical Congress Exposition (GT2021-59188)* **Volume 9A**. (Cited on page 163.)

Oberth, H. 1924 Die rakete zu den planetenräumen. *Nature* **114** (2860), 270–270. (Cited on page 4.)

Opgenoord, Max, Drela, Mark & Willcox, Karen 2019 Influence of transonic flutter on the conceptual design of next-generation transport aircraft. *AIAA Journal* **57**. (Cited on page 102.)

Owen, J M & Rogers, R H 1989 Flow and Heat Transfer in Rotating Disc Systems, Volume 1 : Rotor-stator systems. (Cited on page 54.)

Pan, Jixing 1987 On the origin of rockets. *T'oung Pao* **73** (1), 2–15. (Cited on page 3.)

Parker, R. & Stoneman, S. A. T. 1985 An experimental investigation of the generation and consequences of acoustic waves in an axial flow compressor: Large axial spacings between blade rows. *Journal of Sound Vibration* **99** (2), 169–182. (Cited on page 11.)

Pereboom, H. P., van Beek, P. J. G. & Smeulers, J. P. M. 2016 Experimental Investigation of Fluid Structure Interaction of Impeller Like Disks in Super Critical Carbon Dioxide **Volume 7A: Structures and Dynamics**, v07AT27A009. (Cited on page 19.)

Persillon, H. & Braza, M. 1998 hysical analysis of the transition to turbulence in the wake of a circular cylinder by three-dimensional navier–stokes simulation. *Journal of Fluid Mechanics* **365**, 23–88. (Cited on pages 43, 44, and 46.)

Peskin, Charles S 1977 Numerical analysis of blood flow in the heart. *Journal of Computational Physics* **25** (3), 220–252. (Cited on page 104.)

Pier, B. 2002*a* On the frequency selection of finite-amplitude vortex shedding in the cylinder wake. *J. Fluid Mech.* p. 458. (Cited on page 158.)

Pier, Benoit 2002*b* On the frequency selection of finite-amplitude vortex shedding in the cylinder wake. *Journal of Fluid Mechanics* **458** (May 2002). (Cited on page 158.)

Pier, Benoît 2013 Transition near the edge of a rotating disk. *Journal of Fluid Mechanics* **737**, 1–9. (Cited on page 55.)

Pierrehumbert, R, T & Widnall, E 1982 The two- and three-dimensional instabilities of a spatially periodic shear layer **114**. (Cited on page 157.)

Pikhtov, S.V. & Smirnov, E.M. 1993 Boundary layer stability on a rotating disk with corotation of the surrounding fluid. *Fluid. Dyn.* **27**, 657–663. (Cited on page 63.)

Piperno, Serge & Farhat, Charbel 2001 Partitioned procedures for the transient solution of coupled aeroelastic problems – part ii: energy transfer analysis and three-dimensional applications. *Computer Methods in Applied Mechanics and Engineering* **190** (24), 3147–3170, advances in Computational Methods for Fluid-Structure Interaction. (Cited on page 114.)

Piperno, Serge, Farhat, Charbel & Larrouturou, Bernard 1995 Partitioned procedures for the transient solution of coupled aroelastic problems part i: Model problem, theory and two-dimensional application. *Computer Methods in Applied Mechanics and Engineering* **124** (1), 79–112. (Cited on pages 113 and 114.)

Placzek, A., Sigrist, J. & Hamdouni, A. 2009 Numerical Simulation of an Oscillating Cylinder in a Cross-Flow at Low Reynolds Number: Forced and Free Oscillations. *Computers and Fluids* **38**, 80–100. (Cited on pages 44, 46, 47, 50, 52, and 53.)

Prasad, Anil & Williamson, Charles H. K. 1996 The instability of the separated shear layer from a bluff body. *Physics of Fluids* **8** (6), 1347–1349. (Cited on page 43.)

Queguineur, Matthieu 2019 Dynamic mode tracking and control with a relaxation method. *Physics of fluids* **31**. (Cited on pages 11, 54, and 55.)

Queguineur, Matthieu 2020 Stability and control of unsteady phenomena in rotor/stator cavities using large eddy simulation. PhD thesis, PhD thesis Institut National Polytechnique de toulouse. (Cited on pages 11, 53, 56, 60, 61, 67, 68, 132, 157, 158, 160, 163, and 166.)

Queguineur, Matthieu, Bridel-Bertomeu, Thibault, Gicquel, Laurent & Staffelbach, Gabriel 2018 Local and Global Stability Analysis of an Academic Rotor/Stator Cavity. *Proceedings of ASME Turbo Expo 2018: Turbine Technical Conference and Exposition* **GT2018-750**, V02AT45A001. (Cited on page 166.)

Queguineur, Matthieu, Gicquel, L.Y.M., Dupuy, Fabien & Misdariis, Antony 2019 Dynamic mode tracking and control with a relaxation method. *Physics of Fluids* pp. 1–39. (Cited on page 69.)

Rayleigh, J.W.S.B. 1894 *The Theory of Sound*. *The Theory of Sound* v. 1. Macmillan. (Cited on page 155.)

Rayleigh, John William Strutt 1883 Investigation of the character of the equilibrium of an incompressible heavy fluid of variable density. *Proceedings of the London Mathematical Society* **14**, 170–177. (Cited on page 148.)

Reynolds, O. 1883 An experimental investigation of the circumstances which determine whether the motion of water shall be direct or sinuous, and of the law of resistance in parallel channels. *Philos. Trans. R. Soc.* **174**. (Cited on page 148.)

Richter, Thomas 2017 *Fluid-structure interactions*. Springer Cham. (Cited on page 76.)

Roman, J. E., Campos, C., Romero, E. & Tomas, A. 2019 SLEPc users manual. *Tech. Rep.* DSIC-II/24/02 - Revision 3.11. D. Sistemes Informàtics i Computació, Universitat Politècnica de València. (Cited on page 160.)

Rozov, Vladyslav, Volmering, Andreas, Hermanutz, Andreas, Hornung, Mirko & Breitsamter, Christian 2019 Cfd-based aeroelastic sensitivity study of a low-speed flutter demonstrator. *Aerospace* **6** (3). (Cited on page 102.)

Sadd, M.H. 2009 *Elasticity: Theory, Applications, and Numerics*. Elsevier Science. (Cited on page 77.)

Sagaut, Pierre 2006 *Large Eddy Simulation for incompressible flows*. Springer. (Cited on page 26.)

SCAI 2007 Mpcci user manual v3.0.6 . (Cited on page 127.)

Schlichting, H. 1933 Zur Enstehung der Turbulenz bei der Plattenströmung. *ZAMM 13* . (Cited on page 157.)

Schmid, Peter J 2010 Dynamic mode decomposition of numerical and experimental data. *J. Fluid Mech.* **656**, 5–28. (Cited on pages 37 and 60.)

Schmidt, Oliver T. & Towne, Aaron 2019 An efficient streaming algorithm for spectral proper orthogonal decomposition. *Computer Physics Communications* **237**, 98–109. (Cited on page 37.)

Schott, Benedikt, Ager, Christoph & Wall, Wolfgang A. 2018 A monolithic approach to fluid-structure interaction based on a hybrid eulerian-ale fluid domain decomposition involving cut elements. *CoRR* **abs/1808.00343**. (Cited on page 123.)

Schouveiler, L. 1998 Sur les instabilités des écoulements entre un disque fixe et un disque en rotation. PhD thesis, Université Aix-Marseille II. (Cited on page 64.)

Schouveiler, L 2001 Instabilities of the flow between a rotating and a stationary disk. *J. Fluid Mech.* **443**, 329–350. (Cited on page 56.)

Seguí, Luis M., Gicquel, L. Y.M., Duchaine, F. & De Laborderie, J. 2018 Importance of boundary layer transition in a high-pressure turbine cascade using les. *Proceedings of the ASME Turbo Expo* **2C-2018**, 1–10. (Cited on page 31.)

Serre, Eric, Crespo Del Arco, Emilia & Bontoux, Patrick 2001 Annular and spiral patterns in flows between rotating and stationary discs. *J. Fluid Mech.* **434**, 65–100. (Cited on pages 56 and 60.)

Serre, Eric, Tuliszka-Sznitko, Ewa & Bontoux, Patrick 2004 Coupled numerical and theoretical study of the flow transition between a rotating and a stationary disk. *Phys. Fluids* **16** (3), 688. (Cited on page 54.)

Séverac, Éric, Poncet, Sébastien, Serre, Éric & Chauve, Marie Pierre 2007 Large eddy simulation and measurements of turbulent enclosed rotor-stator flows. *Phys. Fluids* **19** (8), 1–47. (Cited on page 60.)

Shimura, Takashi, Kawasaki, Satoshi, Uchiumi, Masaharu, Kimura, Toshiya, Hayashi, Mitsuaki & Matsui, Jun 2013 Stability of an axial thrust self-balancing system. *Journal of Fluids Engineering, Transactions of the ASME* **135** (1), 1–7. (Cited on page 18.)

Shimura, Takashi, Kawasaki, Satoshi, Uchiumi, Masaharu, Kimura, Toshiya & Matsui, Jun 2012 Internal flow and axial thrust balancing of a rocket pump. *Journal of Fluids Engineering, Transactions of the ASME* **134** (4), 1–8. (Cited on page 18.)

Sieber, Moritz, Paschereit, Christian & Oberleithner, Kilian 2016 Advanced identification of coherent structures in swirl-stabilized combustors. *Journal of Engineering for Gas Turbines and Power* **139**. (Cited on page 37.)

Sigüenza, J., Mendez, S., Ambard, D., Dubois, F., Jourdan, F., Mozul, R. & Nicoud, F. 2016 Validation of an immersed thick boundary method for simulating fluid–structure interactions of deformable membranes. *Journal of Computational Physics* **322**, 723–746. (Cited on page 117.)

Sipp, Denis, Marquet, Olivier, Meliga, Philippe & Barbagallo, Alexandre 2010 Dynamics and Control of Global Instabilities in Open-Flows: A Linearized Approach. *Applied Mechanics Reviews* **63** (3), 030801. (Cited on page 161.)

Smith, David Macleish 1965 *Proceedings of the institution of mechanical engineers* . (Cited on page 10.)

Song, Zhi-Guang & Li, Feng-Ming 2014 Investigations on the flutter properties of supersonic panels with different boundary conditions. *International Journal of Dynamics and Control* **2** (3), 346–353. (Cited on page 102.)

Squire, Herbert Brian & Southwell, Richard Vynne 1933 On the stability for three-dimensional disturbances of viscous fluid flow between parallel walls. *Proceedings of the Royal Society of London. Series A, Containing Papers of a Mathematical and Physical Character* **142** (847), 621–628. (Cited on page 155.)

Stein, K., Tezduyar, Tayfun & Benney, R. 2003 Mesh moving techniques for fluid-structure interactions with large displacements. *Journal of Applied Mechanics* **70**, 58–63. (Cited on page 105.)

Stein, K., Tezduyar, Tayfun & Benney, Richard 2004 Automatic mesh update with the solid-extension mesh moving technique. *Computer Methods in Applied Mechanics and Engineering* **193**, 2019–2032. (Cited on page 105.)

Strouhal, V. 1878 Uber eine besondere art der tonerregung. *Wied, Anna. Phys. und Chem.* **3**, 216–251. (Cited on page 43.)

Séverac, E., Poncet, S., Serre, E. & Chauve, M.P. 2007 Large eddy simulation and measurements of turbulent enclosed rotor-stator flows,. *Phys. Fluids* **19**, 685–704. (Cited on page 56.)

Tezduyar, Tayfun E., Sathe, Sunil, Keedy, Ryan & Stein, Keith 2006 Space–time finite element techniques for computation of fluid–structure interactions. *Computer Methods in Applied Mechanics and Engineering* **195** (17), 2002–2027, fluid-Structure Interaction. (Cited on page 108.)

Theofilis, Vassilios 2011 Global Linear Instability. *Annual Review of Fluid Mechanics* **43** (1), 319–352. (Cited on page 157.)

Timoshenko, S.P. & Gere, J.M. 2012 *Theory of Elastic Stability*. Dover Publications. (Cited on page 149.)

Tollmien, W. 1931 Über die Enstehung der Turbulenz. *Engl. Transl. in NACA TM 609* . (Cited on page 157.)

Towne, Aaron, Schmidt, Oliver T. & Colonius, Tim 2018 Spectral proper orthogonal decomposition and its relationship to dynamic mode decomposition and resolvent analysis. *Journal of Fluid Mechanics* **847**, 821–867. (Cited on page 37.)

Tsiolkovsky, Konstantin 1903 The exploration of cosmic space by means of reaction device. *The Science Review* **3**. (Cited on page 3.)

Tuann, S. Y. & Olson, M. D. 1978 Numerical studies of the flow around a circular cylinder by a finite element method. *Computers and Fluids* **6**, 219–240. (Cited on page 47.)

Tuliszka-Sznitko, E & Zielinski, Artur 2007 Instability of the flow in rotating cavity. *J. Theor. Appl. Mech.* **45** (3), 685–704. (Cited on page 56.)

Tuliszka-Sznitko, E, Zielinski, A & Majchrowski, W 2009 Large Eddy Simulation of transitional flows in rotor/stator cavity. *Arch. Mech.* **61** (2), 95–120. (Cited on pages 54 and 56.)

Turek, Stefan & Hron, Jaroslav 2007 *Proposal for Numerical Benchmarking of Fluid–Structure Interaction Between an Elastic Object and Laminar Incompressible Flow*, , vol. 53, pp. 371–385. (Cited on pages 88 and 102.)

Turek, S., Hron, J., Mádlík, M., Razzaq, M., Wobker, H. & Acker, J. F. 2010 Numerical simulation and benchmarking of a monolithic multigrid solver for fluid-structure interaction problems with application to hemodynamics pp. 193–220. (Cited on page 108.)

Uyttersprot, Laura 2014 Inverse distance weighting mesh deformation. a robust and efficient method for unstructured meshes. *Master of Science Thesis Delft University of Technology* . (Cited on page 123.)

Vierendeels, Jan, Lanoye, Lieve, Degroote, Joris & Verdonck, Pascal 2007 Implicit coupling of partitioned fluid-structure interaction problems with reduce order models. *Computers Structures* **85**, 970–976. (Cited on page 111.)

Wall, W.A. & Ramm, E. 1998 Fluid-Structure Interaction Based upon a Stabilized (ALE) Finite Element Method. *Computational Mechanics-New Trends and Applications. Proc. 4th World Congress on Computational Mechanics, Idelsohn SR, On ate E, Dvorkin EN (eds.), CIMNE, Barcelona: Buenos Aires* . (Cited on pages 123, 126, and 127.)

Williamson, C. H.K. 1988 Defining a universal and continuous Strouhal-Reynolds number relationship for the laminar vortex shedding of a circular cylinder. *Physics of Fluids* **31** (10), 2742–2744. (Cited on page 46.)

Williamson, C H K 1996 Vortex dynamics in the cylinder wake. *Annual Review of Fluid Mechanics* **28** (1), 477–539. (Cited on pages 42 and 45.)

Wolf, K. & Brakkee, E. 1996 Proceedings. second mpi developer's conference pp. 130–137. (Cited on page 101.)

Woodhouse, J. 1991 Book Review: The physics of musical instruments. 1990, by T. D. Rossing and N. H. Fletcher. Berlin: Heidelberg, New York, London, Paris, Tokyo, Hong Kong: Springer-Verlag. 700 (app.) pp., 410 figures. Price DM 148, hardcover. ISBN 3 540 96947 0. *Journal of Sound Vibration* **147** (3), 549–550. (Cited on page 11.)

Zhao, Wei, Zhang, Di & Xie, Yonghui 2019 Vibration analysis of mistuned damped blades with nonlinear friction and contact. *Journal of Low Frequency Noise, Vibration and Active Control* **38**, 146134841983635. (Cited on page 63.)

Zielinska, B. J. A., Goujon-Durand, S., Dus˘ek, J. & Wesfreid, J. E. 1997 Strongly nonlinear effect in unstable wakes. *Phys. Rev. Lett.* **79**, 3893–3896. (Cited on page 158.)

Appendix A

Structural modal analysis validation

The goal of modal analysis is to determine the natural mode shapes and frequencies of a structure under free vibration. In the following, an undamped beam mathematically described by Eq. (1.0.2) is considered. The system is treated as a continuous one in which the beam mass is distributed along with the stiffness of the shaft. The equation of motion is expressed as per (Meirovitch (1967)) as follows,

$$\frac{d^2Y(x)}{dx^2} = \frac{M(x)}{EI}, \tag{1.0.1}$$

$$\frac{d^2}{dx^2}EI(x)\frac{d^2Y(x)}{dx^2} = q. \tag{1.0.2}$$

Where E is the modulus of rigidity of beam material, I is the moment of inertia of the beam cross-section, $Y(x)$ is displacement in y direction at distance s from fixed end and q is the external loading per unit length. This equation is referred to as the static beam equation also known as the Euler-Bernoulli equation.

For the cantilever beam shown in figure A.1, the following boundary conditions apply,

$$at\ x = 0,\ Y(x) = 0,\ \frac{dY(x)}{dx} = 0, \tag{1.0.3}$$

$$at\ x = l,\ \frac{d^2Y(x)}{dx^2} = 0,\ \frac{d^3Y(x)}{dx^3} = 0. \tag{1.0.4}$$

In the absence of a transverse load q, the free vibration equation can be solved using a Fourier decomposition on the displacement into the sum of harmonic vibrations of the

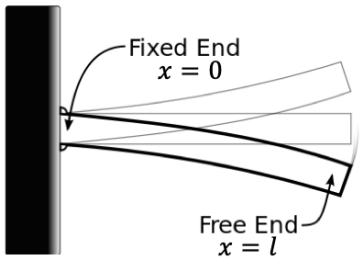

Figure A.1: A cantilever beam under free vibration.

form,

$$y'(x,t) = \mathrm{Re}[Y(x)e^{iwt}]. \tag{1.0.5}$$

replacing this decomposition in Eq. (1.0.2) and setting the right hand side term to zero, the equation of motion hence becomes,

$$\begin{aligned} \frac{d^4Y(x)}{dx^4} - \beta^4 Y(x) = 0, \\ \beta^4 = \frac{\omega^2 m}{EI}. \end{aligned} \tag{1.0.6}$$

The mode shapes for a continuous cantilever beam are given in $1D$ as,

$$Y_n(x) = A_n(sin\beta_n L - sinh\beta_n L)(sin\beta_n x - sin\beta_n x) + (cos\beta_n L - cosh\beta_n L)(cos\beta_n x - cosh\beta_n x) \tag{1.0.7}$$

Where $n = 1, 2, 3...\infty$ and $\beta_n L = n\pi$.
The closed form of the circular natural frequency ω_n from the above equation of motion and boundary conditions can be written as,

$$\omega_n = \alpha_n^2 \sqrt{\frac{EI}{mL^4}} \tag{1.0.8}$$

Where $\alpha_n = 1.875, 4.694, 7.885....$

One Considers a fixed-free $3D$ rectangular homogeneous beam. Its dimensions and mechanical properties summarized in Tables A.1 and A.2. Using the linear beam theory, the first four natural frequencies are calculated.

Geometric parameters		
L	20	m
B	0.5	m
H	1	m

Table A.1: Characteristic parameters of the cantilever beam.

Mechanical properties		
E	20	Pa
ρ_s	10^{-3}	m^3/Kg
I	0.0417	$Kg.m^2$

Table A.2: Mechanical properties of the beam.

	Natural frequencies (Theory)
Mode 1	$2.019\,Hz$
Mode 2	$4.0385\,Hz$
Mode 3	$12.65\,Hz$
Mode 4	$25.31\,Hz$

Table A.3: First four natural frequencies of the cantilever beam obtained via linear theory.

The modal analysis code is developed and solved in FreeFEM++ (Hecht (2012)). To do so, the generalized elastodynamic equation is recast in matrix form to model a multiple degrees of freedom linear mechanical system without damping and external forces, that is,

$$\mathbf{M}\ddot{U}_s + \mathbf{K}U_s = 0. \tag{1.0.9}$$

This is a second order homogeneous differential equation that can be solved by assuming the solutions to be of the form,

$$u_s = \hat{u}_s e^{i\omega_s t}. \tag{1.0.10}$$

Replacing the Fourier decomposition (1.0.10) in Eq. (1.0.9) yields a linear eigenvalue problem of the form,

$$[\boldsymbol{M}\omega^2 + \boldsymbol{K}]\boldsymbol{U}_s = 0. \tag{1.0.11}$$

Solving Eq. (1.0.11) yields the free vibrational responses of the system each being associated to the set of natural frequencies ω_s. To do so, one transforms the PDE into its variational or weak form. It results in the mass matrix $\mathbf{M}$ which corresponds to the unsteady term and the stiffness matrix $\mathbf{K}$ which corresponds to the stress tensor term so,

$$\boldsymbol{M} = \int_{\Omega_s} (\sigma(\mathbf{u}_s) : \epsilon_{ij}(\boldsymbol{\Psi}_s))d\Omega, \tag{1.0.12}$$

$$\boldsymbol{K} = \int_{\Omega_s} \rho_s((\mathbf{u}_s) \cdot (\boldsymbol{\Psi}_s))d\Omega. \tag{1.0.13}$$

where $\boldsymbol{\Psi}_s$ is a linear closed subspace of $H^1(\Omega_s^2)$, ρ_s is the density of the structure and λ_s and μ_s are the Lamé coefficients. $\mathbf{u}_s(x_i)$ is the vector of modal displacements. After taking into account the Fourier decomposition of Eq. (1.0.10), the weak form of Eq. (1.0.9) for the displacement $\mathbf{u}_s(x_i) \in \boldsymbol{\Psi}_s$ is,

$$-\int_{\Omega_s} (\sigma(\mathbf{u}_s) : \epsilon_{ij}(\boldsymbol{\Psi}_s))d\Omega = \omega_s^2 \int_{\Omega_s} \rho_s((\mathbf{u}_s) \cdot (\boldsymbol{\Psi}_s))d\Omega, \tag{1.0.14}$$

$$-\int_{\Omega_s} (\lambda_s \boldsymbol{\nabla} \cdot \mathbf{u}_s \boldsymbol{\nabla} \cdot \boldsymbol{\Psi}_s + 2\mu_s \epsilon_{ij}(\mathbf{u}_s) : (\boldsymbol{\Psi}_s))d\Omega = \omega_s^2 \int_{\Omega_s} \rho_s((\mathbf{u}_s) \cdot (\boldsymbol{\Psi}_s))d\Omega \quad \forall \boldsymbol{\Psi}_s \in V. \tag{1.0.15}$$

Solving this eigenvalue problem yields the natural frequencies associated to a structure fixed in a certain reference frame.

In the following, the natural frequencies and the corresponding mode shapes of the beam are calculated using FreeFEM++. the computational domain is shown on Fig. A.2 and its characteristics are summarized in Tab. A.4.

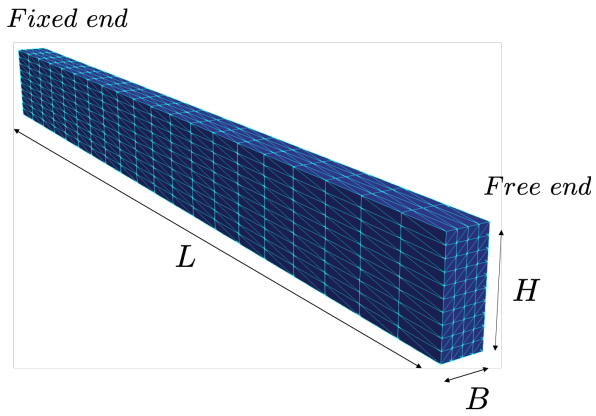

Figure A.2: Computational domain of the cantilever beam.

	Mesh characteristics
Number of elements in the x direction N_x	20
Number of elements in the y direction N_y	4
Number of elements in the z direction N_z	10
Total number of cells N_{cells}	4800
Number of $P1$ nodes	1155
Number of $P2$ nodes	7749

Table A.4: Mesh characteristics of the cantilever beam.

Table A.5 shows a comparative summary of the mode frequencies obtained by FreeFEM++ and linear beam theory. Excellent agreement is found between the two approaches. The first four mode shapes of the cantilever beam are shown on Fig. A.3. The first and fourth vibration modes constitute a bending around the strong axis y, whereas the second and third vibration modes constitute a bending moment around the weak axis z.

	Natural frequencies (FreeFEM++)	Natural frequencies (theory)
Mode 1	2.019 Hz	2.019 Hz
Mode 2	4.03 Hz	4.04 Hz
Mode 3	12.64 Hz	12.65 Hz
Mode 4	25.04 Hz	25.3 Hz

Table A.5: First four natural frequencies of the cantilever beam obtained by FreeFEM++ and linear beam theory.

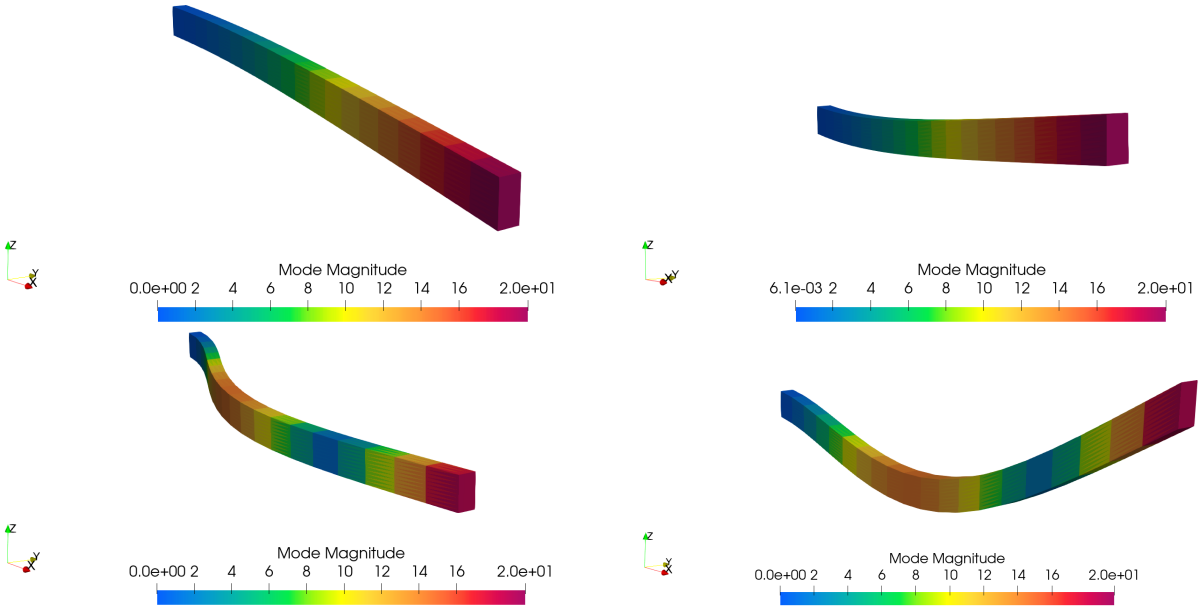

Figure A.3: The first four eigenmodes of the cantilever beam.

Appendix B

Global stability equation for a rotating flow

Linearizing the Navier-Stokes equations in the cylindrical polar coordinate system and introducing the normal mode decomposition in (r, θ, z), one obtains the following scalar equations,

$$\begin{cases} \left(\partial_r + \dfrac{1}{r}\right)\hat{u}_r + i\beta\hat{u}_\theta + \partial_z\hat{u}_z = 0, \\ \left(-i\omega + U_b\partial_r + i\beta V_b + W_b\partial_z + \partial_r U_b - \dfrac{1}{Re}\left(\partial_{zz} - \beta^2 + \partial_{rr} + \dfrac{\partial_r}{r} - \dfrac{1}{r^2}\right)\right)\hat{u}_r \\ \qquad + \dfrac{2m}{r^2 Re}\hat{u}_\theta + \partial_z U_b\hat{u}_z + \partial_r\hat{p} = 0 \\ \left(-i\omega + U_b\partial_r + i\beta V_b + W_b\partial_z + \partial_r U_b - \dfrac{1}{Re}\left(\partial_{zz} - \beta^2 + \partial_{rr} + \dfrac{\partial_r}{r} - \dfrac{1}{r^2}\right)\right)\hat{u}_\theta \\ \qquad - \dfrac{2m}{r^2 Re}\hat{u}_r + \partial_r V_b\hat{u}_r + \partial_z V_b\hat{u}_z + i\beta\hat{p} = 0 \\ \left(-i\omega + U_b\partial_r + i\beta V_b + W_b\partial_z + \partial_z W_b + \dfrac{1}{Re}\left(\partial_{zz} + \beta^2 - \partial_{rr} + \dfrac{\partial_r}{r}\right)\right)\hat{u}_z \\ \qquad \partial_r W_b\hat{u}_r + \partial_z\hat{p} = 0, \end{cases} \tag{2.0.1}$$

These equations can be solved numerically for a given azimuthal wavenumber m.

Proceedings of the ASME 2021 Turbo Expo: Turbomachinery Technical Conference & Exposition Turbomachines for Clean Power and Propulsion Systems
GT2021
June 7-11, 2021, Pittsburgh, USA

GT2021-59188

GLOBAL STABILITY ANALYSIS OF AN ACADEMIC ROTOR/STATOR CAVITY SUBJECT TO PERIODIC AND SIMPLE WALL OSCILLATIONS

Mark Noun[1,2]*, Laurent Gicquel[1], Gabriel Staffelbach[1]

[1]CFD Team CERFACS
Toulouse, France
mnoun@cerfacs.fr
[2]CNES/DLA
Paris, France

ABSTRACT

Complex unsteady phenomena can appear in turbomachinery components and result in the self-sustained oscillatory motion of the fluid as found in aeronautical engines or rocket turbopumps for example. The origin of these oscillations often results from the complex coupling between flow non linearities and structure motion generating major risks for the operation of the engine and even undermining its components. For instance, in turbines, the internal components that are most liable to vibrate are the blades and discs. In this context, it is critical to understand the effect of the vibrating components on the flow stability in rotor/stator cavities. In order to address this problem, an academic rotor/stator cavity subject to periodic wall oscillations is investigated in the current paper where the frequency of the vibrations are imposed and correspond to the previously identified unstable fluid modes inside the cavity. The objective is to understand the behavior of the flow when subject to a periodic forcing imposed by the rotor motion. To do so, predictive numerical strategies are established based on Large Eddy Simulation (LES) in conjunction to a global stability analysis which seem to be a promising method to capture flow instabilities. Focus is here brought to the underlying pressure fluctuations found inside the cavity using spectral analysis complemented with the global stability analysis, demonstrating that such tools can address forced flow problems. More specifically and for all simulations, the results of the global stability analysis are compared to a Dynamic Mode Decomposition (DMD) of LES predictions by reconstructing the corresponding modes through a spatio-temporal approach showing that the new fluid limit cycles present modes that shift or completely disappear compared to the unforced case, the forcing mechanism altering the stability of the entire system.

Nomenclature

Acronyms

ALE	Arbitrary Langrangian Eulerian Method
CFL	Courant Friedrichs Lewis
DMD	Dynamic Mode Decomposition
GLSA	Global Linear Stability Analysis
LES	Large Eddy Simulation
PSD	Power Spectral Density
SGS	Sub-Grid Scale
TTGC	Two-Step Taylor Galerkin C
WALE	Wall Adaptive Local Eddy-viscosity

Greek Symbols

δ	Boundary layer characteristic scale	m
∇	Gradient operator	–
$\nabla.$	Divergence operator	–
∇^2	Laplace operator	–
ν	Kinematic viscosity	$m^2.s^{-1}$
Ω	Angular velocity	$rad.s^1$
ω	Complex frequency	–

Other Symbols

F_0	Frequency of rotation	Hz
f_0	Forcing frequency	Hz
G	Aspect ratio	-
h	Cavity height	m
m	Azimuthal wavenumber	–

*Address all correspondence to this author.

p'_i	Pressure perturbation	$Kg.m.s^{-2}$
P_b	Base flow pressure	$Kg.m.s^{-2}$
r	Radial coordinates	m
R_0	Internal radius	m
R_1	External radius	m
Re	Reynolds number	-
t	time	s
u'_i	Perturbations velocity components	m/s
u_i	Velocity components	m/s
$U_{b,i}$	Base flow velocity components	m/s
z	Axial coordinate	m
z_{max}	Amplitude of vibration	m
z_t	Instantaneous axial position of the rotor	m

INTRODUCTION

A major task in the development of rocket turbopumps is to ensure that that the moving components, such as the blades or discs, as well as the static components have no extreme vibration problem. This means that during the design phase of such devices, the structural integrity of the different components should be maintained at the operating point. This involves frequency calculations and stress analysis. A standard practice is to avoid disc and blade frequencies that are close or multiple of the running speed, the resulting is a Campbell diagram where the frequencies for different running conditions are plotted versus rotor speed. Vibrations in turbomachinery can be split into two types: local vibration and machine vibration. The former refers to the vibration of local components such as the blades or discs of a turbine, whereas the latter involves widespread motion of the rotor and/or stator which induces periodic reactions at the bearings hence causing the static components to vibrate [1]. The origin of these vibrations can also be classified into two classes: imposed or self-excited; depending on whether the vibration is the result of an imposed disturbance such as a rotor experiencing a cyclic pressure fluctuation due to the rotation of the blades in a steady non-uniform field in the azimuthal direction [2], or the disturbance is the consequence of an instability such as flutter or aeroelastic instability which occurs at or near the natural frequency of the rotor blade. The local vibration of the simple academic rotor/stator cavity is studied in this paper by imposing two frequencies previously identified as unstable fluid modes by Bridel [3] based on the use of Large eddy Simulation (LES) and local stability analysis . The presence of these unstable fluid modes were later confirmed by Queguineur *et al.* [4] through a global stability analysis which were the main driver of the rotational instability. Although the problem is exacerbated by the complexity of real world industrial applications, numerous experimental and numerical studies have been dedicated to enclosed rotor/stator cavities which serve as a preliminary model for turbomachinery devices [5] [6] . From a stability analysis perspective, enclosed rotating flows at high Reynolds number develop an intrinsic instability at their limit cycle highlighted by the existence of three dimensional structures taking the form of spiral vortices. Recent experimental and numerical studies (Serre *et al.* [5] [7], Sévrac *et al.* [8], Tuliszka *et al.* [6]) have revealed the existence of these three dimensional patterns. Particular attention is put in the present work on the effect of forced vibration in an enclosed rotor/stator cavity on flow dynamics with special focus on the instabilities that arise in the flow. To do so, two different Large Eddy simulations are carried out on the annular academic cavity introduced by Tuliszka *et al.* [9] and used by Bridel [3] by imposing a certain sinusoidal function for the displacement of the rotor. The frequencies of vibration chosen correspond to the previously identified most unstable modes by Quegineur [4]. Second, a Dynamic Mode Decomposition [10] (DMD) is used whereby successfully showing that the flow dynamics can be captured and the spatial distribution of the spiral patterns can be reconstructed for such forced case. This is also corroborated by using pointwise pressure spectral density analysis thanks to the inherent three dimensional structure of the spiral patterns. Finally, a global stability analysis is conducted on both forced cases subsequently demonstrating that the forcing in the flow has indeed altered its stability hence showing that new modes arises and others disappear.

The paper is organised as follow: The geometric configuration as well as the moving mesh technique are presented in Section 2. The Large Eddy Simulations are discussed and compared with the Dynamic Mode Decomposition of the flow at different heights inside the cavity in section 3. Then, in Section 4, a description of the base flow obtained from LES is given followed by a detailed analysis of the global stability results.

THE GEOMETRIC CONFIGURATION

The configuration of interest is presented on Fig. 1. It is an academic rotor/stator cavity of height h composed of two smooth discs: the rotor and stator. The former rotates at a constant angular velocity $\Omega = 2\pi F_0$ (F_0 is the frequency of the rotor) about the z-axis whereas the latter is stationary and are delimited by a cylindrical shroud at $r = R_1$. The cavity also comprises an annulus of radius R_0 that rotates at the same speed as the rotor. The curvature parameter R_m is usually used to define annular cavities. In the present case $R_m = 1.8$ and is equal to the one used by Sévrac *et al.* [8] experimentally and by Tuliszka *et al.* [11] numerically. The mean flow inside the cavity is driven by the geometrical parameter G that is the aspect ratio of this cavity where $G = h/\Delta R$ ($\Delta R = R_1 - R_0$), and the global Reynolds number $Re_G = \Omega R_1^2/\nu$ where ν is the kinematic viscosity of the fluid. The value of the aspect ratio G is often used in the literature and its value is here fixed so it is a first order approximation of a real turbomachine model [7] [6]. All the geometric and physical parameters are summarized in Table 1.

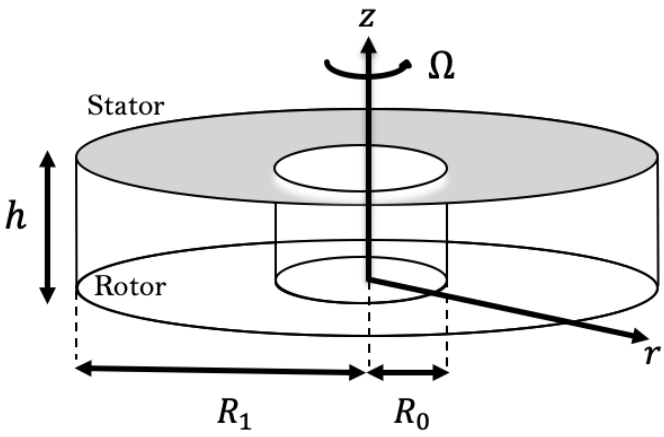

FIGURE 1: Scheme of the academic annular rotor/stator cavity.

TABLE 1: Characteristic parameters of the Tuliszka cavity.

Internal Radius R_0	71 *mm*
External Radius R_1	250 *mm*
Cavity Height h	35 *mm*
Aspect Ratio G	0.2
Curvature parameter R_m	1.8
Angular Velocity Ω	315 rad/s
Global Reynolds Number Re_G	10^5

NUMERICAL METHOD

Boundary conditions and mesh

In order to create the mesh of the configuration shown on Fig. 1, a $2D$ annular disk made of fully unstructured triangular elements is built and extruded in the z direction. Fig. 2a shows a horizontal cut of the cavity. Mesh clustering is carefully taken into consideration to minimize errors at the walls where interactions are important. Note that the final $3D$ mesh is consequently made of only prismatic elements that are equally distant in the z direction. Regarding the movement of the rotor, the Arbitray Langrangian Eulerian (ALE) description given by Hirt *et al.* [12] and implemented in the code by Moureau *et al.* [13] is used. The ALE is a technique that combines the best features of both the Lagrangian and Eulerian approaches. In this framework it allows the nodes to move in the continuum in a normal Langrangian fashion, or be moved in an arbitrary way to provide a continuous banding capability. This freedom in the computational allows a greater deformation of the continuum compared to a Lagrangian approach with a superior resolution than the one allowed by the Eularian method. This method has already been validated on piston engine experiments [14] and in rotating channels [15]. The ALE is implemented in this case by first defining three zones in the mesh configuration as shown on figure Fig. 2b.

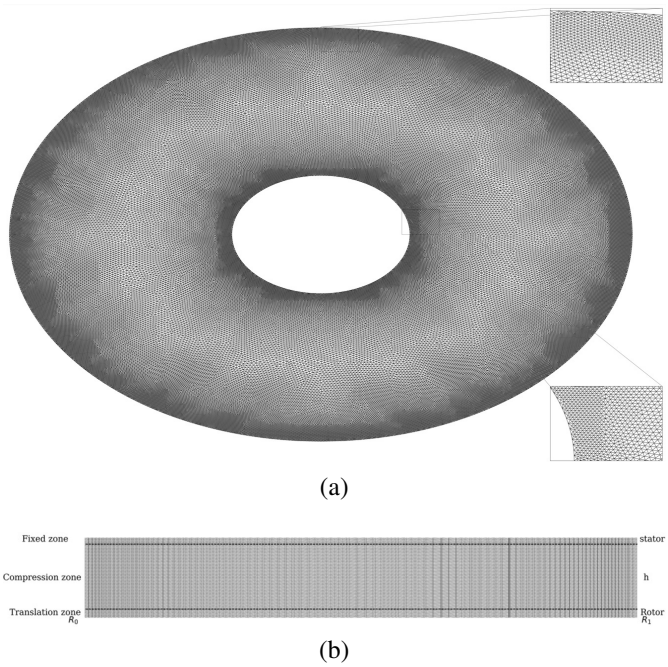

(a)

(b)

FIGURE 2: Transverse cut of the mesh at mid cavity (a), vertical cut of the mesh with the different blocks used

The zones are defined in such a way to facilitate the use of the moving mesh procedure when the rotor oscillates, as well as to preserve the quality of the mesh at the walls by maintaining a first grid node wall normal coordinate $z^+ < 5$ as advised for LES, and by limiting mesh distortion as much as possible. Grid independence tests have already been by Bridel [16] using the same configuration and numerical solver. However, the configuration of the zones and cells have been built according to the observations made in this study. The zone containing the rotor is made of all the first 10 mesh elements in the axial direction and moves in translation along the z direction according to the following imposed velocity function:

$$z_{(t)} = z_{max}|sin(2\pi f_0 t)|, \tag{1}$$

Where $z_{(t)}$ is the instantaneous position of the rotor in space, z_{max} is the maximum amplitude of vibration and f_0 is the frequency

of vibration imposed in Hertz (Hz). In the compression zone all mesh elements move in translation and deform linearly according to the position of rotor. Finally, the zone around the stator is fixed meaning the the nodes do not move inside this region. This zone is defined by taking the first five mesh elements relative to the stator in the z direction to also maintain the quality of the mesh at the wall.

Regarding the treatment of boundary conditions, all walls are adiabatic. Radial and axial no slip conditions are applied on the rotating disc and shaft hence in the system of cylindrical coordinates (r,θ,z) this translates to $u_r = u_z = 0$ and $u_\theta = r\Omega$. A slip-wall condition is enforced on the stationary disc and shroud where $u_r = u_z = u_\theta = 0$.

Large eddy simulation

The code chosen for the simulation is avbp [17] which is a massively parallel code widely used in theoretical and applied research capable of solving the full compressible Navier-Stokes equations using a finite-element scheme TTGC [18] based on a two steps Taylor-Galerkin formulation. This scheme has very low diffusion and dispersion properties making it appropriate for LES by providing a third order accuracy in time and space. The time step in the simulation is not fixed, therefore it is dictated by the acoustic Courant Friedrichs Lewy number (CFL). In the present simulations, the CFL number is set to 0.7 hence 438 time steps are approximately needed for each cycle of vibration for Case 1 and 397 for Case 2. The LES Sub-Grid Scale (SGS) model used is the Wall Adapting Local Eddy-viscosity (WALE) [19] which is suitable for wall bounded flows and capable of yielding better wall stress rate prediction as well as turbulent intensity compared to the classical Smagorinsky [20] model.

The flow field is governed by the Navier–Stokes equations, which translates the following for a Newtonian incompressible fluid:

$$\nabla \cdot u = 0 \tag{2a}$$

$$\frac{\partial u}{\partial t} + (u.\nabla)u = -\nabla p + \frac{1}{Re}\nabla^2 u \tag{2b}$$

This system of differential equations is thereby solved in a cylindrical coordinates reference frame (r,θ,z) where $\nabla \cdot x$, ∇x and $\nabla^2 x$ denote respectively the divergence gradients and Laplace operators. It is also worth mentioning that the rotor axial motion which is taken into account by the fluid model written in the (ALE) formulation introduced previously, slightly modifies the convective term in the Navier-Stokes equations by introducing an additional term related to the mesh velocity. Hence this term is changed to : $[(u-w).\nabla)]u$ where w is the mesh velocity. For both cases used in this study the fluid is initially at rest and the rotor is at its initial position. At time $t = 0$ the rotor is brought to its rotation speed $\Omega = 2\pi F_0\ rad/s$ and the fluid accelerates due to viscous entrainment. At that same instant the stator starts to vibrate. Numerical convergence is obtained when the kinetic energy inside the cavity reaches a plateau when the rotor has completed 30 rotations.

Now that all the computational details are set, the flow inside the cavity can be analyzed. As mentioned earlier, the two cases treated in this study differs only in the forcing frequency imposed where for the first case $f_0 = 3.24F_0$ and for the second one $f_0 = 3.61F_0$. These frequencies correspond to the two most unstable fluid modes found inside the cavity by [21] through LES and linear stability analysis. The amplitude of vibration imposed correspond to $A = 0.057h$. For instance, forced vibration issued from mistuned bladed disks can lead to an axial vibration amplitude of the blades in the range of $0.035h - 0.057h$ depending on the operating conditions of the turbomachine and the structural properties of the rotor as demonstrated by Zhao *et al.* [22].

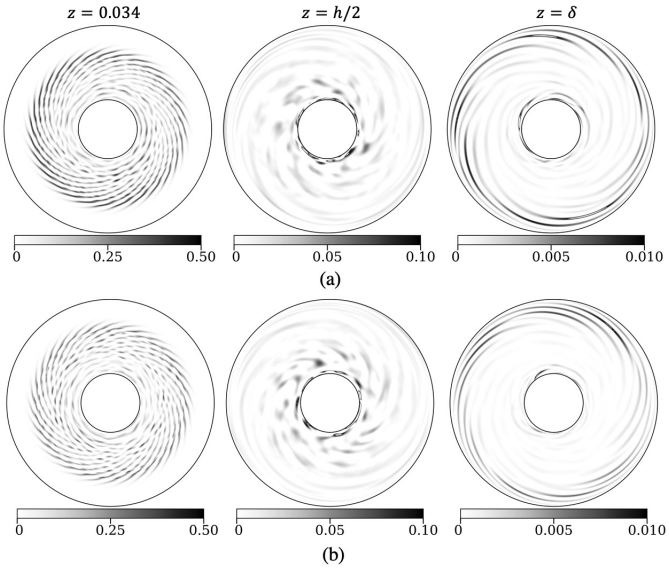

FIGURE 3: Two-dimensional isocontours of the axial velocity fluctuation $u'_z = uz - \langle u_z \rangle$ of Case 1 $f_0 = 3.24F_0$ (a) and Case 2 $f_0 = 3.61F_0$ (b) at different heights inside the cavity (the values are normalized by their corresponding maximum axial velocity fluctuation.

Figure 3 shows $2D$ cuts relative to the rotor of the axial velocity fluctuation $u'_z = u_z - \langle u_z \rangle$ where u_z is the instantaneous axial velocity and $\langle u_z \rangle$ is the mean axial velocity. The boundary layer height δ is measured for the mean flow relative to the rotor average position after one period. The axial velocity fluctuation is an important parameter here because when instability arises in

the flow, the base flow which is stable departs from a purely parallel flow and the perturbations around it can be measured by the magnitude of u_z'. In both cases LES seems to capture the instability pattern as demonstrated by Bridel [3] and Serre [7]. Near the stator boundary layer ($z = 0.034$) of Figure 3, both cases feature the same instability patterns as demonstrated by the outward propagation of spiral vortices starting at $r \approx 0.13$ towards the shroud at $r \approx 0.2$, whereas near the hub at $0.071 < r < 0.13$ a set of dislocated circular patterns are identified. The former instability is three dimensional and is referred to as type I instability, whereas the latter can be interpreted as a type II instability [23] . These two instabilities arise in the flow due to two distinct bifurcations that yield this system of spiral rolls coexisting with the circular one [24]. The statoric boundary layer features 28 and 30 arms spiral structures for case 1 and case 2 respectively existing at high radii whereas near the hub these spiral structures turn into a quasi-concentric annular ones. For the rotating boundary layer, the magnitude of u_z' is small in general due to important viscous forces at the wall that play a role in damping the axial velocity fluctuation. However, at high radii and near the shroud, inertial forces appear to overcome the viscous forces at the wall and their magnitude is relatively higher. The spiral patterns are also identified in this case as co-winding rotating vortices that propagate inward toward to inner wall. The mid-height of the cavity exhibits low amplitude of axial velocity fluctuation in general with a slightly higher activity near the hub and the flow appears to be spatially organized similar to the rotor boundary layer. It is worth to note also that at all heights of the cavity the magnitude of the axial velocity fluctuation is small compared to its maximum value due to the rotor vibration.

Dynamic Mode Decomposition

To further investigate the underlying structures and their stability found by numerical simulation, a widely used modal decomposition in fluid dynamics known as Dynamic Mode Decomposition [10] (DMD) is applied on both cases. The DMD is able to extract the dynamical features of the flow through a sequence of snapshots as well as their corresponding frequencies and growth rate. This coupled spatio-temporal analysis acts like a global stability analysis for linearized flow problems while accurately describing the motion of the flow. A signal with a duration of $1s$ containing all the necessary flow data is taken at steady state after approximately 196 cycles of vibration for Case 1 and 216 cycles for Case 2. This signal contains a sequence of 120 equi-spaced snapshots that are sufficient for the solution to converge. Figure 4 represents the most energetic modes constituting Case 1. Two modes appear to be dominant the inside the cavity. At the stator boundary layer, the first one has a temporal frequency of $F = 3.64F_0$ and a wave number of $m = 28$. It is made of counter-winding vortices starting at $r \approx 0.13$ m, where approximately 3 cylindrical vortices exist around the hub, and propagate outward. This mode appears to coexist with the second one that has a temporal frequency of $F = 4.64F_0$ and the same cylindrical vortices as found in the first mode. In the core of the cavity the two modes appear to shift to a different radial location mainly around the hub and shroud. Overall their magnitude is very low compared to the modes found near the statoric boundary layer. The mode $F = 3.64F_0$ appears to mark the middle of the cavity with 6 spiral vortices compared to 5 for the mode $F = 4.64F_0$. At the rotor boundary layer the flow seems to exhibit modal patterns at the same radial interval as the core of the cavity. Nevertheless, for the two modes, the axial velocity fluctuation seems to be stronger near the shroud as demonstrated by approximately 12 spiral arms for the mode $F = 3.64F_0$ and 10 spiral arms for the mode $F = 4.64F_0$. As previously shown on Fig. 3, the LES predictions appear to match the patterns found by DMD for the mode $F = 3.64F_0$. this mode was also retrieved by Bridel [3] and Quegineur [21] for the same cavity excluding the vibration of the rotor. However, the annular mode found previously had its frequency shifted by $1.4F_0$.

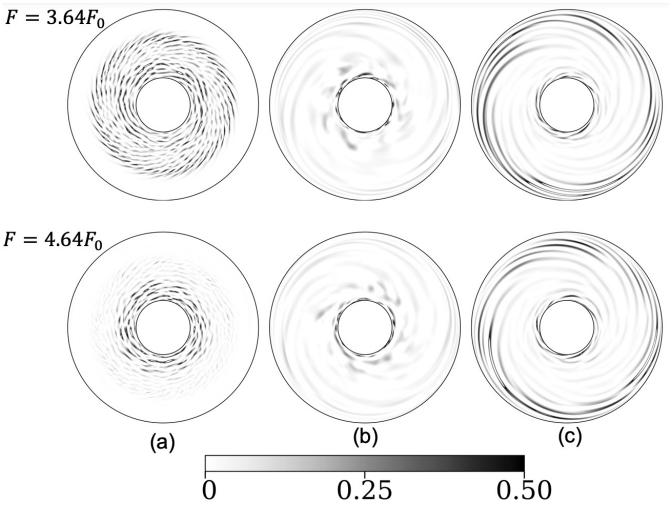

FIGURE 4: Isocontours of the mode amplitude $\hat{u}_z \in [0, 0.5]$ at $z = 0.034$ m (a), $z = h/2$ (b) and $z = \delta$ (c) for the two major DMD modes constituting Case 1.

Fig. 5 shows the isocontours of the axial velocity mode amplitude $\hat{u}_z$ of the DMD modes constituting Case 2. The most energetic modes retrieved correspond to $F = 3.26F_0$ and $F = 5F_0$. The former has also been identified by Bridel [3] and Quegineur [21] in the same cavity as annular mode where the rotor is not vibrating; whereby the latter has emerged and appears to dominate inside the cavity as shown in the LES predictions on Fig. 3b. Both modes exhibit the same radial distribution of

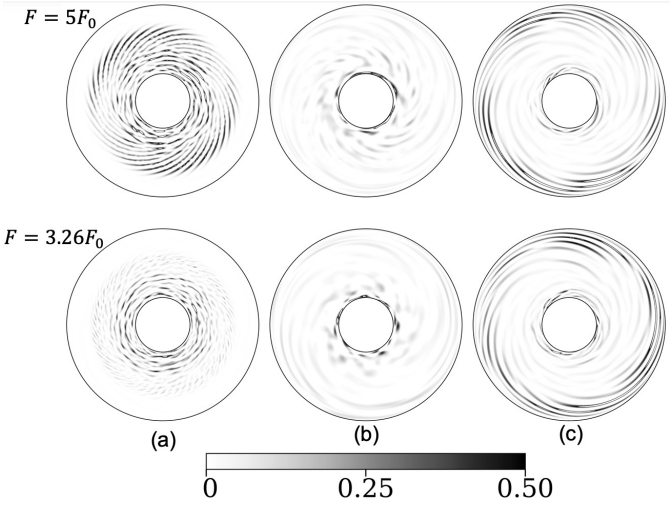

FIGURE 5: Isocontours of the mode amplitude $\hat{u}_z \in [0, 0.5]$ at $z = 0.034$ m (a), $z = h/2$ (b) and $z = \delta$ (c) for the two major DMD modes constituting Case 2.

the modal structures at the rotor boundary layer and the core of the cavity. Near the stator the mode $F = 5F_0$ is characterized by 30 spiral vortices with less dominant cylindrical ones near the hub. The second mode yield the opposite structure organization, a quasi-concentric dislocated circular waves near the hub and spiral arms of negligible magnitude. These preliminary results indicate that the hydrodynamic modes responsible for the flow instability can react due to a forcing of the flow at a matching frequency.

Spectral analysis

The spectral content of the flow and the frequencies responsible for the underlying instabilities can be directly monitored through a point-wise power spectral density that is carried out on multiple numerical probes spread radially and in azimuth at the rotor and stator boundary layer, as well as at the core of the cavity. The objective is to confirm that the driving modes present in the flow are coherent with the Dynamic Mode Decomposition (DMD). Unlike the DMD, this method does not provide the spatial distribution of the modes but can provide a rich spectral content of the flow in real time as well as their corresponding intensity whereby validating the previously identified frequencies. Due to the inherent three dimensional structures of the present patterns (azimuthal and axial distribution) inside the cavity; only the spectral content of the modes present near the stator boundary layer is presented, the core of the cavity and the rotating boundary layer express the same spectral content in terms of frequency but with a slightly different amplitude. A total of 5 circles of 60 probes each are spread in the axial direction of the two discs boundary layers at $z = \delta$ and $z = h - \delta$ as well as the mid section of the cavity at $z = h/2$. Figures. 6 and 7 show the location of the numerical probes in the cavity used to extract all the relevant data and the power spectral density (PSD) of the axial velocity fluctuation u'_z. The power spectral density (PSD) of a signal provides the variation of its intensity in terms of power or energy over an entire range of frequency. The nomenclature C_iP_j will be used to refer to the current probes where $i \in [1,5]$ denotes the number of the circle and $j \in [0,15]$ the number of the probe point. Three

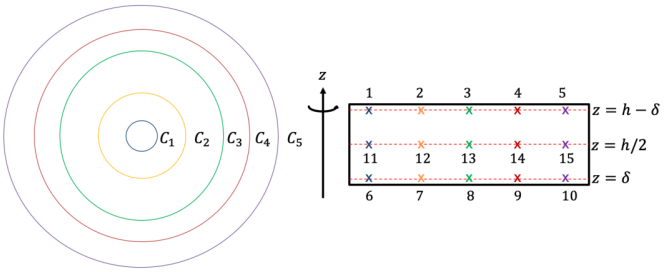

FIGURE 6: Location of the numerical probes in the cavity associated with Case 1 and Case 2 (not to scale). Numbering of the circles match the color of the probes and the corresponding PSD signal.

main frequencies can be identified in Case 1, *i.e.* $3.24F_0$, $3.61F_0$ and $4.7F_0$, and in Case 2, *i.e.* $3.24F_0$, $3.61F_0$ and $5F_0$, all other frequencies are either harmonics or linear combination of these modes that contribute to noise in the system. The magnitude of the peaks appear to be consistent with the radial distribution of the three dimensional patterns inside the cavity. For Case 1 the mode $3.61F_0$ appears to be the same mode identified in the DMD as $3.64F_0$ and the main driver of the statoric instability shown by LES predictions on Fig. 3 . Indeed, this mode is present at $0.13 < r < 0.2$ where the highest peaks of axial velocity PSD are identified by C_3P_0. The emerging mode $4.7F_0$ that is mostly concentrated around the hub, has also its highest axial velocity PSD magnitude present in that region as shown by the point C_1P_0. Finally the frequency of vibration imposed $f_0 = 3.24F_0$ is retrieved which perturbates the flow the most in the region between C_1P_0 and C_3P_0. The constituent frequencies of Case 2 match the ones retrieved by DMD with three major peaking frequencies *i.e.* $3.24F_0$, $3.61F_0$ and $5F_0$. The mode $3.24F_0$ corresponds in this case to the hydrodynamic mode characterized by circular spirals near the hub subsequently yielding the highest peak at the point $C1P_0$ with a magnitude of 40 db. The forcing frequency $f_0 = 3.61F_0$ is also present alongside a build up of a frequency at around $4F_0$. This frequency does not appear to have any contribution in the DMD spectrum hence it might be linked to noise inside the system. The dominant frequency found in the station-

ary disc by LES is identified by the PSD as a peak at $5F_0$ with a magnitude of 60 db between C_2P_0 and C_3P_0. In general both PSD spectrums have the same order of magnitude ($60db$ to $95db$) with the second one having it slightly higher.

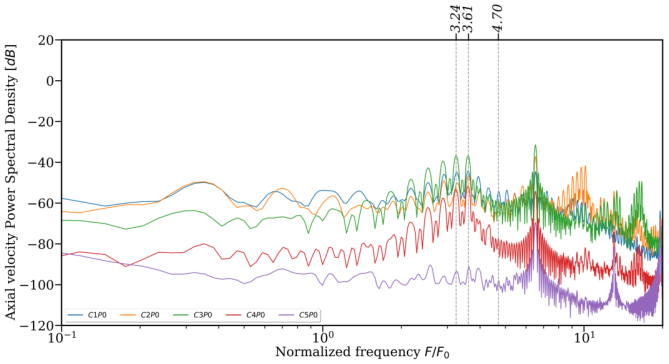

(a)

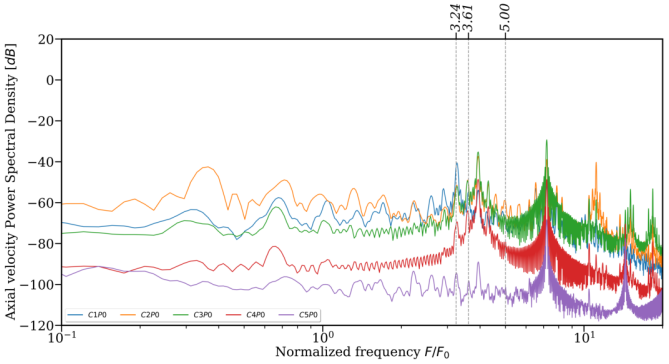

(b)

FIGURE 7: Power Spectral densities of the axial velocity fluctuations u'_z in the statoric boundary layer ($z = h - \delta$) registered by probes C_1P_0 to C_5P_0 of Case 1 ($f_0 = 3.24F_0$) (a) and Case 2 ($f_0 = 3.61F_0$) (b).

LINEAR STABILITY ANALYSIS

Base Flow

In order to gain more insight about the underlying dynamics of the flow and the stability of the dominant modes inside the system, a global linear stability analysis is applied on Case 1 and Case 2. In linear stability theory, the analysis is done around a base flow which is the solution for the corresponding Navier-Stokes equations that model a specific system. In this case, the base flow is defined by the following fields that must be known, *i.e.* velocity $U_b(r,\theta,z,t)$, pressure $P_b(r,\theta,z,t)$ and temperature $T_b(r,\theta,z,t)$. These fields define the basic flow. For instance, analytical solutions can be taken to solve simple hydrodynamic problems. Tollmien [25] and Schlichting [26] defined the analytical solutions of the Orr-Sommerfeld equations that are derived from the full Navier-Stokes equations by making several simplifying assumptions [26]. One of these assumptions is that a flat plate boundary layer can be modelled as a parallel flow. However for complex flow problems the mean flow has proven to be a good substitute for the base flow, and flow non-linearities and the structures of the fluctuations can be predicted by linear stability analysis [27] [28]. Quegineur [4] also succeeded in performing a global local linear stability analysis on this cavity, excluding the motion of the rotor in the axial direction, and found good agreement between the two methods by taking the mean flow as solution for the Navier-Stokes equations. To alleviate the computational cost of the problem, the stability analysis is performed in 2D, hence the mean flow is obtained by taking the temporal and azimuthal averages (the mean flow is not axisymmetric) of the flow as well as the average position of the rotor during multiple periods at the flow limit cycle.

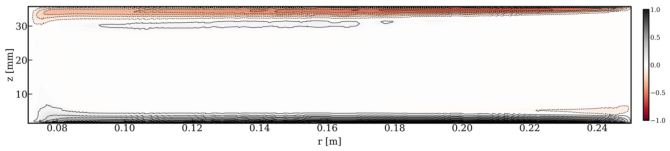

(a)

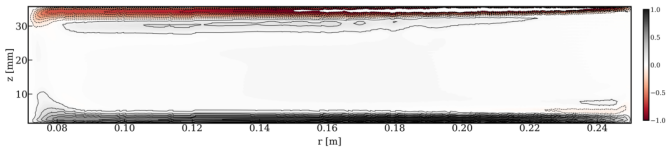

(b)

FIGURE 8: Base flow contour of the time and azimuthal averaged radial velocity component normalized by its maximum magnitude Case 1 (a) and Case 2 (b).

Figure 8 shows the normalized average radial velocity component of Case 1 and Case 2 which is positive at the rotor boundary layer and negative in the statoric one. Forcing in the flow has altered the base flow in both cases and in different ways. Indeed, at the rotor boundary layer the hub and the shroud seem to have a stronger effect on the organization of the flow for Case 2, a higher frequency of vibration generated more turbulence in this region. The two statoric boundary layer also seem to be affected by the hub where their thickness is relatively the highest in this region.

Global linear stability analysis

In the global stability analysis, the dynamics of the small amplitude perturbations around the mean flow is analyzed while relying on the weakly parallel flow assumption [29] [30]. According to Lyapunov [31], a fluid system can be stable if an infinitesimal perturbation around the base flow stays infinitesimal over time and does not grow, or if the perturbed flow stays around the base flow. Note that linear stability analysis can also yield the physical features of the small perturbations *i.e.* frequency and growth rate. The global governing equations for any azimuthally periodic flow are obtained provided that:

First the 2D base flow is defined:

$$U_b = (U_{b,r}(r,z), U_{b,\theta}(r,z), U_{b,z}(r,z)), \tag{3a}$$

$$P_b = P_b(r,z). \tag{3b}$$

Flow variables are then decomposed into a steady axisymmetric base flow and an unsteady three dimensional perturbation following the global decomposition:

$$\begin{cases} U(r,\theta,z,t) = U_b + u'(r,\theta,z,t), \\ P(r,\theta,z,t) = P_b + p'(r,\theta,z,t) \end{cases} \tag{4}$$

The linear stability analysis is then obtained by linearizing the Navier-Stokes equations around the base flow. Subsequently, the equation obtained is linear and homogeneous, so the perturbed variables can be written in the form:

$$[u'_r, u'_\theta, u'_z, p'] = [\hat{u}_r, \hat{u}_\theta, \hat{u}_z, \hat{p}](r,z)\exp\{[i(m\theta - \omega t)]\} \tag{5}$$

These global modes are then injected in the linearized Navier-Stokes equations. The 2D global modes can be obtained by solving the eigenvalue problem for a given set of boundary conditions. In our case, Dirichlet conditions are applied for the velocity perturbations and Neumann conditions are used the pressure. The global stability analysis is performed using the code *GIFIE* [3] which is capable of discretizing the eigenvalue problem using FreeFem++ [32], an open source tool focused on solving partial differential equations using the finite element method.

The eigenvalue problem defined earlier is solved to obtain all the normal modes along with their frequencies and amplifications at each wavenumber. Figures 9 and 10 show a plot of the frequency and growth rates of the most unstable modes at each wavenumber m for Case 1 and Case 2. For the first case, four distinct regions can be identified on Figure 9. The most unstable mode of the first branch corresponds to the axisymmetric mode $m = 0$ that has a frequency of $4.71F_0$. The mode $m = 28$ can also be identified in the fourth branch as having a frequency of

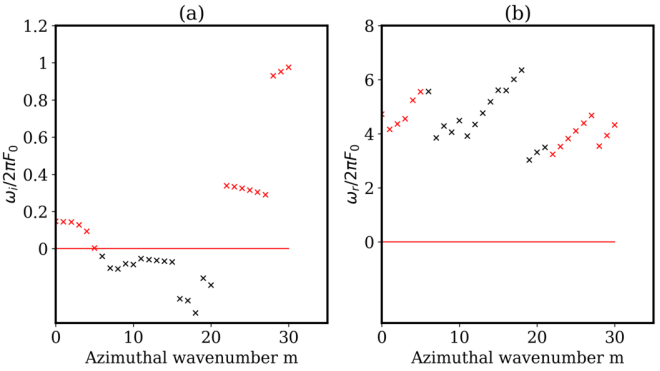

FIGURE 9: Scatter plot of the temporal growth rate (a) and the frequency (b) versus the azimuthal wavenumber m of the linear global modes obtained for Case 1. The ordinate values have been normalized by the pulse of the rotor $2\pi F_0$.

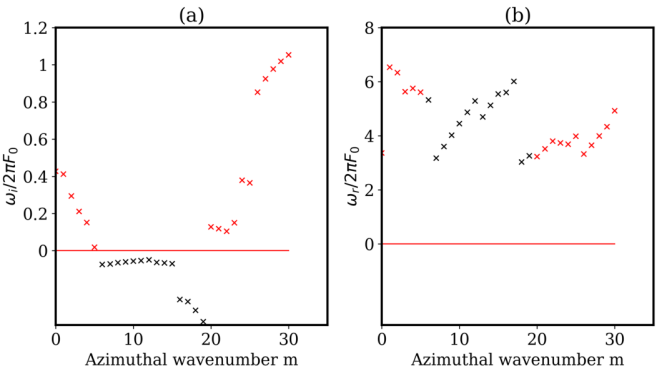

FIGURE 10: Scatter plot of the temporal growth rate (a) and the frequency (b) versus the azimuthal wavenumber m of the linear global modes obtained for Case 2. The ordinate values have been normalized by the pulse of the rotor $2\pi F_0$.

$3.6F_0$. Even though it does not have the highest growth rate, it is the only mode that imposes its spatial organization in the stator boundary layer as shown previously by LES. Similarly for Case 2, the axisymmetric mode $m = 0$ is the most unstable one for the first branch and has a frequency of $3.3F_0$. The second mode with he wavenumber $m = 30$ is also retrieved and has the highest amplification rate in the system for a frequency of $4.92F_0$. The normal modes obtained clearly reflect the presence of the two distinct rotational instabilities identified by LES and DMD. To further understand the results obtained by the global linear stability analysis, the spatial organization of these modes are presented and compared to a dynamic mode decomposition (DMD) where each mode is projected on its corresponding wavenumber.

Note that the forcing frequency for both cases is retrieved by the stability analysis. However the study is here restricted to the fluid modes only.

For Case 1, the spatial organization for the 2D axial velocity modes are represented on Fig. 11 for the wavenumbers $m = 0$ and $m = 28$. A good agreement is found between the DMD and the global linear stability. For the mode $m = 0$, the annular vortices identified by LES and DMD on the circular cuts are also highlighted in this region. Furthermore, a strong recirculation zone is identified near the hub throughout the cavity, this was also shown on the rotor boundary layer and the core of the cavity. The mode $m = 28$ is expressed by the spiral arms located at $0.13 < r < 0.21$ of the stator boundary layer as shown on Fig. 8a. Indeed, this mode appears to be dominant within the stationary disc only as demonstrated by the global stability analysis the DMD projection on to this specific wavenumber. Note also that the frequencies retrieved by the GLSA and DMD for the two modes are quite similar *i.e.* $4.71F_0$ and $4.6F_0$ for $m = 0$, $3.6F_0$ and $3.61F_0$ for $m = 28$.

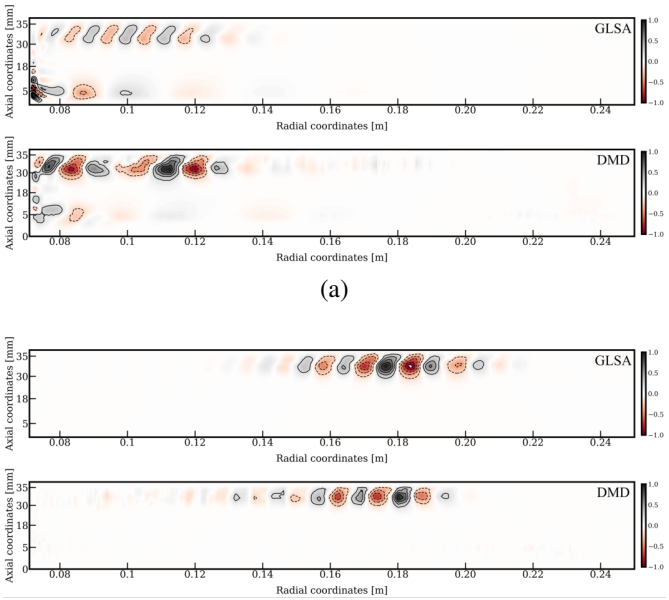

(a)

(b)

FIGURE 11: 2D shape of the axial velocity mode $\hat{u_z}$ obtained by GLSA and compared with the DMD for the two wavenumbers $m = 0$ (a) and $m = 28$ (b) (Case 1)

For Case 2 and as shown by Fig. 12, the 2D mode shape of the axial velocity mode $\hat{u_z}$ obtained by the global linear stability analysis and Dynamic Mode Decomposition (DMD) coincide. The spatial organization of the mode $m = 0$ seems to comply with both methods except for the region near the rotor

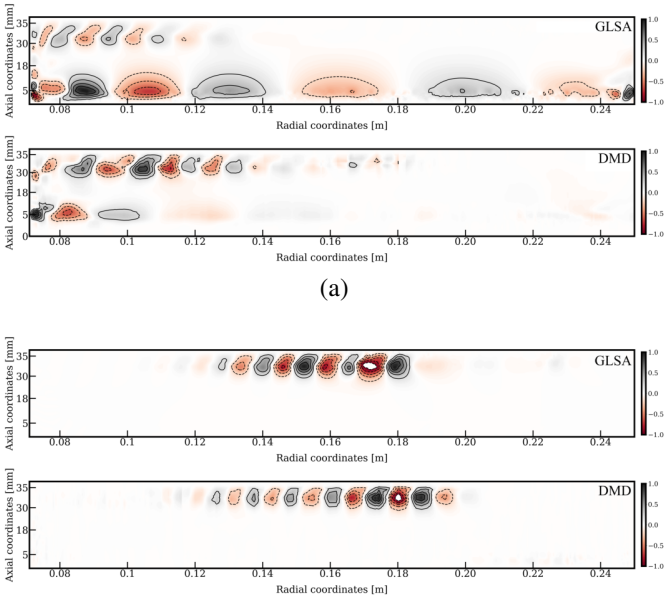

(a)

(b)

FIGURE 12: 2D shape of the axial velocity mode $\hat{u_z}$ obtained by GLSA and compared with the DMD for the two wavenumbers $m = 0$ (a) and $m = 30$ (b) (Case 2)

where the GLSA yields a higher mode amplitude. However, the frequencies retrieved remain similar: $3.3F_0$ and $3.24F_0$ with the DMD. Both spatial distributions furthermore agree with the fact that for this mode, the region with the highest fluctuations expressed by circular vortices is concentrated near the stationary disc for $0.071 < r < 0.12$ and near the hub at very low radii. The magnitude of the mode near the rotating disc is relatively small, this is also valid for the axial velocity fluctuation as explained in the second section. Note that this mode has also been found by Quegineur [4] *via* local and global stability analyses. The second mode pulsates at a frequency of $4.92F_0$ for a wavenumber of $m = 30$, close to the one found by DMD which is at $5F_0$. Its presence is essentially found near the stationary disc for $0.13 < r < 0.20$ where the spiral vortices are manifested. To conclude, just like the stationary case of Quegineur [4], the global linear stability analysis (GLSA) and Large Eddy Simulation (LES) offer mean to access flow modes populating a limit-cycle even in forced conditions.

CONCLUSION

Rotating flow instabilities are an intrinsic phenomenon in enclosed cavities that depend on the Reynolds number *Re*, the geometric configuration of the cavity and its boundary conditions. These instabilities can have a major impact on the structural integrity of a turbomachine. It is therefore crucial to understand

how they work in real life applications. To do so, the local vibration of a rotor for an academic rotor/stator cavity is assessed by imposing two frequencies that correspond to the most unstable fluid modes inside the corresponding cavity of the non-forced case. First Large Eddy simulations are produced to access the flow responses of these two forced cases, showing that new instabilities emerge in the system whereas others disappear. Dynamic Mode Decomposition [10] successfully captured the perturbation of the flow confirming the shape of these new instabilities. Furthermore, pointwise spectral density analyses performed at different locations inside the cavity confirm the wide range of oscillations inside the system . Finally a 2D global linear stability is shown to be able to find the most unstable modes and their shape for the two cases hereby capturing the new modes in the system although it is externally forced. To conclude, the present results confirm that the content, although subject to a external forcing, can be used to analyze forced limit cycles. This opens the door to the use of dedicated control strategies as proposed by Quegineur [21].

ACKNOWLEDGMENT

This study was supported by a grant from the French Space Agency (CNES) and ArianeGroup. We would like to thank both institutions for their financial and technical support for this project. We gratefully thank A. Brandely (ArianeGroup) and S. Le Martelot (CNES) for a fruitful collaboration.

REFERENCES

[1] D., S., 1965. "VIBRATIONS IN TURBO-MACHINERY". *Proceedings of the institution of mechanical engineers*.

[2] Baumgartner M., Kameier F., H. J., 1995. "Non-Engine Order Blade Vibration in a High Pressure Compressor". *Twelfth International Symposium on Airbreathing Engines*.

[3] T., B.-B., 2016. "Investigation of unsteady phenomena in rotor/stator cavities using large eddy simulation,". PhD thesis, INP Toulouse.

[4] Queguineur M., Bridel-Bertomeu T., G. L. S. G., 2018. "Local and global stability analysis of an academic rotor/stator cavity". *Proceedings of ASME Turbo Expo 2018,* ***GT2018-750***.

[5] Serre E., Tuliszka-Sznitko E., B. P., 2004. "Coupled numerical and theoretical study of the flow transition between a rotating and a stationary disk". *Phys. Fluids,* ***16***, p. 688.

[6] Tuliszka-Sznitko E., Z. A., 2007. "Instability of the flow in rotating cavity,". *J. Theor. Appl. Mech.,* ***45***, p. 685–704.

[7] Serre E., Crespo Del Arco E., B. P., 2001. "Annular and spiral patterns in flows between rotating and stationary discs". *J. Fluid Mech.,* ***434***, pp. 65–100.

[8] Séverac É., Poncet S., S. E. C. M.-P., 2007. "Large eddy simulation and measurements of turbulent enclosed rotor-stator flows,". *Phys. Fluids,* ***19***, p. 685–704.

[9] Tuliszka-Sznitko E., Serre E., B. P., 2002. "On the nature of the boundary layers instabilities in a flow between a rotating and a stationary disc,". *Comptes Rendus Mécanique,* ***330***, pp. 91–99.

[10] Schmid, P., 2010. "Dynamic mode decomposition of numerical and experimental data". *J. Fluid Mech.,* ***656***, pp. 5–28.

[11] Tuliszka-Sznito E., Zielinski A., M. W., 2009. "Large Eddy Simulation of transitional flows in rotor/stator cavity.". *Arch. Mech.,* ***61***, pp. 95–120.

[12] Hirt, C. W., Amsden, a. a., and Cook, J. L., 1974. "An arbitrary Lagrangian-Eulerian computing method for all flow speeds". *Journal of Computational Physics,* ***14***(3), pp. 227–253.

[13] Moureau, V., Lartigue, G., Sommerer, Y., Angelberger, C., Colin, O., and Poinsot, T., 2005. "Numerical methods for unsteady compressible multi-component reacting flows on fixed and moving grids". *Journal of Computational Physics,* ***202***(2), pp. 710–736.

[14] Misdariis, A., Vermorel, O., and Poinsot, T., 2015. "A methodology based on reduced schemes to compute autoignition and propagation in internal combustion engines". *Proc. Combust. Inst. ,* ***35***(3), pp. 3001–3008.

[15] Fransen, R., Vial, L., and Gicquel, L. Y. M., 2013. "Large Eddy Simulation of Rotating Ribbed Channel". In ASME Turbo Expo 2013: Turbine Technical Conference and Exposition, no. GT2013-95076.

[16] Bridel-Bertomeu T., Gicquel L., S. G., 2016. "Wall modeled LES and its impact on rotor/stator cavity unsteady features". *Proceedings of ASME Turbo Expo 2016*.

[17] Schønfeld, T., and Rudgyard, M., 1999. "Steady and unsteady flows simulations using the hybrid flow solver avbp". *AIAA Journal ,* ***37***(11), pp. 1378–1385.

[18] Colin, O., and Rudgyard, M., 2000. "Development of high-order taylor-galerkin schemes for unsteady calculations". *J. Comput. Phys. ,* ***162***(2), pp. 338–371.

[19] Nicoud, F., and Ducros, F., 1999. "Subgrid-scale stress modelling based on the square of the velocity gradient". *Flow,Turb. and Combustion,* ***62***(3), pp. 183–200.

[20] Smagorinsky, J., 1963. "General circulation experiments with the primitive equations: 1. the basic experiment.". *Mon. Weather Rev.,* ***91***, pp. 99–164.

[21] Quegineur, M., 2020. "Stability and control of unsteady phenomena in rotor/stator cavities using Large Eddy Simulation". PhD thesis, INP Toulouse.

[22] Zhao W., Zhang D., Y. X., 2019. "Vibration analysis of mistuned damped blades with nonlinear friction and contact". *Journal of Low Frequency Noise, Vibration and Active Control,* ***38***, pp. 1505–1521.

[23] Pikhtov S.V., S. E., 1993. "Boundary layer stability on a ro-

tating disk with corotation of the surrounding fluid". *Fluid. Dyn.,* ***27***, pp. 657–663.
[24] Schouveiler, L., 1998. "Sur les instabilités des écoulements entre un disque fixe et un disque en rotation". PhD thesis, Universite Aix-Marseille II.
[25] Tollmien, W., 1931. "Über die Enstehung der Turbulenz". *Engl. Transl. in NACA TM 609*.
[26] Schlichting, H., 1933. "Zur Enstehung der Turbulenz bei der Plattenströmung". *ZAMM 13*.
[27] Pier, B., 2002. "On the frequency selection of finite-amplitude vortex shedding in the cylinder wake". *J. Fluid Mech.*, p. 458.
[28] Hu C., Yang X., Z. X. D. Z., 2018. "Stability and structural sensitivity analysis of the turbulent flow in the narrow vaneless diffuser with mean flow method". *Computers Fluids*.
[29] Theofilis, V., 2011. "Global linear instability". *Annu. Rev. Fluid Mech,* ***43***, pp. 319–352.
[30] Pierrehumbert R., W. E., 1982. "The two and three-dimensional instabilities of a spatially periodic shear layer". *J. Fluid Mech.,* ***97***.
[31] Lyapunov, A., 1992. "The general problem of the stability of motion". *International Journal of Control,* ***3***, pp. 531–534.
[32] Hecht, F., 2012. "New development in freefem++". *Journal of Numerical Mathematics,* ***3***, pp. 251–265.

RÉPUBLIQUE FRANÇAISE
Liberté
Égalité
Fraternité

Université de Toulouse

Titre : Prédiction et mitigation des instabilités de cavités issues de l'interaction fluide-structure

Mots clés : CFD, stabilité hydrodynamique, interaction fluide-structure, turbomachines, Aeroélasticité, SGE

Résumé : Les phénomènes complexes et instationnaires au sein des cavités rotor/stator des turbopompes spatiales sont renommées en raison de leur capacité à engendrer des problèmes de vibrations ayant un impact dangereux sur le fonctionnement des moteurs. Ces dynamiques, couramment désignées sous le terme de "bandes de pression", résultent d'un mouvement oscillatoire du fluide, induisant un couplage avec la structure environnante, posant ainsi un risque significatif sur le fonctionnement de la turbopompe. L'objectif principal de cette thèse est de comprendre et de prédire numériquement l'origine de ces "bandes de pression" dans un contexte multiphysique. Dans cette optique, cette étude initie une investigation numérique et théorique des problèmes de vibrations forcées au sein d'une cavité académique, ainsi que des problèmes d'interaction fluide-structure, en mettant l'accent sur les instabilités hydrodynamiques et aéroélastiques. Ces écoulements se caractérisent intrinsèquement par leur tridimensionalité, principalement en raison de la présence de couches limites sur le rotor, le stator et le carénage de la cavité. En conséquence, l'instabilité se manifeste sous forme de structures cohérentes, à la fois axisymétriques et/ou sous formes de spirales, qui peuvent être influencées par des forces dynamiques générées soit par la fusée elle-même soit par la turbopompe. Des expériences ont démontré que les écoulements dans les cavités axiales des turbopompes présentent un autre type d'instabilité provoquant un phénomène de flottement du rotor. Ces deux problèmes sont abordés dans cette étude en utilisant une simulation des grandes échelles (SGE), une approche dynamique des fluides numériques instationnaire. Cet outil a en effet révélé que la dynamique sous-jacente de l'écoulement peut être retrouvée, contrairement aux approches stationnaires telles que les simulations de type Navier-Stokes moyennées de Reynolds (RANS). Grâce à cette prédiction, il est démontré que l'instabilité de l'écoulement à l'intérieur d'une turbopompe à hydrogène à échelle réduite est liée à des tourbillons qui présentent le potentiel de se coupler avec le rotor ainsi qu'avec l'acoustique de la cavité. Ce couplage tripartite entre le fluide, le rotor et la cavité est spécifiquement traité en développant un code de mécanique des structures permettant des analyses modales ainsi que des calculs élastodynamiques. Grâce à l'ensemble de ces outils numériques, des problèmes de vibrations forcées sont d'abord étudiés en utilisant une configuration simple comprenant une géométrie cylindrique. Ce premier volet de l'étude est ensuite étendu aux écoulements de cavité en rotation fermée, où la vibration du rotor provoque un décalage des modes hydrodynamiques et, dans certains cas, une suppression totale de ces modes. En réaction à ces réponses de l'écoulement seul, et pour aborder le context multiphysique, le solveur de mécanique des structures est couplé au code LES grâce à une chaîne de couplage numérique. Cette approche permet de résoudre des problèmes instationnaires et couplés fluide-structure. La stratégie de couplage adoptée est d'abord validée avec succès à l'aide de deux cas test: une poutre vibrante immergée dans un fluide immobile et un cas de vibration induite par les tourbillons (VIV). Le solveur couplé est ensuite utilisé pour simuler l'interaction fluide-structure entre le rotor et l'écoulement interne de la turbopompe. Les résultats confirment le couplage vibroacoustique entre le fluide, le disque du rotor et la cavité, tel qu'observé lors des expériences. Cette simulation multiphysique a également permis de calculer la quantité nécessaire d'amortissement pour stabiliser un tel système, démontrant ainsi l'efficacité du couplage développé. Enfin, un cadre d'analyse de stabilité linéaire globale (GLSA) est détaillé et mis en oeuvre pour fournir un aperçu des modes propres dominants et de leurs taux de croissance correspondants à l'intérieur de ces systèmes.

Title: Prediction and mitigation of cavity instabilities resulting from fluid-structure interactions

Key words: hydrodynamic stability, CFD, fluid-structure interaction, turbomachinery, Aeroelasticity, LES

Abstract: Complex unsteady phenomena within rotor/stator cavities of space turbopumps have gained notoriety because of their propensity to induce vibration issues that are clearly detrimental to the operation of the engine. This problem has indeed rendered the development and operation of rocket engines a formidable undertaking. These dynamics, referred to as 'pressure bands', are a consequence of a self-sustained oscillatory motion of the working fluid, thereby engendering a coupling with the solid structure posing a paramount risk to the operation of the turbopump and the structural integrity of its components. Understanding and predicting the source of 'pressure bands' in a multiphysics context is the primary objective of this thesis. For instance, this work provides a numerical and theoretical investigation of forced vibration problems in enclosed rotating flows as well as fluid-structure interaction problems with a focus on hydrodynamic and aeroelastic instabilities. Note that these flows are inherently three dimensional due to the presence of boundary layers on the impeller, stator and cylindrical shroud. Consequently, at high Reynolds numbers, the flow instability is manifested through coherent axisymmetric and/or spiral structures that can be affected by dynamic loads either generated by the rocket or the turbopump itself. Experiments have shown that axial cavity flows also exhibit a different type of instability that lead to a flutter-like phenomena of the rotor. Both problems are addressed in this work using Large Eddy Simulation, an unsteady CFD approach, in conjunction to multiple predictive numerical strategies. All tools show that the underlying dynamics of the flow can be retrieved contrarily to steady approaches like Reynolds Averaged Navier-Stokes Simulations (RANS) that failed in the past to predict such phenomena. Thanks to LES flow only prediction, the flow instability inside a reduced scale hydrogen turbopump is retrieved and has the potential of coupling with the rotor as well as the acoustics of the cavity. To address this problem, a structural mechanics code based on the finite element method is developed to perform modal analyses as well as elastodynamic calculations. Thanks to all these numerical tools, forced vibration problems are first investigated using a bluff body configuration where a 'lock-in' phenomenon is identified whenever a vortex shedding frequency converges to the forced vibration frequency. This first content of this study is later extended to enclosed rotating cavity flows where the vibration of the rotor causes a shift in the hydrodynamic modes and in some cases, a total suppression of these modes. Following these flow only responses and to go further, the structural mechanics solver is further developed and coupled to the LES code thanks to a numerical coupling chain that allows to solve fully unsteady and fully coupled fluid-structure interaction problems. The adopted coupling strategy is first successfully validated through two test cases: a vibrating beam immersed in a still fluid demonstrating that the fluid viscosity dampens the structure motion and brings it back to its initial position, and a Vortex Induced Vibration (VIV) case where a Kármán vortex street sheds from a rigid square and causes large amplitude vibrations of an elastic plate. The coupled solver is then used to simulate the fluid-structure interaction between the rotor disk and working fluid of the turbopump. Results confirm the vibroacoustic coupling between the fluid, rotor disk and cavity obtained by experiments. This multiphysics simulation also allowed the calculation of the necessary amount of damping to stabilize such system demonstrating the capability of the developed coupling. To finish, a Global Linear Stability Analysis (GLSA) framework is detailed and performed to give more insight about the leading eigenmodes and their corresponding growth rate inside such systems.